Uranous sulfate precipitation as a novel route to uranium purification in extractive metallurgy

by

Alexander D. Burns

B.Sc. Mining Engineering, Queen's University, 2008

B.A. Computer Science, Queen's University, 2008

A THESIS SUBMITTED IN PARTIAL FULFILLMENT
OF THE REQUIREMENTS FOR THE DEGREE OF

Doctor of Philosophy

in

THE FACULTY OF GRADUATE AND POSTDOCTORAL STUDIES
(Materials Engineering)

The University of British Columbia
(Vancouver)

July 2015

Abstract

Uranous sulfate can be crystallized from uranium(IV)-containing solutions by raising the temperature and adding sulfuric acid. Several important aspects of the process have never been investigated, however, making its successful application as a real-world extractive metallurgy technology far from certain. This dissertation addresses several fundamental questions surrounding the crystallization of uranous sulfate from acidic process solutions. The effects of various parameters on the solubility of uranous sulfate and the kinetics of its precipitation are demonstrated, including temperature, acid concentration, and agitation, based on the results from a series of bench-scale experiments. The effects of various impurities on the selectivity and efficiency of the crystallization process are also determined. Two new uranous sulfate *x*-hydrate polymorphs, the hexahydrate and the octahydrate, are characterized using single-crystal x-ray diffraction, vibrational spectroscopy, and chemical assay data, and an understanding of the conditions under which they form is developed. The thermal stability and decomposition characteristics of uranous sulfate tetrahydrate, hexahydrate, and octahydrate are demonstrated through fundamental thermodynamic calculations and through the examination of thermal analysis data. The fundamental kinetics of uranium(IV) oxidation in acidic solutions are quantified through the interpretation of experimental data under various conditions of acidity, temperature, and oxygen partial pressure. Finally, a hydrometallurgy flow sheet incorporating uranous sulfate precipitation is presented, and the viability of the complete process is demonstrated experimentally, including electrolytic reduction, precipitation, filtration, drying, and calcining. This work demonstrates that uranous sulfate precipitation is viable as a hydrometallurgical process technology, and that further work is justified.

Preface

The original concept for this project was developed by Cameco Corporation, and was the subject of several prior investigations at their research centre in Port Hope, Ontario, from 1959 to 2005. Their work generally focused on the electrolytic reduction phase of the proposed flow sheet, along with some general studies on the solubility of uranous sulfate in the context of plant design. The work presented in this dissertation is more fundamental in nature and focuses on the characteristics of the precipitate itself, and the kinetics of several related phenomena. It is my original work and does not replicate or otherwise make use of Cameco's previous work.

Chapters 1 and 2. Portions of the introductory text and background information were originally published in my PhD proposal titled *The electrolytic reduction and precipitation of uranous sulfate* (2012).

Chapter 4. A version of this material has been published in Burns, Patrick, Lam, and Dreisinger [14]. Dr. Mati Raudsepp in the Department of Earth, Ocean & Atmospheric Sciences was involved in the early collection of powder diffraction patterns of unknown precipitates that ultimately led to the initiation of this study. Data collection and refinement, as well as the preparation of the Crystallographic Information Framework (`CIF`) files, were conducted by Dr. Brian Patrick and Anita Lam in the Department of Chemistry. The theory of a possible uranous sulfate hexahydrate supercell structure was formulated by Dr. Patrick. The rest of the work, including the synthesis and preparation of the crystals, vibrational spectroscopy, powder x-ray diffraction, analysis, and discussion were conducted by me.

Chapter 6. Preliminary thermogravimetric data were collected using instrumentation at Simon Fraser University, Department of Chemistry, with the assistance of Dr. Dev Sharma. These data were subsequently made redundant by the

more detailed studies conducted at UBC and so were not used in this dissertation.

Chapter 7. The portion of the work concerning the oxidation of uranium(IV) in perchloric acid was presented as a conference paper at Hydro 2014 in Victoria, BC, Canada [13]. All of the work was conduced by me, with supervision from Dr. David Dreisinger.

Chapter 9. The flow sheet was developed as a part of a study for Cameco's research centre titled *Electrolytic reduction and precipitation of uranous sulfate: Flow sheet development, mass balance and operating cost analysis* (2013), with supervision from Dr. David Dreisinger and input from Dr. Michael Murchie and Dr. Angelo Fernando at Cameco. The flow sheet portion of that report is reproduced with minor modifications in this dissertation.

Analysis. Most of the analytical methods were developed and conducted inhouse with input from Dr. Bé Wassink. The total uranium and uranium(IV) titration methods were based on ASTM standard C1267-06 [3]. The titration portion of the sulfate determination method was based on an Application Bulletin published by Metrohm [57]. The full method is available in Appendix C. Free acid determination by standard addition followed Dr. Wassink's method [78], which is reproduced with permission in Appendix D. Many of the titrations were conducted by my undergraduate research assistants, Nicole Kosloski, Jason Midgley, and Kamran Rostam Sadeghi. Atomic absorption (AA) analysis was conducted by Parisa Abbasi, a research engineer in our laboratory, with supervision and help from Dr. Wassink. FTIR spectroscopy was conducted using instrumentation in the Department of Mining Engineering, with training and support from Sally Finora. Raman spectroscopy was conduced using instrumentation in Dr. Guangrui Xia's laboratory, with training and support from her Master's student Ye Zhu.

Table of Contents

List of Tables

List of Figures

List of Terms

AA atomic absorption, an analytical method for determining the concentration of metals in solution.

CIF Crystallographic Information Framework, a standard for information interchange in crystallography maintained by the International Union of Crystallography.

CSTR continuous stirred tank reactor, a type of reactor commonly used in chemical engineering, where the reactor is a tank with equal inflow and outflow rates and aggressive stirring. At steady state, and in the ideal case, the composition is assumed to be uniform throughout the tank. Three or four tanks are usually used in series.

DSA dimensionally stable anode, a titanium anode coated with a proprietary mixed metal oxide consisting of metals such as iridium, ruthenium, platinum, rhodium, and tantalum. Typically used for oxygen evolution.

DSC differential scanning calorimetry, a thermoanalytical technique in which the amount of energy required to raise the temperature of a sample is measured as a function of temperature. It allows for the precise determination of heat capacity and the heat of reaction. Often run simultaneously with TGA.

DTA differential thermal analysis, a thermoanalytical technique similar to differential scanning calorimetry in which the amount of energy required to raise the temperature of a sample is measured as a function of

temperature. It allows for the precise determination of heat capacity and the heat of reaction. Often run simultaneously with TGA.

DTG derivative thermogravimetry, the first derivative of a TGA curve, giving the rate of weight change. Can be used to identify simultaneous chemical reactions. Often gives similar data to DSC and DTA.

ISE ion-selective electrode, an electrode with a membrane at the junction that only allows the specified ion to cross. It can be used to detect the potential of the specified ion while reducing the effect of other ions in solution.

FTIR Fourier transform infrared spectroscopy, a measurement technique for collecting the infrared spectrum of a sample.

m' equivalent molecular weight, a quantity used in thermal analysis to denote the instantaneous average molecular weight of the material in the crucible at any given time.

parisaite A compound related to uranous sulfate that sometimes forms as a metastable intermediary during crystallization of uranous sulfate from acid solutions. Possibly the acid salt. Named in honour of Parisa Abassi, the researcher who first produced it.

TGA thermogravimetric analysis, a thermoanalytical technique in which the weight of a sample is measured as a function of temperature. Weight loss events at a particular temperature indicate the occurrence of a chemical reaction or the loss of a volatile component. Often run simultaneously with DSC.

XRD x-ray diffraction, an analytical method for investigating the structure of a crystalline solid. Powder x-ray diffraction can be used to determine the identity of one or more crystalline phases in a powdered solid based on a database of known structures. Single-crystal x-ray diffraction can be used to elucidate the molecular structure of a crystalline solid.

Acknowledgments

This project never would have happened without help from my very good friend, Fortuitous Circumstance. To Tai Yen, Sadan Kelebek, and Chris Pickles, who sent me to the CMP conference, where I was seated next to Chuck Edwards at dinner, who years later put me in touch with Mike Murchie, who agreed to have lunch with me, after which he agreed to fund this project despite me ordering the most expensive dessert on the menu. To Jan De Bakker, who introduced me to Boyd Davis, who gave me Sam Marcusen's email address, who years later told me, while I was microwaving a vending machine lava cake, that the most important thing about starting a PhD is to choose a project that is interesting even if my life studying it isn't.

Many researchers volunteered their time and equipment to this project free of charge. I thank Anita Lam and Brian Patrick in the Department of Chemistry, who taught me everything I know about crystal structures; Dev Sharma in the Department of Chemistry at Simon Fraser University, who introduced me to thermogravimetry and let me use his TGA; Sally Finora in the Department of Mining Engineering, who let me use her FTIR even after blowing her pellet press shield to smithereens; Dr. Mati Raudsepp in the Department of Earth, Ocean & Atmospheric Sciences, who gave me full use of his laboratory and powder diffractometers, not to mention the time of his staff (particularly Jenny Lai), and never failed to show an honest interest in my endless supply of purple-green powders; Dr. Maggie Xia and her student Ye Zhu for giving me time on the Raman spectrometer; and Bailey Kelly, Laurie Johnson, and Mike Broczkowski at Cameco's research centre in Port Hope, Ontario, who assisted with some analysis. I also greatly appreciate the hard work of my three undergraduate summer students, Nicole Kosloski, Jason Midgley, and

Kamran Rostam Sadeghi. I hope I managed to teach them as much as they taught me.

I thank my parents, who encouraged me to pursue further education, and my aunt Joyce, who made certain that there were no barriers to doing so. I also thank Angelo Fernando and Mike Murchie at Cameco, who were just as concerned about my personal wellbeing as they were about their investment. I will ever be grateful to my supervisor, David Dreisinger, who continues to give me more responsibility and freedom than I deserve. And most of all, I am grateful for Dr. Bé Wassink, who taught me humanity.

Funding through the National Sciences and Engineering Research Council and from Cameco Corporation is gratefully acknowledged.

About the typeface

Minion Pro, 10 point: Minion is an Adobe Originals typeface designed by Robert Slimbach. It was inspired by classical, old style typefaces of the late Renaissance, a period of elegant, beautiful, and highly readable type designs. Its aesthetic and functional qualities, with a full complement of glyphs from all Western alphabets at multiple widths and weights, serves as a reminder that no matter how agonizingly narrow my focus becomes, there exists a breed of professional whose obsessiveness even I cannot approach: the professional typographer.

Powered by liquid propellent!

I am indebted to the forces of evolution, which gave us *Coffea arabica*, and to the social forces that built establishments to serve it to me roasted and soaked in a cup. YVR: AGRO Cafe, Beyond Coffee, East Van Roasters, Euro Bagel, Finch's Market, Forty-ninth Parallel, Heartwood Community Cafe, Lost + Found Cafe, Matchstick Coffee Roasters, Melrichie's, Momento Coffee House, Nelson the Seagull, Prophouse, Uprising Breads, The Wilder Snail Cafe; NYC: B Cafe, Irving Farm Coffee Roasters, Lost Weekend, Tavern on the Green; YKA: The Art We Are, Common Grounds, Zack's; YYZ: Sammy's, Bicerin; YGK: The Sleepless Goat.

Dedication

For Lynn

Chapter 1

Introduction

He has been eight years upon a project for extracting sunbeams out of cucumbers, which were to be put in phials hermetically sealed, and let out to warm the air in raw inclement summers.
— Jonathan Swift, *Gulliver's Travels* (1726)

It takes many steps to convert uranium from its ore into the most energy-dense fuel currently available to humankind. Almost every technique in the extractive metallurgist's toolbox has been applied to uranium extraction at one point, including acidic nitrate, chloride, and sulfate leaching, carbonate leaching, pressure leaching, ion exchange, solvent extraction, selective precipitation, direct fluorination, electrolysis, and calcining under oxidizing and reducing atmospheres. It is therefore rather surprising to learn that there exists one known technique that has barely been studied, let alone applied in practice: the electrolytic reduction and precipitation of uranous sulfate. This is the topic of this dissertation.

The Department of Materials Engineering at UBC has a distinguished history of uranium research. In the 1950s, Dr. Frank Forward co-developed the Beaverlodge carbonate leach process for Eldorado, Canada's uranium company at the time [26], assisted in part by his master's student Ernie Peters, who wrote his thesis on the subject [62]. Forward also conducted research on acid pressure leaching and the hydrometallurgical production of UO_2 for nuclear power plants [27, 77], and later

became the Director of Research at the Canadian Uranium Research Foundation. The University's interest in uranium waned after Forward's departure, however, as governments the world over gradually assumed responsibility for research in the field.

After the twenty-five year slumber that followed the Three Mile Island and Chernobyl crises, nuclear energy is now enjoying a renaissance. This is partly due to the geopolitical and economic uncertainties associated with oil, but it is also due to the rise of responsible environmental stewardship: nuclear power produces virtually no waste compared to conventional sources. Even recent setbacks associated with the Fukushima meltdown seem unlikely to stop the long-term growth of nuclear power. As described by the International Atomic Energy Agency in 2002 [40]:

> Nuclear power currently generates 16% of the world's electricity. It produces virtually no sulfur dioxide, particulates, nitrogen oxides, volatile organic compounds (VOCs) or greenhouse gases (GHGs). The complete nuclear power chain, from resource extraction to waste disposal including reactor and facility construction, emits only 2–6 grams of carbon equivalent per kilowatt-hour (gCeq/kW.h). This is about the same as wind and solar power including construction and component manufacturing. All three are two orders of magnitude below coal, oil, and natural gas (100–360 gCeq/kW.h).

Nuclear power plants require a steady supply of fuel, and mining companies are actively preparing to develop new orebodies to meet rising demand. This dissertation presents research associated with a novel method of uranium purification that could be used at a new or existing uranium mill. Specifically, it addresses various fundamental and engineering aspects of the selective precipitation of uranous sulfate from acidic leach solutions. If proven feasible, this technology could be used as an alternative to solvent extraction, which is relatively costly and hazardous, and could possibly allow for the recovery of acid in a closed-loop system, thus reducing the requirement for acid neutralization.

1.1 Objectives

The overarching objective of this dissertation is to advance the knowledge and practice of the selective precipitation of uranous sulfate as a new uranium hydrometal-

lurgical processing technology. This will be approached by focusing on six questions, each addressing a specific gap in the literature.

1. What are the best operating conditions for the precipitation of uranous sulfate?

Uranous sulfate is known to precipitate from acidic uranium(IV) solutions with the addition of sulfuric acid and the application of heat. The relationship between uranous sulfate solubility, temperature, and sulfuric acid concentration is fairly well understood, but nothing has been reported on optimizing the process to achieve high recovery and fast kinetics. This will be addressed by combining existing knowledge with new experimental results in order to recommend the best conditions for operating a uranous sulfate precipitation process.

2. How do impurities affect the precipitation process?

A successful hydrometallurgical process employing uranous sulfate precipitation must perform well on impure solutions. No work has been reported in the literature, however, on the effect of impurities on the selectivity and recovery of uranous sulfate precipitation, or on the purity of the resulting solids. This gap in the literature will be addressed by discussing a series of laboratory experiments on the effects of Al, Cu, Ni, and Fe.

3. What are the different uranous sulfate polymorphs, and how do they differ from one another?

Several different uranous sulfate hydrate polymorphs have been identified in the literature, with each forming under a specific set of conditions. A deep understanding of the number of different polymorphs, their structures, and the conditions under which they form is lacking, however. New experimental data will be combined with results from the literature to formulate a comprehensive understanding of the genesis and form of the uranous sulfate x-hydrates.

4. How does uranous sulfate respond to drying and calcining?

Uranous sulfate *x*-hydrate will dehydrate and decompose when heated, but a precise understanding of the temperatures and transitions involved is lacking. The decomposition of uranous sulfate will be discussed from both a thermodynamic and experimental perspective.

5. Is aqueous uranium(IV) stable against oxidation by oxygen gas?

The uranium(IV) solution required for the production of uranous sulfate may be exposed to oxygen gas at many points in a potential process, including from oxygen evolved at the anode during electrolytic reduction, or from air while being held in large tanks during crystallization or during a process upset or shutdown. It is therefore important to know what measures are effective to prevent the undesired oxidation of uranium(IV). The oxidation kinetics of uranium(IV) in perchloric acid, and in the presence of sulfate, will be discussed.

6. Can uranous sulfate precipitation be developed into a viable extractive metallurgical technology?

Most aspects of uranous sulfate precipitation have been studied to some extent (if the work presented in this dissertation is included), but an entire industrial process has never been proposed or tested. A proposal for a complete plant flow sheet employing uranous sulfate precipitation will be discussed, and evidence for its viability will be presented.

1.2 Overview of chapters

This dissertation is divided into nine chapters (with this introduction being the first). Each chapter employs a combination of theory, new experimental data, and existing knowledge to address the objectives given above.

In Chapter 2, background information on the project is given, including historical context, thermodynamics, aqueous chemistry, and a review of related industrial processes. It provides context for understanding the purpose and scope of the project. Literature and background information relevant only to a single area of the project is not given here, but is instead presented in the relevant chapter.

In Chapter 3, various aspects of the precipitation process are explored, focusing on the effect of temperature, free acid concentration, and crystallization time. Five unique uranous sulfate *x*-hydrate polymorphs are identified, and each sample is mapped according to the conditions of its genesis to broadly define the stable regions of each polymorph. The effects of various other parameters on the crystallization process, such as seeding and agitation, is also explored.

In Chapter 4, the crystal structures of two of the polymorphs identified in Chapter 3, uranous sulfate hexahydrate and octahydrate, are presented from single crystal x-ray diffraction data. Vibrational spectroscopy on the two polymorphs is also discussed. The structures of these polymorphs is compared to the suite of previously-known uranous sulfate polymorphs, including $U(SO_4)_2 \cdot 4\,H_2O$, to draw connections between the number of crystalline and solvent waters in the hydrated salt to its intra- and intermolecular bonding.

In Chapters 5 and 6, the thermal decomposition of uranous sulfate tetrahydrate, hexahydrate, and octahydrate is discussed. The thermal decomposition process is first treated from a theoretical perspective, focusing on the thermodynamics of the system. These predictions are then tested experimentally by thermogravimetric analysis (TGA), differential scanning calorimetry (DSC), and derivative thermogravimetry (DTG). Unique decomposition paths are identified for the three hydrates, and the existence of multiple forms of $U(SO_4)_2$ is inferred.

In Chapter 7, the kinetics of aqueous uranium(IV) oxidation are investigated through a series of experiments in perchloric acid. The irreproducibility of the kinetics in the presence of sulfate is also discussed.

In Chapter 8, the viability of uranous sulfate precipitation as a processing technology is experimentally demonstrated from beginning to end, including electrolytic reduction, crystallization, washing and filtration, and calcining. It shows that an integrated process that uses uranous sulfate precipitation is viable in principle.

In Chapter 9, a complete flow sheet showcasing uranous sulfate precipitation is proposed. Elements of the design are informed by existing knowledge from the literature and new knowledge presented in this dissertation. The flow sheet could be used as a guide to direct further research and development.

Finally, Chapter 10 gives a summary of the work done, answers the five questions stated in the objectives, and gives suggestions for future work.

Chapter 2

Background information

2.1 A brief history of uranium

The story of uranium is young and brash, complete with politics, pride, celebrity, secrecy, espionage, war, cooperation, and coercion. No other metal has attracted such focus from politicians, generals, scientists, activists, and economists alike. A general understanding of the story is important for anyone working in the field of uranium metallurgy.

Uranium was identified as an element in 1789 by Martin Heinrich Klaproth, a German apothecary and early analytical chemist. Klaproth had in fact produced only the oxide, not the pure element, and in 1841 the french chemist Eugène Péligot isolated the metal by reducing uranium tetrachloride with potassium metal. Uranium remained a curiosity with no significant commercial use until the late 19^{th} century, when the physicist Henri Becquerel discovered that uranium salts emitted invisible rays, now known to be electromagnetic radiation. A flurry of scientific activity followed, quickly leading Marie and Pierre Curie to the discovery of the element radium.

The discovery of radium, and particularly its use in cancer treatment, sparked a demand for the uranium-bearing ore from which it was extracted. The only source of such material was initially the tailings dump of the defunct Jáchymov uranium mine in the Czech Republic, but the rich Shinkolobwe deposit in the Belgian Congo and the Great Bear Lake deposit in northern Canada were soon developed to meet

the explosive demand. The cost of radium soared to over US$70,000 per gram (1932 dollars), justifying the enormous cost of extracting the minuscule amount of radium found in the ore. The tailings, still rich in uranium, were discarded as waste. Eldorado, Canada's radium company, disposed of uranium-containing waste rock wherever it could find space, including in old silos, in the Port Hope harbour, and even as fill for nearby construction sites.

Demand for uranium itself grew in 1939 when physicists announced that nuclear fission was theoretically possible, and that it could be used to produce a powerful weapon. The governments of the United States, Britain and Germany began buying uranium from radium producers to fuel their nuclear weapons programs. After WWII, when everyone in the world learned of its energy and wartime potential, uranium quickly eclipsed radium in importance, and a market for uranium was finally established.

The study of uranium metallurgy only truly began in the 1940s as part of the Manhattan project, but a vast research budget and the commitment and influence of the U.S. military ensured its rapid development. By the mid-1950s, many aspects of uranium metallurgy had been investigated, designed, piloted, and built into operating plants. Most of the processes used today were developed and piloted in the 15-year period following the war.

The uranium industry today is a fully-developed supply chain for the many nuclear power plants around the world. Corporations from many countries, including Canada's Cameco (né Eldorado), France's Areva, Kazakhstan's Kazatomprom, and Anglo-Australian BHP Billiton, mine and refine uranium from orebodies scattered across the world. From its humble position at the beginning as valueless gangue, uranium has become a critical commodity for the world energy market.

Sources: [1, 8, 31, 37, 64]

2.2 Relevant thermodynamic quantities

The rapid development of nuclear technologies following the second world war created an intense need for fundamental knowledge of uranium chemistry. There is therefore no lack of fundamental thermodynamic data related to uranium processing. The thermodynamic values used in this dissertation were curated by the Or-

ganisation for Economic Co-operation and Development (OECD) Nuclear Energy Agency, which maintains an internally-consistent database of the thermodynamics of uranium, neptunium, plutonium, americium, and technetium derived from over one thousand peer-reviewed and government publications. An exhaustive review of the uranium portion of the data set was compiled by Grenthe et al. [34], and updated more recently by Guillaumont and Mompean [35]. A subset of the thermodynamic quantities relevant to the present work is reproduced in Table 2.1.

Table 2.1: Standard state thermodynamic quantities relevant to the decomposition of uranous sulfate (25 °C). Reference: Guillaumont and Mompean [35].

Compound	State	ΔG°, kJ/mol	ΔH°, kJ/mol	S°, J/mol
$U(SO_4)_2 \cdot 8\,H_2O$	c	-3987.898	-4662.6	538
$U(SO_4)_2 \cdot 4\,H_2O$	c	-3033.31	-3483.2	359
$U(SO_4)_2$	c	-2084.521	-2309.6	180
UO_2SO_4	c	-1685.775	-1845.14	163.2
U_3O_8	c	-3369.471	-3574.8	282.54
UO_3†	c	-1145.739	-1223.8	96.11
SO_2	g	-300.095	-296.81	248.223
SO_3	g	-371.02	-395.7	256.77
H_2O	g	-228.582	-241.826	188.835
O_2	g	0	0	205.152
U^{3+}	aq	-476.473	-489.1	-188.172
U^{4+}	aq	-529.86	-591.2	-416.895
$USO_4{}^{2+}$	aq	-1311.423	-1492.54	-245.591
$U(SO_4)_2$	aq	-2077.86	-2377.18	-69.007
$UO_2{}^{+}$	aq	-961.021	-1025.127	-25
$UO_2{}^{2+}$	aq	-952.551	-1019	-98.2
UO_2SO_4	aq	-1714.535	-1908.84	46.01
$UO_2(SO_4)_2{}^{2-}$	aq	-2464.190	-2802.580	135.786
$UO_2(SO_4)_3{}^{4-}$	aq	-3201.801		

† For γ-UO_3

2.3 The aqueous chemistry of uranium

Uranium in solution can exist in the (III), (IV), (V) and (VI) oxidation states. Table 2.2 shows the standard reduction potentials for the transitions between oxidation states. Uranium(VI) and uranium(IV) are both stable in water, making

Table 2.2: Uranium standard reduction potentials. Calculated from the thermodynamics of Guillaumont and Mompean [35].

Ox. State Change	Half-reaction			E°, V
VI ⟶ V	$UO_2^{2+} + e^-$	⟶	UO_2^{+}	0.09
VI ⟶ IV	$UO_2^{2+} + 4H^+ + 2e^-$	⟶	$U^{4+} + 2H_2O$	0.27
V ⟶ IV	$UO_2^{+} + 4H^+ + e^-$	⟶	$U^{4+} + 2H_2O$	0.45
IV ⟶ III	$U^{4+} + e^-$	⟶	U^{3+}	-0.55
IV ⟶ 0	$U^{4+} + 4e^-$	⟶	U	-1.37
III ⟶ 0	$U^{3+} + 4e^-$	⟶	U	-1.65

them relevant in hydrometallurgical processes. Uranium(III) is formed at a potential below that of hydrogen evolution, so it is generally not found in aqueous processes. Uranium(V), if formed, rapidly disproportionates into uranium(IV) and uranium(VI), and so is rarely found in measurable quantities. Since uranium(III) and uranium(V) are only observed under laboratory conditions, their chemistries will not be discussed further. The chemistries of uranium(VI) and uranium(IV), however, are vital to any discussion about the aqueous processing of uranium.

Uranium(VI) is highly soluble, is easily leached, and forms complexes with a variety of ligands. Uranium(IV), in contrast, is much less soluble and generally cannot be leached without first being oxidized. Figure 2.1 shows a Pourbaix diagram of the uranium–water system, constructed using HSC 5.11, for a 0.42 molal uranium solution, omitting complexing ligands and hydrolyzed compounds. UO_2^{2+} is the stable aqueous species under oxidizing, neutral, and acidic conditions, while uranium(IV) is soluble only at very low pH. Uranium(VI) is predicted to precipitate by hydrolysis around pH 4. In reality, however, uranium forms complexes readily with many substances, making the actual pH of precipitation higher.

Like the other actinides and lanthanides, uranium complexes readily with sulfate, which distinguishes it from most base metals. It also complexes readily with chloride, fluoride, and nitrate. Table 2.3 shows the formation constants of uranium complexes with these ligands.

Majima et al. [54] calculated the theoretical speciation of a mixed uranyl/uranous sulfate system by solving the simultaneous equilibrium relationships for a solution containing 100 $g\,L^{-1}$ uranium and 125/288 $g\,L^{-1}$ sulfur. They showed that

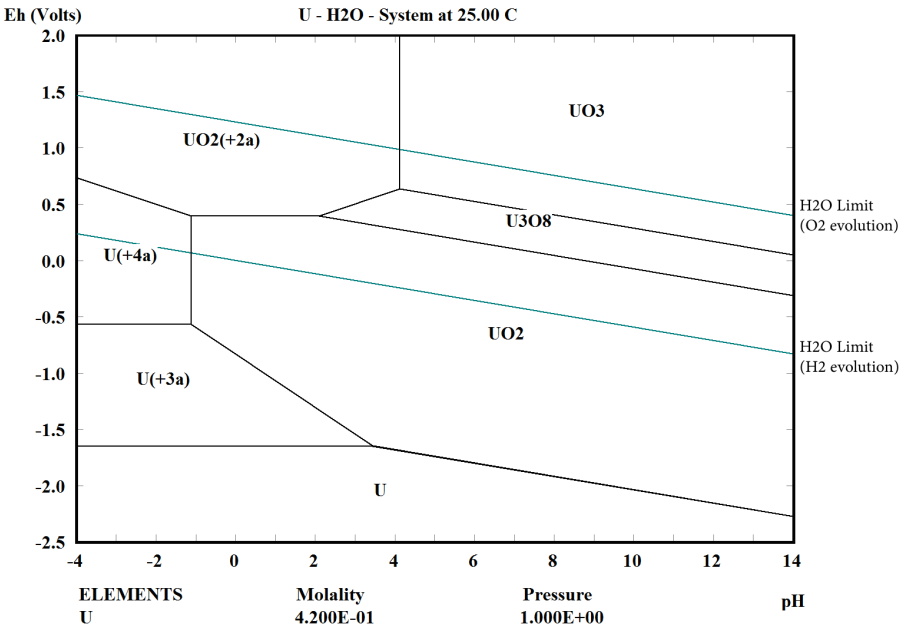

Figure 2.1: Pourbaix diagram of uranium in a non-complexing medium, 25°C, 0.42 molal U. Generated by HSC 5.11.

Table 2.3: Formation constants of aqueous uranium(IV) and uranium(VI) complexes (25 °C, $I = 0$). Reference: Guillaumont and Mompean [35].

	$\log_{10}\beta_1^\circ$	$\log_{10}\beta_2^\circ$	$\log_{10}\beta_3^\circ$	$\log_{10}\beta_4^\circ$
U^{4+}				
F^-	9.42	16.56	21.89	26.34
Cl^-	1.72			
SO_4^{2-}	6.58	10.51		
NO_3^-	1.47	2.3		
UO_2^{2+}				
F^-	5.16	8.83	10.9	11.84
Cl^-	0.17	-1.1		
SO_4^{2-}	3.15	4.14	3.02	
NO_3^-	0.3			

the negatively-charged uranium(VI) disulfate complex $UO_2(SO_4)_2^{2-}$ is dominant over the neutral monosulfate complex $UO_2(SO_4)_{aq}$ at high sulfate levels, but only somewhat dominant at lower sulfate levels. The effect is more pronounced for uranium(IV), where the neutral disulfate complex $U(SO_4)_{2\,aq}$ is dominant over the monosulfate $U(SO_4)^{2+}$ even at low sulfate levels. The authors did not include the trisulfate uranium(VI) complex $UO_2(SO_4)_3^{2-}$ in their analysis.

The hydrolysis of uranium (i.e., complexation with OH^-) is quite complex. A subset of the known hydrolysis equilibria are given in Table 2.4. Uranium(VI) forms a plethora of hydrolyzed species, but generally remains as UO_2^{2+} at low pH. Uranium(IV), however, will hydrolyze even at pH 1 to form UOH^{3+}.

Table 2.4: Hydrolysis reactions for uranium(VI) and uranium(IV) (25 °C, $I = 0$). Reference: Guillaumont and Mompean [35].

Hydrolysis reaction			$\log_{10} K^\circ$
U^{4+}			
$U^{4+} + H_2O_{(l)}$	$\longleftrightarrow$	$UOH^{3+} + H^+$	-0.54
$U^{4+} + 4OH^-$	$\longleftrightarrow$	$U(OH)_{4(aq)}$	-12.15
UO_2^{2+}			
$UO_2^{2+} + H_2O_{(l)}$	$\longleftrightarrow$	$UO_2OH^+ + H^+$	-5.25
$UO_2^{2+} + 2H_2O_{(l)}$	$\longleftrightarrow$	$UO_2(OH)_{2(aq)} + 2H^+$	-12.15
$UO_2^{2+} + 3H_2O_{(l)}$	$\longleftrightarrow$	$UO_2(OH)_3^- + 3H^+$	-20.25
$UO_2^{2+} + 4H_2O_{(l)}$	$\longleftrightarrow$	$UO_2(OH)_4^{2-} + 4H^+$	-32.40
$2\,UO_2^{2+} + H_2O_{(l)}$	$\longleftrightarrow$	$(UO_2)_2OH^{3+} + H^+$	-2.70
$2\,UO_2^{2+} + 2\,H_2O_{(l)}$	$\longleftrightarrow$	$(UO_2)_2(OH)_2^{2+} + 2\,H^+$	-5.62
$3\,UO_2^{2+} + 4\,H_2O_{(l)}$	$\longleftrightarrow$	$(UO_2)_3(OH)_4^{2+} + 4\,H^+$	-11.90
$3\,UO_2^{2+} + 5\,H_2O_{(l)}$	$\longleftrightarrow$	$(UO_2)_3(OH)_5^{+} + 5\,H^+$	-15.55
	etc.		

2.4 Electrolytic reduction of uranium(VI)

The electrolytic reduction of uranium(VI) to form uranium(IV) is a critical precursor to the precipitation of uranous sulfate. While the electrolysis process is not discussed in depth in this dissertation, it is important to understand the process in order to be aware of design constraints.

The electrolytic reduction of uranium(VI) can be described by the following half-cell reactions:

Cathodic half-cell:	$UO_2^{2+} + 4H^+ + 2e^- \longrightarrow U^{4+} + 2\,H_2O$	$E^\circ = 0.27\,V$	(2.1)
Anodic half-cell:	$H_2O \longrightarrow \frac{1}{2}O_2 + 2H^+ + 2e^-$	$E^\circ = -1.23\,V$	(2.2)
Overall:	$UO_2^{2+} + 2H^+ \longrightarrow U^{4+} + \frac{1}{2}O_2$	$E^\circ_{cell} = -0.96\,V$	(2.3)

Since E°_{cell} is negative, the reaction does not proceed spontaneously, and so will only occur if a voltage is applied using an external power supply.

Equation (2.1) shows the reduction of uranium(VI) taking place as a simultaneous two-electron transfer. The true reaction path, however, is more complex. Casadio and Lorenzini [15] investigated the reduction of uranium(VI) at the millimolar level by cyclic voltammetry, and showed that the supporting electrolyte composition and scan speed can cause different reaction mechanisms to dominate. They showed that uranium(VI) $\longrightarrow$ uranium(V) always proceeds by a single electron transfer, but that uranium(V) $\longrightarrow$ uranium(IV) can proceed either by chemical disproportionation or by a second electron transfer. Under high acid conditions, they found that disproportionation dominated. They also found that the addition of sulfate enhanced the disproportionation kinetics, likely due to the strong complexing power of sulfate towards uranium(IV). Kern and Orlemann [42] found that the disproportionation of uranium(V) is extremely rapid, except at millimolar levels in a low-acid, non-complexing matrix, and even then it only survives for tens of seconds. Under the high-acid, high-sulfate conditions being considered in this dissertation, the disproportionation mechanism would clearly dominate. This has few practical implications, however, since the ultimate result – two electrons and two protons consumed per uranium – is the same. It can therefore be assumed for design purposes that the reduction process involves a direct two-electron transfer.

Gurinov and Frolov [36] showed that uranium(VI) reduction is diffusion-limited under typical operating conditions. In electrochemical terms, this means that an electrolyzer designed to produce uranium(IV) will operate at the reaction's limiting current density, where an increase in cell potential does not produce an increase in reduction rate. Under these conditions, the rate-controlling step is the rate of mass transfer of uranium(VI) from the bulk electrolyte to the cathode surface. As the electrolytic reduction of uranium(VI) proceeds, the concentration gradient between the bulk solution and that in contact with the cathode surface becomes smaller,

causing the rate of mass transfer to decline. Eventually, when the uranium cannot transfer from the bulk solution fast enough to consume all of the supplied current (assuming a constant-current cell is being used), hydrogen evolution will occur to make up the difference. Hydrogen evolves according to the following half-cell reactions:

$$\begin{array}{rlll} \text{Cathodic half-cell:} & 2H^+ + 2e^- \longrightarrow H_2 & E^\circ = 0\,V & (2.4) \\ \text{Anodic half-cell:} & H_2O \longrightarrow \frac{1}{2}O_2 + 2H^+ + 2e^- & E^\circ = -1.23\,V & \\ \hline \text{Overall:} & H_2O \longrightarrow \frac{1}{2}O_2 + H_2 & E^\circ_{\text{cell}} = -1.23\,V & (2.5) \end{array}$$

Hydrogen bubbles can "mask" part of the electrode surface, reducing the available surface area and consequently reducing the reaction rate. Conversely, the formation and release of tiny bubbles can actually increase the reaction rate by disturbing the solution next to the cathode and inducing convective flow to a degree not possible by bulk turbulence alone. In theory, turbulence or agitation should decrease the thickness of the mass transfer boundary layer, and thus increase the reaction rate. Gurinov and Frolov [36] found that the rate of reduction can be made tens of times faster by inducing forced convection of the electrolyte. In fact, at very high flow rates it became impossible to distinguish the point at which hydrogen evolution began. Awakura et al. [6] showed that the limiting current increases with temperature, as does overall current efficiency, which is consistent with a diffusion-limited process, since the diffusion coefficient increases with temperature.

The diffusion coefficient (D) and boundary layer thickness are clearly essential parameters for the design of an electrolyzer. Both of these parameters have been determined by several groups under various conditions. Awakura et al. [5] determined the diffusion coefficient of uranium(VI) at several temperatures by comparing the limiting current density to that of copper reduction, for which D is well known. They measured an apparent diffusion coefficient of $3.5–4.5 \times 10^{-6}$ cm^2 s^{-1}, with a higher value observed at higher uranium concentrations. This compares well to the diffusion coefficient determined by Casadio and Lorenzini [15] at 25 °C of $(5.30 \pm 0.08) \times 10^{-6}$ cm^2 s^{-1} in 1 N K_2SO_4 (pH = 2). They also concluded that the thickness of the mass transfer boundary layer is controlled mainly by the agitation speed under conditions of forced convection.

For the purposes of this dissertation, this brief review of the electrolytic reduction of uranium(VI) can be summarized as follows:

- The electrolytic reduction of uranium(VI) is mass transfer-limited.
- The evolution of hydrogen bubbles can be beneficial because it induces convection and disturbs the mass-transfer boundary layer surrounding the cathode.
- The mass transfer boundary layer can be made smaller, and the reaction rate increased proportionally, by operating the electrolytic cell under conditions of forced convection.
- The actual reduction mechanism involves a single-electron transfer, followed by the disproportionation of uranium(V). However, the process can be considered a two-electron transfer for design purposes.

2.5 Industrial processes

The precipitation of uranous sulfate has never been practiced on an industrial or pilot scale. However, the electrolytic reduction of uranium sulfate solutions has been tested in a number of other contexts, mainly with the goal of producing high-purity UF_4, and sometimes uranous sulfate precipitated as scale or silt as an unintended consequence. It is therefore useful to examine previous attempts to electrolyze uranium solutions on a large scale. The United States, Japan, U.K., Spain, and France all operated pilot plants on various scales. The processes are summarized in Table 2.5.

Table 2.5: Summary of industrial processes employing electrolytic reduction

Process	Nation	Year	Concept	Ref.
	UK	1944	$UF_6 \xrightarrow{water} UO_2{}^{2+} \xrightarrow{e^-} UF_4$	[49]
Excer	USA	1956	$Ore \xrightarrow{HCl/H_2SO_4} UO_2{}^{2+} \xrightarrow{IX/DHF} UO_2F_2 \xrightarrow{e^-/DHF} UF_4$	[39]
SIMO	France	1970	$UO_3 \xrightarrow{HNO_3} UO_2{}^{2+} \xrightarrow{H_2SO_4} UO_2{}^{2+} \xrightarrow{e^-} U^{4+} \xrightarrow{DHF} UF_4$	[65]
SAEC	Spain	1973	$U_3O_8 \xrightarrow{H_2SO_4} UO_2{}^{2+} \xrightarrow{e^-} U^{4+} \xrightarrow{DHF} UF_4$	[21]
PNC	Japan	1975	$Ore \xrightarrow{H_2SO_4} UO_2{}^{2+} \xrightarrow{SX/HCl} UO_2{}^{2+} \xrightarrow{e^-} UCl_4 \xrightarrow{DHF} UF_4$	[54]

DHF: dilute hydrofluoric acid
SX: solvent extraction
Ore: uranium ore concentrate

The first attempt at an industrial electrolytic reduction process was developed by the Imperial Chemical Industries Company of Great Britain. A patent filed in 1944 describes a process by which a uranyl fluoride solution is electrolysed to produce solid UF_4 [49]. The patent specifies that the starting material must be a pure uranyl fluoride solution, such as would be obtained by dissolving UF_6 in water. The author mentions that the process could be applied to sulfate or chloride systems, although that was not the objective of the invention.

The Excer process was developed by American researchers at the Oak Ridge National Laboratory in 1956 as a cost-effective way to produce high-purity UF_4 [39]. The process involved ion exchange of a uranium-containing solution, stripping with HCl to create a high-purity uranyl chloride solution, electrolytic reduction and precipitation in the presence of HF, filtration, and finally dehydration. The feed solution could be sulfuric acid leach liquor, sulfate, or chloride concentrate, or nitrate concentrate from solvent extraction. The electrolytic cell consisted of a mercury cathode, lead anode, and an Ionics CR-61 cation exchange membrane. The electrolysis had to be conducted at 80–95 °C because operating at a lower temperature caused the gelatinous $UF_4 \cdot \frac{5}{2} H_2O$ to precipitate rather than the more convenient $UF_4 \cdot \frac{3}{4} H_2O$.

The SIMO process was developed by the French organization Société Ugine Kuhlmann for use in the Eurochemic reprocessing plant in Mol, Belgium [65]. The process involved the dissolution of a uranium feed in nitric acid, followed by contact with sulfuric acid, then distillation of the nitric acid to make a uranyl sulfate solution. The authors emphasized that it was essential to transition from the nitrate system to the sulfate system because of its suitability to the downstream fluorination process. A variety of cathode materials were tested, including platinum and titanium, but a horizontal mercury cathode was chosen because of its resistance to HF and its ability to absorb contaminant cations. Platinum and iridium were used as anodes, and a polypropylene porous membrane separated the anodic and cathodic compartments of the cell. The pilot plant used three reduction cells in series to achieve 99% reduction. While the process seemed to be successful, a consistent problem was fouling of the mercury cathode by precipitated uranous sulfate. To prevent precipitation, the feed solution had to be diluted, resulting in a lower throughput.

The Spanish Atomic Energy Commission (SAEC) also developed an electrolytic sulfate-based process for the production of UF_4 [21]. In addition to electrolysis, their study included details on fluorination, precipitation, filtering, and drying. A variety of electrode and cell body materials were tested for their ability to resist the corrosive electrolyte. Monel, titanium, Hastelloy B, Hastelloy C, graphite, and lead were tested. Platinum, palladium, zirconium, and other expensive metals were not tested because of their excessive cost if used on an industrial scale. Batch electrolytic reduction tests were conducted using a synthetic solution at $137\,g\,L^{-1}$ H_2SO_4 and $67\,g\,L^{-1}$ uranium(VI), a PVC cell, lead cathode, graphite anode, and a PVC porous diaphragm. The electrolysis was run in three stages, with a fluorination/precipitation step between each reduction. The three reduction phases together achieved a 99.5% conversion to U(IV), but taking into account reoxidation and loss of entrained mother liquor, an overall uranium recovery of 83.2% was achieved. A second study was conducted to investigate the influence of sodium and chloride. A solution containing $5\,g\,L^{-1}$ HCl, $137\,g\,L^{-1}$ H_2SO_4 and $80\,g\,L^{-1}$ UO_3 was reduced in a batch electrolyzer using lead electrodes. An unidentified white precipitate, assumed to be lead sulfate, precipitated in the cell. The authors speculated that chloride reacted with the lead cathode to form a soluble lead chloride, which in turn reacted with sulfate to form an insoluble sulfate, thereby freeing the chloride ion to continue to oxidize the lead cathode. The authors concluded that the catholyte must be totally free of Cl^-. Sodium was not found to interfere with electrolysis, but the authors acknowledged that it might interfere with UF_4 precipitation. A large-scale pilot plant was operated for two months to test the process. The plant was apparently quite successful and few problems were reported, but it was necessary to clean the cells periodically to remove a build-up of sludge, assumed to be composed of UF_4, lead oxide, and other metallic oxides, but perhaps also containing uranous sulfate. The authors suggested that a 3-week cell cleaning rotation would suffice to keep the plant operating continuously.

Japan's PNC operated a chloride-based batch electrolytic reduction pilot plant for the production of UF_4 in Ningyo-toge as part of their uranium enrichment research program in the 1980s [54]. No publicly-available information on the project has been published. However, the researchers did publish a series of papers in the scientific literature regarding electrolytic reduction and precipitation in the sulfate

system (reviewed in Chapter 3), apparently as a precursor to converting the plant from the chloride to the sulfate system. It is unlikely that the conversion ever took place, however, since work at the Ningyo-toge site was discontinued in 1987.

2.6 Analytical methods

Many different analytical methods were used to gather and interpret experimental data for this dissertation. X-ray diffraction, Raman spectroscopy, infrared spectroscopy, and atomic absorption spectroscopy were all used, but they are well known techniques and do not require further explanation here. The determinations of total uranium, uranium(IV), total sulfate, and free acid used non-standard or lesser-known techniques, and so are described below. Thermogravimetric analysis (TGA) and differential scanning calorimetry (DSC) are described in detail in Chapter 6.

2.6.1 Total uranium

If the sample was a solid, it was first dissolved in nitric acid. Aqueous samples were used directly. Total uranium was determined using a variation of the well-established Davies and Gray method, as described by ASTM standard C1267-06 [3, 19]. The potassium dichromate titrant was periodically validated against a uranium standard solution (AccuTrace AA66N-5, 1000 $\mu g\,mL^{-1}$).

In the modified Davies and Gray method, an aliquot containing 20-100 mg of uranium is quantitatively transferred to a beaker, where it is combined with phosphoric acid and an excess of ferrous sulfate. The ferrous sulfate reduces all of the uranium to uranium(IV). The residual ferrous sulfate is selectively oxidized using nitric acid, catalyzed by molybdenum. Sulfamic acid shields the uranium(IV) from oxidation by the nitric acid. The solution is rapidly titrated with potassium dichromate using potentiometric endpoint detection on a platinum electrode against a standard calomel reference electrode.

For a detailed description of the reagents, equipment, and procedure, refer to ASTM standard C1267-06 [3].

2.6.2 Uranium(IV)

Uranium(IV) was determined by direct oxidative potentiometric titration with potassium dichromate in phosphoric acid. The procedure was similar to the modified Davies and Gray method described above, except that the ferrous reduction step and the associated reagent additions were not done. A small amount of ferric sulfate was added just before each titration in order to match the conditions of the well-tested Davies and Gray method (which includes residual ferric). Failure to add ferric made it difficult to detect the endpoint, suggesting that the presence of the ferric-ferrous couple is required for detecting the uranium(IV)-uranium(VI) couple on a platinum electrode.

2.6.3 Total sulfate

Total sulfate was determined by potentiometric titration with lead perchlorate in 85 % isopropanol using a Pb^{++} ion-selective electrode. Lead sulfate is insoluble in isopropanol, so the titration endpoints were indicated by a sharp electrode response corresponding to the appearance of unprecipitated Pb^{++} ions in solution. Uranium was found to interfere with the electrode response, so it was first removed by hydrogen peroxide precipitation at ~pH 5. Titrations were conducted in 85 % isopropanol to reduce the solubility of lead sulfate to negligible levels.

This method is based on a method published by Metrohm [57]. A full description of the method can be found in Appendix C.

2.6.4 Free acid

Free acid could not be determined by neutralization because some metals in solution, most notably iron, would hydrolize and precipitate before the equivalence point was reached. Instead, free acid was determined by the method of standard addition, using a method developed internally by Dr. Bé Wassink [78]. A copy of Dr. Wassink's method is provided in Appendix D, with permission.

In the method of standard addition, a pH probe is used to measure the solution potential before and after the addition of a known quantity of sulfuric acid. These values are used to solve two simultaneous Nernst equations, which gives the initial acid concentration. The electrode slope must be known precisely, and is determined

immediately before the analysis using standard solutions. Both the sample and the calibration standards are prepared in a matrix of 2.0 M magnesium sulfate, which provides a very strong and relatively constant background ionic strength between samples. The potential is allowed to fully stabilize before readings are taken. The titration is performed using a pH meter with a precision of 0.1 mV. The additions of standard acid can be performed using an automatic or manual pipette.

2.7 Safe handling of uranium

Uranium is an alpha-emitting radioactive substance, and thus requires special handling procedures beyond what is typical in a metallurgical laboratory. Special precautions undertaken for this project include radiation safety training for everyone working in the laboratory, shielded sample storage, rigorous housekeeping standards, regular monitoring of radiation levels, and special waste disposal arrangements. Details on the safe handling of uranium for this project can be found in Appendix F.

Chapter 3

Crystallization of uranous sulfate: solubility, speed, selectivity, and form

3.1 Introduction

Uranous sulfate hydrate, $U(SO_4)_2 \cdot xH_2O$, is sparingly soluble under acidic conditions, although its solubility varies widely with temperature and sulfate concentration. It can be crystallized out of solution by adding sulfate (typically as sulfuric acid) or by increasing the temperature, although a high recovery is by no means guaranteed. It also does not necessarily result in a quickly-forming, easily-handled precipitate. If left undisturbed, uranous sulfate crystals tend to grow from supersaturated solutions slowly – very slowly – onto preexisting nucleation sites. The resulting large, purple-green crystals make for an excellent show-and-tell piece, but a rather poor hydrometallurgical process. To be useful in the plant, uranous sulfate must crystallize quickly and selectively, with high uranium recovery, into a precipitate with a known composition and good handling characteristics.

In the present work, four aspects of the uranous sulfate x-hydrate crystallization process were investigated: solubility under a wide range of temperatures and sulfuric acid concentrations; the kinetics of crystallization at different temperatures (10 °C, 30 °C, and 60 °C) with stirring and seeding; the purity of precipitates formed from solutions containing Cu, Ni, Fe(II), and Al; and the crystalline form of the pre-

cipitate (i.e., the value of x) under different conditions.

3.2 Background information

The fully oxidized form of uranium, uranium(VI), is very soluble in sulfuric acid. The reduced form, uranium(IV), is much less soluble, and crystallizes from sulfuric acid solutions as the hydrated sulfate salt, $U(SO_4)_2 \cdot xH_2O$. Electrolytic reduction can be used to convert a highly-concentrated (and fully soluble) uranium(VI) sulfate solution into a supersaturated uranium(IV) solution without the addition of any reagents [6, 28, 54].

A cornucopia of $U(SO_4)_2 \cdot xH_2O$ polymorphs have been described in the literature, ranging from $x = 0$ to $x = 9$ [7, 14, 45, 63, 67]. Of these, the most stable is thought to be Kierkegaard's $U(SO_4)_2 \cdot 4\,H_2O$, which has four waters of hydration. The octahydrate, $U(SO_4)_2 \cdot 8\,H_2O$, has classically been considered the other stable polymorph of uranous sulfate, forming at lower temperatures ($<$20 °C) [72]. Various authors [30, 72, 74] have shown that the octahydrate displays normal solubility characteristics, becoming more soluble with increasing temperature, but the tetrahydrate displays inverse solubility characteristics, becoming less soluble upon heating. This leads to the unusual, and potentially useful, situation where uranium(IV) can be precipitated from solution by increasing the temperature and adding sulfate. This is particularly felicitous in the context of selectivity, since many of the contaminants expected in leach solutions become *more* soluble at higher temperature and acid concentration.

The most thorough study of the solubility of uranous sulfate under plant-type conditions was conducted by Suzuki et al. [74] of the Japanese Power Corporation. They studied the solubility of uranous sulfate by heating acidic uranous sulfate solutions for several weeks while periodically assaying the supernatant for uranium(IV) and sulfate. The group also approached equilibrium from the other direction by dissolving an excess of solid uranous sulfate in sulfuric acid solutions, with excellent agreement with the precipitation studies. The authors acknowledged that solids with a form different than $U(SO_4)_2 \cdot 4\,H_2O$ precipitated at lower temperatures, but they did not investigate this in depth. Three important conclusions can be drawn from their work: that solubility decreases with temperature and free sulfate;

that precipitation can be very slow, often taking a week or more to reach equilibrium, with faster kinetics at higher temperatures; and that precipitates other than $U(SO_4)_2 \cdot 4\,H_2O$ can form at lower temperatures.

Virtually no data have been published on the effect of impurities on the solubility of uranous sulfate or the selectivity of its precipitation. The effect of fluoride has been studied in the context of direct uranous tetrafluoride precipitation from a sulfate medium [25], where it was found that uranium(IV) solubility was enhanced by the presence of fluoride up to a F:U molar ratio of 1:1, beyond which solubility declined. The effect of common leach solution impurities, such as Cu, Ni, Fe(II), and Al, have not been reported.

3.3 Experimental setup and data treatment

All of the experiments described in this section proceeded in a similar manner. A quantity of previously-prepared uranium(IV) stock solution was measured into a sealed vessel, typically a 100 mL Pyrex bottle, along with sulfuric acid and metal sulfate salts, if required, to make up the required test solution. The solutions were made on a mass basis, not volumetrically, in order to minimize oxidation of uranium(IV) by contact with air, so the starting uranium concentrations varied slightly from test to test. Deionized water was used to make all solutions using ACS-grade reagents. The exception was uranium, which was supplied from Cameco Corporation's Blind River Refinery as granulated nuclear fuel-grade UO_3. All test solutions were purged with nitrogen or argon to minimize the risk of uranium(IV) oxidation. If periodic sampling was required, an Omnifit Q-series cap with sampling ports was used, and the vessel was purged with inert gas after each sample was taken. All tests were thermostatted in a Thermo Scientific SWB25 shaking water bath, with an attached Isotemp 5150 circulating chiller for cooling. For stirred tests, the solution was agitated with an immersible magnetic stir plate and a PTFE stir bar. For stagnant tests, no agitation was used. A schematic of the general experimental setup is shown in Fig. 3.1.

The procedure for the production of the uranium(IV) stock solutions by electrolytic reduction can be found in Appendix A.

After each test, the contents of the vessels were filtered through an Osmonics

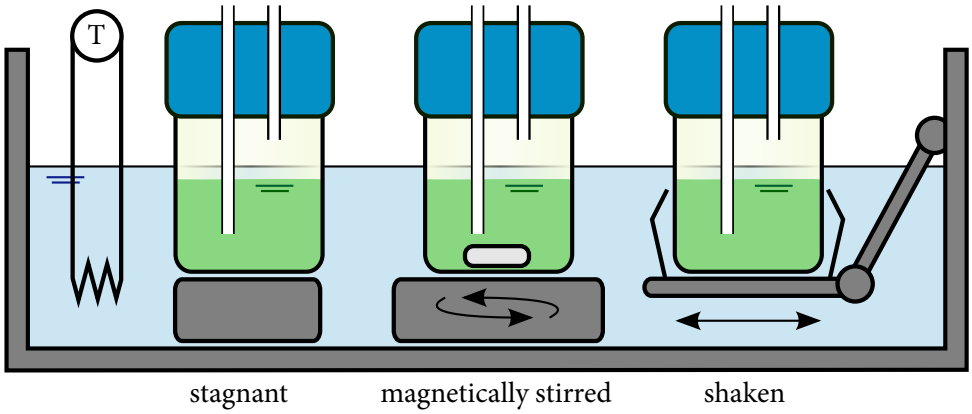

Figure 3.1: Schematic of the experimental setup for the crystallization of uranous sulfate.

nylon 0.22 µm filter. The filtrate was stored in a polypropylene bottle, and analyzed for uranium, sulfate, and impurity metals, as required. The solids were washed with a sulfuric acid solution at the same temperature and concentration used for the test, and then rinsed with ethanol or isopropanol. The solids were then air-dried in a fume hood overnight, or until the odour of alcohol was no longer evident, then stored in a plastic jar. All precipitates were identified by powder x-ray diffraction (XRD), and then digested in 3.5% nitric acid and analyzed for total uranium and sulfate. In tests containing impurities (Al, Cu, Fe(II), or Ni), these elements were assayed by atomic absorption (AA).

The test solutions were always slightly higher in sulfate than in $H_2SO_{4\text{free}}$, with two extra moles of sulfate per mole of uranium. This was because of the acid consumption inherent in the the dissolution of UO_3 and the electrolytic reduction process. Likewise, if the solution was created by dissolving previously-prepared uranous sulfate, it also resulted in the dissolution of two additional moles of sulfate per mole of uranium. To avoid confusion, the concentrations of both sulfate and free sulfuric acid are tabulated.

The experimental conditions for all tests are shown in Table 3.1. The experiments were divided into several different series, each with different goals and slightly different procedures, as described below.

Table 3.1: Experimental conditions for the precipitation of uranous sulfate

		Initial test conditions, mol L^{-1}							
Test	T, °C	H_2SO_{4free}	$SO_4^{2-}{}_T$	U_T	U(IV)	Impurity	Duration, h	Agitation	Seeded?
01-A*	10	1.24	1.67	0.368	0.367	-	1225	shake	no
02-A*	10	1.24	1.67	0.368	0.367	-	1822	shake	no
03-A	10	1.97	2.44	0.367	0.367	-	1606	shake	no
04-A	10	1.97	2.44	0.367	0.367	-	2156	shake	no
05-A	10	2.52	2.98	0.371	0.366	-	1749	shake	no
06-A	10	2.52	2.98	0.371	0.366	-	1823	shake	no
07-A*	30	0.19	0.62	0.288	0.285	-	864	shake	no
08-A*	30	0.60	1.04	0.286	0.283	-	908	shake	no
09-A	30	0.60	1.04	0.286	0.283	-	1199	shake	no
10-A*	30	1.03	1.46	0.286	0.283	-	915	shake	no
11-A	30	1.44	1.88	0.288	0.285	-	1244	shake	no
12-A	30	1.72	1.99	0.411	0.364	-	1680	shake	yes
13-A	30	1.72	1.99	0.411	0.364	-	2689	shake	no
14-A	30	1.86	2.30	0.287	0.284	-	1246	shake	no

Continued on next page

Table 3.1 – continued from previous page

Test	T, °C	Initial test conditions, mol L^{-1}					Duration, h	Agitation	Seeded?
		H_2SO_{4free}	$SO_4{}^{2-}{}_T$	U_T	U(IV)	Impurity			
15-A*	60	0.40	0.66	0.177	0.173	-	1656	shake	no
16-A	60	0.79	1.04	0.177	0.173	-	1654	shake	no
17-A	60	1.20	1.46	0.178	0.174	-	1652	shake	no
18-A	60	1.38	1.63	0.409	0.396	-	1177	shake	yes
19-A	60	1.55	2.04	0.410	0.398	-	979	shake	no
20-A	60	1.55	2.04	0.410	0.398	-	646	shake	yes
21-A	60	1.55	2.04	0.410	0.398	-	671	shake	yes
22-A	60	1.62	1.88	0.177	0.173	-	1632	shake	no
23-A	60	2.01	2.32	0.399	0.389	-	676	shake	yes
24-A	60	2.04	2.29	0.176	0.172	-	1362	shake	no
25-A	60	2.46	2.71	0.178	0.173	-	1293	shake	no
26-A	90	0.51	0.67	0.211	0.198	-	46	shake	no
27-A	90	0.97	1.21	0.218	0.186	-	75	shake	no

Continued on next page

Table 3.1 – continued from previous page

Test	T, °C	Initial test conditions, mol L^{-1}					Duration, h	Agitation	Seeded?
		H_2SO_{4free}	$SO_4{}^{2-}{}_T$	U_T	U(IV)	Impurity			
28-B	60	0.39	2.12	0.148	0.143	-	71	stir	no
29-B	60	0.81	2.06	0.169	0.162	-	49	stir	no
30-B	60	0.82	2.00	0.142	0.137	-	71	stir	no
31-B*	60	1.24	1.97	0.140	0.135	-	71	stir	no
32-B	60	1.88	2.20	0.155	0.149	-	71	stir	no
33-B	60	1.97	2.26	0.145	0.145	-	74	stir	yes
34-B	90	1.85	2.14	0.144	0.144	-	8	stir	no
35-B	90	1.88	2.17	0.144	0.144	-	8	stir	yes
36-B	90	2.31	3.08	0.372	0.332	-	4	stir	yes
37-B	60	0.82	2.08	0.165	0.159	Cu: 1.49E-02	72	stir	no
38-B	60	0.78	1.98	0.158	0.152	Cu: 3.02E-02	72	stir	no
39-B	60	0.79	2.00	0.161	0.155	Cu: 6.82E-02	72	stir	no
40-B*	60	0.77	1.95	0.156	0.150	Cu: 1.40E-01	141	stir	no
41-B	60	1.58	1.96	0.121	0.117	Cu: 1.27E-01	265	stir	no

Continued on next page

Table 3.1 – continued from previous page

Test	T, °C	Initial test conditions, mol L^{-1}					Duration, h	Agitation	Seeded?
		H_2SO_{4free}	$SO_4^{2-}{}_T$	U_T	U(IV)	Impurity			
42-B*	60	0.69	1.77	0.133	0.128	Ni: 1.58E-02	72	stir	no
43-B	60	0.74	1.87	0.144	0.139	Ni: 3.21E-02	72	stir	no
44-B	60	0.80	2.03	0.158	0.152	Ni: 7.81E-02	72	stir	no
45-B†	60	0.80	2.03	0.160	0.154	Ni: 1.64E-01	72	stir	no
46-B	60	1.65	2.06	0.133	0.128	Ni: 1.42E-01	265	stir	no
47-B	60	0.80	2.02	0.134	0.130	Fe: 1.50E-02	71	stir	no
48-B	60	0.77	1.95	0.132	0.127	Fe: 3.12E-02	72	stir	no
49-B†	60	0.76	1.93	0.130	0.126	Fe: 6.45E-02	72	stir	no
50-B*	60	0.73	1.83	0.124	0.120	Fe: 1.32E-01	72	stir	no
51-B	60	1.60	2.00	0.132	0.127	Fe: 1.13E-01	265	stir	no
52-B	60	1.67	2.14	0.128	0.128	Al: 1.53E-01	71	stir	no
53-B	60	1.78	2.07	0.136	0.136	Al: 1.71E-02	71	stir	no

Continued on next page

Table 3.1 – continued from previous page

Test	T, °C	Initial test conditions, mol L^{-1}					Duration, h	Agitation	Seeded?
		H_2SO_{4free}	$SO_4{}^{2-}{}_T$	U_T	U(IV)	Impurity			
54-B	90	2.35	4.68	0.365	0.299	Al: 6.16E-01 Cu: <3.15E-03 Fe: 1.48E-01 Ni: 4.59E-02	4	stir	yes
55-S	4	0.73	0.60	0.297	0.294	-	4	stir	no
56-S	5	1.01	1.25	0.118	0.117	-	16	stir	yes
57-S	5	2.79	2.82	0.352	0.349	-	65	stir	no
58-S	5	0.93	1.15	0.143	0.143	-	336	stagnant	yes
59-S	12	1.01	1.30	0.146	0.144	-	356	stagnant	yes
60-S	60	1.01	1.25	0.118	0.117	-	120	stagnant	no
61-S	70	1.40	1.72	0.159	0.157	-	24	stagnant	yes
62-S	90	1.16	1.56	0.202	0.200	-	88	stir	no
63-S	90	1.65	2.32	0.333	0.332	-	7	stir	yes

* no precipitation was observed

† precipitation was observed, but there was too little sample for analysis

3.3.1 Series A: Slow equilibration

The goal of Series A was to explore how temperature and acid concentration influence the crystalline form of the precipitate, as well as to validate their effect on solubility and precipitation kinetics. The solutions were allowed to come to equilibrium over a long period of time (weeks or months), which generated large, well-defined crystals. The tests were generally terminated when the uranium(IV) concentration did not decline significantly between samples. Shaking at 100 rpm provided gentle agitation, but was not strong enough to suspend the precipitates, and so the crystals grew on the bottom and sides of the vessel. The water bath was set to either 10 °C, 30 °C, or 60 °C. The stock uranium(IV) solution was created by dissolving UO_3 in sulfuric acid, followed by electrolytic reduction in a divided cell using a copper cathode, dimensionally stable anode (DSA), and a Nafion membrane. Nitrogen was used as the inert atmosphere.

Series A tests are indicated with the suffix '-A'.

3.3.2 Series B: Fast precipitation with impurities

The goal of Series B was to study the effect on precipitate purity and the crystallization process of four impurities known to be common in Saskatchewan's uranium ore: Al, Cu, Fe(II), and Ni. Crystallization was encouraged to proceed as quickly as possible by using vigorous magnetic stirring and high temperatures (60 °C and 90 °C). The impurities were all added as their sulfate salts. Each was dissolved at room temperature in a minimal amount of water and sulfuric acid to avoid unnecessary dilution, and then mixed with uranium(IV) stock solution to create a supersaturated uranous sulfate solution when brought to the test temperature. In the case of iron, Fe(II) was used to simulate the likely form after undergoing electrolytic reduction. In some cases, sodium sulfate was also added to hold the sulfate concentration approximately constant across tests, while in others the sulfate concentration was allowed to vary.

The stock uranium(IV) solution was created by dissolving previously-prepared $U(SO_4)_2 \cdot 4\,H_2O$ in sulfuric acid, and was stored in a polypropylene bottle under argon to prevent oxidation. The uranium(IV) content of the stock solution was periodically verified by titration. The impurities M were added such that the molar

M:U ratio varied between 0.1 and 1.0. The tests were generally operated for 72 h, although if a test did not show signs of precipitation, it was allowed to continue longer, and some tests were terminated with no sign of precipitation.

Samples of the supernatant were taken daily, and were analyzed for uranium by titration and impurities by AA. The tests were flushed with argon during sampling.

Series B tests are indicated with the suffix '-B'.

3.3.3 Miscellaneous tests

Some additional experiments were conducted in order to produce bulk amounts of uranous sulfate, typically for use in generating uranium(IV) stock solutions for other purposes. The tests were carried out in much the same way as described above, but usually in larger quantities. Additionally, small amounts of uranous sulfate were produced for the work presented in Chapter 4, primarily with the goal of growing crystals for characterization by single crystal x-ray diffraction. All of the precipitates from these experiments were collected and analyzed in the same way as those from Series A and B, and the results have been included in the discussion where appropriate.

These miscellaneous tests are indicated with the suffix '-S'.

3.3.4 Determining waters of hydration

Waters of hydration (i.e., x in $U(SO_4)_2 \cdot xH_2O$ were determined from TGA data. A complete description of thermal analysis and data processing methods are given in Chapter 6. In summary, the number of waters of hydration was calculated by normalizing the data to weight of its final decomposition product (U_3O_8 at 850 °C), and back-calculating the value of x in $U(SO_4)_2 \cdot xH_2O$ to account for the observed initial weight.

$$x = \frac{m'_0 - \mathrm{MW}_{U(SO_4)_2}}{\mathrm{MW}_{H_2O}} \tag{3.1}$$

where m'_0 is the 'equivalent molecular weight' of the dry room temperature sample, based on the normalization procedure. In some cases, partial weight loss was observed at uncharacteristically low temperatures of <60 °C, probably indicat-

ing the existence of absorbed, not crystalline, water. These occurrences are indicated.

Only a subset of the solid samples were analyzed by TGA owing to the long duration of each determination (approximately 2 hours each).

3.3.5 Minimizing sampling error due to uranium(IV) oxidation and evaporation

While all analytical methods suffer from error to some degree, the determination of uranium(IV) presents a particular challenge due to the ease with which it reoxidizes in air. To minimize exposure to air, samples were withdrawn using a syringe through a downcomer tube permanently installed in the lid of the reaction vessel, while a low-pressure stream of nitrogen was attached a second port in the lid. This had the effect of replacing the volume lost to sampling with inert nitrogen. Samples were diluted and analyzed as soon as possible following withdrawal to minimize air exposure time. A certain amount of waiting time was nevertheless necessary in order to allow the samples to cool to avoid volume-measurement errors related to thermal expansion. In later tests, the sampling syringe was placed into an ice-cooled holder in order to more quickly lower the sample's temperature, speeding up this process.

Evaporative losses were minimized by using sealed reaction vessels, with the pressure equalized by temporarily releasing the sealing stopper several times during the initial heat-up period.

3.4 Results and analysis: solubility and kinetics

3.4.1 The effect of sulfate and temperature on uranium(IV) solubility

It has already been established by Suzuki et al. [74] that the solubility of uranium(IV) decreases with increased sulfate concentration and at higher temperatures. These results were validated through two sets of experiments, where equilibrium was approached slowly from shaken supersaturated solutions (Series A). As expected, the solubility of uranous sulfate at 60 °C declined with higher sulfate concentration, as did the time required to reach equilibrium, as shown in Fig. 3.2. The initial ura-

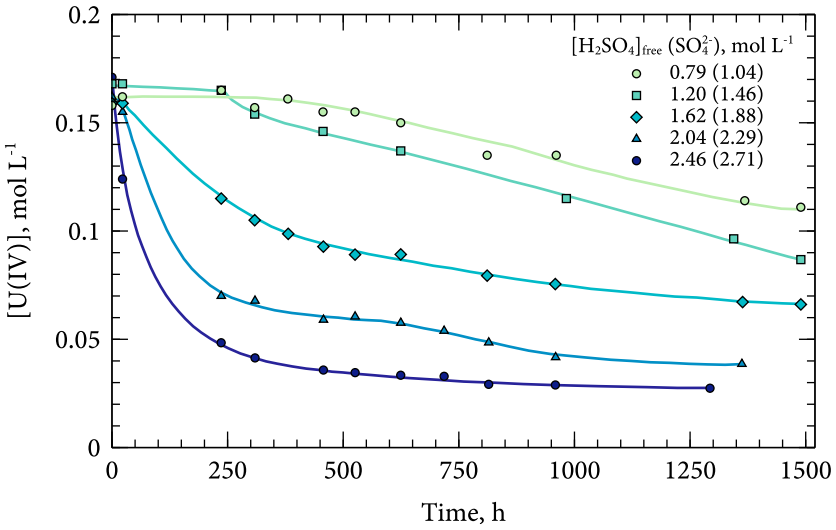

Figure 3.2: The uranium(IV) concentration over time during slow crystallization of uranous sulfate in a shaken vessel at different initial sulfuric acid concentrations at 60 °C (initial sulfate concentrations shown in parentheses). Tests, from top to bottom: 16-A, 17-A, 22-A, 24-A, 25-A.

nium(IV) concentration in all tests was 1.73×10^{-1} mol L^{-1}, and the free acid (and sulfate) concentration was adjusted with concentrated H_2SO_4. At the highest sulfate concentration tested, with an initial concentration of 2.71 mol L^{-1} initial $SO_4^{2-}{}_T$ (2.46 mol l^{-1} H_2SO_{4free}), the solution reached equilibrium at 2.74×10^{-2} mol L^{-1} uranium(IV). At the lowest acid concentration tested, 1.04 mol L^{-1} initial $SO_4^{2-}{}_T$ (0.79 mol l^{-1} H_2SO_{4free}), the uranium concentration declined much less to only 1.11×10^{-1} mol L^{-1} in the same length of time, although it was not clear whether equilibrium had yet been established.

Similar tests were conducted at 10 °C and 30 °C in order to confirm the relationship between uranium(IV) solubility, sulfate concentration, and temperature. Figure 3.3 shows the equilibrium uranium(IV) and $SO_4^{2-}{}_T$ concentrations reached after 55–70 days for tests at 60 °C, 30 °C, and 10 °C. The data align reasonably well with the solubility curves reported by Suzuki *et al*, and extend their work to lower temperatures and higher acid concentrations.

Some of the tests did not show any signs of precipitation, even though reference

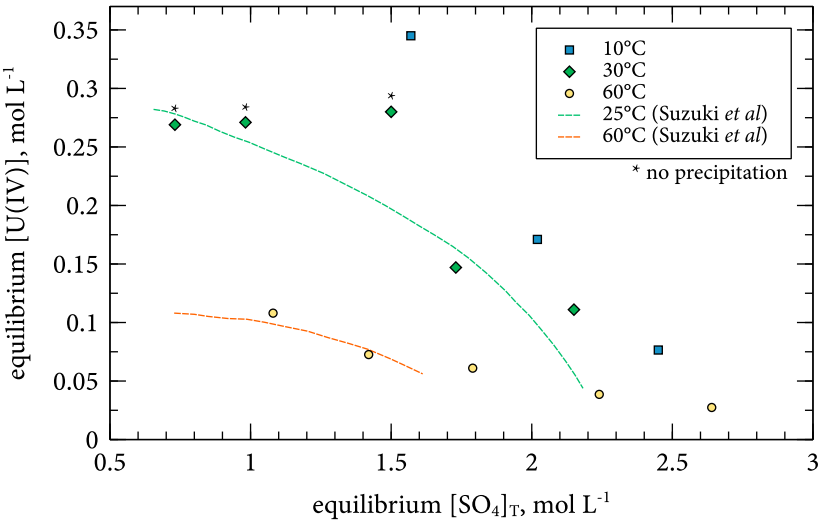

Figure 3.3: Equilibrium uranium(IV) and sulfate concentrations achieved after shaking for 55–70 days at 60 °C, 30 °C, and 10 °C. The solubility curves from Suzuki et al. [74] are shown for reference. Tests: 02-A,04-A, 06-A, 07-A, 08-A, 10-A, 11-A, 14-A, 16-A, 17-A, 22-A, 24-A, 25-A.

to the solubility curves by Suzuki *et al* suggests that precipitation should have occurred. This may have been a (very long) example of an induction period related to a barrier to homogeneous nucleation.

3.4.2 The effect of seeding on the kinetics of precipitation

The kinetics of precipitation are driven by two phenomena: nucleation, which is the formation of a new crystal, and growth, which is the addition of additional atoms to an existing crystal. Many of the precipitation tests had an induction period, where initially no precipitation occurred for a period extending from several hours to many days. The induction period was particularly protracted under conditions of higher solubility, such as at lower temperatures or lower H_2SO_{4free} concentration – in other words, tests with less of a driving force to precipitate. This suggests that the induction period was reflective of a barrier to homogeneous nucleation, and that its length could be influenced by the availability of nucleation sites for heterogeneous nucleation, or other uranous sulfate particles for crystal growth.

It would be preferable from a process engineering standpoint if precipitation were to occur immediately and quickly. In theory, adding seed uranous sulfate particles would provide sites for heterogeneous nucleation and crystal growth, thus avoiding the induction period. To test this theory, 1.0 g of previously-prepared fine powdered $U(SO_4)_2 \cdot 4\,H_2O$ precipitate was added to one of two identical tests at 90 °C using rapid magnetic stirring to create a suspension. Figure 3.4 shows that the induction period all but vanished in the presence of seed, reducing the time needed to reach equilibrium in a stirred vessel by several hours in an 8-hour test. The ultimate concentration reached was the same whether seeded or not.

The addition of seed was found not only to shorten or eliminate the induction period, but also to enhance the kinetics of precipitation even after the induction period had been overcome. Figure 3.5 shows how seeded tests at 30 °C and 60 °C proceeded more quickly than identical unseeded tests, even though the shaking agitation was not aggressive enough to create a suspended slurry. In this case, the layer of fine seed material settled on the bottom of the vessel, providing a layer of material for nucleation and growth. It is likely that the particle size of the seed would have a significant effect on the precipitation kinetics, with a smaller particle size offering more surfaces for growth, and therefore faster kinetics.

3.4.3 The effect of impurities

Without exception, the concentration of impurity was virtually unchanged over the duration of a precipitation test (see Table 3.2), suggesting that no impurities precipitated alongside the uranium sulfate. However, the presence of impurities did appear to increase the solubility of uranium(IV). Figure 3.6 shows how various *M*:U molar ratios influenced the amount of uranium remaining in solution after 72 hours. In all cases, the uranium recovery declined as the amount of impurity was increased[1]. In other words, the presence of impurities had no deleterious effect on selectivity, but did worsen recovery.

It is worth noting that the four impurities tested (Al, Cu, Fe, and Ni) all have substantially smaller ionic radii than uranium, as well as very different chemistries, and so would not be expected to substitute for uranium in the crystal structure of

[1]Note that the starting uranium concentrations were slightly different in each test because the solutions were prepared by mass, not volumetrically, to minimize exposure to oxygen during mixing.

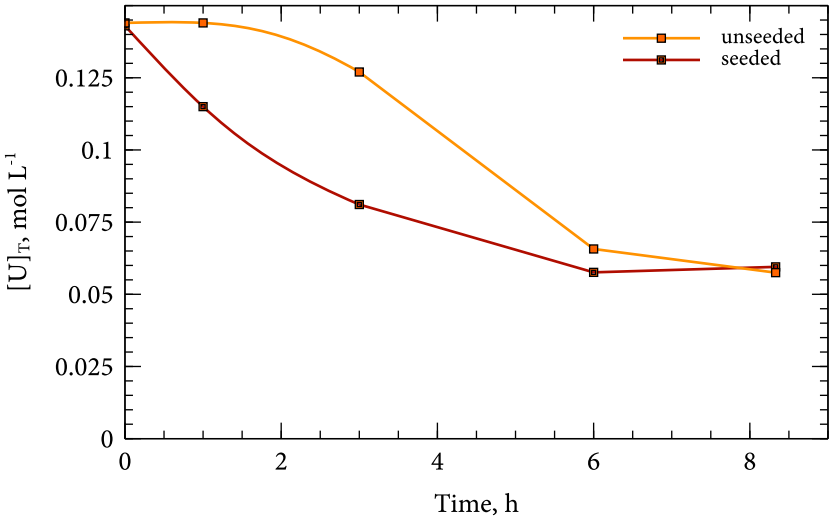

Figure 3.4: The effect of seeding with 1.0 g of $U(SO_4)_2 \cdot 4\,H_2O$ on crystallization kinetics. 90 °C, magnetic stirring. Tests: 34-B, 35-B.

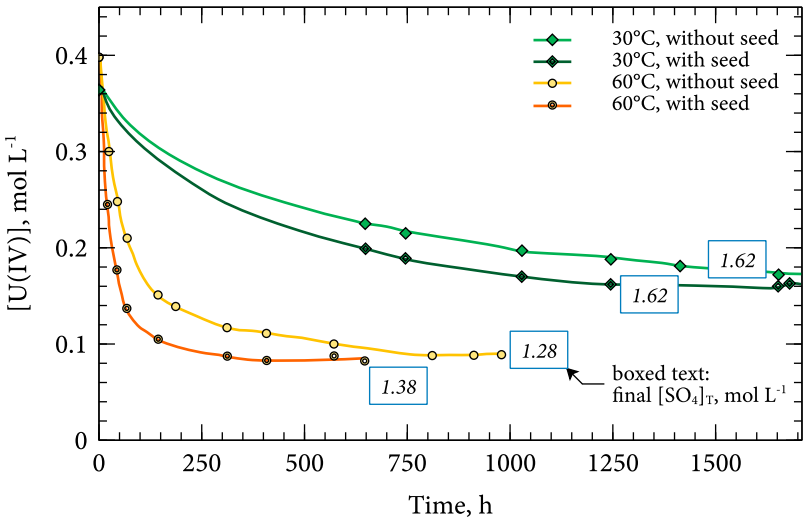

Figure 3.5: The effect of temperature and of seeding with 1.0 g of $U(SO_4)_2 \cdot 4\,H_2O$ on crystallization kinetics. Initial composition: 2.0 M $[SO_4^{2-}]_T$, 1.5 M $[H_2SO_4]_{free}$. Flasks agitated on a shaking table at 100 shakes per minute. Final sulfate concentrations indicated as boxed number. Tests: 12-A, 13-A, 19-A, 20-A.

uranous sulfate. Other actinides and lanthanides, however, do have similar atomic radii and chemistries to uranium, and thus might be more problematic. For example, both thorium and cerium are known to form M(SO4)2.4H2O salts.

The tests with the highest impurity concentrations did not precipitate at all. It is unclear whether the apparent increase in solubility was due to an abnormally long induction period, or whether the solubility of uranium(IV) was enhanced by the presence of the impurity. These cases are marked with *. All other tests showed evidence that equilibrium, or something close to it, had been reached.

Table 3.2: Aqueous-phase impurity assays before and after each test. Sulfate was adjusted to approximately 2.0 mol L^{-1} with sodium sulfate (actual concentration varied from 1.8–2.0 mol L^{-1}).

Test	Impurity M	$[M]_{t=0}$, mol L^{-1}	$[M]_{t=72h}$, mol L^{-1}
37-B	Cu	1.49E-02	1.52E-02
38-B	Cu	3.02E-02	3.00E-02
39-B	Cu	6.82E-02	6.90E-02
40-B	Cu	1.38E-01	1.35E-01
41-B	Cu	1.27E-01	1.26E-01
42-B	Ni	1.58E-02	1.61E-02
43-B	Ni	3.21E-02	3.35E-02
44-B	Ni	7.81E-02	7.97E-02
45-B	Ni	1.64E-01	1.67E-01
46-B	Ni	1.42E-01	1.39E-01
47-B	Fe	1.50E-02	1.57E-02
48-B	Fe	3.12E-02	3.18E-02
49-B	Fe	6.45E-02	6.59E-02
50-B	Fe	1.32E-01	1.34E-01
51-B	Fe	1.13E-01	1.08E-01
52-B	Al	1.53E-01	1.50E-01
53-B	Al	1.71E-02	1.60E-02
54-B	Al	6.16E-01	6.32E-01
	Cu	<3.15E-03	1.92E-03
	Fe	1.48E-01	1.38E-01
	Ni	4.59E-02	4.70E-02

This apparent increase in the solubility of uranium(IV) with the addition of impurities does not have an obvious explanation. One culprit could be the increased ionic strength of the solutions, since that could have made the solutions more hospitable to highly-charged ions such as U^{4+}. However, sodium sulfate was added to the tests to equalize their sulfate concentrations, so the ionic strengths were nearly the same. Another explanation could be that sulfate was 'tied up' in metal-sulfate complexes, lowering the amount of sulfate available to uranium(IV). This also seems unlikely, however, since the sulfate concentration was at least an order of magnitude greater than both the uranium and impurity concentrations.

It is possible that the impurities somehow decreased the kinetics of the crystallization process, and that the observed decline in recovery was in fact only a failure to reach equilibrium in the 72 h period allowed for each test. It has already been shown that a substantial induction period can precede precipitation, so this is certainly possible. This theory was tested by taking samples of the supernatant daily during the copper tests to follow the uranium concentration over time. Figure 3.7 shows that there was no induction period at low copper, a 24-hour induction period at medium copper, and no precipitation at all at high copper. It seems, then, that the length of the induction period did indeed increase in the presence of copper, but that equilibrium was nevertheless reached after 72 h. Similar results for iron did not serve to clarify the situation further.

It is apparent that Cu, Ni, Fe, and Al all act to suppress crystallization of uranous sulfate in some way, though it is unclear whether it is a kinetic or thermodynamic limitation. Equation (3.2) shows the general relationship between the observed solubility with the activity coefficients α and the ostensibly-constant solubility product k_{sp}:

$$\begin{aligned} \alpha_{U^{4+}}[U^{4+}]\alpha^2_{SO_4^{2+}}[SO_4^{2+}]^2 &= k_{sp} \\ [U^{4+}][SO_4^{2+}]^2 &= \frac{k_{sp}}{\alpha_{U^{4+}}\alpha^2_{SO_4^{2+}}} = K_{sp} \end{aligned} \tag{3.2}$$

If the presence of impurity metals increases the activity coefficients, the apparent solubility product K_{sp} would show a corresponding increase. It is unclear, however, what might cause such a change in the activity coefficients. The sulfate concentration of every test was adjusted to approximately 2 mol L^{-1} with sodium sulfate,

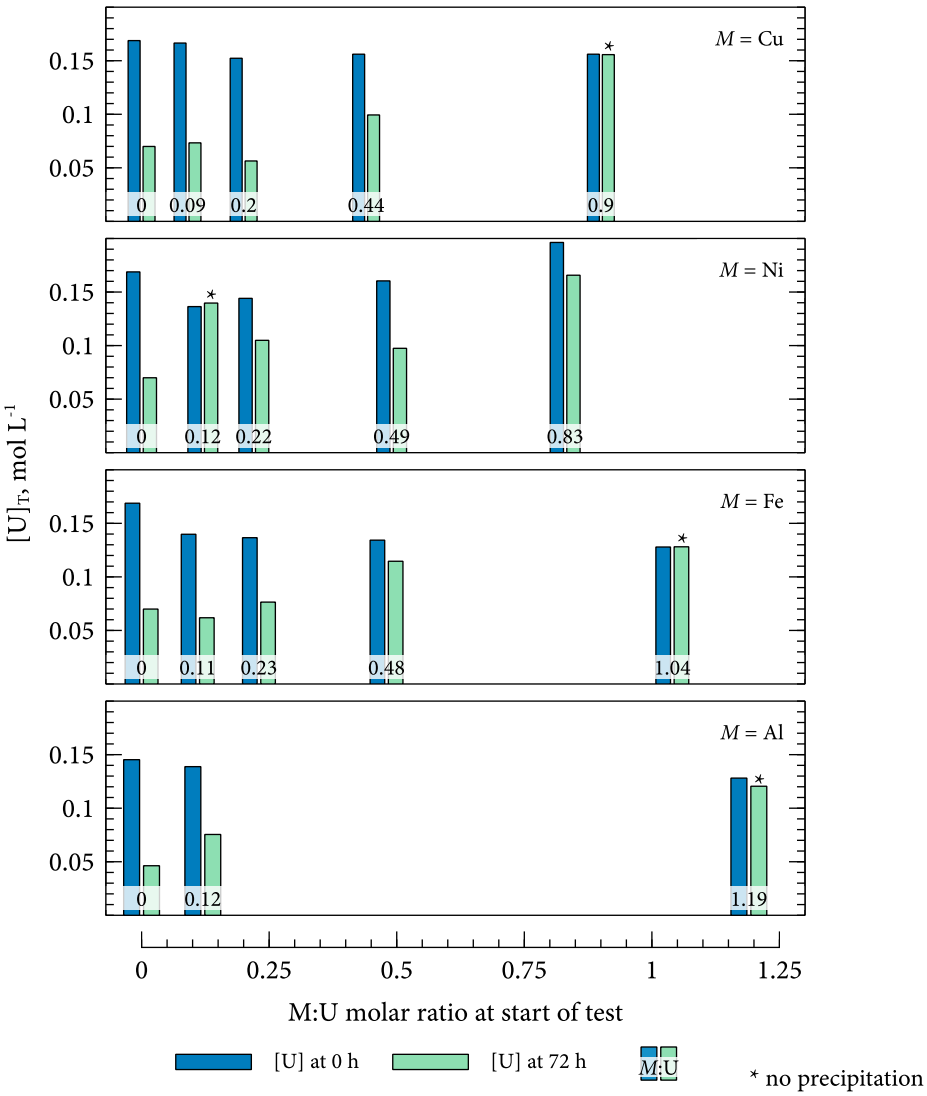

Figure 3.6: The effect of impurities on uranium recovery during uranous sulfate precipitation. From top to bottom, Cu, Ni, Fe, and Al. Bars show the aqueous uranium concentration at 0 and 72 hours. Cu, Ni and Fe tests: 60 °C, 2.0 M SO_4, 1.6 N H_2SO_{4free}. Al tests: 60 °C, 2.1 M SO_4, 3.4 N H_2SO_{4free}. Tests: 29-B, 37-B through 53-B.

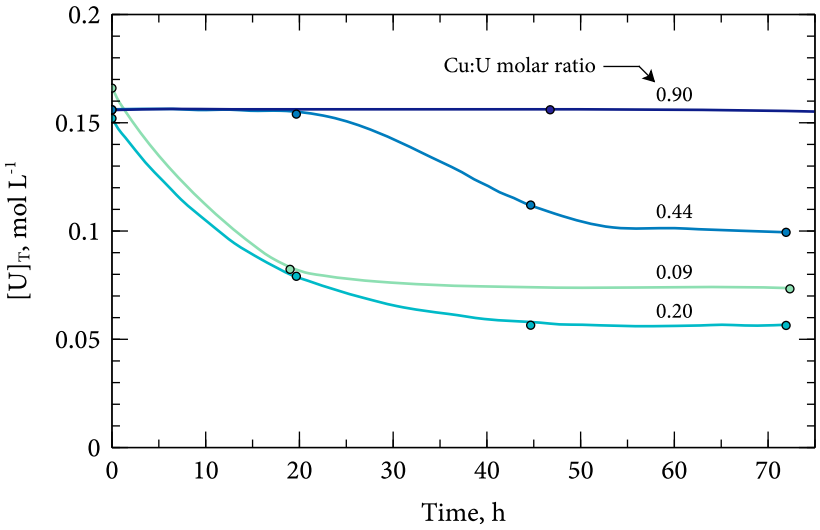

Figure 3.7: Uranous sulfate crystallization kinetics in the presence of copper. 60 °C, ~0.8 mol L^{-1} free sulfuric acid, agitation by stirring. Tests: 37-B, 38-B, 39-B, 40-B.

so it is unlikely that the effect can be explained on the grounds of differing ionic strength. One possibility is that some impurities form a bisulfate complex, thus lowering the free acid concentration and as a consequence increasing the solubility of uranium(IV). In any case, it seems that these metals make a passive contribution on uranium(IV) solubility, since their concentrations did not change as uranium dropped from solution. The effects of impurities on the solids themselves are discussed in the next section.

3.5 Results and analysis: precipitate characterization

The discussion thus far has focused on aqueous-phase phenomena, relating the concentration of uranium in solution to various parameters. It is equally important, however, to look at the solid precipitates themselves.

All of precipitates generated over the course of work were collected and analyzed, providing there was enough material to allow it. In the shaken or stagnant tests, large crystals tended to grow slowly on the bottom of the vessel, whereas in the stirred tests a finer powder-like precipitate formed. The fine precipitates settled rapidly, usually within a few seconds, when stirring was stopped. In all, 46 different solid samples were characterized. Chemical and XRD analysis results for the solids derived from pure solutions are shown in Table 3.3, and those from solutions containing impurities in Table 3.4.

3.5.1 Theoretical chemical composition and x-ray patterns

The theoretical chemical composition of the different uranous sulfate hydrates can easily be calculated from stoichiometry, as shown in Table 3.5. A simple way of determining a precipitate's most likely crystalline form is to compare its chemical assays to these theoretical values.

Powder XRD offers a more direct method of identifying the crystal structure of an unknown precipitate. Figure 3.8 shows the theoretical powder x-ray patterns for the various known uranous sulfate hydrates generated from published Crystallographic Information Framework (CIF) files (disclaimer: one of these publications was authored using data presented in Chapter 4 of this dissertation). The XRD patterns are different enough from one another (and from the pattern of any other known substance, for that matter) to easily distinguish one structure from another in experimental x-ray data, with one exception. The pentahydrate, $U(SO_4)_2 \cdot 5\,H_2O$, is virtually indistinguishable from the tetrahydrate. In the pentahydrate identified by Schnaars and Wilson [67], the additional interstitial water molecule rests in vacancies within the planes of cross-linked $U(SO_4)_2 \cdot 4\,H_2O$ monomers, which apparently has no effect on its XRD pattern. This means that supplementary analysis is required to be certain of the amount of water present in solids nominally showing the pattern of $U(SO_4)_2 \cdot 4\,H_2O$.

Table 3.3: XRD identity, chemical assays, and waters of hydration for solids precipitated from pure solutions. Waters of hydration determined by TGA. Note that not all tests listed in Table 3.1 yielded enough solid sample for analysis.

Test #	XRD Identity	Solids assay, mass %		Waters of hydration
		U	SO_4	
03-A	$U(SO_4)_2 \cdot 6\,H_2O$	44.03%	36.32%	
04-A	$U(SO_4)_2 \cdot 6\,H_2O$	43.78%	35.05%	6.09
05-A	$U(SO_4)_2 \cdot 6\,H_2O$	44.61%	35.09%	5.73
06-A	$U(SO_4)_2 \cdot 4\,H_2O$	44.03%	35.44%	
09-A	$U(SO_4)_2 \cdot 4\,H_2O$	47.22%	37.68%	
11-A	mix*	44.27%	35.07%	5.84
12-A	mix*	46.59%	35.72%	
13-A	mix*	45.18%	35.37%	
14-A	mix*	43.74%	35.78%	5.81
16-A	$U(SO_4)_2 \cdot 4\,H_2O$	46.76%	38.10%	
17-A	$U(SO_4)_2 \cdot 4\,H_2O$	45.53%	37.84%	
18-A	$U(SO_4)_2 \cdot 4\,H_2O$	47.43%	36.40%	
19-A	$U(SO_4)_2 \cdot 4\,H_2O$	47.39%	36.51%	4.11
20-A	$U(SO_4)_2 \cdot 4\,H_2O$	47.22%	37.60%	4.14
21-A	$U(SO_4)_2 \cdot 4\,H_2O$	47.12%	37.58%	
22-A	$U(SO_4)_2 \cdot 4\,H_2O$	46.56%	38.66%	4.08
23-A	$U(SO_4)_2 \cdot 4\,H_2O$	47.30%	38.11%	4.12
24-A	$U(SO_4)_2 \cdot 4\,H_2O$	46.45%	37.91%	
25-A	$U(SO_4)_2 \cdot 4\,H_2O$	46.59%	38.07%	3.97
26-A	unknown	55.02%	32.77%	
27-A	$U(SO_4)_2 \cdot 4\,H_2O$	47.80%	37.00%	3.95
28-B	$U(SO_4)_2 \cdot 4\,H_2O$	43.30%	37.60%	5.2
29-B	*parisaite*	28.12%	47.80%	

Continued on next page

Table 3.3 – continued from previous page

Test #	XRD Identity	Solids assay, mass %		Waters of hydration
		U	SO_4	
30-B	*parisaite*	27.47%	49.66%	
32-B	*parisaite*	25.04%	48.55%	
33-B	$U(SO_4)_2 \cdot 4\,H_2O$	46.63%	37.73%	
34-B	$U(SO_4)_2 \cdot 4\,H_2O$	46.91%	37.69%	
35-B	$U(SO_4)_2 \cdot 4\,H_2O$	47.83%	37.41%	4.2
36-B	$U(SO_4)_2 \cdot 4\,H_2O$	47.02%	37.08%	
55-S	$U(SO_4)_2 \cdot 8\,H_2O$	42.31%	32.67%	8.24
57-S	mix†	41.59%	33.69%	7.25
58-S	$U(SO_4)_2 \cdot 8\,H_2O$	41.45%	33.00%	7.91
59-S	$U(SO_4)_2 \cdot 8\,H_2O$	NES	NES	7.06
60-S	$U(SO_4)_2 \cdot 4\,H_2O$	47.73%	NES	4.27
62-S	$U(SO_4)_2 \cdot 4\,H_2O$	47.57%	37.68%	
63-S	$U(SO_4)_2 \cdot 4\,H_2O$	47.49%	37.22%	4.03

* mixture of $U(SO_4)_2 \cdot 6\,H_2O$ and $U(SO_4)_2 \cdot 4\,H_2O$

† mixture of $U(SO_4)_2 \cdot 6\,H_2O$ and $U(SO_4)_2 \cdot 8\,H_2O$

Table 3.4: XRD identity, chemical assays, and waters of hydration for solids precipitated from solutions containing impurities. Waters of hydration determined by TGA. Note that not all tests listed in Table 3.1 yielded enough solid sample for analysis.

Test #	XRD Identity	Solids assay, mass %						Waters of hydration
		U	SO_4	Al	Cu	Fe	Ni	
37-B	*parisaite*	29.7%	53.0%	-	<0.01%	-	-	
38-B	*parisaite*	28.1%	51.5%	-	0.01%	-	-	
41-B	$U(SO_4)_2 \cdot 4\,H_2O$	41.0%	38.0%	-	0.04%	-	-	7.61*
44-B	*parisaite*	27.5%	52.3%	-	-	-	<0.02%	
46-B	$U(SO_4)_2 \cdot 4\,H_2O$	46.7%	37.5%	-	-	-	<40.02%	4.6*
47-B	*parisaite*	25.9%	49.5%	-	-	<0.01%	-	
51-B	$U(SO_4)_2 \cdot 4\,H_2O$	43.2%	38.8%	-	-	0.06%	-	
52-B	NES	43.1%	NES	<0.15%	-	-	-	
53-B	$U(SO_4)_2 \cdot 4\,H_2O$	45.2%	38.7%	<0.19%	-	-	-	4.8*
54-B	$U(SO_4)_2 \cdot 4\,H_2O$	47.1%	37.6%	<0.37%	<0.003%	<0.01%	<0.01%	4.23

* The TGA signatures and chemical assays of these samples suggest a greater amount of water in the structure than their XRD identities of $U(SO_4)_2 \cdot 4\,H_2O$ suggest. Some weight loss was observed immediately upon commencing TGA analysis, suggesting that some of this water was loosely bound.

Table 3.5: Theoretical mass fractions uranium and sulfate for various uranous sulfate hydrates.

	theoretical mass %		
	U	SO_4	H_2O
$U(SO_4)_2$	55.3%	44.7%	0.0%
$U(SO_4)_2 \cdot 4\,H_2O$	47.4%	38.3%	14.4%
$U(SO_4)_2 \cdot 5\,H_2O$	45.8%	36.9%	17.3%
$U(SO_4)_2 \cdot 6\,H_2O$	44.2%	35.7%	20.1%
$U(SO_4)_2 \cdot 8\,H_2O$	41.4%	33.5%	25.1%

3.5.2 Solid phase stability under various conditions

Most of the solid samples matched one of the theoretical XRD reference patterns unambiguously, and chemically assayed close to the theoretical values, and thus were easy to classify. The sulfate to uranium molar ratio in these samples was close to 2:1, matching the expected stoichiometry. They also had well-defined TGA signatures with weight-loss events corresponding to the expected number of waters of hydration, as shown in Fig. 3.9 (these decomposition reactions are discussed in more detail in Chapter 6). In general, the octahydrate formed at cold temperatures ($\leq$12 °C), the tetrahydrate at high temperatures ($\geq$30 °C), and the hexahydrate at temperatures in between, although only from long-duration tests. Some of the samples, however, defied easy classification and required further analysis.

One of these was a precipitate with the characteristic, but unknown, XRD pattern shown in Fig. 3.10. This solid has been christened *parisaite* in this dissertation, after the research assistant who first produced it. It was frequently found as a product during the Series B tests. *Parisaite* was characterized by a relatively low uranium content of 25–30%, a high sulfate content of 48–53%, and a penchant for reacting with, and expensively destroying, the alumina crucibles used for TGA analysis. The sulfate to uranium molar ratio varied between 4.2 and 4.9. The single TGA scan that was collected showed a series of small weight loss events, culminating in a slow apparent weight loss probably linked to the destruction of the crucible. Its experimentally-determined XRD pattern is shown in Fig. 3.10. The extra sulfate, and possibly even its tendency to chemically attack the alumina crucible at high

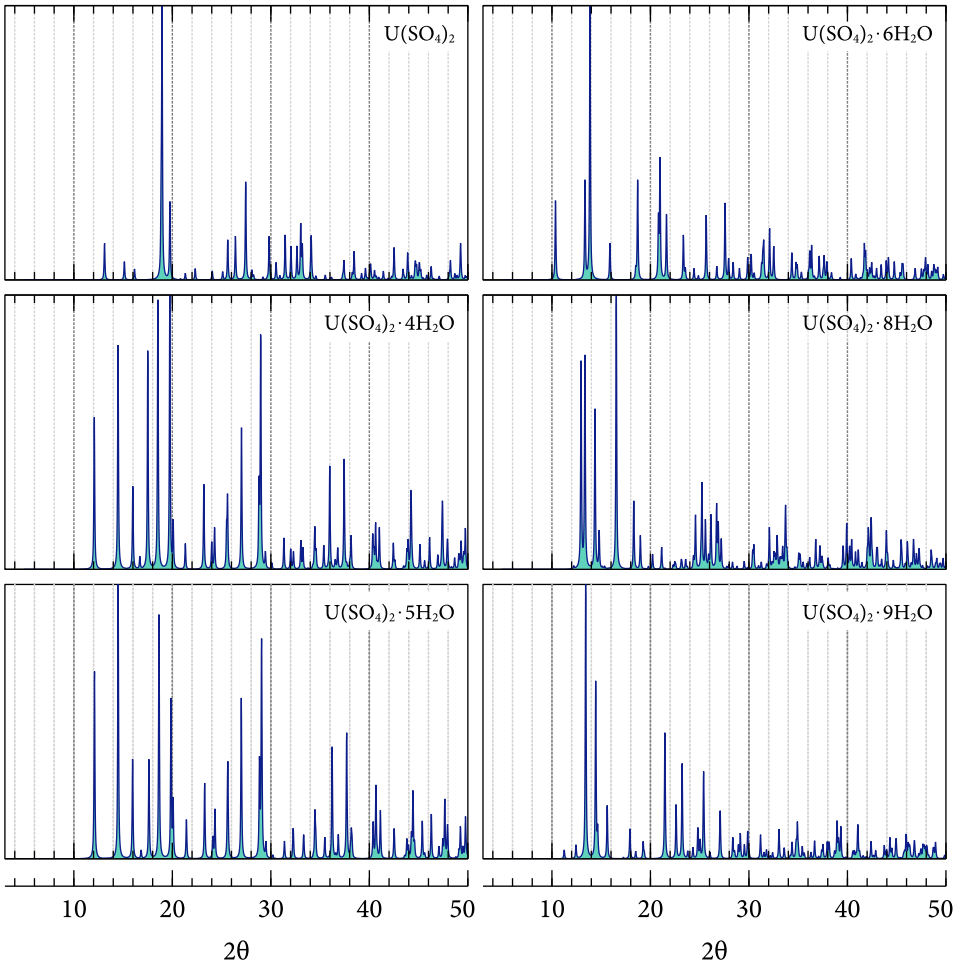

Figure 3.8: Powder x-ray diffraction reference patterns for the known uranous sulfate *x*-hydrates, from $2\theta = 3$–$50°$, generated by Mercury 3.1.1 [53] from published `CIF` files [7, 14, 63, 67].

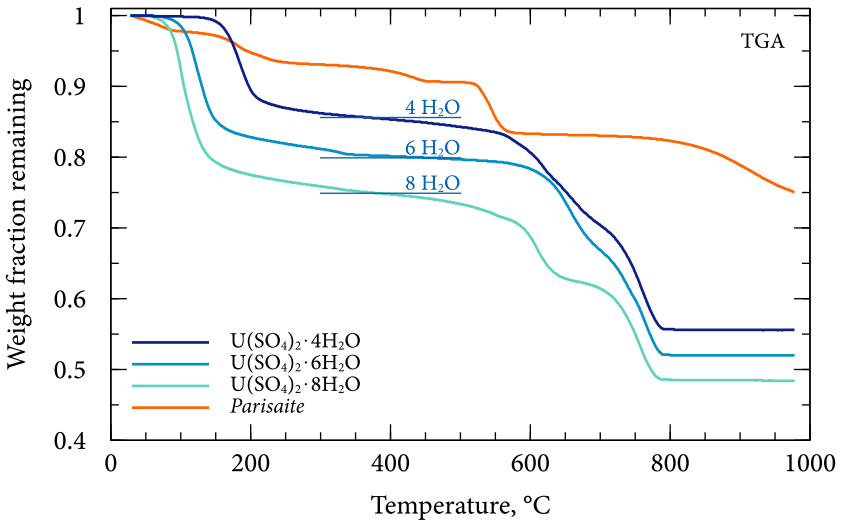

Figure 3.9: Gravimetric analysis of uranous sulfate tetrahydrate, hexahydrate, octahydrate, and *parisaite*. Samples: 63-S, 04-A, 55-S, 29-B.

temperatures, may reflect the presence of crystalline sulfuric acid, H_2SO_4, in the structure. Formulations such as $U(SO_4)_2 \cdot 2\,H_2SO_4$ or $U(HSO_4)_4$ might be possible, but it is impossible to reach a conclusion in the absence of specific evidence.

A second type of difficult-to-classify precipitate, referred to here as 'overhydrated tetrahydrate', or 4+hydrate, displayed an XRD pattern matching that of uranous sulfate tetrahydrate, and had a sulfate to uranium ratio of 2:1. However, the amount of water varied quite substantially, from slightly over 4, in the case of 46-B, to as high as 7.6, in the case of 41-B. The TGA signatures varied, often showing a series of small water loss events, as shown in Fig. 3.11. This extra water was not simply a symptom of careless sample drying, as oven-drying overnight at 60 °C had little effect. A possible explanation is that the extra water was strongly absorbed to $U(SO_4)_2 \cdot 4\,H_2O$ in such a way as not to interfere with the x-ray pattern, and to give it some measure of stability against drying, in a similar manner to Schnaars's pentahydrate. Interestingly, 4+hydrate only precipitated from solutions containing impurities.

It could be that both 4+hydrate and *parisaite* represent intermediary compounds along the pathway to $U(SO_4)_2 \cdot 4\,H_2O$ formation. *Parisaite* was only found in 60 °C

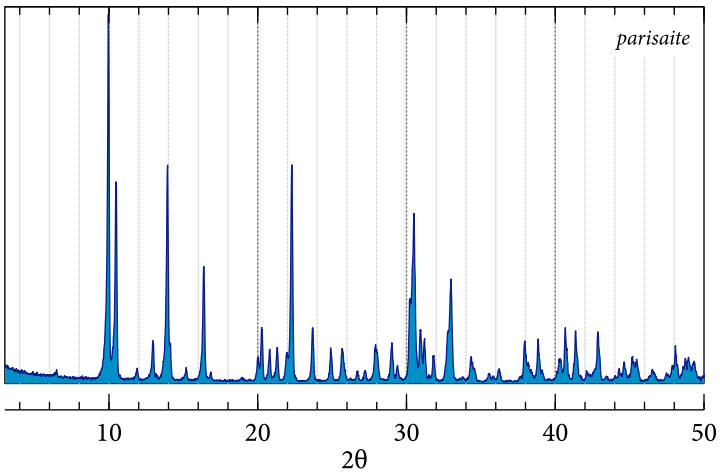

Figure 3.10: Powder XRD pattern of *parisaite*. Sample: 43-B.

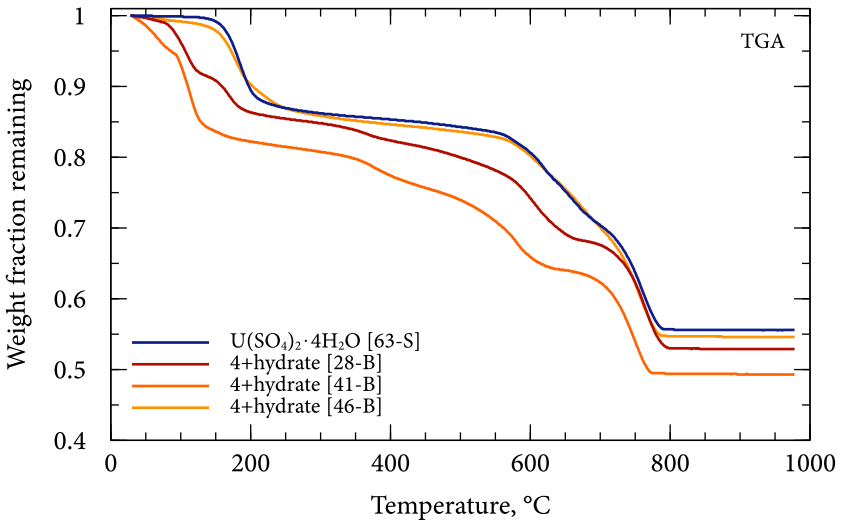

Figure 3.11: Gravimetric analysis of several over-hydrated samples of uranous sulfate tetrahydrate, 4+hydrate, after oven-drying overnight at 60 °C. The pattern for $U(SO_4)_2 \cdot 4\,H_2O$ is shown for reference. Samples: 63-S, 28-B, 41-B, 46-B.

tests less than 72 h in duration, and could apparently be avoided by increasing the temperature or test duration, lowering the amount of acid relative to sulfate, or by adding seed. There was no obvious cause or cure for the appearance of 4+hydrate.

The conditions under which each of the five identified phases – uranous sulfate tetrahydrate, hexahydrate, and octahydrate, 4+hydrate, and *parisaite*– form are easier to visualize as a phase map. Figure 3.12 shows three projections of the relationship between crystalline phase and temperature, acid concentration, and test duration, incorporating every solid sample produced over the course of the present work. $U(SO_4)_2 \cdot 4\,H_2O$ formed at temperatures $\geq$30 °C under a wide variety of conditions. $U(SO_4)_2 \cdot 8\,H_2O$ formed at temperatures $\leq$12 °C. For long-duration slow crystallization tests of more than 40 days, $U(SO_4)_2 \cdot 6\,H_2O$ formed at temperatures as high as 30 °C. *Parisaite* and 4+hydrate are more difficult to classify with respect to temperature because they were only ever observed at 60 °C, the most common temperature tested. Generally, though, it seems that both were intermediary products, with *parisaite* forming first, followed by 4+hydrate, then finally settling on tetrahydrate as a final product. None of the solids showed a clear preference for free acid concentration except hexahydrate, although this may simply have been because the longest-duration low-temperature tests tended to be higher in acid. Note that the possible effects of the different agitation types (i.e., stagnant, shaken, or stirred) on fluid circulation and mass transfer, which might influence the same underlying mechanisms as test duration, are not considered here.

3.5.3 Precipitate quality in the presence of impurities

Perhaps the most important question for the viability of uranous sulfate precipitation as a process technology – and one that has never been addressed in the literature – is whether the process can be done selectively in the presence of impurities. It has already been shown that the aqueous-phase assays for Cu, Ni, Fe(II), and Al remained unchanged during the crystallization of uranous sulfate, even when these metals were present at very high concentrations. Nevertheless, direct analysis of the solids themselves was necessary to confirm this apparent selectivity.

In all cases, the uranous sulfate precipitate remained very pure despite the presence of impurities in the mother liquor, as shown in Table 3.4. In all cases, the im-

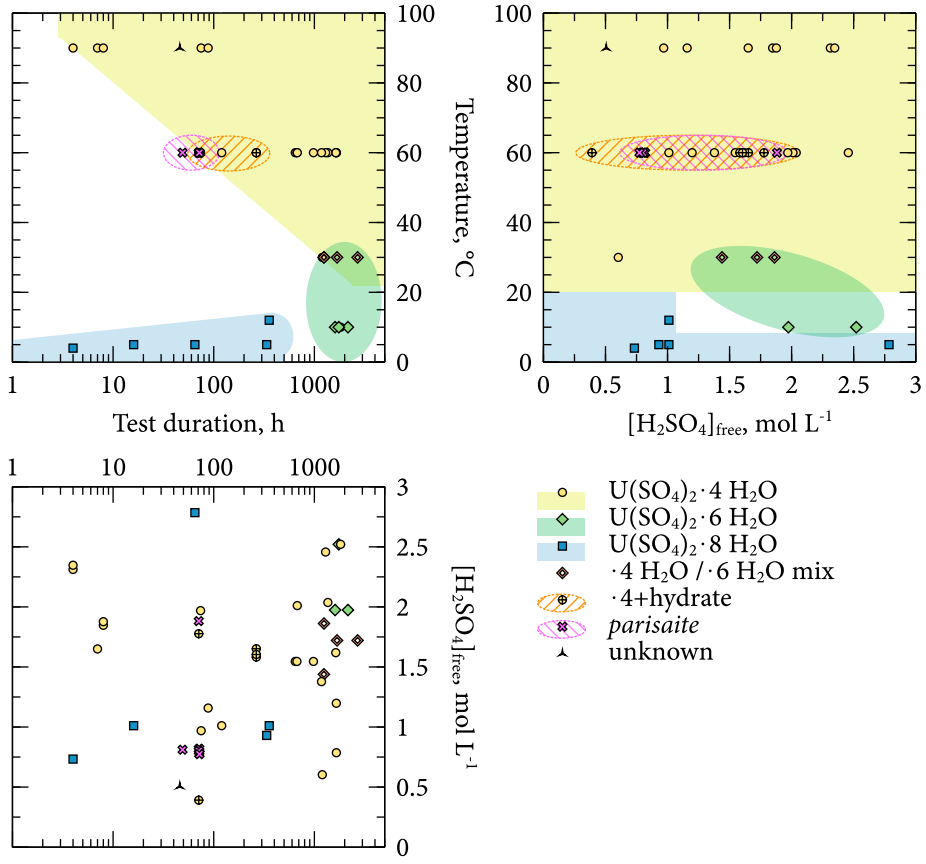

Figure 3.12: Map of the different polymorphs of uranous sulfate with respect to the temperature, free acid, and duration of the tests from which they were harvested. Phases determined by XRD and TGA. Shaded areas indicate the apparent regions of stability for each polymorph.

purity was near or below the detection limit of the AA analytical instrument, even when the sample was prepared with the lowest possible dilution. For the purpose of interpreting these results, it is useful to consider the worst case observed, *CRYST-22*, which was precipitated from a solution containing a 1:1 molar ratio of Fe:U. The solid assayed at 0.06% Fe and 43.2% uranium, which is a 720-fold difference by mass, or a 170-fold difference by atom-fraction – rather good, considering the high amount of Fe in the mother liquor – but nevertheless not a negligible amount. The

Fe in the solid could not have derived from entrained mother liquor, since 0.24 mL would have been required – an unlikely prospect in a 2.88 g sample of thrice-washed solids. It is possible that the Fe derived from residual undissolved $Fe(SO_4) \cdot 7\,H_2O$, particularly since the experimental procedure required the preparation of an extremely concentrated Fe solution. Only 8.6 mg of undissolved ferrous sulfate would be necessary to produce an iron assay of 0.06 %, so this is entirely possible. More simply, the value may represent an error in the analysis, caused by imperfect matrix matching or drift in the calibration. In any case, such fastidiousness sidelines the more important conclusion of these experiments: that uranous sulfate precipitation is highly selective in the presence of large amounts of Al, Cu, Fe(II), or Ni.

The question arises whether uranous sulfate precipitation is so selective that it might be possible to convert the product directly into nuclear fuel. Given the extremely rigorous specifications applied to nuclear fuel, this seems quite unlikely, and indeed, ASTM standard C788 lists its impurity specification for uranyl nitrate feed to a UO_2 conversion facility in micrograms per gram of uranium [4]. When these specifications are applied to uranous sulfate tetrahydrate (47.1 % uranium by weight), each of Al, Cu, Fe, and Ni must be $<$0.01 %, and the sum of *all* impurities must be $<$0.071 %. In most cases, the AA instrument used for solids analysis was not sensitive enough to even detect such small quantities, and when it could detect the presence of these metals, they exceeded the specification (see Table 3.4). It is almost certain, then, that uranous sulfate precipitated from impure solutions would not be able to bypass the refining currently applied to mill concentrates.

3.6 Summary and conclusions

Uranous sulfate crystallization is different from a typical hydrometallurgical precipitation process because it takes place at very high acid concentration, proceeds relatively slowly, and is greatly affected by temperature. To make a viable process, it must produce a crystalline powder in the shortest possible time, while maximizing uranium recovery. The optimal operating conditions in the lab were achieved at 90 °C and $>$2.0 mol L^{-1} sulfuric acid, with aggressive stirring and the addition of seed material. The kinetics of crystal growth appeared be a significant limit on the speed of the process.

Five different polymorphs of uranous sulfate were identified over the course of work, each of which formed under different conditions. Each demonstrated unique x-ray and thermogravimetric signatures. $U(SO_4)_2 \cdot 4\,H_2O$ formed at high temperatures, $U(SO_4)_2 \cdot 8\,H_2O$ at low temperatures, and $U(SO_4)_2 \cdot 6\,H_2O$ at low temperatures and long duration. The so-called over-hydrated tetrahydrate, 4+hydrate, formed from tests containing impurities, and were identical to $U(SO_4)_2 \cdot 4\,H_2O$ except for the presence of additional absorbed water. *Parisaite* formed as an intermediary crystallization product at 60 °C. It had an unknown structure, although the unusually high amount of sulfate relative to uranium suggests the incorporation of sulfuric acid or bisulfate in the structure.

The selectivity of the process was unaffected by the presence of Cu, Ni, Fe(II), or Al, with no evidence of precipitation in either the aqueous or solid assays. These impurities did negatively affect the solubility or kinetics of the process, however, with a substantial suppression of uranium recovery associated with higher levels of impurities.

Chapter 4

The crystal structures of uranous sulfate hexahydrate and octahydrate and a comparison to the other known hydrates

Note: This work has been previously published [14] in collaboration with Dr. Brian Patrick and Anita Lam in the Department of Chemistry and Dr. David Dreisinger in the Department of Materials Engineering. The work presented in this dissertation is largely taken from that publication, but with additional analysis to provide context.

4.1 Introduction

In Chapter 3, four different crystallographically-distinct uranous sulfate polymorphs were identified in the solids precipitated from uranium(IV)-sulfuric acid solutions. These have thus far been described as uranous sulfate 'tetrahydrate', 'hexahydrate', 'octahydrate', and *parisaite*. Each of these phases was found to give a unique powder XRD pattern, which provided a convenient 'fingerprint' for quickly identifying which phase (or combination of phases) was present in a given precipitate. When their four x-ray patterns were searched for in two popular crystallographic databases, the Powder Diffraction File (PDF) and the Open Crystallographic Dat-

abase (OCD), surprisingly only the tetrahydrate was found. A further search of the literature confirmed that the octahydrate had never before been crystallographically characterized (although it had been identified chemically), and hexahydrate and *parisaite* had never been observed at all. Given this gap in the literature, it was decided to structurally characterize the undescribed uranous sulfate hydrates.

While the pursuit of detailed crystallographic data may seem peripheral to the needs of a process engineer, knowledge of a structure actually has many uses beyond the arcane practice of tabulating bond distances and torsion angles. One tangible benefit is the ability to calculate a substance's theoretical powder XRD pattern, which grants a concrete method of identifying its presence in powder samples. It can also provide explanations for macroscopic behaviour. For example, knowledge of the positioning and connectivity of coordinated and solvent water molecules (collectively described here as 'waters of hydration') could explain why the different uranous sulfate polymorphs lose their water at such different temperatures when heated (this phenomenon is explored in Chapter 6).

In the present work, two new uranium(IV) sulfate salt hydrates were structurally characterized by single crystal x-ray diffraction and analyzed by vibrational spectroscopy: $\{[U(SO_4)_2(H_2O)_5] \cdot H_2O\}_n$ (complex **1**) and $[U(SO_4)_2(H_2O)_6] \cdot 2\,H_2O$ (complex **2**). The editors of *Acta Crystallographica* helpfully advised that the proper names for these compounds are *catena*-poly[[pentaaquauranium(IV)]-di-μ-sulfato-κ^4O:O'] monohydrate] and hexaaquabis(sulfato-κ^2O,O')uranium(IV)-dihydrate, respectively, but to mitigate the risk of causing a nomenclature-induced aneurysm in the reader, they will simply be referred to as hexahydrate and octahydrate.

Other compounds with the general formula $[U(SO_4)_2(H_2O)_a] \cdot bH_2O$, where a is the number of coordinated waters and b is the number of solvent waters, have been characterized in the past by other authors [7, 45, 67], all of which consist of a central uranium(IV) atom coordinated to at least two sulfates and between zero and seven water molecules. Some of the complexes have additional solvent water molecules that contribute to hydrogen bonding. The binding mode of the sulfate to the uranium and the degree of bridging between units is different in each case.

Parisaite was not characterized because no single crystals of sufficient size were isolated.

4.2 Experimental

4.2.1 Synthesis and crystallization

For complex **1**, a solution of 100 g L^{-1} uranium and 100 g L^{-1} sulfate was made by dissolving 61.7740 g of UO_3 in 51.08 g of concentrated sulfuric acid diluted to 500 ml with deionized water. The solution was electrolytically reduced at a current of 5.0 A for five hours to 98.4 % conversion in an electrolytic cell consisting of a copper cathode, a TIR-2000® dimensionally-stable anode (titanium substrate with a proprietary coating of iridium and tantalum oxidides), and a Nafion membrane. In order to create a supersaturated solution, 48.24 g of concentrated sulfuric acid was slowly mixed with 300 mL of the reduced solution in a nitrogen-purged glass bottle sitting in a chilled water bath, being mindful to not allow the temperature to rise above 10 °C. The bottle was then sealed and placed in a 10 °C shaking water bath set at 100 shakes per minute. The solution was allowed to crystallize for 90 days, after which the crystals were separated from the supernatant using a 0.22 mm nylon filter. The solids were washed three times with a 5 % sulfuric acid solution, three times with deionized water, and twice with ethanol. The crystals were dried in air for 2 hours, then placed in a desiccator with silica gel desiccant overnight. The yield was 19.11 g of small purple-green rod-like crystals. Powder XRD analysis confirmed that the the crystals consisted entirely of an unidentified phase, with no traces of any known uranium(IV) or uranium(VI) compounds.

To synthesize complex **2**, 11.2992 g of previously-prepared crystalline uranous sulfate (identified by powder XRD as the tetrahydrate) was dissolved in 100 ml of 0.93 mol L^{-1} sulfuric acid at room temperature under nitrogen. 15 ml of the resulting uranium(IV) solution was added to a glass vial. The vial was placed without a cap inside a larger bottle containing 50 ml of absolute ethanol, such that the ethanol was able to diffuse into the mother liquor, thus lowering the uranium(IV) solubility over time and encouraging slow crystallization. The outer bottle was purged with nitrogen, sealed, and placed inside a 12 °C water bath. After 15 days, the contents were filtered, and the resulting crystals were washed with 12 °C 1.0 mol L^{-1} sulfuric acid, followed by 12 °C ethanol.

4.2.2 Data collection and refinement

Crystal data, data collection methods, and structure refinement details are summarized in Table 4.1.

For complex **1**, a green rod crystal having approximate dimensions of 0.065 × 0.192 × 0.568 mm was mounted on a glass fibre with epoxy. Measurements were made on a Bruker X8 APEX II diffractometer with graphite monochromated Mo-Kα radiation. The data were collected in a series of ϕ and ω scans in 0.50° oscillations using 30.0 s exposures at a temperature of 23.0 °C, to a maximum 2θ value of 60.1°. The crystal-to-detector distance was 37.98 mm.

For complex **2**, a green crystal having approximate dimensions of 0.06 × 0.06 × 0.09 mm was mounted on a glass fibre under a drop of oil. Measurements were made on a Bruker APEX DUO diffractometer with graphite monochromated Mo-Kα radiation. The data were collected in a series of ϕ and ω scans in 0.50° oscillations using 5.0 s exposures at a temperature of −183.0 °C, to a maximum 2θ value of 60.08° . The crystal-to-detector distance was 39.99 mm.

The data were collected and integrated using the Bruker SAINT software package [10]. For complex **1**, face-indexed absorption correction was performed on the data, with minimum and maximum transmission coefficients of 0.016 and 0.239, respectively. All hydrogen atoms were refined isotropically. For complex **2**, the data were corrected for absorption effects using the multi-scan technique (SADABS) [11]. All hydrogen atoms were refined isotropically and located on the water molecules by difference maps, except hydrogen atoms 16A and 16B, which were placed in calculated positions and were refined as riding on O16. The data for both were corrected for Lorentz and polarization effects.

4.2.3 Vibrational spectroscopy

IR samples were diluted with dry potassium bromide to 0.4–0.5 wt.% and pressed into a pellet. Spectra were collected on a PerkinElmer Spectrum 100 Fourier transform infrared spectroscopy (FTIR) Spectrometer using 25 scans over the range 4000–250 cm^{-1} with a resolution of 2 cm^{-1}. The background, determined by scanning a pure potassium bromide pellet, was subtracted from each data set. Raman data were collected on single crystals using a HORIBA Jobin Yvon LabRAM HR Raman mi-

Table 4.1: Single crystal x-ray diffraction experimental details

	Complex **1**	Complex **2**
Crystal data		
chemical formula	$[U(SO_4)_2(H_2O)_5] \cdot H_2O$	$[U(SO_4)_2(H_2O)_6] \cdot 2\,H_2O$
crystal habit, color	rod, purple-green	prism, purple-green
formula weight ($g\,mol^{-1}$)	538.25	574.28
crystal system, space group	monoclinic, $I2/a$	monoclinic, $P2_1/n$
collection temperature (K)	296	90
a, (Å)	7.5190(2)	8.4071(3)
b, (Å)	13.2464(3)	11.7144(4)
c, (Å)	11.5073(4)	13.2659(4)
α, β, γ, (°)	90, 104.388(1), 90	90, 92.5100(10), 90
volume ($Å^3$)	1110.18(5)	1305.23
Z	4	4
abs. coefficient μ (mm^{-1})	15.07	12.84
crystal size (mm)	$0.095 \times 0.192 \times 0.568$	$0.06 \times 0.06 \times 0.09$
Data collection		
diffractometer	Bruker X8 APEXII area-detector diffractometer	Bruker DUO APEXII CCD area-detector diffractometer
radiation type	Mo $K\alpha$	Mo $K\alpha$
Absorption correction		
T_{min}, T_{max}	0.016, 0.239	0.408, 0.463
total no. reflections	20300	15278
unique reflections	1642	3784
R_{int}	0.032	0.023
$(\sin\Theta/\lambda)_{max}(Å^{-1})$	0.705	0.704
Refinement		
$R[F^2 > 2\sigma(F^2)]$, $wR(F^2)$, S	0.011, 0.028, 1.31	0.017, 0.035, 1.02
no. of reflections	1642	3784
no. of parameters	104	231
H-atom treatment	all H-atom parameters refined	H atoms treated by a mixture of independent and constrained refinement
$\Delta\rho_{max}, \Delta\rho_{min}$ (e $Å^{-3}$)	1.44, -0.93	0.82, -0.64

Table 4.2: Assay results for uranous sulfate hexahydrate and octahydrate (complexes **1** and **2**). Values in parentheses are the theoretical stoichiometric values.

	Complex **1** $[U(SO_4)_2(H_2O)_5] \cdot H_2O$	Complex **2** $[U(SO_4)_2(H_2O)_6] \cdot 2\,H_2O$
Uranium (wt %)	43.8% (44.2%)	41.5% (41.4%)
Sulfate (wt %)	35.0% (35.7%)	33.0% (33.5%)
Water (wt %)	20.1% (20.1%)	24.8% (25.1%)
Implied waters of hydration	6.0 (6.0)	7.9 (8.0)
Trace metals	below detection limit	

croscope with a linearly polarized excitation line of 442 nm (complex **1**) and 633 nm (complexes **1** and **2**). The second laser was used for complex **2** in order to confirm that certain broad, strong peaks were due to fluorescence and not Raman scattering.

4.2.4 Chemical analysis

A sample of each crystal was digested in 3.5% nitric acid and diluted to a known mass and volume. Uranium and sulfate were determined by titration, trace metals by ICP-MS, and waters of hydration by thermal analysis. The assay results, shown in Table 4.2, were within 2 % of the theoretical stoichiometric values.

4.2.5 Software

All refinements were performed using SHELXL-2012 [68] using the OLEX2 [20] interface for complex **2** and the WinGX [24] interface for complex **2**. Both structures were solved by direct methods using the SIR97 program [2]. Images of the structures were generated using CrystalMaker® [18].

4.3 Results

Schematic representations of the two complexes are shown in Fig. 4.1. Select bond lengths are shown in Table 4.3. The complete set of crystallographic data can be downloaded in `CIF` format from the *A*cta Crystallographica C website.

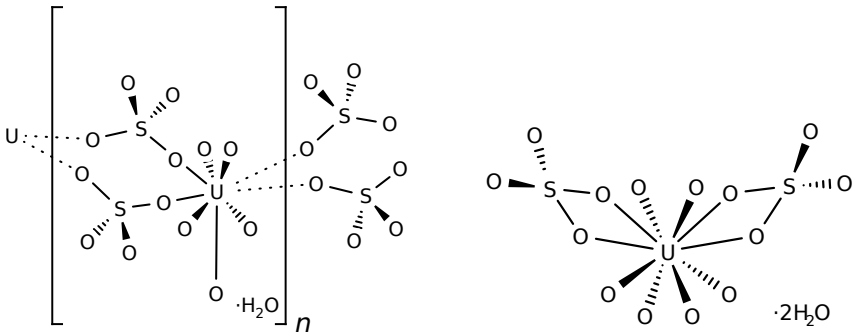

Figure 4.1: Schematic of the structures of uranous sulfate hexahydrate and octahydrate (complexes **1** and **2**).

Table 4.3: Selected bond (–) and hydrogen bond (donor ··· acceptor) lengths (Å) for $[U(SO_4)_2(H_2O)_5] \cdot H_2O$ (**1**) and $[U(SO_4)_2(H_2O)_6] \cdot 2\,H_2O$ (**2**).

Complex **1** $[U(SO_4)_2(H_2O)_5] \cdot H_2O$				Complex **2** $[U(SO_4)_2(H_2O)_6] \cdot 2\,H_2O$			
U1—O1	2.3133(15)	O3···O5	2.714(3)	U1—O1	2.4686(19)	O1···O15	2.832(3)
U1—O2	2.3234(14)	O3···O7	3.033(2)	U1—O2	2.5408(19)	O2···O14	2.644(3)
U1—O5	2.4563(15)	O3···O7	2.806(2)	U1—O5	2.4721(19)	O2···O16	2.899(3)
U1—O6	2.536(2)	O4···O8	2.864(2)	U1—O6	2.5337(19)	O3···O10	2.681(3)
U1—O7	2.4589(14)	O4···O7	2.703(2)	U1—O9	2.417(2)	O3···O12	2.661(2)
S1—O1	1.4827(16)	O5···O8	2.733(3)	U1—O10	2.400(2)	O4···O11	2.752(2)
S1—O2	1.4888(14)	O6···O7	3.0140(19)	U1—O11	2.462(2)	O4···O14	2.672(3)
S1—O3	1.4583(17)			U1—O12	2.381(2)	O5···O16	2.864(3)
S1—O4	1.4517(15)			U1—O13	2.406(2)	O6···O15	2.903(3)
				U1—O14	2.428(2)	O7···O10	2.709(3)
				S1—O1	1.5073(19)	O7···O13	2.650(3)
				S1—O2	1.483(2)	O8···O12	2.696(3)
				S1—O3	1.462(2)	O8···O9	2.701(3)
				S1—O4	1.463(2)	O9···O16	2.812(3)
				S2—O5	1.5035(19)	O11···O15	2.807(3)
				S2—O6	1.484(2)	O13···O15	2.770(3)
				S2—O7	1.464(2)	O14···O16	2.770(3)
				S2—O8	1.461(2)		

4.3.1 Crystal structures

The neutral U(IV) sulfate $\{[U(SO_4)_2(H_2O)_5] \cdot H_2O\}_n$, (1), crystallizes as purple-green rods in the body-centred monoclinic space group $I2/a$. The molecular complex consists of a uranium atom coordinated to four bidentate bridging sulfate ligands and five water molecules, resulting in a nine-coordinate complex which forms herringbone chains in the direction of the c-axis (Figs. 4.2 and 4.3). Four of the five coordinated water molecules are approximately the same distance from the uranium centre (2.4563(15) Å and 2.4589(14) Å for U1–O5 and U1–O7, respectively), but the fifth bound water, O6, is further, at 2.536(2) Å. The solvent water atom O8 resides in a vacant space between neighbouring chains. There is extensive hydrogen bonding both within each unit and extending between chains.

The neutral U(IV) sulfate $[U(SO_4)_2(H_2O)_6] \cdot 2\,H_2O$, (2), crystallizes as purple-green prisms in the primitive monoclinic space group $P2_1/n$. The molecular complex consists of a uranium atom bound by two terminal bidentate chelating sulfate ligands and coordinated to six water molecules, resulting in a 10-coordinate complex with no bridging (Figs. 4.4 and 4.5). Each of the free waters, O15 and O16, is held by hydrogen bonding to two bound waters and two bound sulfate oxygens, connecting a total of three neighbouring molecules in the crystal structure. Hydrogen bonds are also observed between each of the unbound sulfate oxygens and the bound water of a neighbouring molecule in the crystal structure.

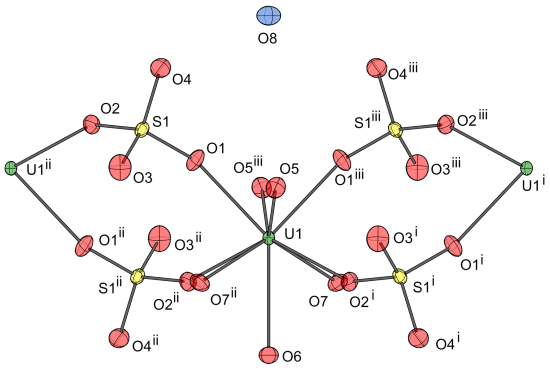

Figure 4.2: Displacement ellipsoid model (50% probability level) depicting the extended structure of $\{[U(SO_4)_2(H_2O)_5] \cdot H_2O\}_n$ (**1**). Hydrogen atoms have been omitted for clarity. Symmetry codes: (i) $x, -y+\frac{1}{2}, z-\frac{1}{2}$; (ii) $-x+\frac{1}{2}, -y+\frac{1}{2}, -z+\frac{3}{2}$; (iii) $-x+\frac{1}{2}, y, -z+1$.

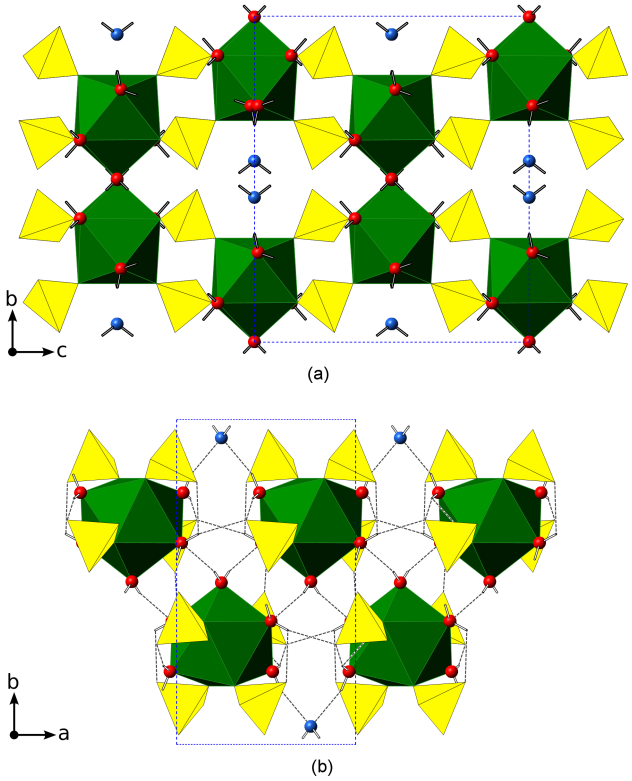

Figure 4.3: Polyhedral model of $[U(SO_4)_2(H_2O)_5] \cdot H_2O$ (**1**). (*a*) A view down the *a* axis, showing the herringbone chain connectivity in the direction of the *c* axis. (*b*) A view down the *c* axis, showing the chains head–on and demonstrating that individual chains are connected only through hydrogen bonding (dashed lines). Colour key: uranium in green, sulfate in yellow, coordinated water in red, and free water in blue.

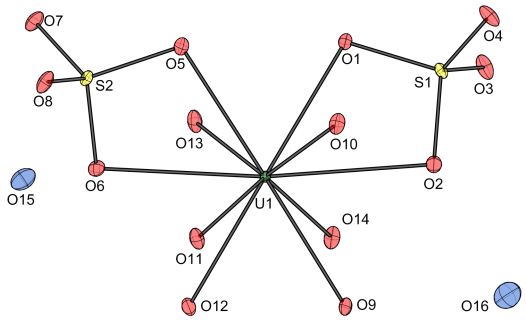

Figure 4.4: Displacement ellipsoid model depicting the connectivity of $[U(SO_4)_2(H_2O)_6] \cdot 2\,H_2O$ (**2**). Hydrogens are omitted for clarity.

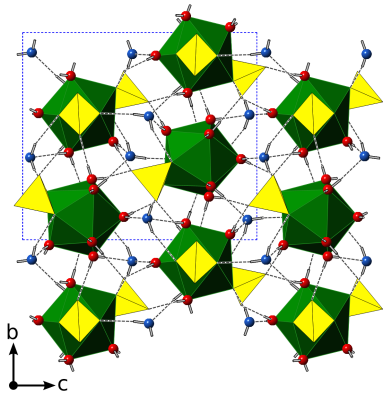

Figure 4.5: Polyhedral model of $[U(SO_4)_2(H_2O)_6] \cdot 2\,H_2O$ (**2**) showing hydrogen bonding (uranium in green, sulfate in yellow, coordinated water in red, and free water in blue).

4.3.2 Vibrational spectroscopy

The vibrational spectra of both complexes are dominated by signals corresponding to the sulfate anion and the total water. Free sulfate, which has tetrahedral geometry (T_d), has four Raman-active and two IR-active vibrational modes [60]. As the symmetry of the sulfate is reduced through coordination, additional vibrational modes arise from the lifting of degeneracies, resulting in a change in the number and position of the peaks seen in the Raman and IR spectra. The different sulfate binding modes – bidendate bridging for complex **1** and chelating terminal for complex **2** – can therefore be distinguished by their Raman and IR spectra. The most active region of the Raman and IR spectra from 400–1300 cm^{-1} are given in Fig. 4.6. The extended spectra are available in Appendix B.

For complex **1**, the intense signal at 1025 cm^{-1} in the Raman spectrum has been assigned to the ν_1 symmetric stretching mode, with the corresponding signal in the IR spectrum at 1012 cm^{-1}. Also in the Raman spectrum, there are two ν_2 (453 and 435 [sh][1] cm^{-1}), two ν_3 (1186 [sh] and 1124 [sh] cm^{-1}) and three ν_4 signals (638 [w], 623 [sh] and 595 cm^{-1}) for a total of nine ligand vibrational modes. In the IR spectrum, signals are observed at ν_1 (one band), ν_2 (two bands), ν_3 (three bands) and ν_4 (three bands). The IR spectrum also exhibits a medium band with two local peaks at 1609 and 1665 cm^{-1}, corresponding to the total water.

For complex **2**, all four vibrational modes are also active. The strongest Raman signal is again ν_1 at 979 cm^{-1}, with the corresponding band in the IR spectrum at 971 cm^{-1}. Two ν_2 (519 [sh] and 423 [sh] cm^{-1}] and three ν_3 signals (1157, 1119 [sh] and 1042 cm^{-1}) are also clear in the Raman spectrum. Two weak ν_4 bending bands are visible in the Raman spectrum (645 [w] and 605 [w] cm^{-1}), with much stronger corresponding peaks in the IR spectrum (653 and 603 cm^{-1}). The IR spectrum shows up to six closely-overlapping signals in the ν_3 region, compared with three in the Raman spectrum. Similar to complex **1**, a multicomponent band corresponding to the total water is observed at 1585–1700 cm^{-1}. Intense fluorescence was observed from 2000–4000 cm^{-1} when using the 442 nm laser, but these peaks disappeared when using the 663 nm laser.

[1] sh = sharp, w = weak

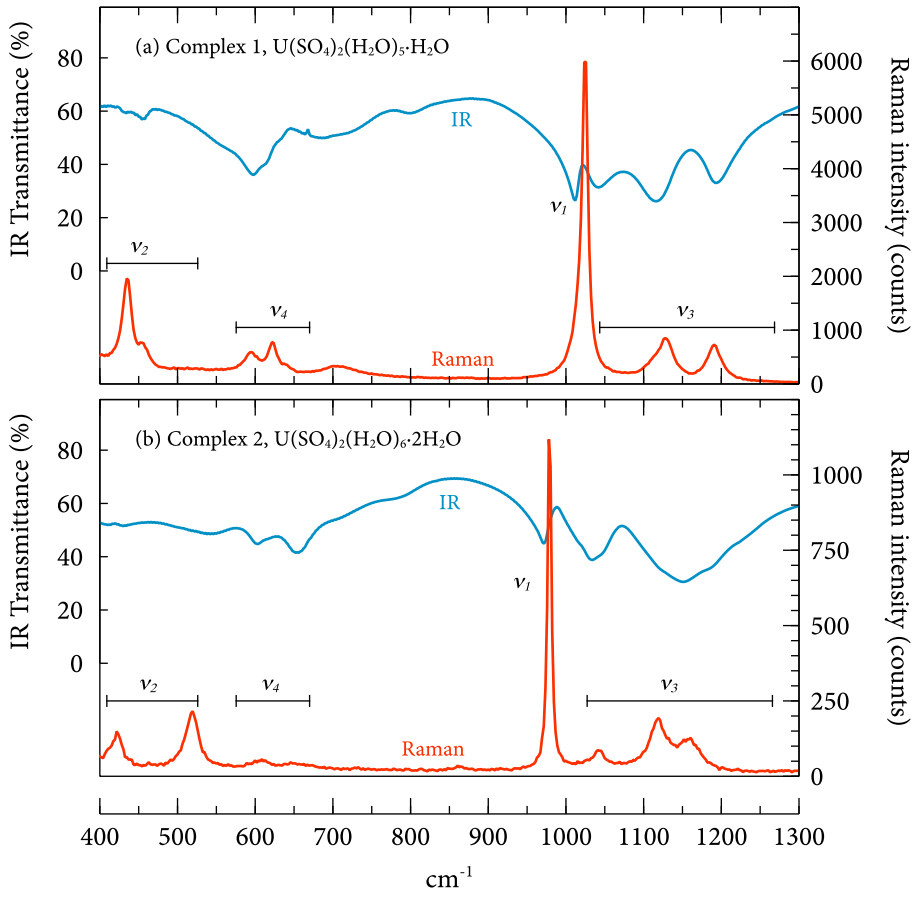

Figure 4.6: FTIR (blue) and Raman (red) spectra of uranous sulfate hexahydrate and octahydrate (complexes **1** and **2**).

4.4 Discussion and comparison with other known uranium(IV) sulfate hydrates

With the addition of the two structures presented in this work, five distinct structures of the neutral U(IV) sulfate *x*-hydrate complex are now known: anhydrous $U(SO_4)_2$ [7], tetrahydrate $U(SO_4)_2(H_2O)_4$ [45], hexahydrate $[U(SO_4)_2(H_2O)_5] \cdot H_2O$, octahydrate $[U(SO_4)_2(H_2O)_6] \cdot 2\,H_2O$, and 9-hydrate $[U(SO_4)_2(H_2O)_7] \cdot 2\,H_2O$ [67]. A pentahydrate structure, $[U(SO_4)_2(H_2O)_4] \cdot H_2O$ [67], is also known [67], but it is structurally identical to the 4-hydrate except for an additional loosely co-

ordinated water molecule situated in vacancies within the cross-linked planes. The uranium atoms in these compounds are bound by between two and eight sulfate ligands, zero to seven water molecules in the primary coordination sphere, and zero to two free (solvent) water molecules.

The coordination of an increasing number of water molecules significantly alters the structures of these compounds, affecting the binding mode of the sulfate ligands, bond lengths and angles, and the degree of bridging (Table 4.4). Generally, the addition of more coordinated waters is correlated with an increase in the unit cell volume and a reduction in the degree of bridging between individual monomers. As additional waters are incorporated into the structure, they appear to displace coordinated sulfate bonds, thus reducing the opportunity for sulfate bridging. Four different sulfate binding modes, shown schematically in Fig. 4.7, are observed in these complexes: tetradentate bridging, bidentate bridging, chelating terminal, and monodentate terminal. Bidentate bridging results in either sheet-like connectivity in the case of the tetrahydrate, or chain-like connectivity in the case of the hexahydrate.

Differences in the sulfate binding mode for each complex can be observed in their Raman and IR spectra. In all of the hydrated species, all four vibrational modes for sulfate are active; in particular, the ν_1 mode is very strong. The position of the ν_1 peak in the Raman spectrum is shifted depending on the binding mode: 1025 cm^{-1} for both the bidentate-bridging complexes, the tetrahydrate [63] and the hexahydrate; 1006 cm^{-1} for the monodentate terminal nonahydrate; and 979 cm^{-1} for the bidentate chelating octahydrate. This seems to reflect a lowering of symmetry of the sulfate group, compared to the T_d tetrahedral geometry of free sulfate, with lower symmetry associated with a shift of the ν_1 band towards lower energy. Table 4.5 shows the O−S−O angles within the sulfate tetrahedra for complexes **1** and **2**. Compared to the ideal sulfate tetrahedron angles of 109.5°, the octahydrate (**2**) is less symmetric than the hexahydrate (**1**), supporting this hypothesis. There is no spectrographic data available for the anhydrous compound, but it is reasonable to postulate that the near-ideal tetrahedral geometry of the sulfate group should produce spectra similar to free sulfate, with a ν_1 band at higher energy than the 1025 cm^{-1} seen for cases of bidentate coordination.

Table 4.4: Comparison of the normalized cell volumes, intercell connectivity, and sulfate binding modes of the known uranous sulfate hydrates.

Complex	Normalized Cell Volume*	Intercell Connectivity	Coordinated Sulfates	Sulfate Binding Mode	Ref.
$U(SO_4)_2$	142.39	3D	8	Tetradentate bridging	[7]
$[U(SO_4)_2(H_2O)_4]$	231.471	2D sheets	4	Bidentate bridging	[45, 63]
$[U(SO_4)_2(H_2O)_4] \cdot H_2O$	228.80	2D sheets	4	Bidentate bridging	[67]
$[U(SO_4)_2(H_2O)_5] \cdot H_2O$	277.55	1D chains	4	Bidentate bridging	[14]
$[U(SO_4)_2(H_2O)_6] \cdot 2\,H_2O$	326.31	None	2†	Chelating terminal	[14]
$[U(SO_4)_2(H_2O)_7] \cdot 2\,H_2O$	340.831	None	2	Monodentate terminal	[67]

* $Å^2$. Cell volume divided by Z, the number of molecules per cell

†Each of the two sulfates is coordinated twice in a chelating fashion, for a total of four bonds

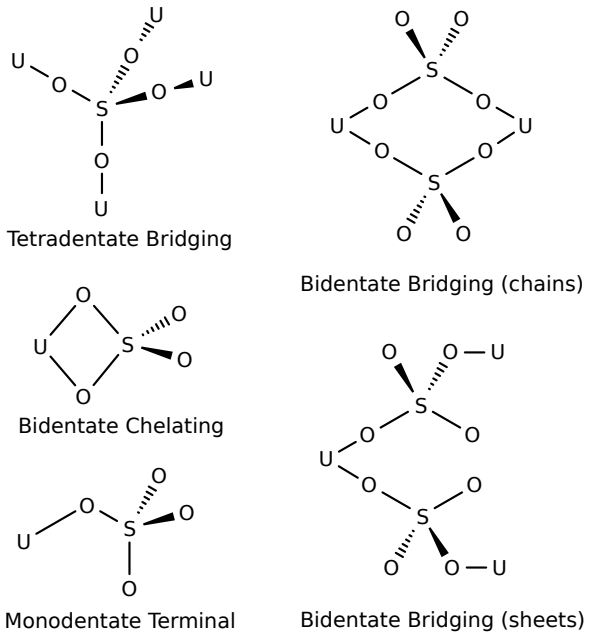

Figure 4.7: Schematic of the different sulfate binding modes observed in the known uranous sulfate hydrate complexes.

4.5 Note on the observed superstructure of uranous sulfate hexahydrate

During the data collection and refinement on complex **1**, it was noticed that very faint additional reflections were present that could not be accounted for by the basic structure presented here. Figure 4.8 shows a pseudo-precession image of the *h*0*l* zone, with the extra faint reflections visible only to a resolution of approximately 1.6 Å. These extra reflections could simply be interference from the inclusion of a minor amount of a second phase in the analyzed crystal. More intriguing, however, is the possibility that they identify the existence of a larger super-cell within the structure, with slightly offset identical sub-cells.

If refined as a supercell, the solution for complex **1** gives a super-cell eight times the volume of the sub-cell described previously. While the super-cell structure solves and refines well in space group *I*2 as a racemic twin, the hydrogen atoms could be located but not refined, and bond length and angle standard uncertainties

Table 4.5: Sulfate tetrahedra angles (°) for uranous sulfate hexahydrate and octahydrate (complexes **1** and **2**).

Complex 1 $[U(SO_4)_2(H_2O)_5]\cdot H_2O$		Complex 2 $[U(SO_4)_2(H_2O)_6]\cdot 2\,H_2O$	
O1−S1−O2	107.67(10)	O1−S1−O2	103.15(11)
O1−S1−O3	109.81(10)	O1−S1−O3	110.04(11)
O1−S1−O4	108.67(10)	O1−S1−O4	111.29(11)
O2−S1−O3	108.73(10)	O2−S1−O3	110.45(12)
O2−S1−O4	109.22(9)	O2−S1−O4	111.07(11)
O3−S1−O4	112.63(10)	O3−S1−O4	110.63(11)
		O5−S2−O6	102.95(11)
		O5−S2−O7	111.43(11)
		O5−S2−O8	110.27(12)
		O6−S2−O7	109.92(12)
		O6−S2−O8	111.50(11)
		O7−S2−O8	110.56(11)

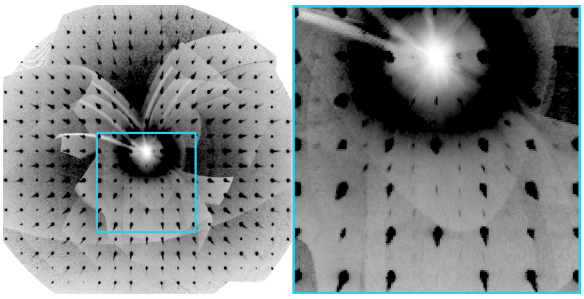

Figure 4.8: Pseudo-precession image of $h0l$ zone for uranous sulfate hexahydrate (complex **1**), and a magnified view of the boxed region showing the faint spots resulting from the super-cell.

were considerably worse than the sub-cell. In the reported sub-cell structure (solved and refined in space group $I2/a$) all hydrogen atoms could be refined isotropically, and standard uncertainties of bond lengths and angles were considerably improved. Table 4.6 gives a comparison of the sub- and super-cell structures.

The connectivity in the superstructure is identical to the substructure, and the bond lengths and angles are very similar. The cell dimensions and angles remain identical, except for the doubling in size in each direction. The main difference appears to be a slight variation in the placement and orientation of the free water

Table 4.6: Comparison of crystal parameters for uranous sulfate hexahydrate (complex **1**) sub- and super-cells.

	Sub-cell	Super-cell
a (Å)	7.5190(2)	15.0395(4)
b (Å)	13.2464(3)	26.4955(7)
c (Å)	11.5073(4)	23.0157(7)
α (°)	90	90
β (°)	104.388(1)	104.388(1)
γ (°)	90	90
volume (Å^3)	1110.18(5)	8883.6(4)
Unique reflections	1642	26027
Reflections (I/2sigI)	1638	3885
space group	$I2/a$	$I2$ (racemic twin)
S−O bond precision (Å)	0.0017	0.0287

molecules, labeled O8 in the substructure.

4.6 Conclusion

Two new uranium(IV) sulfate hydrate species have been synthesized and characterized, and their characteristics compared to four other known structures. These two new compounds add to the current body of structurally characterized uranium(IV) sulfates and advance the understanding of how waters of hydration affect their connectivity. They also offer insight into the wide variation in sulfate binding mode present in uranium(IV) compounds with otherwise-similar chemical formulae.

Chapter 5

Thermal stability of uranous sulfate I: Thermodynamics and theory

The stability of solid uranous sulfate hydrate under various conditions, as well as the decomposition products and gases, can be predicted by thermodynamics. The following topics are treated here from a theoretical perspective: water loss; decomposition of $U(SO_4)_2$; the SO_2/SO_3 equilibrium; and the construction of a phase diagram.

Chemical equations in this section are written in the following format:

$$A \xrightarrow{T_{eq}^{\circ}} B + C$$

where T_{eq}° is the temperature that satisfies $\Delta G^{\circ}(T) = 0$. The T_{eq}° values were calculated using the thermodynamic values given by Guillaumont and Mompean [35], which were introduced in Chapter 2, according to Eq. (5.1):

$$T_{eq} = \frac{\Delta H^{\circ}}{\Delta S^{\circ} - R \ln Q} \tag{5.1}$$

where Q is the reaction quotient, which is the ratio of the activities of the product species divided by the activities of the reactant species, each raised to the power of its stoichiometric coefficient.

Data for the construction of the phase diagram was obtained from the software package HSC 7.1 [61], which takes into account the slight temperature dependence

of ΔH° and S°, giving slightly more accurate results than if the values at 25 °C were used.

5.1 Water loss

The thermodynamic database published by Guillaumont and Mompean [35] contains thermodynamic quantities for two uranous sulfate hydrates: the tetrahydrate and the octahydrate. Reactions for their complete dehydration can be written as follows:

$$\mathrm{U(SO_4)_2 \cdot 4\,H_2O} \xrightarrow{85\,^\circ\mathrm{C}} \mathrm{U(SO_4)_2 + 4H_2O_{(g)}} \qquad \Delta G^\circ = 206.30 - 0.5763T \tag{5.2}$$

$$\mathrm{U(SO_4)_2 \cdot 8\,H_2O} \xrightarrow{90\,^\circ\mathrm{C}} \mathrm{U(SO_4)_2 + 8H_2O_{(g)}} \qquad \Delta G^\circ = 418.38 - 1.1527T \tag{5.3}$$

The uncertainties in the published S° values for the two hydrates is around ± 10 %, however, making the calculated T°_{eq} values only accurate to ± 20 °C. The enthalpies of reaction for the tetrahydrate and the octahydrate are 206.3 kJ mol^{-1} and 418.4 kJ mol^{-1}, respectively, which amounts to approximately 52 kJ mol^{-1} per water molecule. If stable intermediary hydrates exist, as seems likely, the true transition temperatures and heats of reaction would be different than calculated here.

5.2 The SO_2/SO_3 equilibrium

When uranous sulfate decomposes, the sulfate is released as either SO_2 or SO_3 gas. Thus an important aspect of this system, from a theoretical perspective, is the thermodynamic equilibrium between SO_2 and SO_3, and the kinetics of this reaction.

The gas-phase equilibrium between SO_2, SO_3, and O_2 can be written as shown in Eq. (5.4):

$$\mathrm{SO_3} \xleftrightarrow{779\,^\circ\mathrm{C}} \mathrm{SO_2} + \tfrac{1}{2}\mathrm{O_2} \qquad \Delta G^\circ = 98.89 - 0.0940T \tag{5.4}$$

As temperature increases, there is a shift in gas-phase equilibrium from SO_3 towards SO_2. The ratio of SO_2 to SO_3 at equilibrium can be calculated using the relationship shown in Eq. (5.5), and is a function of temperature (via the equilibrium

constant K) and oxygen partial pressure.

$$\log \frac{p\mathrm{SO_2}}{p\mathrm{SO_3}} = \log K - 0.5 \log p\mathrm{O_2} \tag{5.5}$$

A plot of this relationship is shown in Fig. 5.1. As $p\mathrm{O_2}$ decreases, the equilibrium shifts to the left. In air ($p\mathrm{O_2}$ = 0.209 atm), $\mathrm{SO_2}$ and $\mathrm{SO_3}$ are equimolar at 742 °C.

If $p\mathrm{O_2}$ is not fixed, and instead is allowed to float according to the stoichiometry of Eq. (5.4), the calculations become more complex. To understand this scenario, it is useful to imagine a sample of uranous sulfate decomposing at a fixed rate under a stream of nitrogen in an unpressurized vessel (i.e., $P_\mathrm{T} = 1$ atm). The released $\mathrm{SO_3}$ would decompose to $\mathrm{SO_2}$ and $\mathrm{O_2}$ to a certain extent, but the combined flow of $\mathrm{SO_2}$ and $\mathrm{SO_3}$ would remain constant. If the flow of nitrogen increases, $\left[p\mathrm{SO_2} + p\mathrm{SO_3}\right]$ must decrease accordingly.

This system can be solved by applying stoichiometric restraints, and by fixing $\left[p\mathrm{SO_2} + p\mathrm{SO_3}\right]$, as shown in Eq. (5.6). This leads to Eq. (5.7), which can be solved numerically for any $\left[p\mathrm{SO_2} + p\mathrm{SO_3}\right]$, and then plotted to show the relationship between gas composition and temperature, as shown in Fig. 5.2.

$$\begin{aligned} p\mathrm{O_2} &= 0.5 p\mathrm{SO_2} \\ p\mathrm{SO_2} + p\mathrm{SO_3} &= \text{constant} \end{aligned} \tag{5.6}$$

$$\begin{aligned} \log K &= 0.5 \log(0.5) + 1.5 \log p\mathrm{SO_2} - \log\left(\left[p\mathrm{SO_2} + p\mathrm{SO_3}\right] - p\mathrm{SO_2}\right) \\ \log \frac{p\mathrm{SO_2}}{p\mathrm{SO_3}} &= \log p\mathrm{SO_2} - \log\left(\left[p\mathrm{SO_2} + p\mathrm{SO_3}\right] - p\mathrm{SO_2}\right) \end{aligned} \tag{5.7}$$

As $\left[p\mathrm{SO_2} + p\mathrm{SO_3}\right]$ decreases, the equilibrium shifts to the left, with $\mathrm{SO_2}$ becoming more favourable at lower temperatures. Put another way, $\mathrm{SO_2}$ is favoured if the decomposition gases are dilute, while $\mathrm{SO_3}$ is favoured if they are concentrated. Quite by coincidence, equimolar $\mathrm{SO_2}/\mathrm{SO_3}$ is again reached at 742 °C for $P_\mathrm{T} = 1$ atm ($p\mathrm{SO_3} = p\mathrm{SO_2} = 0.4$ atm, $p\mathrm{O_2} = 0.2$ atm).

It would be foolish to accept these thermodynamic predictions without casting a critical eye towards kinetics. The kinetics of the $\mathrm{SO_2}/\mathrm{SO_3}$ equilibrium are well

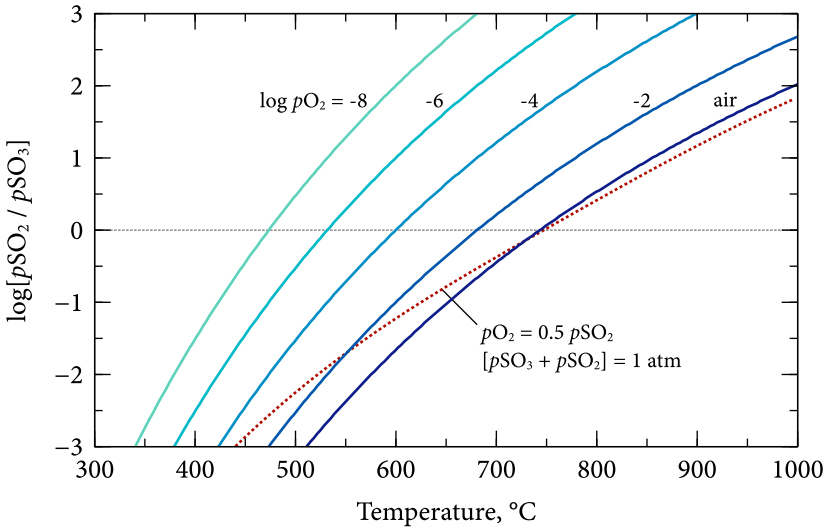

Figure 5.1: Equilibrium SO_2/SO_3 ratio as a function of temperature and oxygen partial pressure. The dashed line indicates the equilibrium if pO_2 is not fixed, but rather builds up according to the stoichiometry of the reaction with $pSO_3 + pSO_2 = 1$ atm.

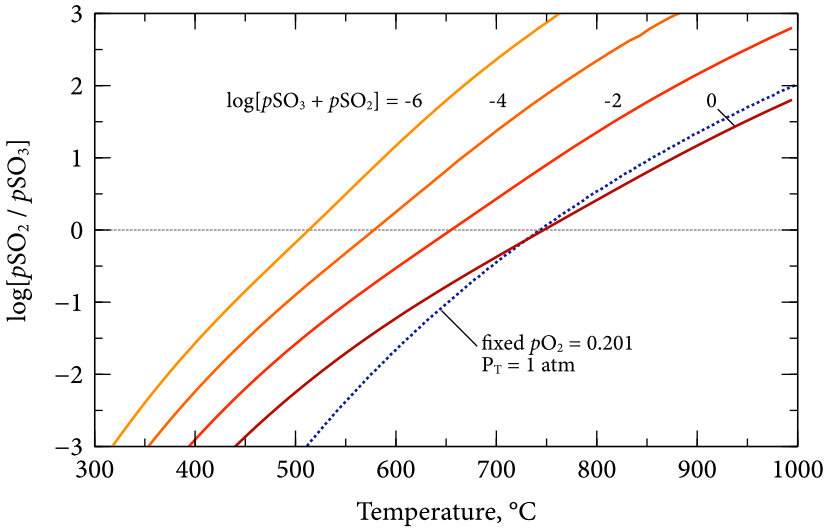

Figure 5.2: Equilibrium SO_2/SO_3 ratio as a function of temperature and pSO_3 + pSO_2, with pO_2 set according to reaction stoichiometry. The dashed line indicates the equilibrium in air, with $pO_2 = 0.209$ atm.

known to extractive metallurgists due to its importance in SO_2-capture technologies. According to Louie [52], the reverse reaction (i.e., the homogenous oxidation of SO_2 with O_2), is severely kinetically limited, occurring primarily above 1200 °C, where in any case it is not thermodynamically favoured. In the presence of a catalyst such as V_2O_5 or Fe_2O_3, however, the reaction can take place at an appreciable rate below 700 °C, though still not particularly fast, with the highest conversion obtained between 570–640 °C. Below 570 °C the kinetics are too slow for appreciable conversion to take place. The forward reaction scarcely fares better, with Yilmaz et al. [80] determining that the homogenous decomposition of SO_3 in nitrogen is slow below 825 °C.

Given the dubious kinetics of the SO_2/SO_3 equilibration reaction, it seems unlikely that it would play a significant role during the thermal decomposition of uranous sulfate. Nevertheless, it must still be understood in order to properly interpret the results from thermodynamic simulations, and also could be useful when considering the downstream affect of the off-gases.

5.3 Anhydrous uranous sulfate decomposition

To begin understanding the thermodynamics of the decomposition of anhydrous uranous sulfate, $U(SO_4)_2$, it is useful to start with a simulation. HSC 7.1 [61], which contains both an extensive thermodynamic database and tools for solving equilibrium equations, was used for this purpose. Only a subset of the possible species in the database were found to have regions of stability under the conditions tested: $U(SO_4)_2$, UO_2SO_4, UO_3, and U_3O_8 in the solid phase, and O_2, N_2, SO_2, and SO_3 in the gaseous phase. All other species were removed to simplify the calculations. The gaseous uranium species were also removed to prevent HSC from erroneously predicting their formation.

In the first simulation, shown in Fig. 5.3, 1 mol of $U(SO_4)_2$ was allowed to come to equilibrium in an isobaric batch reactor initially containing an excess of nitrogen as the temperature was raised from 0–1000 °C, and allowing the decomposition gases to stay in equilibrium with the solids. The first stage of decomposition, the homogenous oxidation of $U(SO_4)_2$ to UO_2SO_4, was accompanied by the release of SO_2, with sulfur acting as oxidant to uranium. The second stage of decomposi-

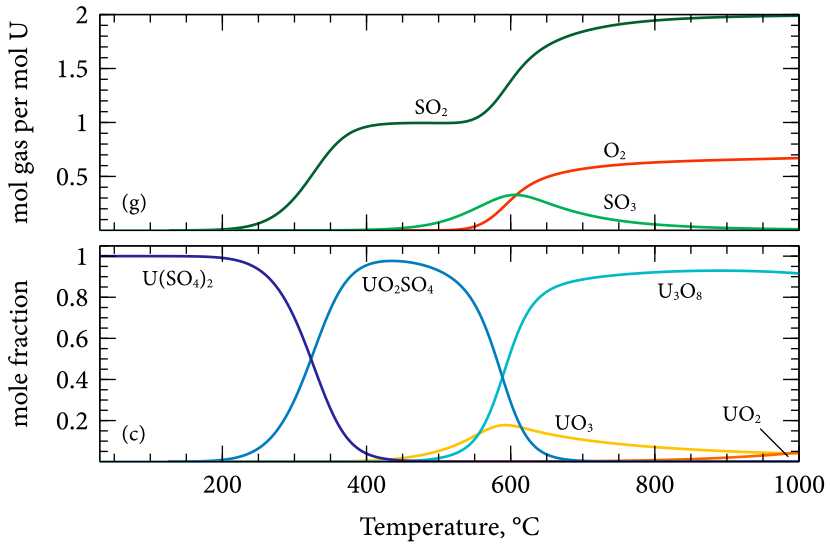

Figure 5.3: Theoretical thermodynamic equilibrium of the decomposition of $U(SO_4)_2$ from 30–1000 °C in an inert atmosphere, initially containing 500 mol N_2 per mol uranium as solid. (g) gas phase; (c) condensed phase. Data generated by HSC 7.1 [61]

tion, to U_3O_8, saw the release of the remaining sulfate as SO_3. A small amount of oxygen gas was also generated in the second step as the uranium reduced to U_3O_8. The SO_2 released in the first decomposition step remained as such because of a lack of oxygen to react with. Above 600 °C, however, the SO_2/SO_3 equilibrium preferred SO_2.

Figure 5.4 shows a simulation of the same system, except carried out in air instead of nitrogen. The presence of oxygen has a significant effect on the thermodynamic stability of the various species. Of particular note is a broadening of the UO_2SO_4 stability region to both lower and higher temperatures. Also of significance is the increased stability of UO_3.

In air, UO_2SO_4 was predicted to be stable at both higher and lower temperatures. The low-temperature stability was due to the heterogeneous oxidation of $U(SO_4)_2$ with O_2, which has a lower equilibrium temperature than for homogeneous oxidation. At higher temperatures, further decomposition was delayed due to the leftward pressure on the reaction equilibrium from the presence of oxygen

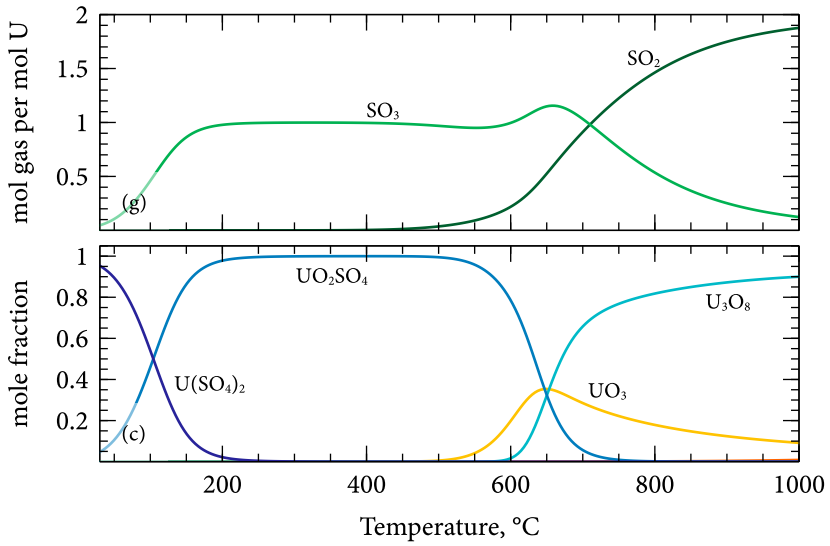

Figure 5.4: Theoretical thermodynamic equilibrium of the decomposition of $U(SO_4)_2$ from 30–1000 °C in an atmosphere fixed at $pO_2 \approx 0.209$, initially containing 500 mol N_2 and 149 mol O_2 per mol uranium. (g) gas phase; (c) condensed phase. Data generated by HSC 7.1 [61]

gas. Under air, the predicted stability of UO_3 was enhanced.

These two simulations suggest that the following five solid decomposition reactions (as well as the SO_2/SO_3 equilibrium) could play a part in the thermal decomposition of uranous sulfate:

$$U(SO_4)_2 \xrightarrow{451\,^\circ C} UO_2SO_4 + SO_2 \qquad \Delta G^\circ = 167.65 - 0.2314T \qquad (5.8)$$

$$U(SO_4)_2 + \tfrac{1}{2}O_2 \xrightarrow{227\,^\circ C} UO_2SO_4 + SO_3 \qquad \Delta G^\circ = 68.76 - 0.1374T \qquad (5.9)$$

$$UO_2SO_4 \xrightarrow{889\,^\circ C} \tfrac{1}{3}U_3O_8 + SO_3 + \tfrac{1}{6}O_2 \qquad \Delta G^\circ = 257.84 - 0.2219T \qquad (5.10)$$

$$UO_2SO_4 \xrightarrow{916\,^\circ C} UO_3 + SO_3 \qquad \Delta G^\circ = 225.64 - 0.1897T \qquad (5.11)$$

$$UO_3 \xrightarrow{725\,^\circ C} \tfrac{1}{3}U_3O_8 + \tfrac{1}{6}O_2 \qquad \Delta G^\circ = 32.20 - 0.0323T \qquad (5.12)$$

In order to evaluate the importance of UO_3 as an intermediary product, it is useful to examine the conditions under which Eqs. (5.11) and (5.12) would be expected to take place. Given that the T°_{eq} value for the first reaction is higher than for

the second, UO_3 should not form under standard state conditions. Only at the right combination of high pO_2 and low pSO_3 could UO_3 be formed, and even then only over a relatively narrow temperature range. It therefore seems unlikely that UO_3 would play a significant role in the thermal decomposition of uranous sulfate.

The equilibrium temperature of the final decomposition to U_3O_8, Eq. (5.11), can be calculated by substituting the appropriate thermodynamic and stoichiometric values into Eq. (5.1):

$$T_{\text{final}} = \frac{257\,840\,\text{J mol}^{-1}}{\left(221.942\,\text{J mol}^{-1}\,\text{K}\right) - \left(8.3145\,\text{J mol}^{-1}\,\text{K}\right)\ln\left(p_{SO_3}p_{O_2}^{1/6}\right)} \tag{5.13}$$

5.4 Uranous sulfate decomposition phase diagram

The simulation results shown in Figs. 5.3 and 5.4 are misleading because they assume that the product gases remain in contact with the solids. A phase diagram can give a better sense of the stability of the various species at different gas compositions. Figure 5.5 shows a phase diagram of the system between 0–1000 °C. The y-axis represents the partial pressure of either SO_2 or SO_3, depending on which gas is evolved during that stage of decomposition. The effect of oxygen partial pressure on the second decomposition step, Eq. (5.10), is shown with three pO_2 isobars. Also shown is the stability region of UO_3 at two different pO_2 isobars. U_3O_8 is the dominant phase at any oxygen partial pressure above ~875 °C, demonstrating that it is always possible to convert $U(SO_4)_2$ into U_3O_8 as long as it is calcined at a high enough temperature.

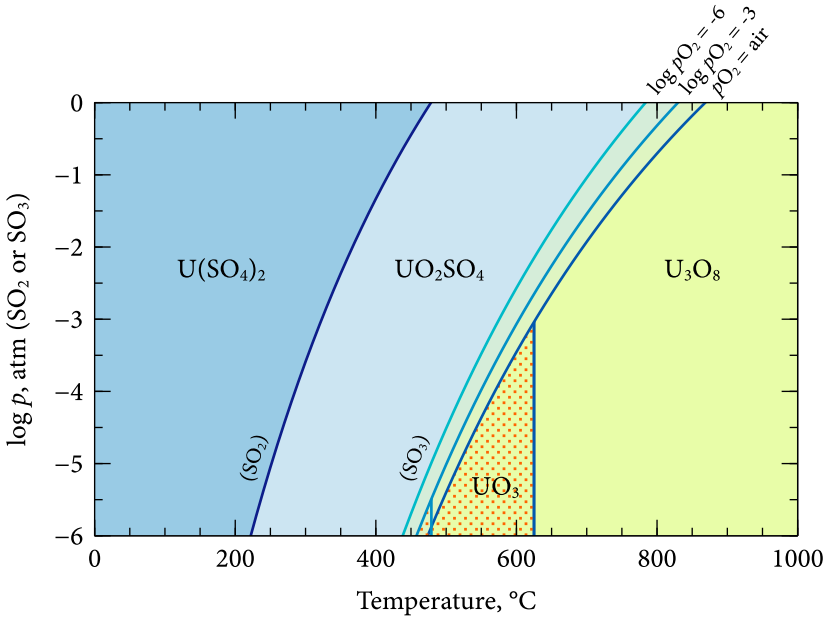

Figure 5.5: Phase diagram of the U-S-O system for homogenous decomposition of $U(SO_4)_2$. pO_2 isobars are shown, along with their effect on the stability of UO_3.

Chapter 6

Thermal stability of uranous sulfate II: Experimental examination

6.1 Introduction

Three different uranous sulfate *x*-hydrate polymorphs were identified in Chapter 3: $U(SO_4)_2 \cdot 4\,H_2O$, $U(SO_4)_2 \cdot 6\,H_2O$, and $U(SO_4)_2 \cdot 8\,H_2O$. Each was found to be crystallographically unique, with different sulfate binding modes and different numbers of crystalline waters. In this chapter, the thermal stability and decomposition pathways of the three hydrates are described, and decomposition mechanisms are proposed.

To begin understanding the system, samples of the three hydrates were heated in an oven or furnace for a period of time, allowed to cool, and then analyzed by powder x-ray diffraction in an attempt to directly identify the resulting material. These experiments were only partly successful, with many of the intermediary compounds found to be x-ray amorphous, thus making them unidentifiable. However, weight loss measurements provided indirect evidence of the processes involved. Furthermore, these experiments brought attention to the slow solid-phase recrystallization kinetics of $U(SO_4)_2$.

The system was studied more closely using the thermoanalytical techniques of differential thermal analysis (DTA) and differential scanning calorimetry (DSC).

From these data, the onset temperatures and enthalpies of transformation of the various weight loss and thermal events from 30–1000 °C were identified, and the intermediate decomposition products were identified. The effect of operating under different atmospheres, primarily nitrogen vs. air, was also explored.

This chapter is concluded by combining the experimental results with thermodynamic and kinetic theory to propose chemical decomposition pathways for the three uranous sulfate hydrates. The different behaviour of the three hydrates are explained by a transition from amorphous to crystalline anhydrous uranous sulfate. This fills a gap in the literature and brings the understanding of the thermal decomposition of the uranous sulfate hydrates to the same level as the uranyl sulfate hydrates.

6.2 Background information

It has long been recognized that there are several different uranous sulfate *x*-hydrates [30], and that they have distinct thermal decomposition fingerprints [74]. Leroy and Tridot [46] reported that $U(SO_4)_2 \cdot 4\,H_2O$ dehydrates in two steps, with $U(SO_4)_2 \cdot H_2O$ as an intermediary, followed by oxidation to UO_2SO_4, and finally decomposition to U_3O_8, according to the following reaction pathway in air (temperatures approximated from published curves):

$$U(SO_4)_2 \cdot 4H_2O \xrightarrow{\sim 135\,^{\circ}C} U(SO_4)_2 \cdot H_2O \xrightarrow{\sim 224\,^{\circ}C}$$

$$U(SO_4)_2 \xrightarrow{\sim 575\,^{\circ}C} UO_2SO_4 \xrightarrow{\sim 710\,^{\circ}C} U_3O_8$$

Gil et al. [29] reported on the thermal decomposition of ten different uranous-*M* sulfate *x*-hydrate double salts (with *M* = Cd, La, Li, Mg, Mn, Ni, V, and Zn), but not on pure uranous sulfate. Suzuki et al. [74] used TGA to identify a tetrahydrate, a trihydrate, and a *n*-hydrate ($n \approx 1.7 - 2.1$), all of which decomposed to $U(SO_4)_2$ by 410 °C, but they did not study the process in depth. No data on the thermal decomposition of the hexahydrate or octahydrate have been reported.

Given the lack of published information on the compounds of interest, it is useful to review a closely-related compound, uranyl sulfate *x*-hydrate. The decomposition of $UO_2SO_4 \cdot xH_2O$ has been studied by a number of authors [16, 17, 47, 58, 66],

who have proposed the various water loss mechanisms shown in Fig. 6.1. In each study, the authors used TGA and DTA to suggest a decomposition pathway for water loss. The sheer quantity of identified phases, as well as the lack of agreement between authors, only serves to confirm Walter McCrone's droll observation on the usefulness of studying polymorphism[1]. Notz and Jaffe [58] observed three distinct endotherms during the decomposition of $UO_2SO_4 \cdot 3\,H_2O$, which they attributed to the stepwise loss of single water molecules. Leroy et al. [47] found that two different decomposition pathways exist, starting with either the tetrahydrate or the hemiheptahydrate, each distinguished by different decomposition temperatures and intermediary XRD patterns. Cordfunke [16, 17] subsequently confirmed the two distinct pathways, but identified the 2.5-hydrate as the true form of the compound previously assumed to be 3-hydrate, and also identified several different phases of the monohydrate. Sato et al. [66] found a stepwise pathway similar to Notz's, and the x-ray diffraction patterns for their 3- and 2.*x*-hydrates were the same, supporting Cordfunke's theory that the 3-hydrate is simply a more-hydrated version of the 2.5-hydrate. In all, at least twelve crystallographically-unique phases of uranyl sulfate hydrate and anhydrate have been identified.

The high-temperature thermal decomposition of both uranous and uranyl sulfate is more straightforward. Tridot [76] reported that $U(SO_4)_2$ first oxidizes to UO_2SO_4, accompanied by the release of SO_2. Notz and Jaffe [58] and Tridot [76] both observed a sharp endothermic event centred at 755 °C which they attributed to a phase transition from αUO_2SO_4 to βUO_2SO_4. Upon heating in an oxidizing atmosphere to high temperature, all uranium oxides, and many other uranium compounds, ultimately decompose or convert to U_3O_8 [75]. Uranyl sulfate is no exception, itself decomposing to U_3O_8 at high temperature.

The operating atmosphere during thermal decomposition has been shown to have an effect on the decomposition pathway and the stability of the intermediary products. Tridot [76] observed that the onset temperature for the oxidation of $U(SO_4)_2$ was approximately 450 °C in a 10^{-2} mm Hg vacuum, 535 °C in dry oxygen,

[1] Walter McCrone stated that 'every compound has different polymorphic forms, and that, in general, the number of forms known for a given compound is proportional to the time and money spent in research on that compound.' Physics and Chemistry of the Organic Solid State,1965, vol. 2, pp. 725-767.

Notz and Jaffe [58] (1963)

$$UO_2SO_4 \cdot 3H_2O \xrightarrow{\sim 63\,^\circ C} UO_2SO_4 \cdot 2H_2O \xrightarrow{\sim 187\,^\circ C} UO_2SO_4 \cdot H_2O \xrightarrow{\sim 309\,^\circ C} UO_2SO_4$$

Leroy et al. [47] (1965)

Series A: $UO_2SO_4 \cdot 4H_2O \xrightarrow{\sim 65\,^\circ C} UO_2SO_4 \cdot 3H_2O \xrightarrow{\sim 125\,^\circ C} UO_2SO_4 \cdot H_2O \xrightarrow{\sim 163\,^\circ C} UO_2SO_4$

Series B: $UO_2SO_4 \cdot 3.5H_2O \xrightarrow{RT} UO_2SO_4 \cdot 3H_2O \xrightarrow{\sim 84\,^\circ C} UO_2SO_4 \cdot H_2O \xrightarrow{\sim 168\,^\circ C} UO_2SO_4$

Cordfunke [17] (1972)

Series A: $UO_2SO_4 \cdot 2.5H_2O \xrightarrow{\sim 129\,^\circ C} \text{x-ray amorphous} \xrightarrow{+160\,^\circ C} UO_2SO_4$

Series B: $UO_2SO_4 \cdot 3.5H_2O \xrightarrow{RT} UO_2SO_4 \cdot 3H_2O \xrightarrow{\sim 70\,^\circ C}$

$$\beta UO_2SO_4 \cdot H_2O \xrightarrow{\sim 171\,^\circ C} UO_2SO_4 \cdot \tfrac{1}{2}H_2O \xrightarrow{\sim 235\,^\circ C} UO_2SO_4$$

Sato et al. [66] (1980)

$$UO_2SO_4 \cdot 3H_2O \xrightarrow{\sim 82\,^\circ C} UO_2SO_4 \cdot xH_2O (2.5 \leq x \leq 3) \xrightarrow{\sim 106\,^\circ C}$$

$$UO_2SO_4 \cdot 2H_2O \xrightarrow{\sim 206\,^\circ C} UO_2SO_4 \cdot H_2O \xrightarrow{\sim 257\,^\circ C} UO_2SO_4$$

Figure 6.1: Thermal water loss pathways for uranyl sulfate *x*-hydrate, 25-400 °C, as determined by various authors. Quoted temperatures are the onset temperatures estimated graphically from the published DTA curves (no DTA curve was presented by Cordfunke, so the TGA curve was used instead). 'RT' indicates room temperature, with immediate water loss observed at the commencement of the test.

and 580 °C in SO_2. Under vacuum, the decomposition proceeded directly to U_3O_8, with only an inflection point in the TGA curve (as opposed to a plateau) to indicate the transitory presence of UO_2SO_4. Notz and Jaffé [59] found that the atmosphere also affected the onset temperature for the final decomposition to U_3O_8: 690 °C in helium, 750 °C in air, and 825 °C in a mixture of SO_2 and O_2.

6.3 Experimental procedures and data treatment

Thermal decomposition experiments were conducted on samples of solid uranous sulfate tetrahydrate, hexahydrate, and octahydrate. All of the solids were crystallized from aqueous uranium(IV)–sulfuric acid solutions in the course of other research activities. A description of sample genesis can be found in Chapter 3.

6.3.1 Bulk drying and calcining for x-ray analysis

Bulk drying of solids was conducted in a standard laboratory oven set to 60 °C or 90 °C for 24 h. The weights of the solids were recorded before and after each experiment, and XRD was used to identify the crystalline phases.

Calcining at 300 °C was conducted on approximately 100 mg of sample in an alumina crucible in the STA-6000 furnace in an air atmosphere. High-temperature calcining was conducted at 900 °C in an electric furnace inside a ceramic crucible.

6.3.2 Thermal analysis instrumentation and calibration

Thermogravimetric analysis (TGA) and differential scanning calorimetry (DSC) were used to investigate the stability and decomposition of the three uranous sulfate x-hydrate phases from 30–1000 °C. Most tests were carried out at UBC on approximately 25 mg of ground sample in an alumina crucible under nitrogen or air using a PerkinElmer STA-6000 TGA/DSC. The tests under ammonia and hydrogen atmospheres were carried out at Cameco Corporation's laboratory in Port Hope, Ontario using a TA Instruments SDT Q600 TGA/DSC. Unless otherwise mentioned, all scans used the following program:

1. Switch gas to nitrogen at 20.0 ml min^{-1}
2. Hold for 1.0 min at 30 °C
3. Heat from 30 °C to 995 °C at 10.0 °C min^{-1}

```
4. Hold for 5min at 995°C
```

Unless otherwise stated, quoted temperatures for thermal events refer to the DSC extrapolated peak onset temperature, T_e, which is the "temperature where the inflectional tangent at the ascending peak slope intersects the linearly extrapolated initial baseline" [32]. This method proved to be reasonably objective in its application, corresponded well with DTG data, and showed less dependence on scan rate than the equally-arbitrary 'peak' temperature. T_e should not be confused with the initial peak temperature, T_i, which is the temperature at which the DSC curve begins to deviate from the extrapolated baseline[2]. For events above 500 °C, for which the DSC data was not clear enough to define an onset temperature, an approximate temperature or range is given based on visual inspection.

The PerkinElmer STA-6000 was calibrated for mass against a certified-weight steel bead. TGA data were baseline-corrected using data collected on an empty crucible. This succeeded in correcting for systematic error (i.e., the buoyancy effect), but could not correct for the irregular drift in the microbalance seen over longer tests. During one 18 h test, the weight error, as measured by the indicated weight of the empty crucible, reached ±0.25 mg. This represents an error of ±1 % in a typical 25 mg sample, or the weight of one third of a water molecule, which explains why results from long tests did not match the theoretical values as crisply as those from short tests.

Temperature was calibrated against the known transition temperatures of indium (156.60 °C) and silver (961.78 °C) using the onset temperature determined at two scan rates, 5 °C min^{-1} and 10 °C min^{-1}. Heat flow was calibrated against the transition heat of indium (28.62 J g^{-1}). The calibration was checked by running these samples again, as shown in Fig. 6.2.

6.3.3 TGA data treatment

All weight measurements were normalized to the weight of the final decomposition product, U_3O_8, in order to eliminate uncertainty in the amount of water in the original samples, and to provide a common point to compare the different hydrates.

[2] A more thorough explanation of the terminology applied to the graphical interpretation of DSC curves can be found in Gmelin and Sarge [32]

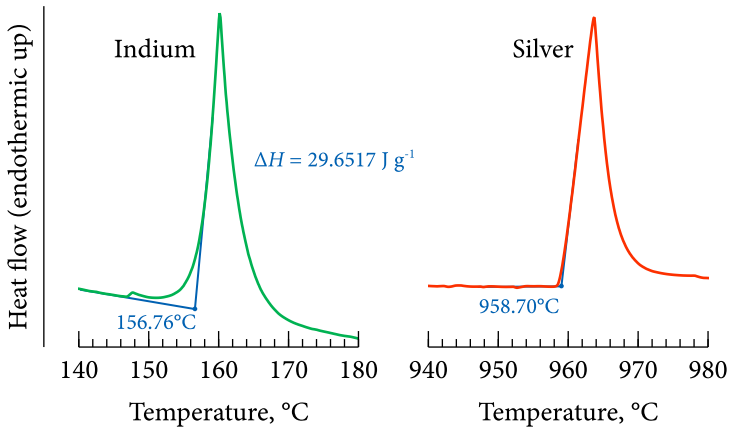

Figure 6.2: Validation of thermal analyzer temperature and heat flow calibration using indium and silver. 10 °C min^{-1}, nitrogen atmosphere.

This was possible because uranous sulfate x-hydrate decomposes stoichiometrically to U_3O_8 at high temperatures (this was shown to be true thermodynamically and experimentally). Thus the number of moles of uranium in the crucible, N_U, could be calculated by dividing the final decomposition weight at 850 °C by the molecular weight of $UO_{2.666}$, regardless of the starting material, as in Eq. (6.1) (note: U_3O_8 = $UO_{2.666}$). The TGA data were then scaled to 'equivalent molecular weight', m', by dividing the raw weight readings by N_U.

$$N_U = \frac{m(850\,^\circ\mathrm{C})}{\mathrm{MW}_{UO_{2.666}}} \qquad [\mathrm{mol}] \quad (6.1)$$

$$m'(T) = \frac{m(T)}{N_U} \qquad [\mathrm{g\,mol^{-1}}] \quad (6.2)$$

First derivatives of the TGA curves (i.e., derivative thermogravimetry (DTG)) were calculated by finite difference approximation using 6 s intervals (1 °C at a scan rate of 10 °C min^{-1}), and were expressed as a time-based rate by multiplying the data by the constant scan rate. Peak deconvolution and integration of the DTG data were performed using Fityk 0.9.8 [79], a software package for generic peak fitting and signal deconvolution.

6.3.4 DSC data treatment and baseline correction

In classical DSC analysis, the difference in heat flow is measured between a sample and an inert reference. The STA-6000 does not include a reference sample holder, instead relying on an integrated 'reference ring'. This method is reasonably effective, insomuch as thermal events are clearly visible as peaks (endothermic) or troughs (exothermic) in the DSC curve, with the area under the curve representing ΔH_{rxn}. However, the lack of a true reference results in a significant background signal, particularly at high temperatures, that can obscure small or broad features and make it difficult to determine the onset temperature of an event, and impossible to accurately integrate the peak area.

The DSC curves were relatively flat below 400 °C, but suffered from a continuously-increasing background signal above 500 °C. A similarly-shaped background signal was observed on a scan of a 25 mg sample of previously-calcined uranous sulfate (i.e., U_3O_8), but without the peaks associated with chemical reactions or phase changes. With this in mind, all DSC data were corrected for baseline effects by subtracting the weight-corrected U_3O_8 scan, as shown in Fig. 6.3. The weight-corrected 'transformed baseline' was calculated from the raw baseline by multiplying it by the weight fraction remaining of the sample, which accounted for the declining sample weight as decomposition progressed, and thus the sample's lower heat capacity, relative to the unchanging weight of the reference. 850 °C, the same temperature used for weight normalization, was selected as the 'zero' point when scaling the baseline. This yielded relatively flat baseline-corrected curves with identifiable thermal events, but the substantial uncertainty at higher temperatures made it unsuitable for quantitative use above 500 °C.

6.4 Validation of thermal analysis method

6.4.1 Selection of representative samples

Representative samples of uranous sulfate tetrahydrate (63-S), hexahydrate (04-A), and octahydrate (55-S) were chosen from the forty-six solids that were produced over the course of work described in Chapter 3. The choice was largely arbitrary, since nearly all of the solids were found to be of high quality and purity. The sam-

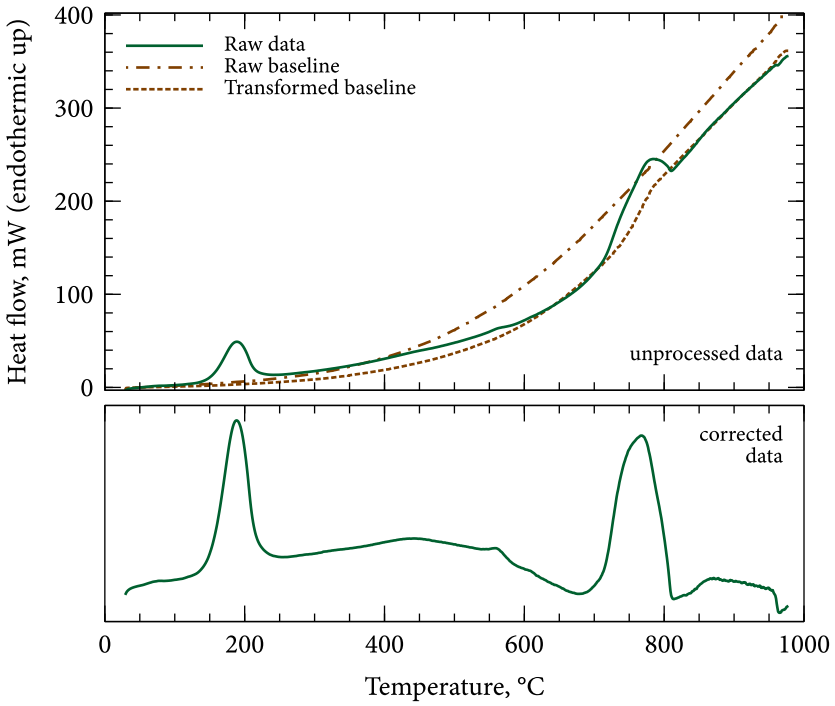

Figure 6.3: Correction of the DSC signal using a baseline collected on a pre-calcined sample of U_3O_8 to approximate the heat capacity effect.

ples were therefore chosen based on the available sample volume, each being large enough to accommodate dozens of thermoanalytical experiments if necessary.

The identity of each was confirmed by XRD and chemical analysis. Samples 63-S and 55-S were both precipitated as powders, and so could be used directly, but 04-A had to be ground with a mortar and pestle.

6.4.2 Choice of scan rate

The effect of scan rate was evaluated on $U(SO_4)_2 \cdot 4\,H_2O$ at 20 °C min^{-1}, 10 °C min^{-1} and 5 °C min^{-1}, with the results shown in Fig. 6.4. In theory, a slow scan rate is better suited to pinpointing the start of a thermal or weight loss event, but it also makes the differential heat flow less pronounced, resulting in a weaker DSC signal.

The TGA weight loss curve was sharpest at the slowest scan rate, but the same final weights were ultimately achieved regardless. The difference between the onset

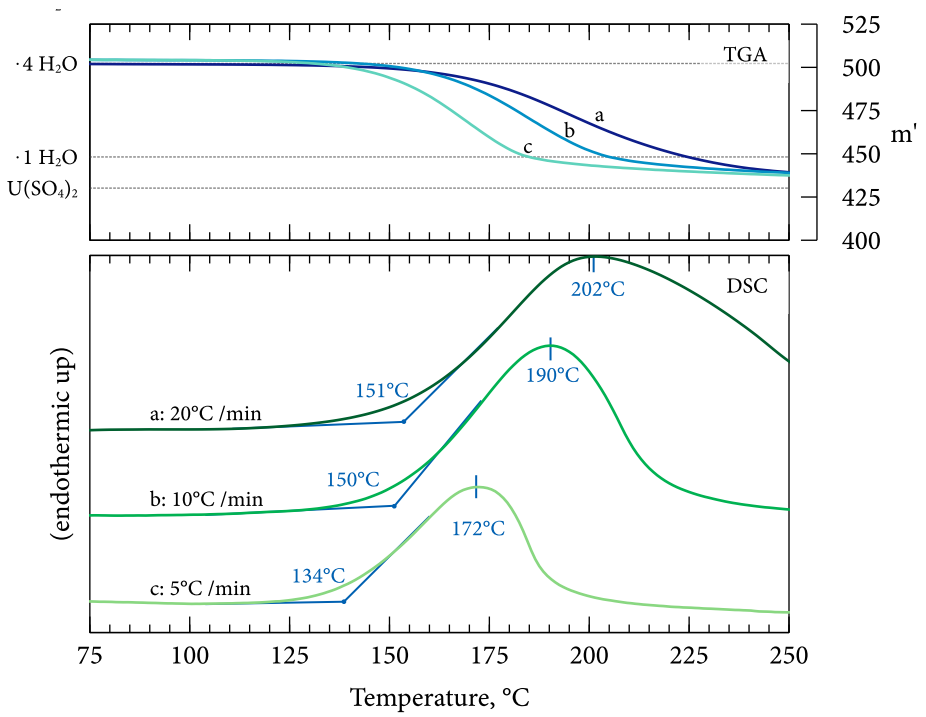

Figure 6.4: TGA and DSC curves for the same sample of $U(SO_4)_2 \cdot 4\,H_2O$ at different scan rates (a, 20 °C min^{-1}; b, 10 °C min^{-1}; c, 5 °C min^{-1}). Sample: 63-S.

temperatures for water loss at 10 and 20 °C was negligible (unlike the peak temperatures), at 150 °C and 151 °C, respectively. However, at 5 °C min^{-1}, the onset temperature registered substantially lower, at 134 °C. A similar difference was seen for higher-temperature events.

The temperature shift observed at different scan rates makes it clear that the apparent onset temperature should not be regarded as absolute. It also highlights the importance of only comparing data collected at identical scan rates. With this in mind, a default scan rate of 10 °C/min was chosen for all tests in order to balance accuracy with expediency.

6.4.3 The effect of particle size

Particle size could theoretically influence both heat and mass transfer during TGA analysis, with both becoming less efficient with increasing size. This would seem particularly important if the kinetics of a process were solid-diffusion limited, since the larger diffusion distance inherent in a larger particle would slow the reaction rate. Ideally, the samples could be ground to the same particle size in a micronizing mill to minimize this effect, but efforts to do so were unsuccessful because the samples were found to either dissolve (in water) or dehydrate (in ethanol). The samples were instead ground by hand with a mortar and pestle to a fine powder.

The effect of particle size was investigated experimentally by collecting TGA scans on ground and unground examples of the same material. For tetrahydrate, two different samples were tested: 63-S, a powder sample, and 24-A, a sample consisting of large, chunky crystals. The crystals of 24-A were crushed slightly to allow them to fit into the crucible, but were not finely ground, while 63-S was used as-is. For hexahydrate, the same sample of 04-A was tested twice, the first time using the original 100 μm × 2 mm needle-like crystals, and the second time grinding them with a mortar and pestle.

The difference in particle size had no obvious effect for tetrahydrate, while for hexahydrate the decomposition reactions took place slightly more quickly, as shown in Fig. 6.5. It was concluded that no further sample preparation beyond hand-grinding was necessary to generate comparable results between the three hydrates.

6.4.4 Reproducibility

Several thermal analysis tests were repeated to ensure reproducibility, as shown in Fig. 6.6. The TGA curves overlapped so closely that they were nearly indistinguishable. The DSC signals were also reproducible, with peak temperatures within 4 °C.

Two samples of $U(SO_4)_2 \cdot 4\,H_2O$ produced under very different conditions also had nearly the same TGA signature, as shown in Fig. 6.5. 25-A was grown slowly as large crystals at 60 °C in a shaken flask over 54 days, while 63-S was precipitated quickly as a powder at 90 °C in a stirred vessel over 7 hours. These results confirmed that the thermoanalytical behaviour of uranous sulfate *x*-hydrate was independent of preparation method.

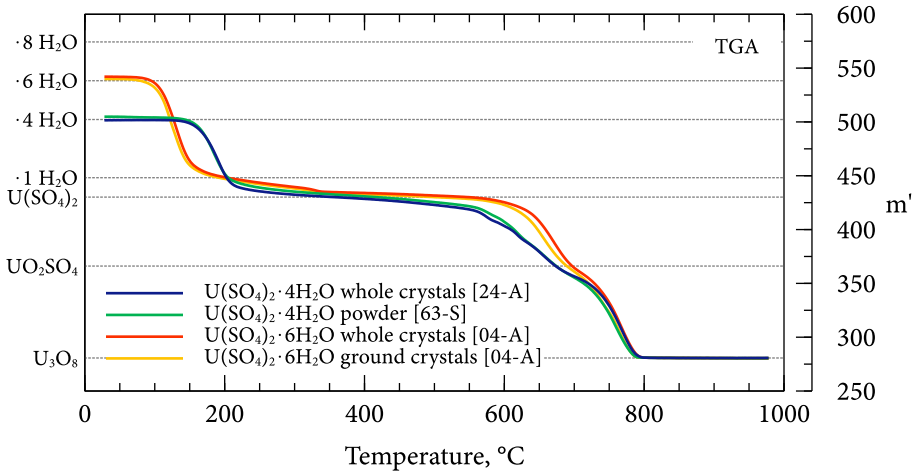

Figure 6.5: The effect of particle size on the TGA curves for $U(SO_4)_2 \cdot 6\,H_2O$ and $U(SO_4)_2 \cdot 4\,H_2O$, by analyzing whole crystals vs. powders. Samples: 63-S, 25-A, 04-A.

6.5 Results: x-ray analysis of bulk sample decomposition

The weight loss and powder XRD results for the three uranous sulfate hydrates after sustained heating in an air atmosphere are shown in Table 6.1. The results provide basic information on their stability at 60 °C, 90 °C, 300 °C, and 900 °C.

None of the solids lost a significant amount of weight or changed in crystallographic identity at 60 °C, showing that all three hydrates are stable under regular ambient conditions. After 24 h at 90 °C, the tetrahydrate again remained unchanged, but the hexahydrate and octahydrate both lost weight equivalent to 4.2 and 5.1 crystalline waters, respectively, not including the small amount of adsorbed water lost at 60 °C. These samples were found to be be x-ray amorphous, suggesting that the samples had not recrystallized as a coherent lower hydrate.

At 300 °C, uranous sulfate tetrahydrate quickly lost weight corresponding to complete dehydration after one hour, but was found to be x-ray amorphous. A sample of hexahydrate held for 40 h at 300 °C did appear to undergo partial solid-phase recrystallization, with its characteristic x-ray peaks visible above the broad amorphous background.

Uranous sulfate tetrahydrate completely decomposed to U_3O_8 at 900 °C. After

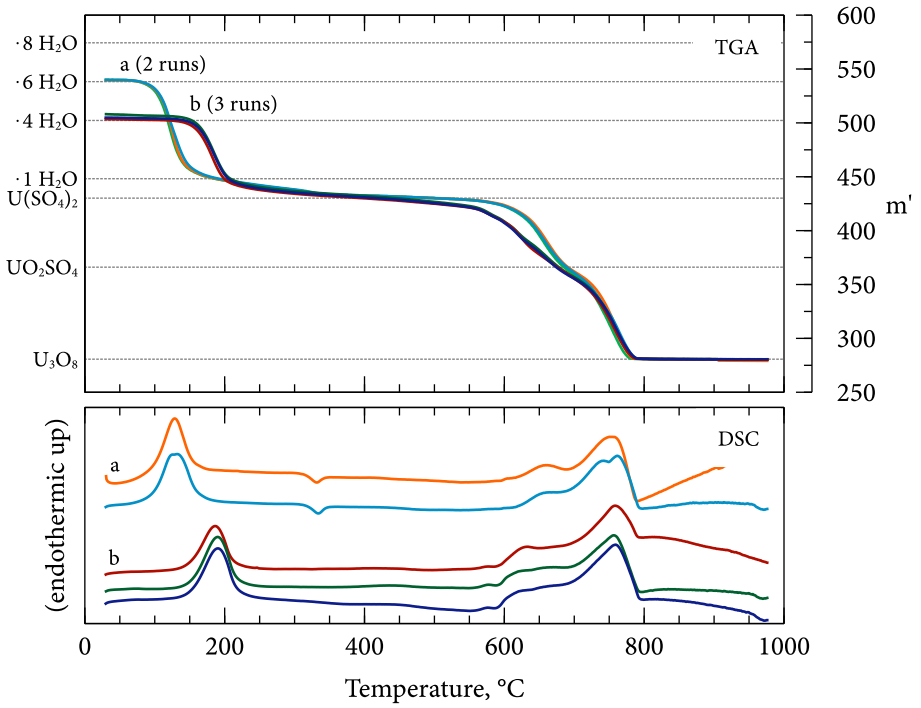

Figure 6.6: Reproducibility of the TGA and DTA curves (a, $U(SO_4)_2 \cdot 6\,H_2O$; b, $U(SO_4)_2 \cdot 4\,H_2O$) in a nitrogen atmosphere, scan rate 10 °C/min. Samples: 04-A, 63-S.

24 h at 900 °C, the furnace was turned off, and the sample was allowed to return to room temperature slowly inside the oven over a further 24 h. X-ray analysis confirmed that the resulting black powder was U_3O_8. The weight loss was not measured because of damage to the crucible.

The bulk dehydration and calcining tests provided some useful information on the decomposition of the three uranous sulfate hydrates, in particular confirming that the final decomposition product at high temperatures is U_3O_8. However, the difficulty in obtaining coherent x-ray diffraction patterns of the intermediary products in a reasonable length of time limited the use of this method, and it was not pursued further, instead favouring the more detailed data provided by TGA.

Table 6.1: Thermal treatment of the uranous sulfate hydrates at 60°C, 90°C, 300°C, and 900°C. Identity determined by XRD.

		63-S $U(SO_4)_2 \cdot 4\,H_2O$	04-A $U(SO_4)_2 \cdot 6\,H_2O$	55-S $U(SO_4)_2 \cdot 8\,H_2O$
60°C	Duration	24 h	24 h	24 h
	Identity	$U(SO_4)_2 \cdot 4\,H_2O$	$U(SO_4)_2 \cdot 6\,H_2O$	$U(SO_4)_2 \cdot 8\,H_2O$
	Wt loss	-0.20%	-0.23%	-2.21%
90°C	Duration	24 h	24 h	24 h
	Identity	$U(SO_4)_2 \cdot 4\,H_2O$	x-ray amorphous	x-ray amorphous
	Wt loss	-0.16%	-14.36%	-18.07%
300°C	Duration	1 h	40 h	
	Identity	x-ray amorphous	$U(SO_4)_2$†	-
	Wt loss	-14.12%	-20.10%	
900°C	Duration	48 h	-	-
	Identity	U_3O_8		

† Sample was mostly x-ray amorphous, but showed very faint peaks corresponding to $U(SO_4)_2$. Sample was entirely amorphous after a 1 h hold.

6.6 Results: Thermal analysis

TGA, DTG, and DSC curves for uranous sulfate tetrahydrate, hexahydrate, and octahydrate in nitrogen and air are shown in Figs. 6.7 to 6.12. These figures will be referred to throughout the discussion. The onset temperatures for thermal events below 500 °C are marked on the DSC curves. The deconvoluted DTG peaks are shown overlaid on the raw data (these will be discussed in a later section). Various characteristic peaks or regions are marked, corresponding to water loss (W), phase change (P), and sulfur loss (S) events.

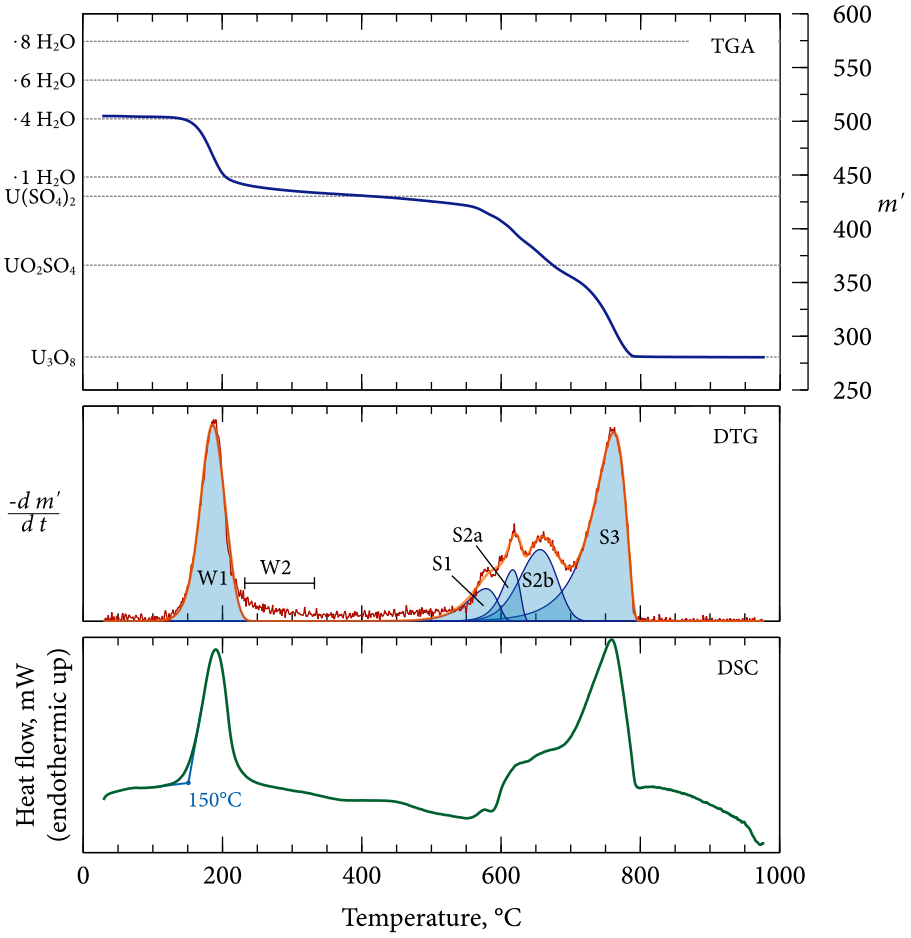

Figure 6.7: TGA, DTG, and DSC curves for $U(SO_4)_2 \cdot 4\,H_2O$ in a nitrogen atmosphere.

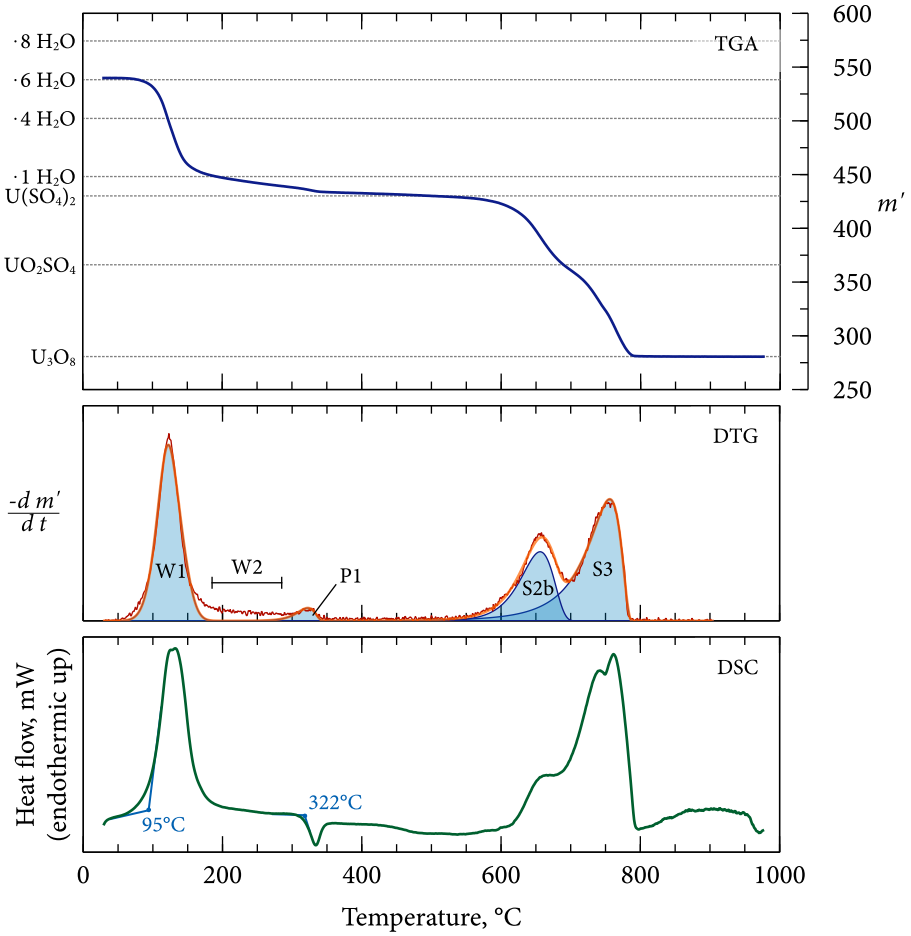

Figure 6.8: TGA, DTG, and DSC curves for $U(SO_4)_2 \cdot 6\,H_2O$ in a nitrogen atmosphere.

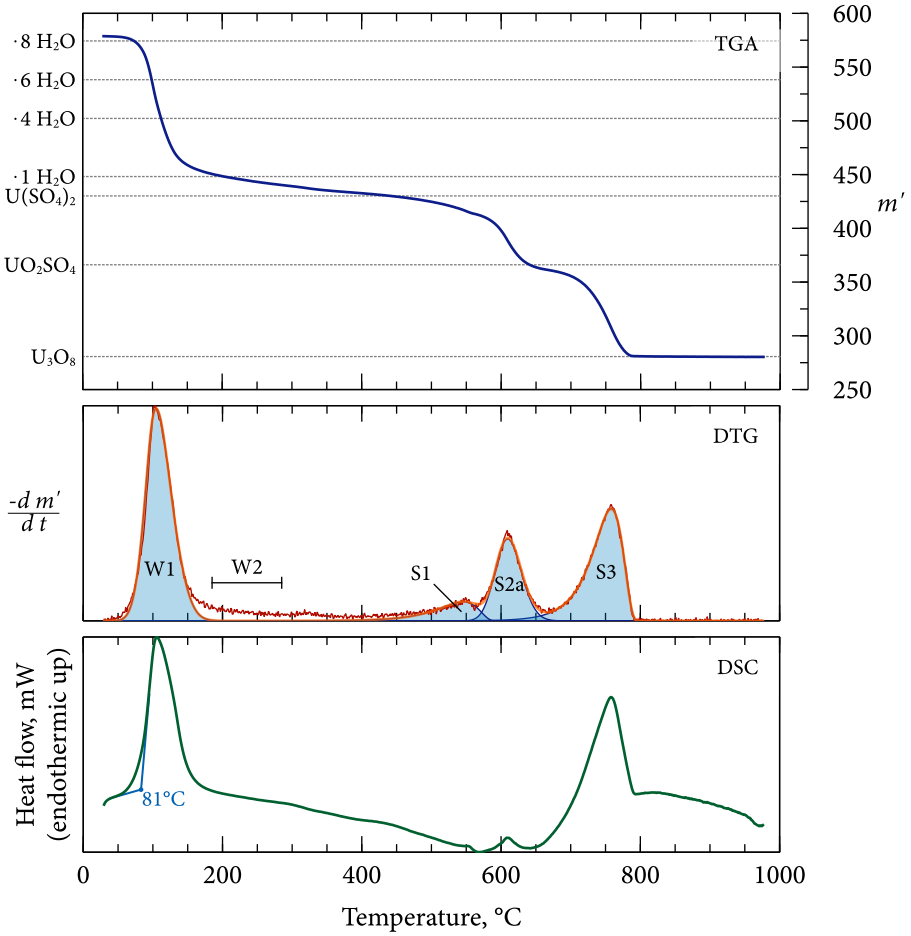

Figure 6.9: TGA, DTG, and DSC curves for $U(SO_4)_2 \cdot 8\,H_2O$ in a nitrogen atmosphere

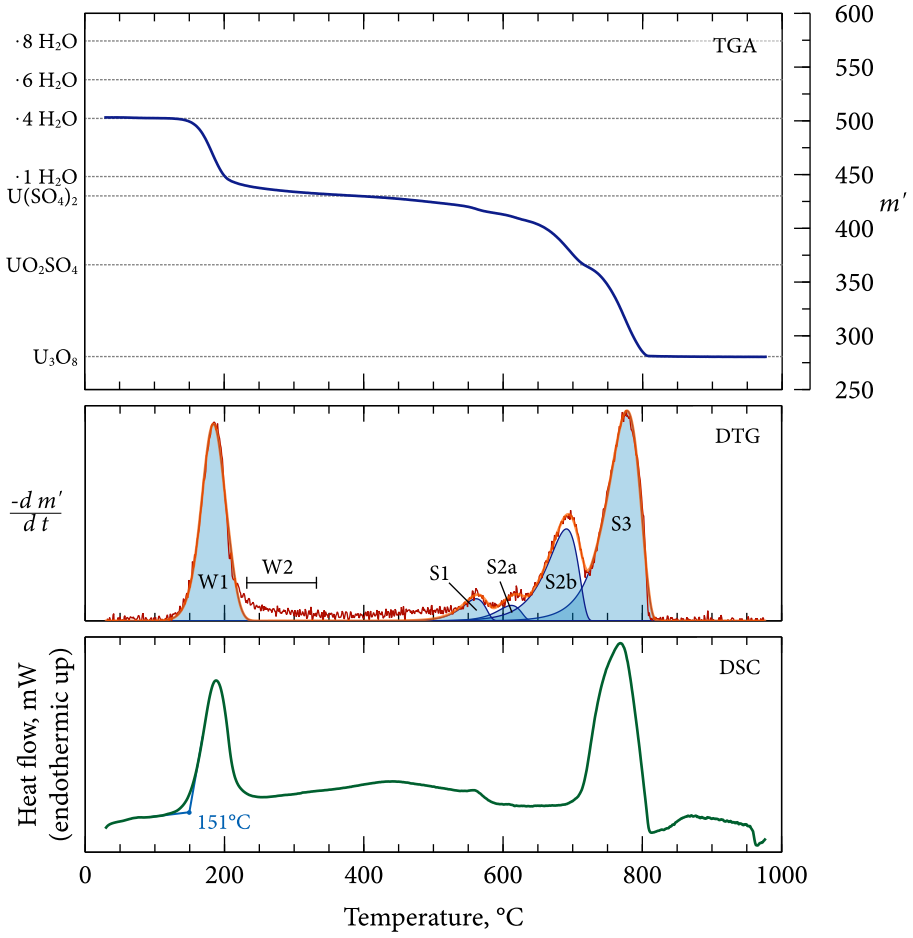

Figure 6.10: TGA, DTG, and DSC curves for $U(SO_4)_2 \cdot 4\,H_2O$ in an air atmosphere.

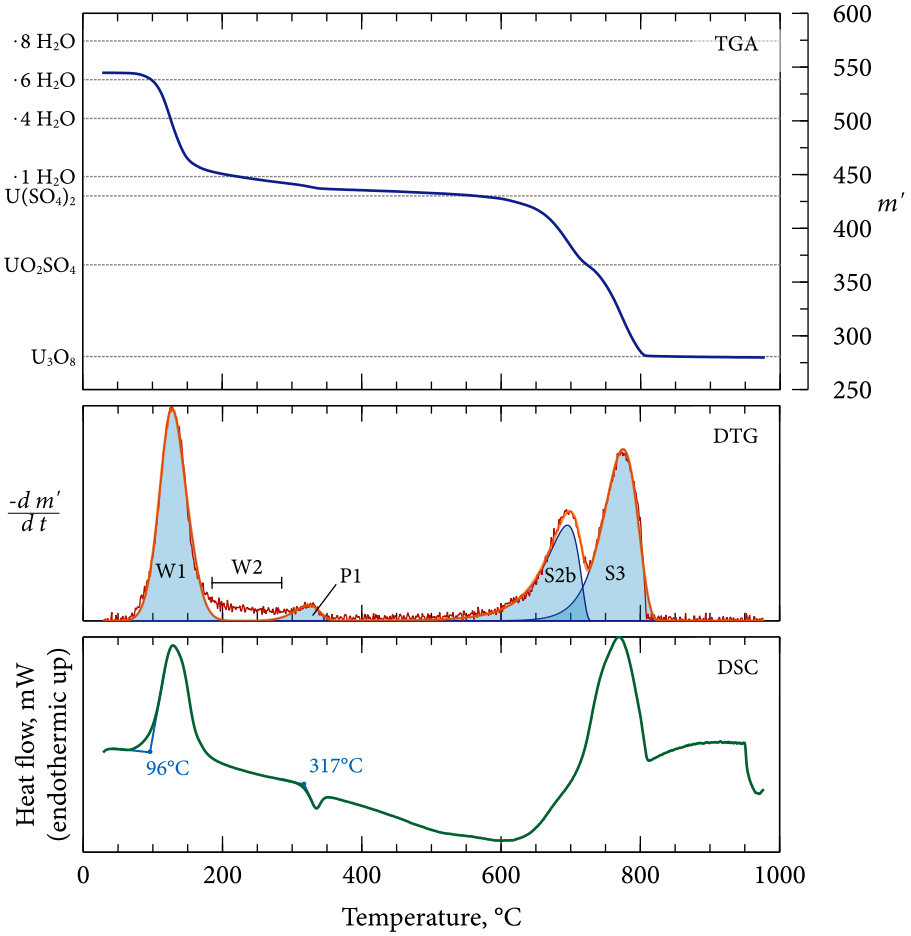

Figure 6.11: TGA, DTG, and DSC curves for $U(SO_4)_2 \cdot 6\,H_2O$ in an air atmosphere.

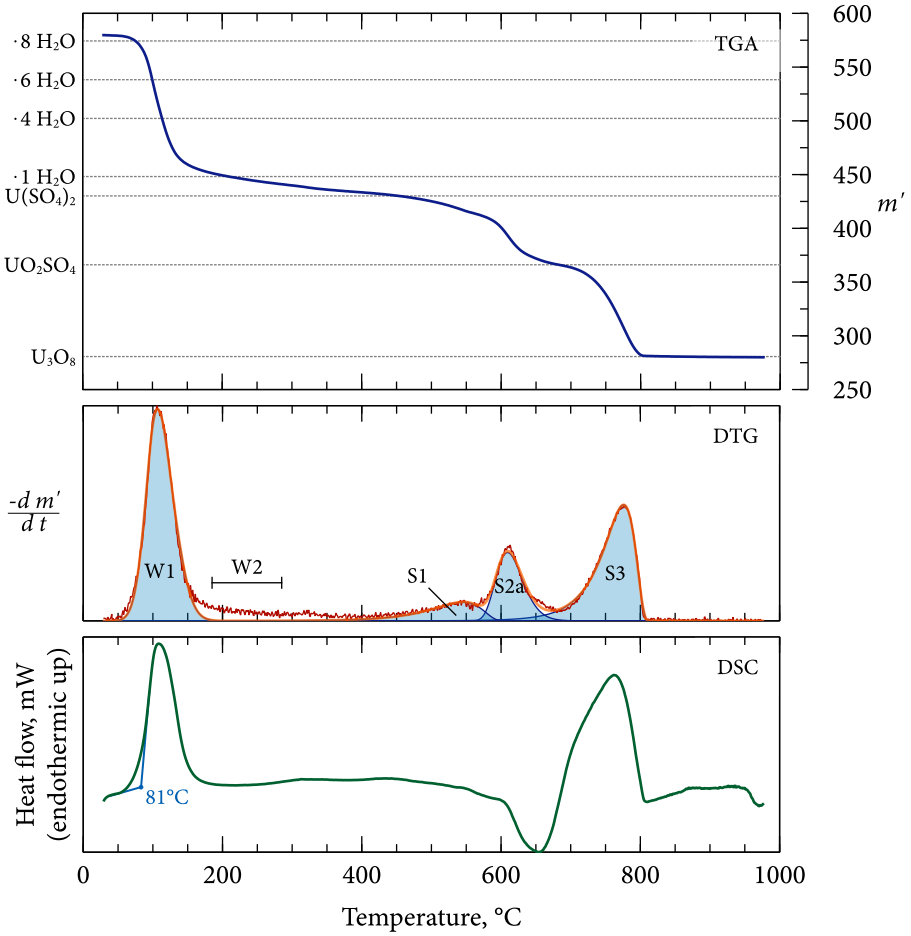

Figure 6.12: TGA, DTG, and DSC curves for $U(SO_4)_2 \cdot 8\,H_2O$ in an air atmosphere.

6.6.1 Decomposition in nitrogen

For all three hydrates, there were four stages of decomposition: initial rapid water loss to form an intermediary lesser hydrate; slow loss of the remaining water to form anhydrous uranous sulfate; oxidation to UO_2SO_4; and finally decomposition to U_3O_8. In addition, the hexahydrate showed a small but prominent thermal event at 322 °C which was absent from the other two hydrates. The initial and final materials were weight-stable, but the intermediary compounds often declined in weight somewhat over time.

The number of waters of hydration implied by the TGA data agreed broadly with the theoretical values, giving 4.10, 6.09, and 8.24 waters of hydration for the tetrahydrate, hexahydrate, and octahydrate, respectively. The slight excess over the theoretical value in each case corresponded with the adsorbed water that was removed at 60 °C in the oven-drying experiments described earlier.

The onset temperatures for initial water loss were different for the three species, at 150 °C, 95 °C, and 81 °C for the tetrahydrate, hexahydrate, and octahydrate, respectively. An inflection point in the TGA curves after initial water loss points to the existence of a transient lower hydrate. The remaining water in the lower hydrate was then lost slowly and continuously over a several hundred degree range. Interestingly, neither the hexahydrate nor the octahydrate showed a tendency to form $U(SO_4)_2 \cdot 4\,H_2O$ as an intermediary

The three (former) hydrates showed different decomposition behaviour even after converting to $U(SO_4)_2$. The hexahydrate had the greatest stability as $U(SO_4)_2$, maintaining a steady weight to a higher temperature than the other two species and decomposing to UO_2SO_4 at 620 °C. The octahydrate did not maintain a steady weight as $U(SO_4)_2$, but rather lost weight slowly starting around 400 °C, followed by more rapid decomposition to UO_2SO_4 around 585 °C. The tetrahydrate also lost weight slowly starting around 400 °C, with an acceleration around 585 °C, but did not show the characteristic 's-shaped' curve of the other two hydrates, instead losing weight at a more-or-less constant rate.

After reaching UO_2SO_4, all three hydrates behaved the same, with decomposition to U_3O_8 starting in the range 650–700 °C.

6.6.2 Decomposition in air

Thermal analysis in an air atmosphere was performed in the same manner as the nitrogen tests. Operating in air had no effect on water loss (W) or the exothermic event in the hexahydrate (P1). The sulfur loss decomposition steps (S), from $U(SO_4)_2$ to U_3O_8, however, were affected by the presence of oxygen, with the reactions generally shifting to a higher temperature. The first stage, $U(SO_4)_2$ to UO_2SO_4, was delayed to higher temperature in the tetrahydate and the hexahydrate, but was unaffected in the octahydrate. The second stage of decomposition, from UO_2SO_4 to U_3O_8, proceeded more or less the same for each polymorph, but approximately 20 °C hotter than under nitrogen.

6.6.3 Decomposition under hydrogen and ammonia

A sample of $U(SO_4)_2 \cdot 4\,H_2O$ (63-S), was sent to Cameco Corporation's technology centre in Port Hope, Ontario for further TGA analysis under four different atmospheres: nitrogen, air, hydrogen, and ammonia. Hydrogen and ammonia are both reducing gasses, and thus could be used to produce UO_2, which is the fuel used in nuclear reactors, directly from uranous sulfate. The following program was used:

1. Switch gas to nitrogen
2. Hold for 20 min at 30 °C
3. Switch gas to chosen atmosphere (N_2, air, H_2, or NH_3)
4. Heat from 5 °C to 1000 °C at 5 °C min^{-1}
5. Hold for 20 min at 1000 °C
6. Switch gas to air
7. Hold for 20 min at 1000 °C

The data were provided as a function of time, rather than temperature, so the temperature at any given point was estimated by dividing the elapsed time by the scan rate. The results were normalized as before, with the final weight at step 7 (1000°C, air) used as the U_3O_8 basis weight. Results for all four gases are shown in Fig. 6.13.

The sample behaved identically between 30–400 °C under nitrogen, air, and hydrogen, losing water at the same point and showing the characteristic slow loss of the last water. Under nitrogen and air, the sulfate was driven off between 500–800 °C in the same manner as was observed at UBC, with air delaying the onset of

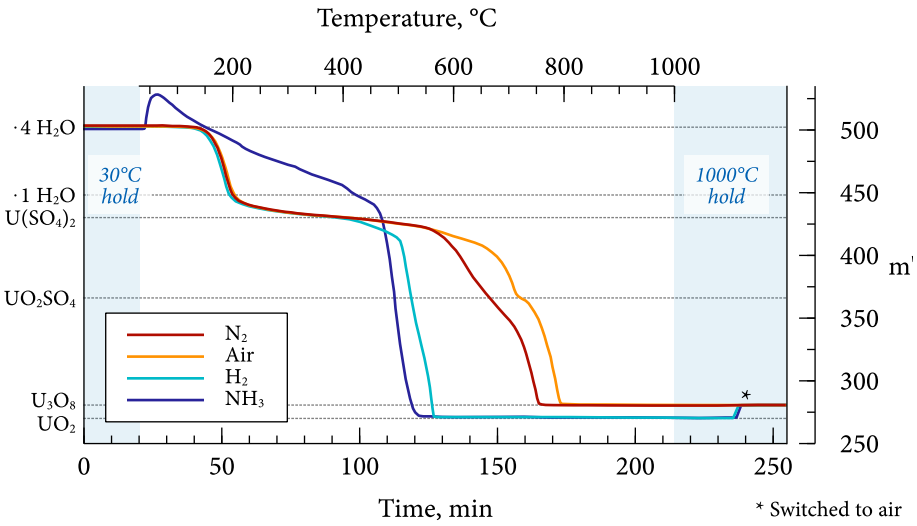

Figure 6.13: Normalized TGA scans of $U(SO_4)_2 \cdot 4\,H_2O$ under nitrogen, air, hydrogen, and ammonia. The atmosphere was switched to air at the end of every test (*). Scan rate 5 °C /min. Temperature axis approximated from the recorded time using the scan rate.

decomposition, and leaving U_3O_8 as the residual product. Under hydrogen, the intermediary UO_2SO_4 was skipped altogether, instead decomposing directly to UO_2 around 500 °C. When the atmosphere was switched to air, the UO_2 immediately oxidized to U_3O_8.

Under ammonia, decomposition proceeded quite differently. As soon as the atmosphere was switched to ammonia, the sample increased in weight equivalent to $\Delta m' = 27.47$, which corresponds to the absorption of 1.6 NH_3 molecules. This was followed immediately by a slow and consistent weight loss until 460 °C, at which point the mass dropped to the equivalent of UO_2. The UO_2 again oxidized to U_3O_8 immediately upon switching the atmosphere to air.

6.6.4 The use of isothermal holds to identify intermediary products

The thermoanalytical data presented so far have pointed to the existence of several intermediary compounds that form during the thermal decomposition of uranous sulfate *x*-hydrate. In some cases, their existence is obvious: anhydrous $U(SO_4)_2$, for

example, has a clear region of stability around 500 °C. For others, only an inflection point in the TGA data identifies a possible intermediary. UO_2SO_4 is one such case, occurring around 650 °C. The existence of at least one lower hydrate is also suggested by an inflection point between 175–200 °C, depending on the starting material.

These intermediaries were investigated further by running the TGA with a series of isothermal hold steps at 90 °C, 160 °C, 300 °C, 640 °C and 750 °C, in both nitrogen and air, using to the following program:

1. Switch gas to nitrogen or air at 20.0 ml min^{-1}
2. Hold for 1.0 min at 30 °C
3. Heat from 30 °C to 90 °C at 50.0 °C min^{-1}
4. Hold for 180 min at 90 °C
5. Heat from 90 °C to 160 °C at 50.0 °C min^{-1}
6. Hold for 180 min at 160 °C
7. Heat from 160 °C to 300 °C at 50.0 °C min^{-1}
8. Hold for 60 min at 300 °C
9. Heat from 300 °C to 640 °C at 50.0 °C min^{-1}
10. Hold for 60 min at 640 °C
11. Heat from 640 °C to 750 °C at 50.0 °C min^{-1}
12. Hold for 60 min at 750 °C
13. Heat from 750 °C to 995 °C at 50.0 °C min^{-1}
14. Hold for 1 min at 995 °C

The TGA curves from the isothermal holds at 90 °C and 160 °C, showing water loss, are given in Fig. 6.14. The hexahydrate and octahydrate both decomposed to a lower hydrate at 90 °C, reaching a weight equivalent to $U(SO_4)_2 \cdot 1.25H_2O$, while the tetrahydrate remained unchanged. At 160 °C, all three solids decomposed to a lower hydrate with between 0.5 and 0.75 waters.

Figure 6.15 shows the full isothermal hold program for uranous sulfate tetrahydrate under both air and nitrogen. During the 300 °C hold, the solid dehydrated completely to $U(SO_4)_2$, although, interestingly, it did so at a much slower rate under nitrogen than under air. The behaviour diverged further at 640 °C, with stable UO_2SO_4 appearing to form under air, but under nitrogen showing only an inflection point. During the 750 °C hold, the sample decomposed rapidly to U_3O_8 under both air and nitrogen.

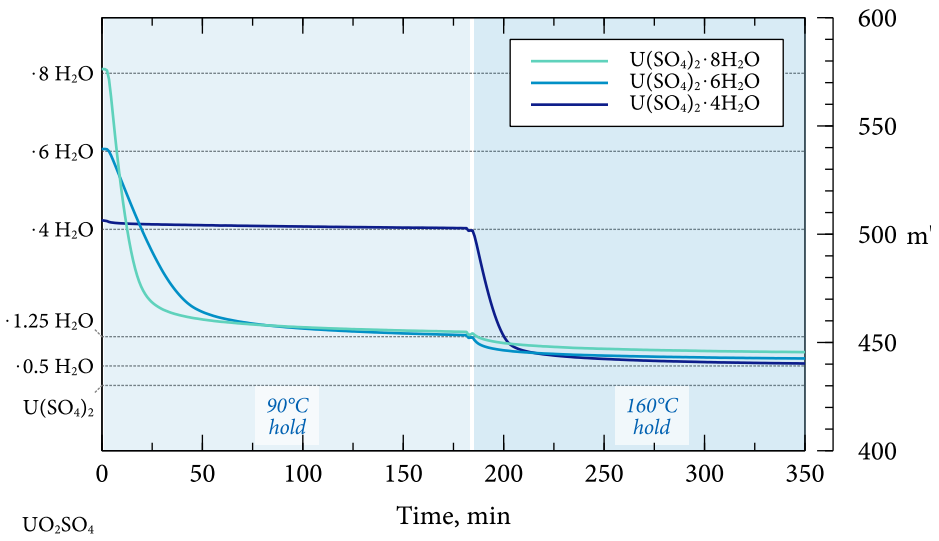

Figure 6.14: Isothermal holds at 90 °C and 160 °C under nitrogen showing water loss for $U(SO_4)_2 \cdot 4\,H_2O$, $U(SO_4)_2 \cdot 6\,H_2O$, and $U(SO_4)_2 \cdot 8\,H_2O$.

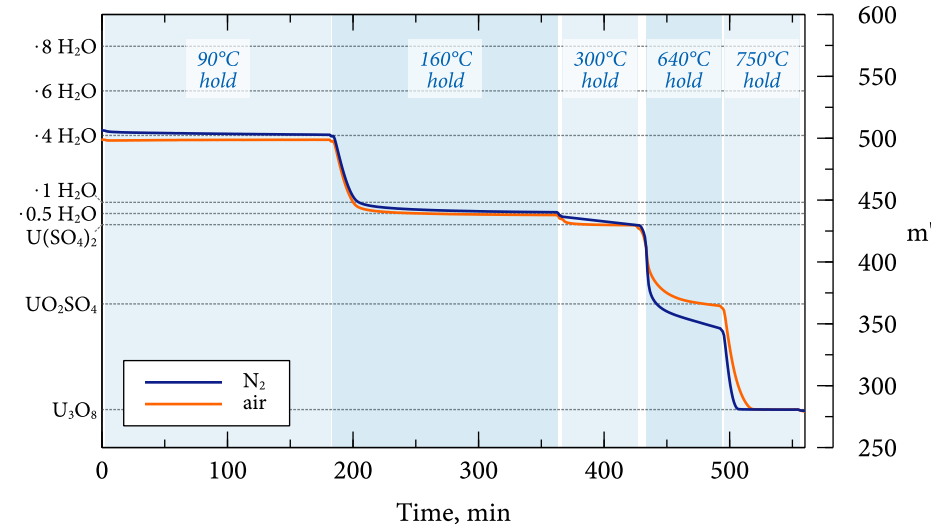

Figure 6.15: Isothermal holds at 90 °C, 160 °C, 300 °C, 640 °C, and 750 °C for $U(SO_4)_2 \cdot 4\,H_2O$ under air and nitrogen.

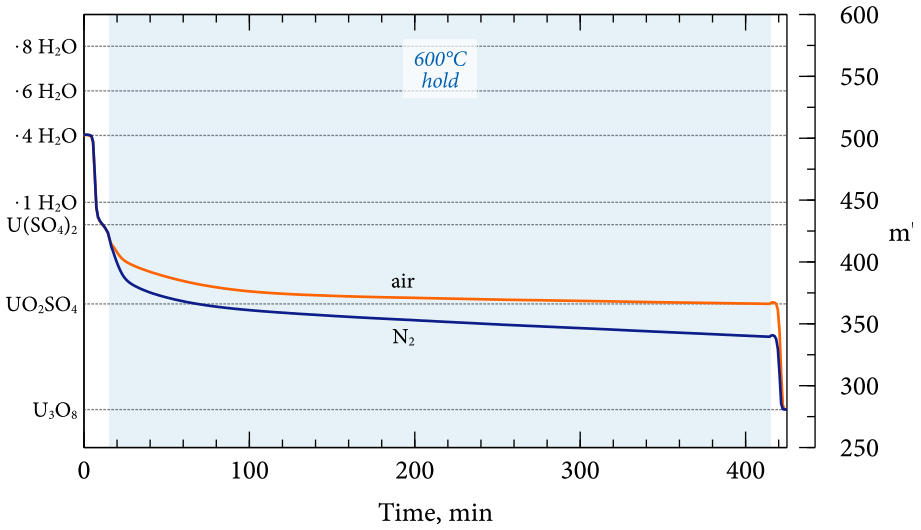

Figure 6.16: 600 °C isothermal holds of $U(SO_4)_2 \cdot 4\,H_2O$ in air and nitrogen.

The UO_2SO_4 intermediary was investigated more closely by using a 400 min hold at 600 °C in both nitrogen and air according to the following program:

1. Switch gas to nitrogen or air at 20.0 ml min^{-1}
2. Hold for 1.0 min at 30 °C
3. Heat from 30 °C to 600 °C at 40.0 °C min^{-1}
4. Hold for 400 min at 600 °C
5. Heat from 600 °C to 995 °C at 40.0 °C min^{-1}

The weight loss profiles shown in Fig. 6.16 confirm that stable UO_2SO_4 formed at 600 °C under air, but not under nitrogen.

6.6.5 Further study on the phase change in the hexahydrate

Uranous sulfate hexahydrate was unique in producing an exothermic event (P1) in its DSC signature. This event corresponded to a small peak in the DTG curve that marked the completion of water loss. This was unusual because, in all other cases, water loss was associated with an endothermic event. It is therefore likely that the energy released from the P1 event was actually due to a phase change.

To see if the P1 event was reversible, a sample of hexahydrate was temperature-cycled according to the following program:

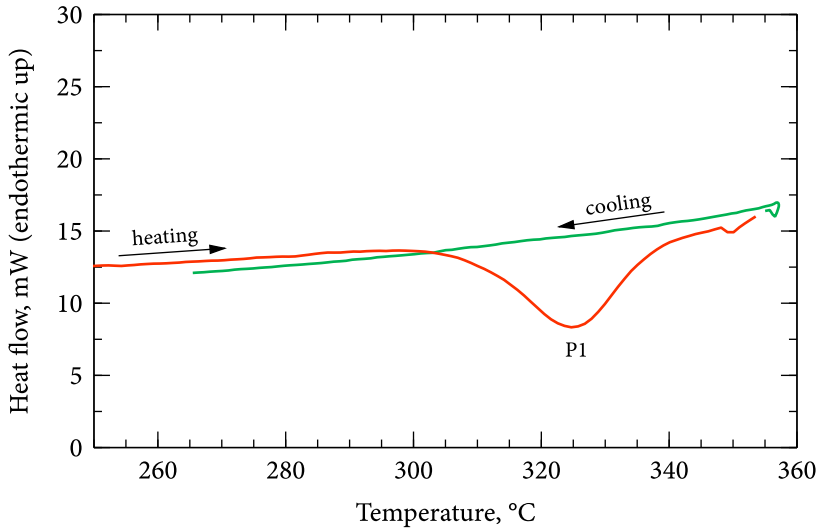

Figure 6.17: DSC signal during the sequential heating and cooling of $U(SO_4)_2 \cdot 6\,H_2O$, showing that the P1 peak is not reversible. Heating/cooling rate 10 °C min^{-1}, nitrogen atmosphere.

1. Switch gas to nitrogen at 20.0 ml min^{-1}
2. Hold for 1.0 min at 30 °C
3. Heat from 30 °C to 360 °C at 10.0 °C min^{-1}
4. Hold for 5 min at 360 °C
5. Cool from 360 °C to 250 °C at 10.0 °C min^{-1}

As shown in Fig. 6.17, there was no corresponding endothermic event when the sample was cooled, meaning that the phase change was irreversible.

6.7 Interpretation of DTG curves

The DTG curves included in Figs. 6.7 to 6.12 are the numerically-determined derivatives of the TGA data, $\frac{dm'}{dt}$, not independent data sets. The TGA and DTG curves are simply different representations of the same reaction rate data, with the former in integral form and the latter in differential form. Nevertheless, the DTG curves are useful for identifying simultaneously-occurring reactions, being composed of a set of overlaid peaks, each representing an individual weight-losing chemical reaction. In addition, since DTG peaks often mirror DSC peaks, they offered an opportunity

to examine events obscured in the DSC signal by background interference above 500 °C.

6.7.1 Peak deconvolution methodology

The magnitude of the DTG signal at any point can be considered a proxy for the instantaneous rate of the underlying weight-losing chemical reaction, with the integrated area under the curve representing the sum change in equivalent molecular weight over the period of the integration. If two or more weight-losing events take place simultaneously, the observed DTG curve is the sum of the underlying reaction rates when scaled to represent the stoichiometric weight change associated with each reaction. For instance, the decomposition of $U(SO_4)_2$ to U_3O_8 was composed of at least two overlapping events, which registered as an inflection point in the TGA signal, but resolved into several overlapping peaks in the DTG signal.

Peak deconvolution techniques were used to estimate the size and shape of distinct, but overlapping, DTG peaks. The peak-fitting software Fityk 0.9.8 [79] was used to minimize the error between the experimentally-determined DTG curves and the sum of any number of adjustable log-normal peaks. The log-normal model was chosen because of its ability to simulate asymmetric peaks superficially similar to those seen in the data, thereby granting a good approximation of peak area and position, even without having a physical significance to this system. As such, information derived from the deconvoluted peaks, particularly when several events overlap closely, should not be considered conclusive, but rather as supporting evidence to be combined with thermodynamic and kinetic theory or other experimental results. No attempt was made to fit a model to the slow weight-loss regions without a clear peak.

Integrating under a deconvoluted peak yielded the total change in equivalent molecular weight associated with a single event n, $\Delta m'_n$.

$$\int \left[\frac{dm'_n}{dt}\right] \left[\frac{dT}{dt}\right]^{-1} dT = dm'_n = \Delta m'_n \qquad [\mathrm{g\,mol^{-1}}] \quad (6.3)$$

This represents the change in the equivalent molecular weight of the material in the crucible as a result of a single deconvoluted peak n (e.g., W1, S3, etc.). The integrated DTG peak areas for the three uranous sulfate hydrates in nitrogen and

Table 6.2: Integrated areas under the deconvoluted DTG (thermogravimetry) peaks for the tetrahydrate, hexahydrate, and octahydrate, representing $\Delta m'$ for each weight loss event.

	Tetrahydrate		Hexahydrate		Octahydrate	
Peak #	nitrogen	air	nitrogen	air	nitrogen	air
W1	62.4	61.5	86.5	90.6	125.6	123.2
P1	-	-	4.9	5.8	-	-
S1	13.2	7.07	-	-	18.6	22.0
S2a	12.6	4.97	-	-	47.3	39.3
S2b	34.0	38.8	50.0	57.3	-	-
S3	86.0	92.0	98.9	94.1	82.9	90.2

air are tabulated in Table 6.2.

The expected $\Delta m'_n$ for a given event can be calculated from the stoichiometry of its associated chemical reaction, recognizing that only solid (and liquid) species register on the TGA. For example, the expected change in equivalent molecular weight expected for the oxidation of $U(SO_4)_2$ to UO_2SO_4 can be calculated as follows:

$$\begin{aligned} \Delta m' \left\{ U(SO_4)_2 \text{ oxidation} \right\} &= MW_{U(SO_4)_2} - MW_{UO_2SO_4} \\ &= 430.15 - 366.09 \\ &= 64.07 \end{aligned} \tag{6.4}$$

If the reaction is for a homogenous decomposition of a single solid reactant (which is the case for all reactions in this system), $\Delta m'_n$ is simply the stoichiometrically-weighted sum of the molecular weights of the evolved product gases (SO_2 in the case of Eq. (6.4)). For the decomposition of uranous sulfate x-hydrate, the possible product gases are H_2O, SO_2, SO_3, and O_2, with the equivalent molecular weight losses shown in Table 6.3. These can be matched to the areas under the deconvoluted peaks to gain insight into the underlying reactions.

6.7.2 Peak assignment and interpretation

The weight loss events fell into three categories: water loss (W), sulfur loss (S), and a small weight change associated with the hexahydrate phase change (P). Each peak

Table 6.3: Theoretical change in equivalent molecular weight, $\Delta m'$, corresponding to the losses of various molecules from a structure.

Stoichiometric loss	$\Delta m'$
$\cdot 0.25\ H_2O$	4.50
$\cdot 0.5\ H_2O$	9.01
$\cdot 1\ H_2O$	18.02
$\cdot 3.5\ H_2O$	63.07
$\cdot 4\ H_2O$	72.08
$\cdot 5\ H_2O$	90.10
$\cdot 6\ H_2O$	108.12
$\cdot 7\ H_2O$	126.14
$\cdot 8\ H_2O$	133.16
SO_2	64.07
SO_3	80.07
$SO_3 + \frac{1}{6}\ O_2$	85.40

was numbered in the same way for each dataset according to its behaviour and temperature of occurrence.

Water loss always proceeded as two concurrent events: initial rapid loss of most of the water (W1), and slow loss of the remaining water (W2). W1 occurred at different temperatures for the three hydrates, but W2 showed less variation, occurring over a similar temperature range for all three hydrates. There was no significant difference between air or nitrogen. The areas under the W1 curves for the tetra-, hexa-, and octahydrate were equivalent to approximately 3.5, 5, and 7 waters, respectively. This is fairly consistent with the isothermal hold results presented earlier in Fig. 6.14.

The second type of event, the exothermic phase change (P1), appeared definitively only in the hexahydrate, and was the same under both nitrogen and air. It seemed to mark an acceleration of water loss after a longer period of slow diffusion-controlled dehydration. A possible faint indication of the same event was also observed for the octahydrate, although it was not accompanied by a corresponding exothermic peak in the DSC curve. There was no P1 peak for the tetrahydrate. The area of this peak corresponded roughly to 0.25 H_2O.

The final category of weight-loss event, sulfur loss, was markedly different for each of the three hydrates. Close examination of the deconvoluted peaks, however,

reveals commonalities. The highest-temperature event, the S3 peak, occurred at the same temperature for all of the hydrates, peaking at 755–760 °C under nitrogen and 775–780 °C under air. Thermodynamic calculations indicate that the S3 event represents the decomposition of UO_2SO_4 to U_3O_8, and indeed, the area of the S3 peaks corresponded quite well to the loss of $SO_2 + \frac{1}{6} O_2$, with a $\Delta m'$ of 80–85 under nitrogen. Under an air atmosphere, the S3 peak was slightly larger, representing a $\Delta m'$ of 90–94. The reasons for this are unclear.

The remaining peaks, S1, S2a, and S2b, must have therefore collectively represented the oxidation of $U(SO_4)_2$ to UO_2SO_4. Although each of the three hydrates gave a seemingly unique response in this zone, close examination of the deconvoluted peaks reveals telling similarities. Figure 6.18 gives a closer look at the DTG signals of the three uranous sulfate hydrates in the sulfur loss region between 500–850 °C. The S1 zone was active in the tetrahydrate and octahydrate (albeit at a higher temperature in the latter), and absent entirely in the hexahydrate. This behaviour was repeatable in air and nitrogen, across several runs of the same sample, and in two different samples of tetrahydrate. The bulk of the weight loss occurred after this, either as the S2a peak for the octahydrate (610–615 °C in nitrogen and air), the S2b peak for the hexahydrate (655 °C in nitrogen, 690–695 °C in air), or a combination of both for the tetrahydrate. The sum of the areas of the S1, S2a, and S2b peaks corresponded approximately to the loss of SO_2.

6.8 Interpretation of DSC curves

6.8.1 Heats of transformation

Differential scanning calorimetry (DSC) was conducted alongside TGA. In most cases, each peak in the DTG signal was accompanied by a corresponding change in the DSC signal. In theory, the integrated area under a peak in a DSC curve represents the heat of reaction, ΔH_{rxn}, associated with that event.

As has already been discussed, the quality of the DSC data above 500 °C was poor, requiring aggressive background correction. In addition, the simultaneous occurrence of the S1, S2a, S2b, and S3 events made it difficult to distinguish the heat flow associated with a single event. This limited the quantitative use of the

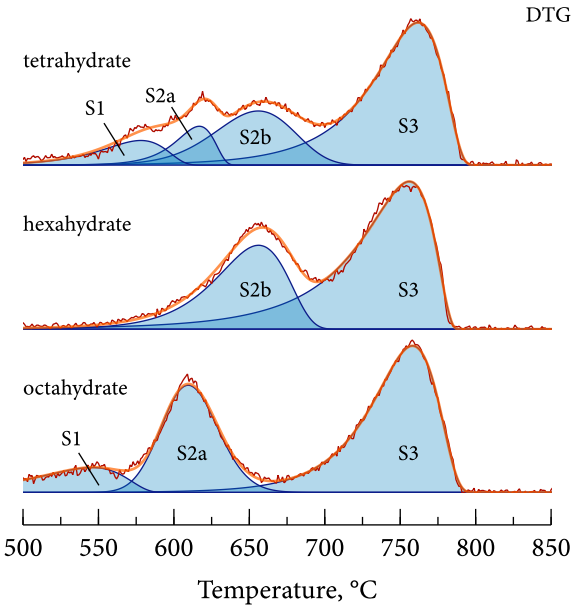

Figure 6.18: A comparison of the raw and deconvoluted DTG signals of the three uranous sulfate hydrates from 500–850 °C. Nitrogen atmosphere, scan rate 10 °C min^{-1}.

DSC data to below 500 °C: in other words, the W1, W2, and P1 events.

The initial water loss (W1) and phase change (P1) events both gave clear peaks in the DSC signal. The calculated peak areas are shown in Table 6.4. For the W1 peak, the energy per water molecule is also shown, assuming the number of waters calculated earlier from the DTG data (3.5 for the tetrahydrate, 5 for the hexahydrate, and 7 for the octahydrate).

Table 6.4: Heats of reaction for thermal events observed by DSC (differential scanning calorimetry) during the dehydration of uranous sulfate *x*-hydrate, 30–400 °C. A positive value indicates an endothermic event.

	Tetrahydrate		Hexahydrate		Octahydrate	
Peak #	nitrogen	air	nitrogen	air	nitrogen	air
W1 (kJ mol^{-1})	222.01	212.98	270.79	289.41	379.50	358.80
W1 (kJ mol^{-1} of H_2O)	63.43	60.85	54.16	57.88	54.21	51.26
P1 (kJ mol^{-1})	-	-	-18.64	-19.67	-	-

In Chapter 5 it was shown that the theoretical ΔH° for complete dehydration of both the tetrahydrate and octahydrate is approximately 52 kJ mol^{-1} of H_2O. This is consistent with the experimental results for the octahydrate and the hexahydrate, which both gave 54 kJ mol^{-1} of H_2O (under nitrogen), only slightly higher than predicted by the thermodynamic calculations. For the tetrahydrate, however, the observed heat of reaction was higher, at 63 kJ mol^{-1} of H_2O (in nitrogen). If the total energy is divided by 4 waters instead of 3.5, however, the value becomes 55 kJ mol^{-1} of H_2O, bringing it in line with the other two hydrates. It is likely, then, that the water loss peak in the DSC signal incorporates the energies for both the W1 and W2 events, as might be expected considering the considerable overlap of the two events.

The P1 event, which occurred only in the hexahydrate, registered as an exothermic peak with an integrated area of −18.64 kJ mol^{-1}. The significance of this will be discussed later.

6.9 Reaction kinetics during thermal decomposition

The thermoanalytical experiments described in this chapter were conceived as a way to study the stability and decomposition pathways of the uranous sulfate *x*-hydrates, not their decomposition kinetics. Still, a deeper look at the DTG data allows for a qualitative assessment of the kinetics of the system.

6.9.1 Theoretical kinetics under ideal behaviour

Broadly speaking, two different kinetic regimes could control the kinetics of decomposition – diffusion control, and activation energy-control (i.e., Arrhenius). To analyze these in the context of the current system, it is useful to introduce the unitless parameter *conversion*, X, which represents the mass (or mole) fraction of a reactant that has been consumed by the reaction. Since the temperature increases at a fixed rate in TGA analysis, there is a linear relationship between temperature and time:

$$\left[\frac{dT}{dt}\right] = \text{constant} \qquad [^\circ\text{C s}^{-1}] \quad (6.5)$$

The governing rate laws during TGA analysis can therefore be written as a func-

tion of temperature instead of time.

Under diffusion control, mass transfer of the product gases across a boundary layer controls the reaction rate. This can be modelled in its simplest sense according to Fick's Law:

$$\left[\frac{dX}{dt}\right] = D\left(p_{\mathrm{G}} - p_{\mathrm{G}}^{\mathrm{bulk}}\right) \qquad [\mathrm{s}^{-1}] \quad (6.6)$$

where p_{G} is the partial pressure of the product gas 'G' in direct contact with the solids, and $p_{\mathrm{G}}^{\mathrm{bulk}}$ is its partial pressure in the bulk gas phase above the sample. If both p_{G} and $p_{\mathrm{G}}^{\mathrm{bulk}}$ are assumed to be constant in the short term (the former being set by thermodynamic equilibrium, and the latter a function of reaction rate and purge gas flow), this results in a constant reaction rate.

Under activation energy control, the reaction rate follows the Arrhenius rate law:

$$\left[\frac{dX}{dt}\right] = k\exp\left(\frac{-E_{\mathrm{a}}}{RT}\right) \qquad [\mathrm{s}^{-1}] \quad (6.7)$$

Both diffusion-controlled and activation energy-controlled kinetics could also be influenced by conversion X, with the rate decreasing as the amount of remaining reactant declines. For example, this might occur if a growing product layer acts as a mass transfer barrier that increases in length as the reaction progresses. A rough estimation of this effect can be included in the kinetic models by including a $(1-X)$ term:

$$\left[\frac{dX}{dt}\right] = (1-X)D\left(p_G - p_G^{\mathrm{bulk}}\right) \qquad [\mathrm{s}^{-1}] \quad (6.8)$$

$$\left[\frac{dX}{dt}\right] = (1-X)k\exp\left(\frac{-E_{\mathrm{a}}}{RT}\right) \qquad [\mathrm{s}^{-1}] \quad (6.9)$$

The solutions to these four scenarios are plotted in both differential and integral form in Fig. 6.19. Each has a signature shape. Thus, by comparing the experimentally-determined DTG peaks to these theoretical differential rate curves, it is possible to gain insight into the underlying kinetic control mechanism at a given point during thermal analysis.

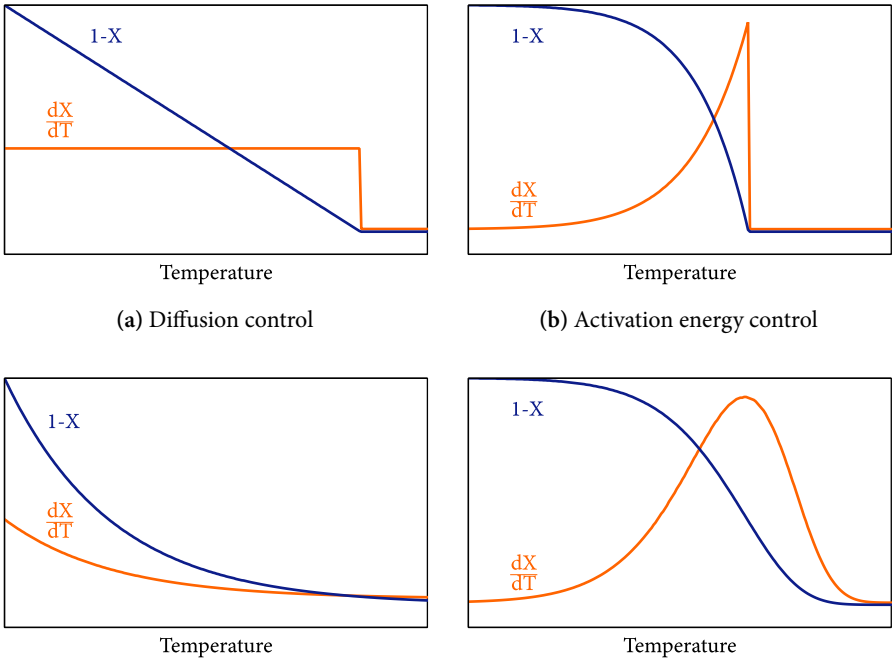

(a) Diffusion control

(b) Activation energy control

(c) Diffusion control with $(1 - X)$ dependency

(d) Activation energy control with $(1 - X)$ dependency

Figure 6.19: Non-dimensionalized solutions for three possible reaction rate control mechanisms as temperature is increased at a constant rate.

6.9.2 Inferring reaction kinetics from peak shape

It is possible to make a qualitative assessment of the kinetics behind each decomposition reaction by comparing the shape of the DTG curves to the theoretical shapes given in Fig. 6.19. In general, flat, non-zero regions in the DTG represent diffusion-like kinetics, while peaks represent activation energy-controlled kinetics.

Initial water loss (W1) clearly had a strong element of activation energy-control. The rate declined somewhat as the reaction progressed, however, suggesting that the rate was dependent somewhat on the amount of water remaining in the structure. The remaining water (W2) departed at a slow, fairly constant rate akin to diffusion, again with the rate slowing as the amount of water approached zero. The phase change peak P1, seen only in hexahydrate, was too small to interpret easily, but it

could be seen as the sudden vaporization of released bound water as a result of a structural phase change, since free water would rapidly evaporate at >300 °C.

The S1, S2a, and S2b peaks all appeared to represent the same chemical reaction, the oxidation of $U(SO_4)_2$, but under different kinetic regimes. The first event, S1, initially seemed to follow diffusion-like kinetics, but was followed by an acceleration and drop-off similar in nature to the P1 peak. This was immediately followed by the activation energy-controlled kinetics of the S2a and/or S2b events. It seems, then, that the oxidation of $U(SO_4)_2$ proceeded slowly by diffusion-like kinetics at low temperature, then switched to activation energy-controlled kinetics at higher temperature, with different variations depending on the original structure of the solid.

The final event, S3, corresponded to the final decomposition of UO_2SO_4 to U_3O_8, and consistently showed an activation energy-controlled shape for all samples.

6.10 Analysis and mechanism proposal

6.10.1 An argument in support of the occurrence of a uranous sulfate recrystallization phase transformation

The oxidation of $U(SO_4)_2$ to UO_2SO_4 proceeded along markedly different paths depending on the amount of crystalline water in the original hydrate. What could explain the different high-temperature decomposition behaviours of three chemically-similar uranous sulfate hydrate polymorphs that should ostensibly converge to the same anhydrous form at a thermodynamically-predicted temperature of less than 100 °C? It has already been shown that these differences could not have been caused by differences in particle size, and the data have proven reproducible, so experimental error cannot be blamed. A clue lies in the fundamentally different structures of the three hydrates, which was discussed in Chapter 4. Betke and Wickleder [7] showed that crystalline $U(SO_4)_2$ has a highly cross-linked structure, with each uranium atom coordinated in a monodentate fashion to eight sulfate groups, a structure not shared by any of the uranous sulfate hydrates. This suggests that the conversion to $U(SO_4)_2$ involves not only the ejection of water molecules, but also the reconfig-

uration of the uranium-sulfur bonds within the crystal lattice.

It can be supposed, then, that after water ejection, the three hydrates must transition through an amorphous phase, *am*-$U(SO_4)_2$, on their way to recrystallizing as orthorhombic uranous sulfate, *cry*-$U(SO_4)_2$. It is possible that this phenomenon was observed during the bulk decomposition of $U(SO_4)_2 \cdot 4\,H_2O$, where a sample calcined in air at 300 °C for 1 h was found to be x-ray amorphous, but a sample of $U(SO_4)_2 \cdot 6\,H_2O$ calcined for 40 h showed signs of the characteristic x-ray pattern of crystalline $U(SO_4)_2$. It might be, then, that the exothermic P1 event represents the cross-linking of the hexahydrate's chains into the structure of crystalline anhydrous uranous sulfate. Following the same logic, S1 could represent the same event, but occurring at a higher temperature, reflecting a higher energy barrier for reconfiguring the sulfate bonds in the tetrahydrate and the octahydrate.

Continuing with the theory that the P1 peak represents the conversion of amorphous *am*-$U(SO_4)_2$ to crystalline *cry*-$U(SO_4)_2$, the difference in internal energy between the two phases should manifest as an irreversible thermal event in the DSC curve. This was indeed observed in the P1 event in the hexahydrate, as an exothermic peak with an integrated area of $-18.64\,\mathrm{kJ\,mol^{-1}}$. This implies that the crystalline phase has a lower internal energy than the amorphous phase, and therefore should decompose to UO_2SO_4 at a higher temperature. This, too, was observed, with the S2a peak representing the decomposition of *am*-$U(SO_4)_2$, and the S2b peak representing the decomposition of *cry*-$U(SO_4)_2$. If S1 represents the same phase change as P1, an exothermic thermal event should be associated with it too. Unfortunately, the low quality of the DSC data above 500 °C made it impossible to unequivocally distinguish a small exothermic phase change event from the much larger endothermic events that occurred simultaneously. Nevertheless, slope changes in the DSC curve around 575 °C suggest that something did occur.

6.10.2 Proposed decomposition mechanism in nitrogen

The following thermal decomposition mechanism for the uranous sulfate hydrates is proposed based on the experimental and thermodynamic evidence.

Water loss for all three uranous sulfate hydrates proceeds in two stages: initial rapid water loss of most of the water (W1), followed by the slow diffusion-like loss

of the remaining water (W2). Each has a transiently-stable intermediary hydrate, containing approximately 0.5, 1.0, and 1.0 waters, respectively, with the two monohydrates having different structures, denoted α and β, respectively. The remainder of the water departs more slowly under diffusion-like kinetics.

After all of the water is ejected from the crystal structure, the resulting anhydrous uranous sulfate must undergo structural reorganization to reach its crystalline form. Two forms of $U(SO_4)_2$ therefore exist at different points during thermal decomposition: first, the amorphous form *am*-$U(SO_4)_2$, then the crystalline form *cry*-$U(SO_4)_2$. The temperature at which this happens depends on the structure of the original solid: ~320 °C for the chain-bridged hexahydrate, ~500 °C for the sheet-bridged tetrahydrate, and possibly not at all for the solitary $U(SO_4)_2 \cdot 8\,H_2O$.

The oxidation of *am*-$U(SO_4)_2$ to UO_2SO_4 is initially characterized by slow diffusion-like kinetics (S1) starting around 400 °C, followed by a transition to rapid activation energy-controlled kinetics (S2a) starting around 550 °C. *cry*-$U(SO_4)_2$, in contrast, is weight-stable, showing no low-temperature diffusion-like decomposition, until activation energy-controlled oxidation (S2b) starts around 575 °C.

The final decomposition of UO_2SO_4 to U_3O_8 (S3) starts around 650 °C for each of the three hydrates, overlapping significantly with the oxidation of *cry*-$U(SO_4)_2$. The resulting final product, U_3O_8, is stable to at least 995 °C, the highest temperature tested.

Each of the weight loss and heat flow peaks can be matched to specific chemical reactions, as shown in Eqs. (6.10) to (6.14). A graphical representation of the proposed decomposition pathways for the three uranous sulfate hydrates is given in Fig. 6.20.

$$\text{W1:} \quad U(SO_4)_2 \cdot x H_2O \longrightarrow U(SO_4)_2 \cdot y H_2O + (x\text{-}y) H_2O \tag{6.10}$$

$$\text{W2:} \quad U(SO_4)_2 \cdot y H_2O \longrightarrow U(SO_4)_2 + y H_2O \tag{6.11}$$

$$\text{S2a:} \quad \textit{am}\text{-}U(SO_4)_2 \longrightarrow UO_2SO_4 + SO_2 \tag{6.12}$$

$$\text{S2b:} \quad \textit{cry}\text{-}U(SO_4)_2 \longrightarrow UO_2SO_4 + SO_2 \tag{6.13}$$

$$\text{S3:} \quad UO_2SO_4 \longrightarrow \tfrac{1}{3}U_3O_8 + SO_3 + \tfrac{1}{6}O_2 \tag{6.14}$$

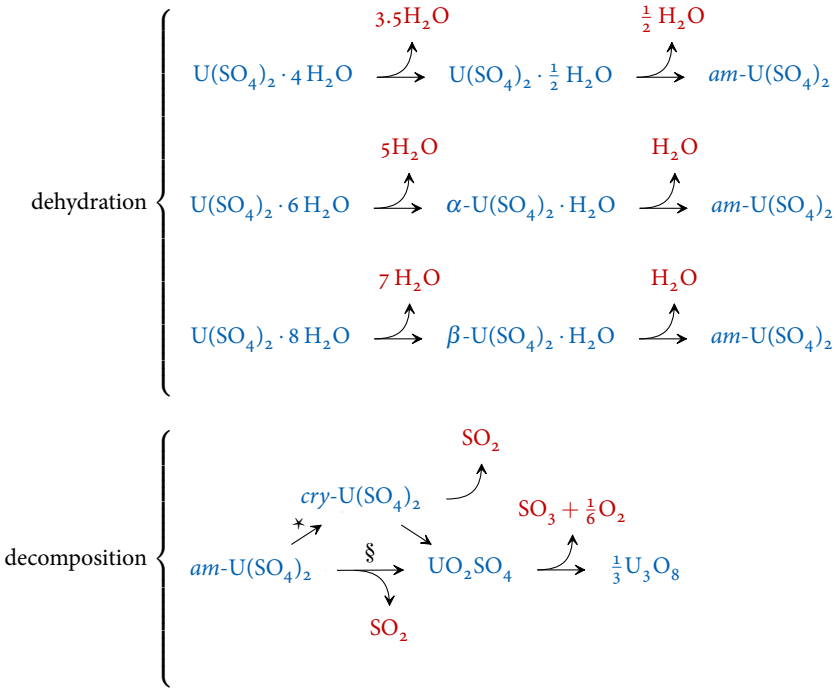

Figure 6.20: The thermal decomposition pathways for $U(SO_4)_2 \cdot 4\,H_2O$, $U(SO_4)_2 \cdot 6\,H_2O$, and $U(SO_4)_2 \cdot 8\,H_2O$ in nitrogen. Solids in blue, gases in red. ⋆ The recrystallization temperature of amorphous uranous sulfate depends on the structure of the original hydrate. § The decomposition of *am*-$U(SO_4)_2$ takes place at a lower temperature than *cry*-$U(SO_4)_2$.

6.10.3 The influence of oxygen

Operating in an air atmosphere had only a small effect on the thermal decomposition of the uranous sulfate hydrates. The water loss steps, W1 and W2, were unaffected by the presence of oxygen gas. The amorphous-to-crystalline phase change steps, P1 and S1, were likewise unaffected. This is unsurprising, since oxygen does not feature in any of these reaction.

The S2a and S3 peaks, representing the decompositions of *am*-$U(SO_4)_2$ and UO_2SO_4, respectively, also behaved as expected. The S2a peak did not shift in the presence of oxygen, again because oxygen gas is not featured in that reaction. The decomposition of UO_2SO_4 shifted by approximately 20 °C towards higher temperature in an air atmosphere, reflecting the leftward pressure on the equilibrium by the

increased presence of oxygen gas. This shift explains why UO_2SO_4 was stable during a long isothermal hold at 600 °C in air, but not under nitrogen, as was shown in Fig. 6.16. It also matches the observations of Tridot [76], who found that UO_2SO_4 was stable under air and SO_2, but not under vacuum.

The S2b peak, representing the decomposition of *cry*-$U(SO_4)_2$, showed a 35 °C shift to higher temperature, which at first seems surprising given that the reaction is not envisioned to be any different than the decomposition of *am*-$U(SO_4)_2$ in terms of reactants and products. One explanation could be be that, given the significant overlap of the S2b and S3 events, their product gases would effectively dilute one another, lowering their respective partial pressures and shifting both equilibrium temperatures lower than they would be at standard state (i.e., 1 atm). If S3 takes place at a higher temperature, the rate of SO_3 evolution shifts with it, diluting the S2b reaction less, and consequently shifting *its* equilibrium temperature as well. This did not affect the S2a reaction simply because it takes place at too low of a temperature to be influenced by the product gases of S3.

The behaviour of the system in the presence of oxygen also serves to clarify the role of (and ultimately show that they don't take place) two reactions that are predicted by thermodynamics, but have thus far been ignored: the heterogeneous oxidation of $U(SO_4)_2$ with oxygen gas, and the equilibrium-shift reaction between SO_2 and SO_3. The heterogeneous oxidation of $U(SO_4)_2$ is predicted to take place nearly 250 °C lower than homogeneous oxidation, and yet the temperature at which oxidation takes place actually *increases* in air, suggesting that heterogeneous oxidation simply does not take place due to kinetic or mechanistic limitations. Likewise, if the SO_2/SO_3 equilibrium were active, there would be a gas-phase equilibrium shift away from SO_2 in the presence of air between 570–640 °C, where the reaction is known to be both thermodynamically and kinetically feasible. The resulting lowering of the SO_2 partial pressure could cause a corresponding shift in the oxidation of $U(SO_4)_2$ to lower temperature, which did not occur. This suggests that even if the SO_2/SO_3 equilibrium-shift reaction does take place, it does not happen quickly enough to be relevant during TGA analysis.

6.10.4 Estimation of reaction rates and gas-phase composition

The molar reaction rates, the associated gas evolution rates, and from them the gas-phase composition, can be estimated from the peaks in the DTG curves (i.e., W1, S2, etc.). First, each of the peaks must be normalized by dividing the $\frac{dm'}{dt}$ values by the peak area (i.e., $\Delta m'_n$) to give the reaction rate in terms of conversion X. The molar reaction rate associated with each peak, $-r_n$, can then be calculated by multiplying the normalized rate by the total number of moles of uranium present, N_U, which remains unchanged throughout the decomposition process[3].

$$-r_n = \left(\frac{dN}{dt}\right)_n = \frac{\frac{dm'_n}{dt}}{\Delta m'_n} N_U \qquad [\mathrm{mol\,s^{-1}}] \quad (6.15)$$

It has already been shown that each peak is associated with an individual chemical reaction (Eqs. (6.10) to (6.14)). It is therefore straightforward to estimate the gas production rates from stoichiometry:

$$\begin{aligned} r_{H_2O} &= (x-y) r_{W1} + (x-y) r_{W2} \\ r_{SO_2} &= r_{S1} \\ r_{SO_3} &= r_{S2a} + r_{S2b} \\ r_{O_2} &= \frac{r_{S2a} + r_{S2b}}{6} \\ \hline r_{total} &= r_{H_2O} + r_{SO_2} + r_{SO_3} + r_{O_2} \end{aligned} \qquad [\mathrm{mol\,s^{-1}}] \quad (6.16)$$

The bulk gas composition above the solids (and in the exhaust) is a function of the total rate of gas evolution and the flow of purge gas, r_{purge}. Neglecting the very small contribution to total gas volume from the evolved gases (the purge gas flow rate in the present analysis was three orders of magnitude greater than the maximum gas evolution rate), the partial pressure of a gas in the well-mixed zone above the sample is simply its evolution rate divided by the purge gas flow rate. This represents the *minimum* possible gas partial pressure in thermodynamic contact with the solids. The *maximum* possible gas partial pressure, such as would occur deep within the sample away from the turbulent flow of the purge gas, is the ratio of that

[3] In the general case, each reaction rate must also be divided by an appropriate stoichiometric coefficient. For the homogenous decomposition of uranous sulfate, however, all of the proposed reactions involve exactly one mole of uranium, so no adjustment is necessary.

gas's evolution rate and the total gas evolution rate. The range of possible gas partial pressures in contact with the solid is therefore represented by Eq. (6.17).

$$\frac{r_G}{r_{purge}} < p_G < \frac{r_G}{r_{total}} \tag{6.17}$$

This range of possible partial pressures can be used to compare the observed temperatures during thermal analysis with the values predicted by thermodynamics.

6.10.5 A thermodynamic interpretation of uranous sulfate decomposition

The thermal decomposition of uranous sulfate *x*-hydrate broadly followed the thermodynamic predictions given in Chapter 5. For some of the weight loss events, the initial peak temperature (T_i) was below the thermodynamic standard state equilibrium temperature (T_{eq}°). This was unambiguously the case for water loss in the octahydrate (W1) and for the final decomposition of UO_2SO_4 to U_3O_8 (S3). The long diffusion-like period before S1, representing the slow oxidation of $U(SO_4)_2$, also seemed to begin below its standard state equilibrium temperature, although the signal was too faint to be certain. The reason for this phenomenon can be explained by the way T_{eq}° is calculated.

T_{eq}° is the temperature at which $\Delta G_{rxn} = 0$ when all reactants and products are at standard state – meaning, in the ideal system, an activity of 1 for solids and a partial pressure of 1 atm for gases. This is always true for the left-hand side of the heterogenous decompositions reactions under consideration, which consist of a single solid reactant. However, as has already been shown, the partial pressures of the product gases in thermodynamic contact with the solid must be < 1. This lowers the reaction quotient below standard state, which pushes the actual equilibrium temperature down.

As an example, the thermodynamic feasibility of the final decomposition of UO_2SO_4 to U_3O_8 (S3) can be calculated using Eq. (6.18):

$$\Delta G_{S3}(T) = \Delta H^{\circ} - T\Delta S^{\circ} + RT \ln\left(p_{SO_3} p_{O_2}^{1/6}\right) \tag{6.18}$$

The minimum and maximum gas partial pressures can be calculated from the experimental DTG curves using Eqs. (6.15) to (6.17). Choosing decomposition of the octahydrate in nitrogen at 700 °C as an example, the range of possible gas partial pressures were $0.00204 < p_{SO_3} < 0.857$ and $0.00034 < p_{O_2} < 0.143$ atm. This yields values of $-19.03\,\mathrm{kJ\,mol^{-1}}$ at the minimum gas activity and $37.99\,\mathrm{kJ\,mol^{-1}}$ at the maximum gas activity. Therefore it is quite feasible thermodynamically for UO_2SO_4 to decompose at 700 °C or lower – but only if the gas phase is substantially diluted.

The amount of gas-phase dilution required to make a reaction *just* thermodynamically feasible (i.e., $\Delta G = 0$) can be calculated iteratively based on thermodynamics and the stoichiometry of the reaction. For the decomposition of UO_2SO_4 at 700 °C, a 115-times dilution is required, with greater dilution required at lower temperatures. Eventually, the required dilution becomes unachievably high and so the reaction cannot occur – this is T_i.

Two events did not behave according to the gas dilution theory discussed above: the main water loss event for $U(SO_4)_2 \cdot 4\,H_2O$ (W1), and the oxidation of $U(SO_4)_2$ (S2a/S2b). The thermodynamics predict a standard state temperature of 85 °C for tetrahydrate water loss, and yet the observed T_i was approximately 125 °C – higher than the standard state equilibrium temperature. One reason for this could simply be the uncertainty in the thermodynamic data: the S° values for $U(SO_4)_2 \cdot 4\,H_2O$ listed in Guillaumont and Mompean [35] has a variance of ±10 %, which could account for a ±20 °C difference in the predicted T_{eq}°. It could also be related to the thermodynamic stability of the intermediary hemihydrate phase. In the absence of an easily-distinguishable event in the DSC data to confirm this, however, no explanation from the available data is forthcoming.

The oxidation of $U(SO_4)_2$ (S2a/S2b) also did not conform to thermodynamic theory. While slow oxidation of $U(SO_4)_2$ represented by the S1 zone did commence around the standard state equilibrium temperature of 451 °C, rapid decomposition did not begin until at least 100 °C higher. This suggests that the reaction is diffusion-controlled to a temperature well above its thermodynamic equilibrium. No obvious explanation for this behaviour is forthcoming.

6.11 Summary and conclusion

The thermal stability and decomposition of three uranous hydrates was investigated: $U(SO_4)_2 \cdot 4\,H_2O$, $U(SO_4)_2 \cdot 6\,H_2O$, and $U(SO_4)_2 \cdot 8\,H_2O$. All were shown to be stable at room temperature, and to follow a different dehydration series, with different intermediary hydrates. The onset temperatures for initial water loss (W1) were approximately 150 °C, 95 °C, and 81 °C, respectively, decomposing into lower hydrates with the estimated composition of hemihydrate, α-monohydrate, and β-monohydrate, respectively. This was followed by a period of slow diffusion-driven loss of the remaining water.

The product after water loss was amorphous uranous sulfate, *am*-$U(SO_4)_2$, which transitioned to its crystalline form, *cry*-$U(SO_4)_2$, after a period of time. In the hexahydrate, this transformation took place around 320 °C (P1) at a scan rate of 10 °C min^{-1} and was associated with an exothermic release of energy equivalent to 18.64 kJ mol^{-1}. The same phase transformation appeared to take place in the tetrahydrate (S1), but at ~575 °C, although it was partly masked by the simultaneous occurrence of other decomposition events. The considerable differences between the hydrates in this respect might reflect the different sulfate bonding modes and cross-linking of the crystal structures of the original hydrates.

Oxidation to UO_2SO_4 behaved differently for *am*-$U(SO_4)_2$ than *cry*-$U(SO_4)_2$. The amorphous form began decomposing rapidly at ~575 °C (S2a). This was preceded by slow decomposition with diffusion-like kinetic characteristics (S1), possibly reflecting the lack of stabilizing cross-linking in the amorphous structure. The crystalline form began decomposing rapidly at ~600 °C (S2b), which was not preceded by slow diffusion-like decomposition.

Final decomposition of UO_2SO_4 to U_3O_8 began at ~650 °C for all three hydrates in nitrogen, and 20 °C higher under air. This shift reflected the leftward pressure on the thermodynamic equilibrium by the increased presence of $O_{2(g)}$. This had an indirect effect on the decomposition of *cry*-$U(SO_4)_2$, pushing it to higher temperatures as well, possibly due to the shift in the relative quantities of SO_2, SO_3, and O_2 that influence the equilibrium reactions.

The results presented in this chapter could be used in the design of a drying or calcining circuit for uranous sulfate *x*-hydrate. If $U(SO_4)_2 \cdot 4\,H_2O$ were to be the

main feed material to such a process, as seems likely, a minimum temperature of 150 °C would be required to dehydrate the material fully. The resulting material could be either amorphous or crystalline, depending on the operating conditions, which could have downstream implications. Further decomposition to U_3O_8 would require a temperature of >650 °C, with a higher requirement in the presence of an air atmosphere. This would see the release of equal amounts of SO_2 and SO_3, as well as a small amount of O_2, which would have implications for equipment corrosion and acid plant design.

Chapter 7

The kinetics of uranium(IV) oxidation with molecular oxygen

Note: The portion of this work concerning the oxidation of uranium(IV) in perchloric acid was presented as a conference paper at Hydrometallurgy 2014 in Victoria, BC, Canada [13].

7.1 Introduction

Under aqueous processing conditions, uranium can exist in its oxidized form (uranium(VI) as UO_2^{2+}) or in its reduced form (uranium(IV) as U^{4+}). Uranium(IV) will oxidize in the presence of oxygen gas according to the overall reaction given in Eq. (7.1):

$$U^{4+} + 0.5O_2 + H_2O \longrightarrow UO_2^{2+} + 2H^+ \qquad \Delta G^\circ = -184.5\,\mathrm{kJ\,mol^{-1}} \qquad (7.1)$$

The unintended oxidation of uranium(IV) would be detrimental to a uranous sulfate precipitation process. It is therefore important to understand how different parameters affect the kinetics of oxidation. In the present work, the kinetics of uranium(IV) oxidation by molecular oxygen are examined in the non-complexing perchlorate medium under varying conditions of acid concentration (0.1–0.75 N), oxygen partial pressure (0.21 and 0.995 atm), uranium(VI) concentration, and temperature (30–50 °C). An apparent overall rate equation is proposed as a function of

uranium(IV), H^+, and oxygen partial pressure. The effect of sulfate, both by operating in sulfuric acid and by adding sodium sulfate to a perchloric acid solution, is also examined, although the results are inconclusive.

7.2 Background information

7.2.1 Oxidation with molecular oxygen in perchloric acid

The first rigorous study of the oxidation of aqueous uranium(IV) by molecular oxygen in perchloric acid was conduced by Halpern and Smith [38]. They proposed a simplified overall rate law that was first order in uranium(IV), first order in oxygen, and inverse-first order in H^+. Their rate law was based on the initial reaction rates, not data from the entire duration of the tests, and significant deviation was noted as oxidation progressed. This was particularly true when acid was >0.2 N, which they attributed to a slow secondary reaction or the influence of an unknown impurity or by-product. Halpern and Smith did not state how they calculated oxygen concentration, making it difficult to validate the results.

Halpern and Smith also investigated the effect of various other ions on the oxidation kinetics. They found that Fe^{2+}, Cl^-, and Ag^+ inhibit the reaction, Hg^{2+} and Cu^{2+} enhance it, and Co^{2+} and Mg^{2+} have no effect. They attributed the enhancing effect of Cu^{2+} to the cycling of Cu^{2+} and Cu^+, while the effect of the inhibiting ions was explained as an interruption of the chain mechanism through the destruction of the intermediary products HO_2 or $UO_2{}^+$.

Sobkowski [71] investigated the same system a decade later, observing that the reaction kinetics fell somewhere between first-order and second-order in uranium(IV). He noted that the underlying reaction mechanism appeared to change with free acid and temperature, with the most notable difference occurring at low acid. He observed a five-fold increase in kinetics when using oxygen gas instead of air, in line with Halpern and Smith's proposed first-order relationship in oxygen.

Most recently, Shilov et al. [69] studied the oxidation of uranium(IV) with oxygen gas in weakly acidic and neutral solutions, finding that the reaction proceeds according to pseudo-first order kinetics after an induction period. They found that the kinetics of oxidation are enhanced by uranium(VI), essentially demonstrating

an autocatalytic effect since uranium(VI) is a reaction product. They also observed that rapid oxidation was usually preceded by an induction period. It is unlikely that their results apply to the strongly acidic system described in the present work, however.

7.2.2 Oxidation with molecular oxygen in sulfuric acid

McCoy and Bunzel [56] were the first to study the oxidation of aqueous uranium(IV) in sulfuric acid, nearly fifty years before Halpern and Smith studied the simpler perchloric acid system. The authors noted that the apparent rate constant varied capriciously between tests, which they blamed on inconsistency in the free acid resulting from their method of producing uranium(IV) by zinc metal reduction, although they claimed to obtain more consistent results when using electrolytic reduction. The authors concluded that the oxidation of uranium(IV) in sulfuric acid is first order in uranium(IV) and inverse second-order in free acid.

Russian researchers Sudarikov et al. [73] studied the same system fifty years later. Similar to McCoy and Bunzel, they found an inverse second-order relationship in H^+. They noted that their assumed first-order rate constant appeared to increase over the duration of the test. The addition of more sulfate as sodium sulfate slowed the kinetics of the reaction, which the authors took as evidence for the formation of inactive polynuclear U(IV)-SO_4^{2-} complexes. Sobkowski [71] investigated the same system much more thoroughly a few years later (and helpfully published their results in English). He also found that sulfate has an inhibitory effect on the kinetics of uranium(IV) oxidation. The kinetics were complex, following neither a first-order or a second-order relationship in uranium(IV), and displayed autocatalytic behaviour, becoming faster as the reaction progressed. Južnič and Fedina [41] confirmed that the reaction rates in sulfuric acid were much slower than in perchloric acid. The authors proposed a first-order rate law, but noted that its validity was restricted to certain concentrations, and that there appeared to be a significant induction period. They found the rate to be inversely proportional to H_2SO_4 activity.

7.2.3 Tracer studies

The underlying mechanism for the oxidation of uranium(IV) was studied by Gordon and Taube [33] in a series of clever tracer studies using oxygen gas labeled with the isotope ^{18}O. Their results showed that the final oxidation product, UO_2^{2+}, contained one atom of ^{18}O derived from the isotopically-labeled oxygen gas, and one atom of ^{16}O presumably derived from hydrolysis with the water of the solution. Given that the oxidation of uranium(IV) to uranium(VI) involves the donation of two electrons, and each oxygen atom in O_2 can accept two electrons, this represents the maximum theoretically-possible amount of oxygen that can be supplied by O_2 as the oxidizing agent. 100 % of labeled oxygen reported to the UO_2^{2+}, with none found in the water or elsewhere.

The authors did not report on the effect of sulfate, so it is impossible to say whether their results also apply in the presence of sulfate.

7.2.4 Underlying reaction mechanism

In all of the studies described above, the authors conclude that the hydrolyzed ion UOH^{3+} is the actively-oxidized species [38, 56, 71]. This is supported by the inverse relationship between oxidation speed and free acid, since any increase in acid would shift the hydrolysis reaction away from UOH^{3+}.

Many of the studies concluded that the oxidation of uranium(IV) is a first-order process, despite evidence from their own data to the contrary. More cautious authors only noted that the rate behaved somewhere between first- and second-order in uranium(IV), with substantial variation depending on conditions. This was particularly true in the sulfate system.

Sobkowski suggested that the apparent change in kinetic behaviour at low acid is due to the formation of the higher hydrolysis product $U(OH)_2^{2+}$ with different kinetics than UOH^{3+}, although he claimed that the kinetics of the latter are so slow that they can be neglected. Lotnik et al. [50] point out that, in any case, $U(OH)_2^{2+}$ only exists in appreciable amounts above pH 2.7, which is well outside of the range under consideration here.

Halpern and Smith proposed a chain reaction mechanism in perchloric acid involving a series of single-electron transfers, with the intermediary products UO_2^{+}

and HO_2. However, this mechanism was disproved by Gordon and Taube, who pointed out that such a mechanism would result in 0.5–0.6 oxygens in $UO_2{}^{2+}$ deriving from the O_2 gas, rather than the 1.0 observed from their isotopic tracer studies.

Fallab [23] proposed a direct two-electron process that is compatible with Gordon and Taube's tracer studies involving the formation of a uranium–oxygen adduct:

$$\begin{aligned} UOH^{3+} + O_2 &\longrightarrow U(O_2)OH^{3+} \\ U(O_2)OH^{3+} + UOH^{3+} &\longrightarrow 2UO_2{}^{2+} + 2H^+ \end{aligned} \tag{7.2}$$

Shilov et al. [69] proposed a multi-step mechanism involving uranium(IV) hydrolysis, the reaction of both uranium(IV) and uranium(V) with oxygen, and the dissociation of uranium(V). Their experiments were conducted in the pH range 1.5–7.4, however, and so likely do not apply to the present work.

Explanations for the effect of sulfate on the oxidation kinetics are less robust and fraught with speculation. Sobkowski [71] proposed that the presence of sulfate slows the oxidation kinetics because uranium(IV) forms strong sulfate complexes which compete with the hydrolysis reaction, thus reducing the amount of UOH^{3+} available to be oxidized. In their study on photoelectrical properties of uranium(V) [70], the authors also advanced a theory that the presence of sulfate promotes the disproportionation of uranium(V), thus interrupting the oxidation reaction chain and consequently slowing the oxidation reaction.

Elliot et al. [22] found that introducing 2-propanol as a radical scavenger made the reaction rate faster in sulfuric acid, implying that free radicals, such as the hydroxyl radical, are involved in the mechanism. They proposed a complex mechanism involving a free-radical chain sequence that applies to the sulfate system at pH 0.7.

7.2.5 Other related studies

Sobkowski [70] showed that exposure to light from a tungsten lamp causes the redox potential of uranium(IV)/uranium(VI) to fall, corresponding to the photoreduction of uranium(VI) to uranium(V). They also observed that UV light has a significant effect on the kinetics of oxidation by oxygen gas [71].

Lotnik, Khamidullina, Kazakov, published a series of papers on the chemilumi-

nescence produced during the oxidation of uranium(IV) with molecular oxygen in perchloric acid [43, 44, 50, 51]. The authors were only able to detect chemilluminescence in <0.1 N perchloric acid, and not at all in sulfuric acid. They proposed that the oxidation of UO_2^+ to UO_2^{2+} is the luminescent step, with the electron-excited $(UO_2^{2+})^*$ being the chemiluminescent emitter. The authors followed the kinetics of the reaction using light intensity as a proxy for concentration, apparently without ever measuring uranium(IV) concentration directly, so it is difficult to know whether their conclusions on the reaction kinetics are valid. They found that the oxidation kinetics depend heavily on the surface area of glass packing in contact with the solution, which they explained as the heterogeneous decay of radicals at the solid-liquid interface. They also found that UO_2^{2+} catalyzes the reaction, possibly due to a shift in the uranium(V) dissociation reaction. They noted that it takes some time to reach the maximum light emission, suggesting that the maximum rate of UO_2^{2+} generation does not occur at the time of maximum U^{4+} removal (the beginning of the reaction), which is indicative of consecutive reactions.

7.3 Experimental

Twenty oxidation tests were conducted in perchloric acid under varying conditions of acid concentration, oxygen partial pressure, temperature, total uranium concentration, and sulfate concentration. Four additional tests were run in sulfuric acid. All tests were conducted in a jacketed 500 mL glass reactor with a five-port glass lid. A titanium gas-shearing impeller rotating at 700 rpm was used to both mix the solution and disperse the gas. Gas was injected through a fritted glass lance positioned directly below the impeller. A schematic of the setup is shown in Fig. 7.1. The test parameters are given in Table 7.1. A blank copy of the operational worksheet and checklist that was completed for each test is given in Appendix E.

7.3.1 Solution preparation

The uranium used to create all test solutions came from unenriched reactor-grade UO_3 from Cameco Corporation's Blind River Refinery in Blind River, Ontario, Canada. The oven-dried UO_3 assayed 82.5 % uranium (theoretical value 83.2 %), and ICP analysis confirmed that no trace metals were present (<3.2 $\mu g\, g^{-1}$ Ag, Al,

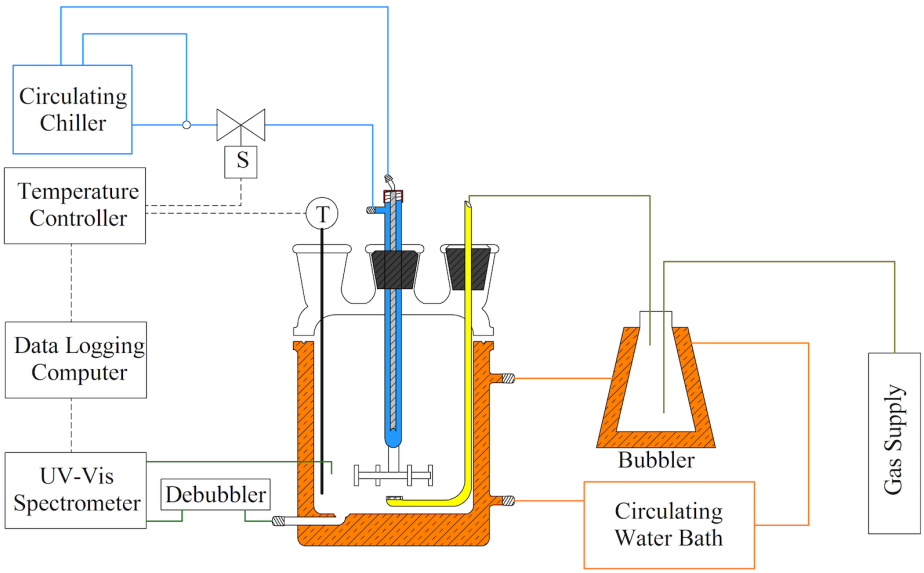

Figure 7.1: Schematic of oxidation study experimental setup

As, Ba, Be, Cd, Co, Cr, Cs, Cu, Fe, Ga, Mn, Mo, Ni, Pb, Rb, Se, Sr, Tl, V, Zn).

The stock uranium(IV) solutions were prepared differently depending on whether the oxidation studies were to be conducted in perchloric acid (tests 1–20) or sulfuric acid (21–24). For tests 1–20, to ensure the solutions were free from all impurities, the UO_3 was dissolved in dilute perchloric acid, precipitated as uranyl peroxide by hydrogen peroxide addition, and then filtered and washed thoroughly with deionized water. The precipitate was then redissolved in hot 2.0 mol L^{-1} perchloric acid to create a pure uranium(VI) stock solution. For tests 21–24, the uranium was purified by dissolving UO_3 in sulfuric acid, precipitating it as uranous sulfate by applying heat, and then redissolving the precipitate in sulfuric acid. The purified solutions were then reduced in several batches by electrolytic reduction in a two-electrode membrane cell according to the procedure outlined in Appendix A. Each batch was assayed for uranium(IV), total uranium, and free acid, and was stored under a nitrogen atmosphere in a Sigma Aldrich Sure/Stor air-free storage flask until needed.

The test solutions for each experiment were made as needed by diluting the re-

Table 7.1: Test conditions for the oxidation studies. All studies were conducted in perchloric acid, except tests 21–24, which were conducted in sulfuric acid.

Test #	$[U_T]$, mol L^{-1}	$[H^+]$, N	Temp., °C	Gas	$[SO_4^{2-}]_T$, mol L^{-1}
1	0.01	0.08	30.0	Oxygen	-
2	0.01	0.09	30.0	Oxygen	-
3	0.01	0.20	30.0	Oxygen	-
4	0.01	0.31	30.0	Oxygen	-
5	0.01	0.30	30.0	Oxygen	-
6	0.01	0.39	30.0	Oxygen	-
7	0.01	0.49	30.0	Oxygen	-
8	0.01	0.50	30.0	Oxygen	-
9	0.01	0.75	30.0	Oxygen	-
10	0.007	0.50	30.0	Oxygen	-
11	0.014	0.51	30.0	Oxygen	-
12	0.01	0.50	39.9	Oxygen	-
13	0.01	0.50	49.9	Oxygen	-
14	0.01	0.10	30.0	Air	-
15	0.01	0.49	30.0	Air	-
16	0.01	0.20	30.0	Oxygen	0.00095
17	0.01	0.20	30.0	Oxygen	0.0095
18	0.01	0.20	30.0	Oxygen	0.095
19	0.01	0.30	27.8	Oxygen	0.054
20	0.01	0.30	30.0	Oxygen	0.101
21–24†	0.01	0.51	30.3	Oxygen	0.272

† sulfuric acid

quired reagents in a 500 mL volumetric flask while purging the headspace of the flask with inert gas to minimize oxidation during mixing. For tests 1–20, acidity was adjusted with 60 % perchloric acid, which was first diluted to 2.0 mol L^{-1} and standardized by titration with standard sodium hydroxide. For tests 21–24, acidity was adjusted with concentrated sulfuric acid similarly diluted and standardized. The compositions of all test solutions were validated by chemical analysis, and in all cases agreed well with the theoretical dilution values.

7.3.2 Continuous monitoring of uranium(IV) concentration by UV-Vis spectroscopy

The uranium(IV) concentration was monitored continuously *in situ* using a Perkin-Elmer Lambda 35 UV-Vis spectrometer connected to a flow-through cuvette and continuous sampling pump. Using this method provided immediate feedback throughout the experiment, and also eliminated some of the problems associated with the more traditional technique of periodic sampling, such as sample decay by continued oxidation. So many data points were collected that the concentration vs. time curves could be considered continuous functions, which allowed for numerical differentiation techniques[1] to be applied to calculate the instantaneous reaction rate at any point during a test.

Solution was continuously drawn from a sampling port at the bottom of the reactor using a peristaltic pump, passed through a debubbler to remove any entrained gas bubbles, and then pumped through a 2 cm quartz flow-through cuvette inside the spectrometer. A software interface to the spectrometer recorded the absorbance of the solution at 650.9 nm once per second (less frequently for long tests). The sampling system had a total holdup volume of 5 mL and a flow rate of 21 mL min^{-1}, which was deemed adequate for providing a representative sample of the contents of the reactor at any given time without skewing the kinetics by withholding a large amount of solution from exposure to oxygen.

Before each experiment, a calibration curve was generated relating absorbance at 650.9 nm to uranium(IV) concentration using six standard solutions, ranging from 0.001–0.01 mol L^{-1} uranium(IV). The standards were matrix-matched to the test solution, and were prepared fresh for each experiment. The composition of the uranium(IV) stock solution used to prepare the standards was validated by titration every day. The standards were temperature-controlled in a water bath set to the same temperature of the test to account for the effect of temperature on absorbance.

7.3.3 Gas injection

99.5 % oxygen gas or breathing-grade air was supplied from a compressed gas cylinder through a fritted glass lance positioned just below a gas-shearing impeller. Be-

[1] Numerical differentiation was performed using the Python package NUMDIFFTOOLS [9].

fore entering the reactor, the dry gas was saturated with water vapour by bubbling it through a magnesium sulfate solution at the same temperature and ionic strength as the test solution in order to prevent evaporative losses. Flow was controlled using an Aalborg flow tube meter set to 2900 std mL min^{-1} (oxygen) or 4100 std mL min^{-1} (air). Before the commencement of each test, the reactor was continuously purged with water-saturated nitrogen in order to prevent premature oxidation from infiltrate air.

7.3.4 Temperature monitoring and control

The temperature of the solution was controlled using a heated circulating water bath connected to the jacketed reactor. The temperature was continuously monitored and recorded using a PTFE-coated RTD probe and an Omega logging temperature controller connected to a computer. The temperature probe was calibrated against deionized ice water (0 °C) and boiling water (100 °C).

During preliminary tests, it was found that the solution temperature often increased by 2 °C or more over the course of an experiment. This may have been due to the exothermic nature of the reaction, or the heat generated by the aggressive agitation. In any case, such variation in the temperature was deemed unacceptable for the accurate study of kinetics. In order to gain finer control over the temperature, a glass "cooling finger" was immersed in the solution. The temperature controller was set to open and close a solenoid valve as needed, pulsing 12 °C water through the finger, on an as-needed basis. Temperature control of ± 0.1 °C was achieved by using both the cooling finger and the water jacket together.

7.4 Validation of experimental method

7.4.1 UV-Vis spectroscopy

Scans from 200–1350 nm showed that uranium(IV) has several strong absorbance peaks in the 350–700 nm spectral range in both perchloric and sulfuric acids, with the two strong peaks centered around 547.7 nm and 648.9 nm both free from interference from uranium(VI) (Figs. 7.2 and 7.3). A position near the top of the strongest peak, at 650.9 nm, was chosen for continuous monitoring in both systems.

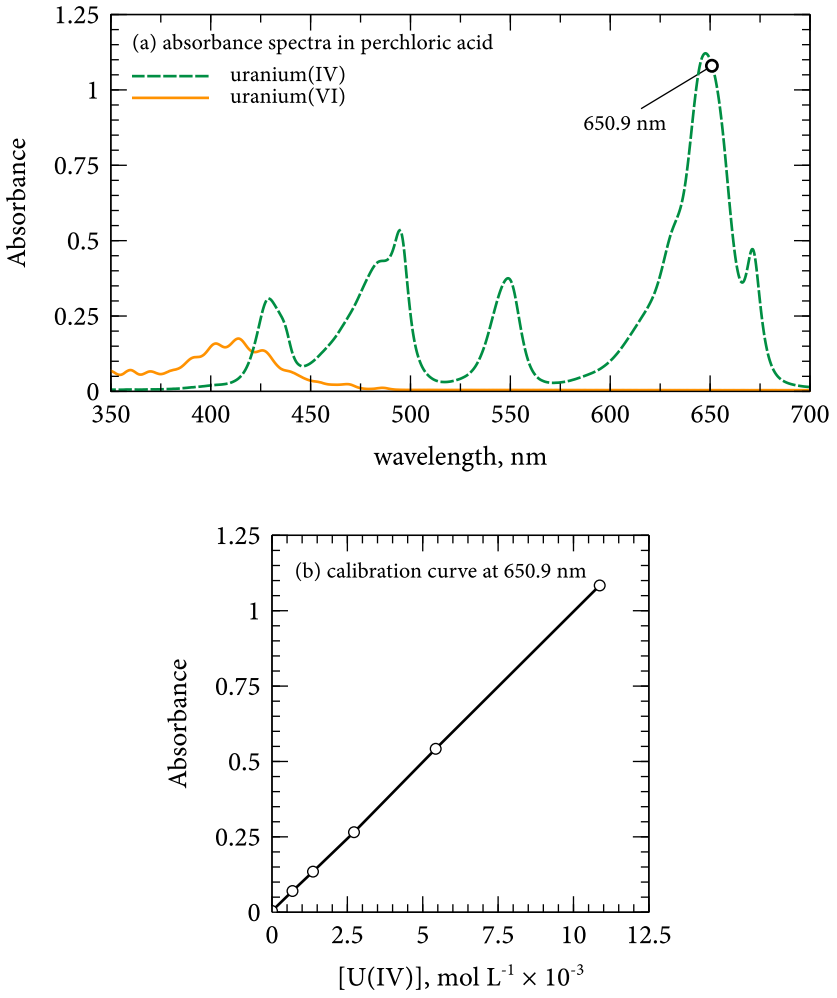

Figure 7.2: UV-Vis spectra in 0.3 N perchloric acid, 30°C, quartz cell, 2 cm path length, deionized water as background reference. (a) UV-Vis spectra for 0.01 mol/L uranium(IV) or uranium(VI); (b) absorbance vs. uranium(IV) concentration at 650.9 nm.

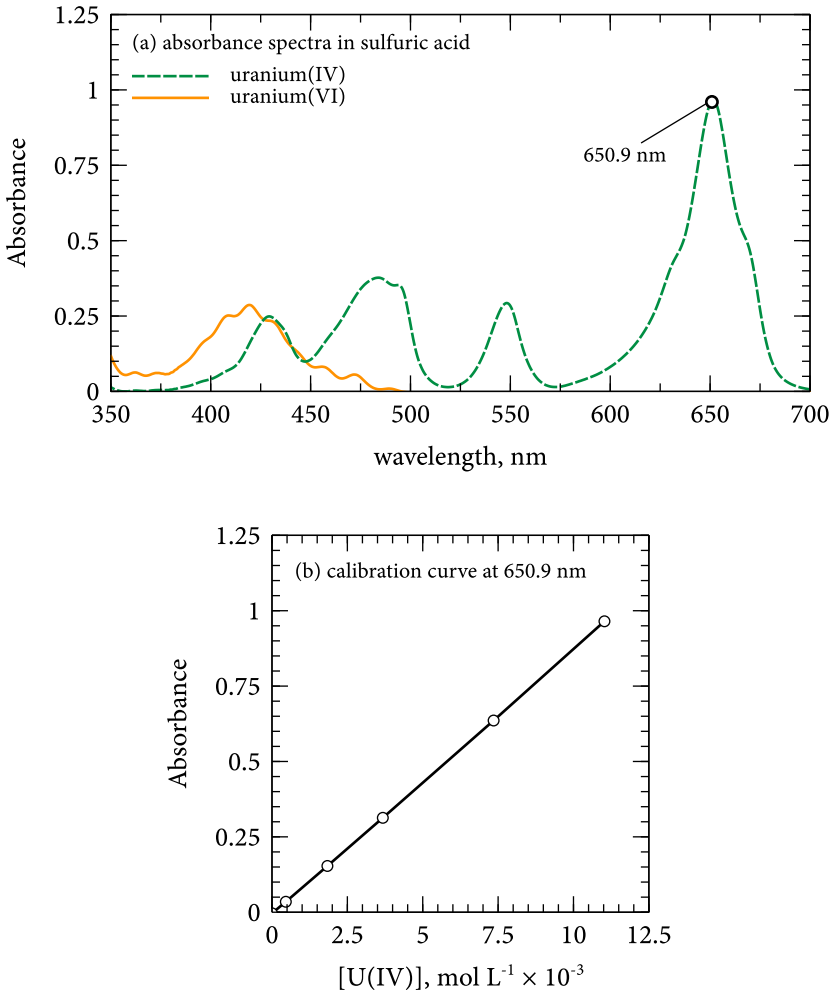

Figure 7.3: UV-Vis spectra in 0.5 N sulfuric acid, 30°C, quartz cell, 2 cm path length, deionized water as background reference. (a) UV-Vis spectra for 0.01 mol/L uranium(IV) or uranium(VI); (b) absorbance vs. uranium(IV) concentration at 650.9 nm.

The relationship between absorbance and concentration at 650.9 nm was found to be linear in the range 0.001–0.01 mol L^{-1} in both perchloric and sulfuric acids, regardless of acid concentration, which made it possible to calculate the uranium(IV) concentration of a solution directly from absorbance measurements using Beer's Law:

$$A = e\ell c \tag{7.3}$$

where A is the measured absorbance, ℓ is the path length, e is the extinction coefficient, and c is the concentration. The value of e was calculated from the straight-line fit of the calibration curve constructed from measurements on standard solutions.

The oxidation of one mole of uranium(IV) by oxygen gas produces two moles of H^+ (see Eq. (7.1)), which caused the acidity of the test solutions to increase slightly over the course of an experiment. Absorbance spectra are often affected by pH, so even this minor increase in acid could invalidate a calibration curve to convert absorbance to concentration. Figure 7.4 shows that there is a positive relationship between the extinction coefficient, e, and perchloric acid concentration, with a particularly strong effect at low acid. This introduced a systematic error into every experiment, with the magnitude of the error growing as H^+ was generated. Based on the relationship shown in Fig. 7.4 for a test containing 0.01 mol L^{-1} uranium and $\geq$0.2 N acid, the corresponding increase in H^+ of 0.02 mol L^{-1} would result in a measurement error of about 1 % at completion, and proportionally less than that earlier in the oxidation process. This error was deemed minor enough to be accepted within standard experimental error.

The method of monitoring uranium(IV) concentration using UV-vis spectroscopy was validated during test 23 by periodically withdrawing samples from the reactor and immediately titrating them for uranium(IV), with the results shown in Table 7.2. The error was within 1 % for the first three samples, and showed bias consistent with the continued oxidation of the sample between the time of sampling and the time of analysis. The error on the last sample, however, was 17 %. This sample was taken five hours into the test after more than 80 % of the uranium(IV) had oxidized. Some of the error can be explained by the inherently lower accuracy of a titration when titrating for small amounts, and also by the magnifying effect of calculating error on small values. Signal drift in the spectrometer's zero-

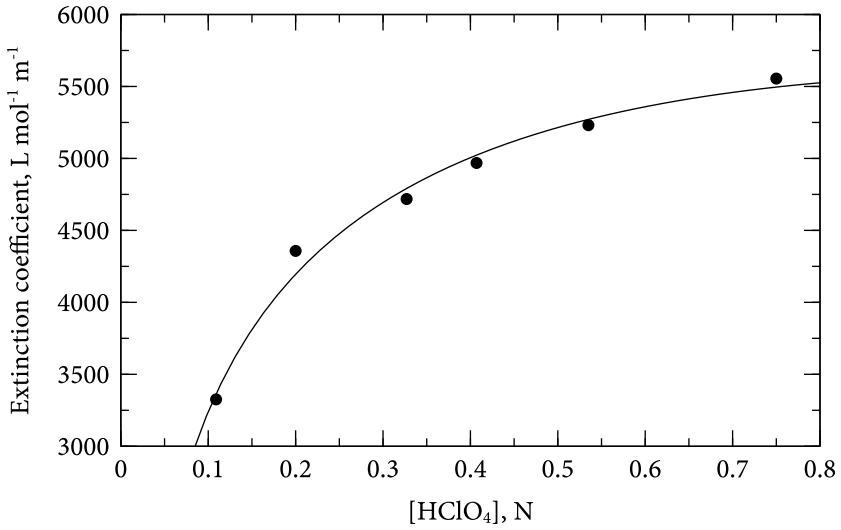

Figure 7.4: The change in extinction coefficient observed with increasing perchloric acid concentration, for uranium(IV) at 30 °C.

baseline over the long time span of the test could also have introduced error, as could the inherently higher error associated with measuring low absorbances. Whatever the cause, it was clear that measurements at low absorbance or after a substantial amount of time had elapsed since calibration were less accurate than those made at higher absorbance or soon after calibration. For this reason, only data collected above 0.0025 mol L^{-1} were used in the present analysis. This was not detrimental to the quality of the results, however, since it still allowed for the collection of thousands of data points per test spanning a four-fold drop in concentration.

Table 7.2: Comparison of uranium(IV) assays by titration and continuous UV-Vis spectroscopy on samples withdrawn from the reactor during test 23.

Elapsed	[U(IV)], mol L^{-1}		Error	
time, min	Titration	UV-Vis	mol L^{-1}	Percent
0	0.01	0.01	+0.0000	0.30%
77	0.0075	0.0076	+0.0001	0.80%
190	0.0042	0.0042	+0.0000	0.20%
304	0.0017	0.0014	-0.0003	-17.00%

7.4.2 Gas flow rate and stirring speed

The fastest observed oxidation rate of any test was 8.5×10^{-6} mol L^{-1} s, which occurred at the beginning of test 1. Assuming stoichiometric oxygen consumption and a reactor volume of 0.5 L, this amounted to an O_2 consumption of 2.1×10^{-6} mol s^{-1}, or ~2.9 mL min^{-1}. Oxygen was injected at 2900 mL min^{-1}, or 1000 times the maximum consumption rate. No change in the oxidation rate was observed when reducing the gas flow rate by 50 %, confirming that enough gas was being supplied to ensure oxygen saturation.

No decrease in reaction rate was observed with a 50 % reduction in stirring rate, from 700 rpm to 350 rpm, confirming that the reactor was well-mixed and that the oxygen bubbles were being adequately dispersed.

7.4.3 Evaporative losses

The dry gas was pre-saturated with water vapour in order to prevent evaporation of the test solution. To test the effectiveness of this method, nitrogen was bubbled through the reactor at 2900 std mL s^{-1} for 2.5 h while monitoring the uranium(IV) concentration by UV-Vis spectroscopy. As can be seen in Fig. 7.5, [U(IV)] remained stable throughout the test, neither increasing (from evaporation) or decreasing substantially (from oxidation), confirming that the practice of pre-saturating the gas with water vapour with a bubbler was effective. The very slight decrease over the 150 min duration of the test amounted to approximately 0.4 % and was deemed to be acceptable within experimental error.

7.4.4 Reproducibility

Several tests were repeated in order to confirm the reproducibility of the results. In perchloric acid, the repeated tests 1 and 2, 4 and 5, and 7 and 8 all gave near-identical results. In sulfuric acid, however, repeated tests 21–24 gave widely different results. This will be discussed later in the chapter.

7.5 Rate equation methodology

The rate of uranium(IV) oxidation could be affected by several parameters, including uranium(IV) concentration, $[H^+]$, oxygen partial pressure, uranium(VI) con-

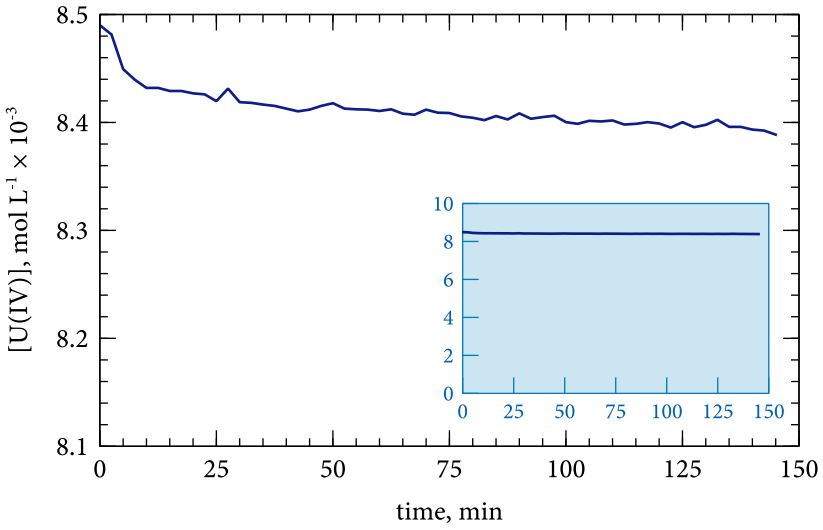

Figure 7.5: The stability of uranium(IV) over time during the bubbling of water-saturated nitrogen. Main graph: exaggerated y-axis, showing a very slight decline in concentration over time; Inset: full range.

centration, and temperature. The following generalized overall rate law is therefore proposed as a basis for analyzing and interpreting the oxidation kinetics[2]:

$$-\frac{d[\mathrm{U(IV)}]}{dt} = k[\mathrm{U(IV)}]^a[\mathrm{H^+}]^b(p_{\mathrm{O_2}})^c[\mathrm{U(VI)}]^d \qquad k = A\exp\left(-\frac{E_a}{RT}\right) \tag{7.4}$$

In this model, the reaction rate is an exponential function of the various concentrations or partial pressures (a, b, c, and d), and follows an Arrhenius relationship with temperature. This leads to the concept of a *reaction order*. For example, if $a = 1$, the reaction is said to be *first order in uranium(IV)*, and if $b = -2$, the reaction is said to be *inverse-second-order in* H^+.

[2]The general rate equation shown in Eq. (7.4) includes separate terms for uranium(IV) and uranium(VI), even through the two are related through a constant representing total uranium, $[\mathrm{U(VI)}] = [\mathrm{U_T}] - [\mathrm{U(IV)}]$. Applying this substitution removes a degree of freedom from the equation, thus technically making it mathematically simpler. Nevertheless, uranium(VI) is a distinct entity in solution, and removing it from the rate equation using a stoichiometric link obscures the fundamental understanding of the oxidation rate with respect to the two distinct forms of aqueous uranium. It also make it more difficult to isolate uranium(IV) for the graphical interpretation of kinetic data. Given that the uranium(VI) concentration is trivial to calculate, the stoichiometric simplification has not been applied here.

The general rate equation shown in Eq. (7.4) can be rearranged such that all of the parameters except [U(IV)] are lumped into the *apparent rate constant*, k'. This gives the following equation:

$$-\frac{d[\mathrm{U(IV)}]}{dt} = k'[\mathrm{U(IV)}]^a \qquad\qquad k' = k[\mathrm{H^+}]^b(p_{\mathrm{O_2}})^c[\mathrm{U(VI)}]^d \tag{7.5}$$

Each of the parameters shown in Eq. (7.5) can be resolved by measuring the oxidation rate across several tests where one parameter is varied while every other parameter is held constant. For $p_{\mathrm{O_2}}$ this is straightforward, and can be accomplished by varying the composition of the gas sparged into the reactor. $\mathrm{H^+}$ is similarly straightforward, if it is assumed that the acidity is constant throughout a given test. This is not strictly true, as examination of Eq. (7.1) shows that two moles of $\mathrm{H^+}$ are generated per mole of uranium(IV) oxidized. However, if the amount of acid initially in the test solution is much greater than the amount generated, the effect should be small. The effects of uranium(IV) and uranium(VI) are more difficult to examine independently, given that both are in flux throughout a test. It is therefore essential that comparisons between different tests are only made at a point where the concentrations of uranium(IV) and of uranium(VI) match.

This technique can be demonstrated using $\mathrm{H^+}$ as an example. In this case, ξ is the lumped parameter incorporating the effects of everything except $\mathrm{H^+}$. Providing that a point of identical uranium(VI) and uranium(IV) is selected for comparing the rates of different tests, ξ should be a constant when comparing tests at different $[\mathrm{H^+}]$. Taking the logarithm of both sides of Eq. (7.5) and rearranging to separate out the constant ξ yields Eq. (7.6):

$$\begin{aligned} \xi &= k(p_{\mathrm{O_2}})^c[\mathrm{U(VI)}]^d = \text{constant} \\ \ln k' &= b\ln[\mathrm{H^+}] + \ln\xi \end{aligned} \tag{7.6}$$

If the apparent rate constants k' for several tests at different $[\mathrm{H^+}]$ are plotted against $[\mathrm{H^+}]$ on a log-log scale, the resulting data should be linear, where the slope is b, the reaction order in acid. The same procedure can be repeated for a series of tests varying $p_{\mathrm{O_2}}$ to get the reaction order c in oxygen.

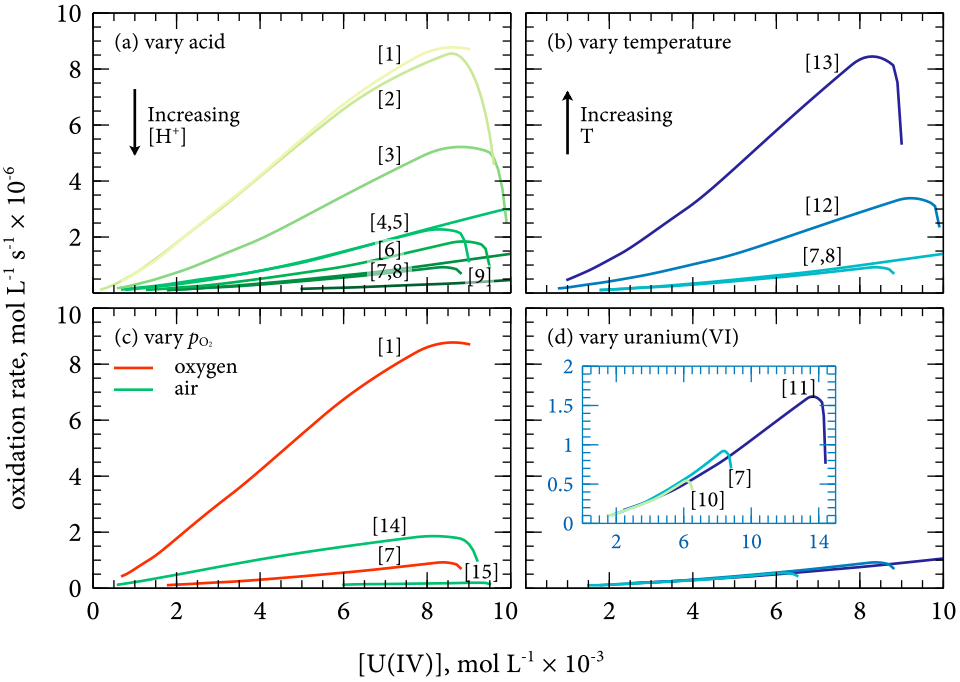

Figure 7.6: Oxidation rate vs. concentration plots for tests 1-15, illustrating the effect of (a) $[H^+]$, (b) temperature, (c) p_{O_2}, and (d) [U(VI)], inset: scaled axes. Test number shown in square brackets. Refer to Table 7.1 for test conditions.

7.6 Results and discussion: oxidation in perchloric acid

Plots of the oxidation rate vs. uranium(IV) concentration for tests 1–15 are shown in Fig. 7.6. These plots show clear trends with respect to H^+, oxygen partial pressure, and temperature, indicating that all three are involved in the rate law. These data can be used to determine the reaction orders in uranium(IV), H^+, p_{O_2}, and uranium(VI).

7.6.1 Reaction order in uranium(VI)

To determine the reaction order with respect to uranium(VI), d, several tests were run at 30 °C with oxygen gas, but with total uranium concentrations of 0.007 (test 10), 0.01 (test 7), and 0.014 (test 11) mol L^{-1}. This had the effect of introducing a

different ratio of uranium(VI) to uranium(IV) at equivalent points of uranium(IV) concentration (at 0.005 mol L^{-1} uranium(IV), this amounted to a VI to IV ratio of 0.4, 1.0, and 1.8, respectively). The oxidation rates for these tests are shown in Fig. 7.6d.

On the main graph shown in Fig. 7.6d, the oxidation rates appear to overlap closely, regardless of uranium(VI) concentration. When the graph is scaled to better show the differences (Fig. 7.6d inset), the rates still appear to overlap quite closely, and do not show a particular trend with respect to increasing uranium(VI). It is clear, then, that [U(VI)] does not significantly affect the rate of uranium(IV) oxidation under the conditions tested, leading to the conclusion that the reaction is zero-order with respect to uranium(VI) (i.e., $d = 0$).

7.6.2 Reaction order in uranium(IV)

It has been shown that the reaction kinetics are zero-order in uranium(VI). The apparent overall rate constant k' can therefore be considered a constant over the duration of a single test (neglecting the small change in $[H^+]$ caused by acid generation). Since the only kinetically-important parameter that changes throughout a test is the uranium(IV) concentration, the reaction order in uranium(IV), a, can be determined directly from the concentration vs. time data.

The classic technique for determining the reaction order is to integrate the apparent rate equation shown in Eq. (7.5) for various assumed values of a and plot the results, with a linear plot indicating a good fit to the assumed order. Figure 7.7 shows two such plots, for $a = 1$ (ln [U(IV)] vs. time) and $a = 2$ ($[U(IV)]^{-1}$ vs. time), for representative tests at high and low acid. The low-acid test (test 14, 0.1 N) fits a first-order model well. The high-acid test (test 7, 0.5 N), however, fits neither a first-order or a second-order model, falling somewhere in between. All tests with $[H^+] \geq 0.2$ N gave plots where $1 < a < 2$.

The actual value of a could be guessed by solving Eq. (7.5) for various values of $1 < a < 2$, plotting the results, and trying to find a value for a that causes the data to fall in a straight line. Passing judgement on a line's "straightness", however, seems to be a rather subjective exercise, particularly when a is not limited to particular whole-number values. Fortunately, the availability of instantaneous reaction

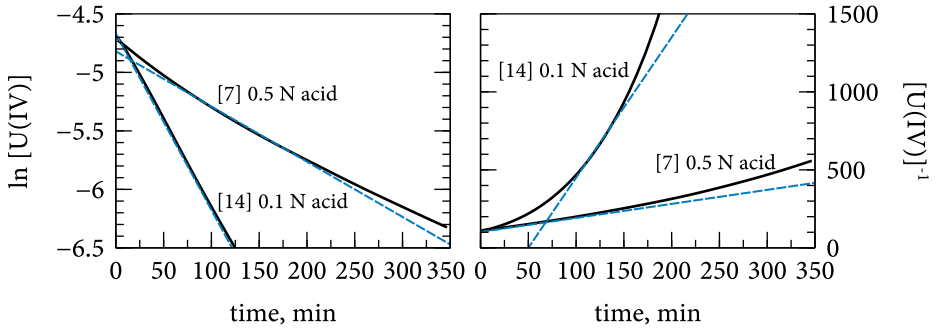

(a) first-order test (b) second-order test

Figure 7.7: First- and second-order rate plots of two tests in perchloric acid. Straight lines indicate that the model applies to the data.

rate data made available an alternate method for determining the reaction order in uranium(IV). Taking the logarithm of both sides of Eq. (7.5) yields Eq. (7.7):

$$\ln\left(-\frac{d[\mathrm{U(IV)}]}{dt}\right) = \ln k' + a\ln[\mathrm{U(IV)}] \tag{7.7}$$

By plotting $\ln(-d[\mathrm{U(IV)}]/dt)$ vs. $\ln[\mathrm{U(IV)}]$, the reaction order a can be determined directly from the slope of the line. These are shown in Fig. 7.8. For tests with $\geq$ 0.2 N acid (Fig. 7.8a), the straight-line fit to the data consistently has a slope very close to 1.5. This suggests an effective 1.5 order relationship in uranium(IV). Tests at ~0.1 N acid, however, appeared to follow first-order kinetics (Fig. 7.8b), agreeing with the straight-line fit to the first-order rate plot seen in Fig. 7.7b. This points to the potential existence of two competing reaction pathways, one dominant at high acid and the other at low acid. Notable in the low-acid tests is the slight negative deviation from the first-order straight line that grows as the reaction progresses. This could be reflective of the small systematic error introduced by the H^+ generated by the oxidation process, which has the effect of slowing the reaction, and is not necessarily a departure from the first-order relationship. The effect of H^+ generation is much less significant in tests with proportionally more acid, hence the absence of the phenomenon in those tests.

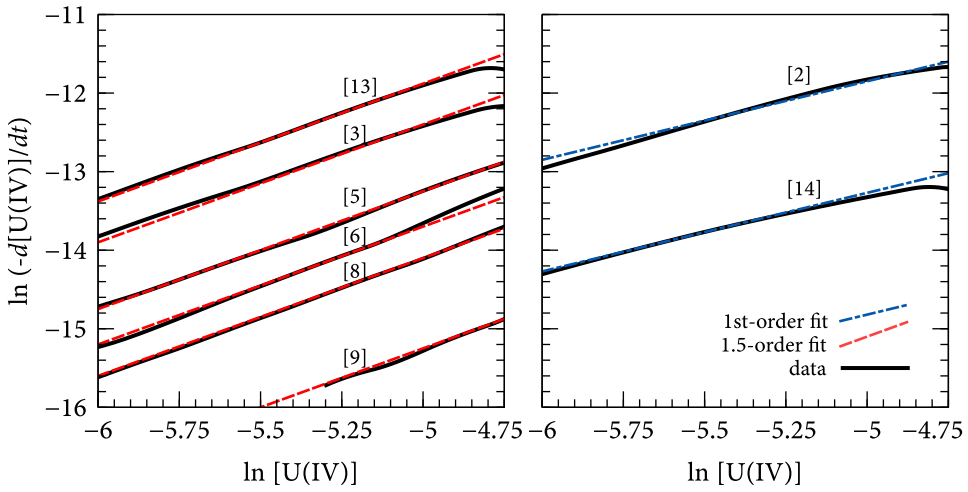

(a) $[H^+] \geq 0.2$ N (b) $[H^+] \approx 0.1$ N

Figure 7.8: ln-ln plots of oxidation rate vs. [U(IV)], with data from a representative selection of tests in perchloric acid. The slope of the line indicates the reaction order.

7.6.3 Reaction order in H^+ and oxygen

The apparent rate constant k' was calculated for each experiment by dividing the instantaneous oxidation rate at [U(IV)] = 0.005 mol L^{-1} (50 % completion for most tests) by $0.005^{1.5}$ (the assumed reaction order a), according to Eq. (7.5). Though the choice of 0.005 mol L^{-1} as the reference point to compare tests is somewhat arbitrary, it is suitable because it is well within the range where the UV-Vis gives accurate results (0.0025–0.01 mol L^{-1}), and it also avoids the "ramp up" period when oxygen gas is still reaching saturation at the beginning of the test.

The reaction order in $[H^+]$, b, was determined by varying $[H^+]$ between 0.1–0.75 N (initial concentration) in a series of tests at 30 °C using oxygen gas. The acid concentrations used in the calculations were based on the assays on the fully-oxidized final solutions, which were then back-calculated to the assumed value at 0.005 mol L^{-1} uranium(IV) to take into account the H^+ generated by the oxidation process. Figure 7.9 shows a plot of $\ln k'$ vs. $\ln [H^+]$. Between 0.2–0.5 N, the relationship is linear with a slope of -1.95, suggesting that inverse second-order kinetics with respect to $[H^+]$ are valid in this region. At 0.75 N, there is some deviation from the

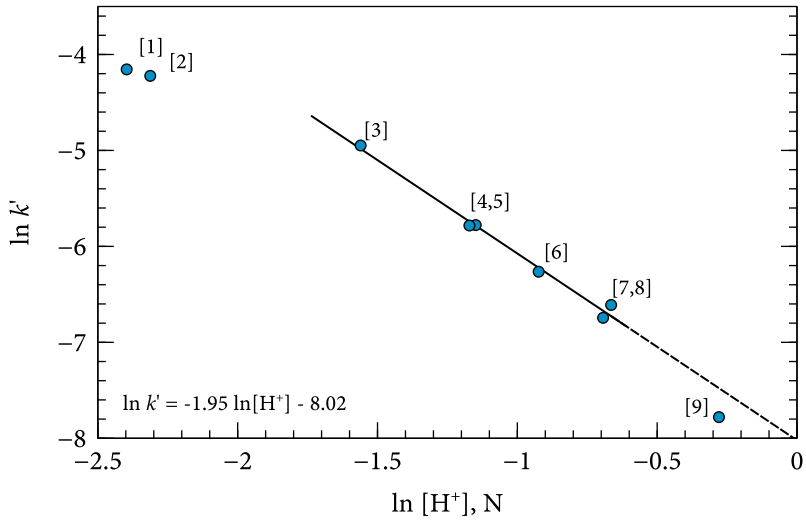

Figure 7.9: The effect of H^+ on the apparent rate constant in perchloric acid, showing the linear region when $[H^+] \geq 0.2$ N.

inverse second-order relationship, although it is not clear whether the deviation is significant. At 0.1 N, the data show a significant departure from the inverse second-order relationship. If the fundamental reaction order in uranium(IV) is different in low acid, however, as was shown earlier, the apparent rate constants cannot be directly compared and thus cannot be expected to fall on the same line.

To determine the reaction order with respect to oxygen, c, the oxygen partial pressure was varied by running tests with oxygen gas (99.5 % O_2) and air (20.9 % O_2). At atmospheric pressure, this corresponds to $p_{O_2} = 0.995$ and 0.209 atm, respectively. Two sets of tests were run: the first set in 0.5 N acid, and the second in 0.1 N acid. In both cases, the oxidation rate was found to be very close to first-order with respect to oxygen partial pressure, as shown in Fig. 7.10.

If these data are plotted on a linear scale instead of a linear scale, a third data point can be added at the origin. This is because the reaction rate was observed to be zero under a nitrogen atmosphere, or $p_{O_2} = 0$. All three points fall on the same line passing through the origin for both the high and low acid conditions.

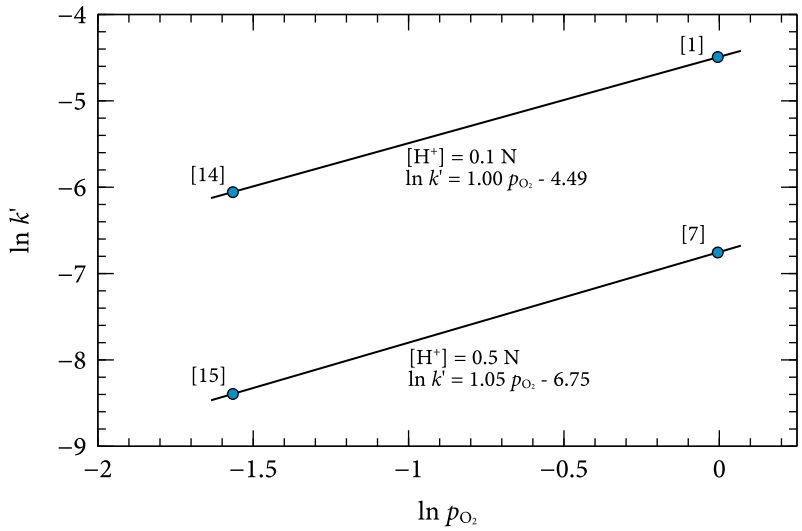

Figure 7.10: The effect of oxygen partial pressure on the apparent rate constant.

7.6.4 The effect of temperature

The effect of temperature on the rate constant was assumed to follow an Arrhenius relationship, $k = A\exp(-E_a/RT)$. Tests at 30 °C, 40 °C, and 50 °C were run in 0.5 N perchloric acid using oxygen gas. The Arrhenius plot of $\ln k'$ vs. $1/T$ is shown in Fig. 7.11. From the plot, the Arrhenius parameters were calculated as E_a = 96,485 J mol^{-1} and $A = 1.25 \times 10^{13}$ mol$^{1.5}$L$^{-1.5}$atm^{-1}s^{-1}, with A calculated from Eq. (7.4) assuming 1.5 order kinetics in uranium(IV), inverse second-order kinetics in H^+, and 0 order kinetics in uranium(VI). This activation energy is consistent with a chemical reaction-controlled mechanism.

7.6.5 Proposed apparent overall rate equation

Based on the analysis above, the apparent overall rate law for the oxidation of uranium(IV) by oxygen gas in perchloric acid when $[H^+] \geq 0.2$ N is as follows:

$$-\frac{d[\mathrm{U(IV)}]}{dt} = k\frac{[\mathrm{U(IV)}]^{1.5}p_{O_2}}{[H^+]^2} \tag{7.8}$$

$$k = 1.25 \times 10^{13}\exp\left(-\frac{9.65 \times 10^4\,\mathrm{J\,mol^{-1}}}{RT}\right)$$

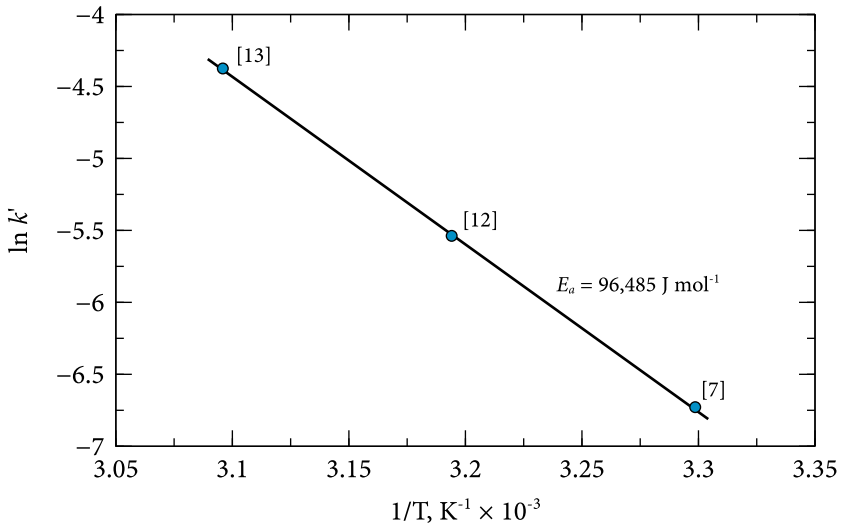

Figure 7.11: Arrhenius plot showing temperature dependence of oxidation kinetics at 0.005 mol L^{-1} uranium(IV), $[H^+]$ = 0.5 N.

In this case, k has the units $mol^{1.5}L^{-1.5}atm^{-1}s^{-1}$. There has been no attempt to take into account or otherwise interpret the underlying elementary reactions that ultimately dictate the overall reaction rate. Not enough data were collected at low acid to draw conclusions on the rate law under those conditions, although the current evidence suggests it is 1st order with respect to uranium(IV).

Figure 7.12 shows a comparison of experimental data to the modelled proposed rate law. For the model, the inputs consisted of the initial operating parameters from each test, as shown in Table 7.1, and took into account the H^+ generated over the course of the reaction. The experimental data are shown time-shifted in order to establish a uniform starting condition. The model appears to give a good fit to the experimental data, accurately predicting the effect of acid, oxygen partial pressure, and temperature. Low-acid samples exhibit substantial deviation from the modelled rate law, as expected given that 1.5-order kinetics were found not to apply at low acid.

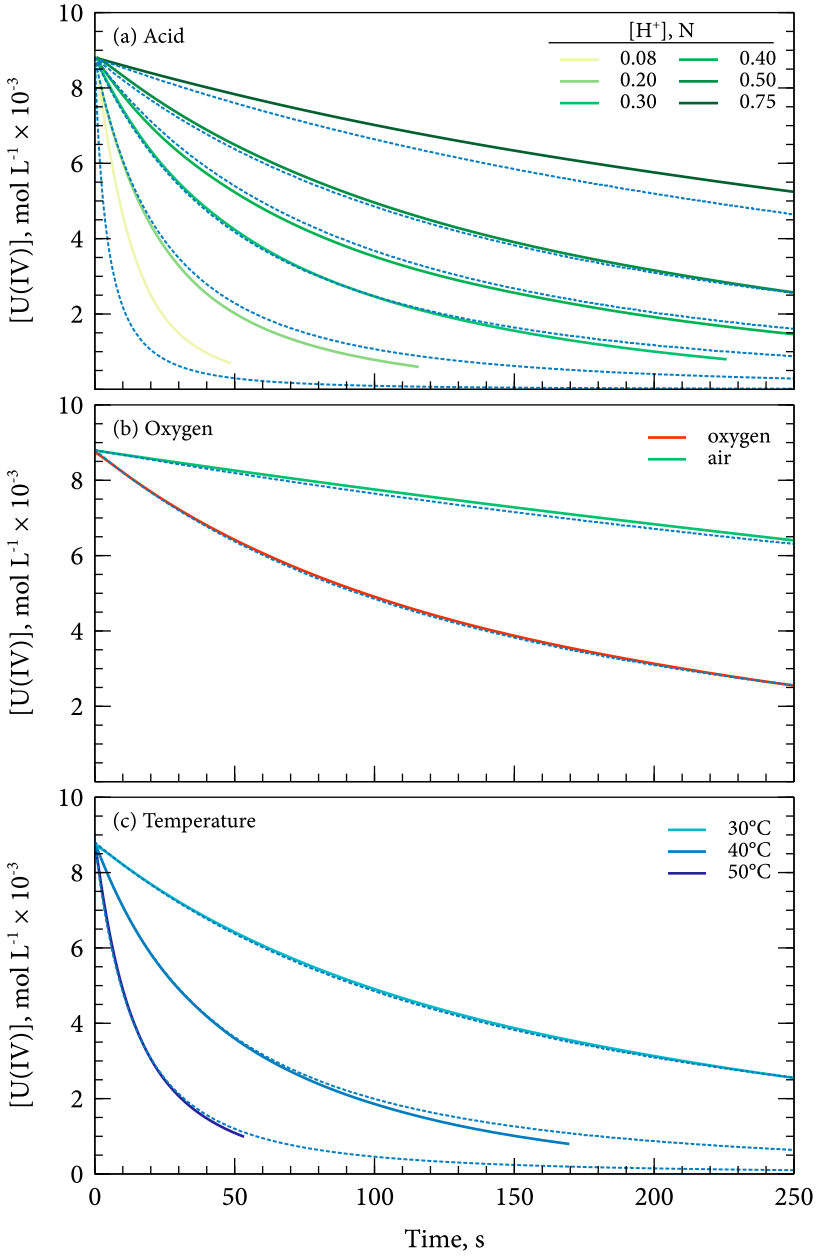

Figure 7.12: Comparison of modelled and experimental data. Model from Eq. (7.8) using initial experimental parameters. Solid lines: experimental data. Dashed lines: simulation results.

7.7 Results and discussion: the effect of sulfate

The oxidation of uranium(IV) in perchloric acid gives a glimpse of the underlying chemistry under simple, non-complexing conditions, but does not represent the reality of an industrial processes. Sulfuric acid would almost certainly be the choice of acid in a real plant design. It would therefore be more useful to understand the oxidation kinetics in sulfuric acid.

Figure 7.13 shows the results from four identical oxidation studies, at 0.5 N sulfuric acid, 30 °C, using oxygen gas. The results from a test in 0.5 N perchloric acid is shown for reference. The sulfuric acid tests were completely unreproducible, with the initial oxidation rate of the fastest case (test 22) approximately 7 times greater than the slowest (test 23). The slopes of the ln-rate vs. ln-concentration plots (Fig. 7.13c) also did not give a consistent reaction order, ranging from a slope of 0.85 in the fastest case (test 22), to nearly zero (i.e., constant rate) in the slowest case (test 23).

No explanation for the unreproducible behaviour in sulfuric acid is forthcoming. The tests used identical equipment, reagent bottles, stock solutions, and procedures, and were even run at the same time of day (starting between 11:00-12:00). Given that the same reagents were used to prepare each test, there was no obvious source of an inhibiting or enhancing spectator ion that would vary between tests. There was no obvious induction period in any of the tests.

To gain some insight into why the tests in sulfuric acid were unreproducible, several tests were run in perchloric acid with sulfate added with sodium sulfate. Figure 7.14 shows the effect of adding sodium sulfate in a 0:1, 5:1, and 10:1 SO_4^{2-}:U molar ratio to tests in 0.3 N perchloric acid. The presence of sulfate caused a dramatic slowdown in kinetics; a 15-fold decrease in initial oxidation rate was observed at the highest sulfate:uranium ratio. More revealing, however, is the change in the apparent reaction order in uranium(IV). Figure 7.14c shows that the apparent reaction order in uranium(IV) (as indicated by the slope of the ln-rate vs. ln-concentration plots) drops from 1.5 in the case of no sulfate, to 0.42 at medium sulfate, to essentially zero at high sulfate. This means that the reaction kinetics become less dependent on uranium(IV) in the presence of sulfate, suggesting a change in the underlying reaction mechanism to a rate-limiting step not directly involving uranium(IV).

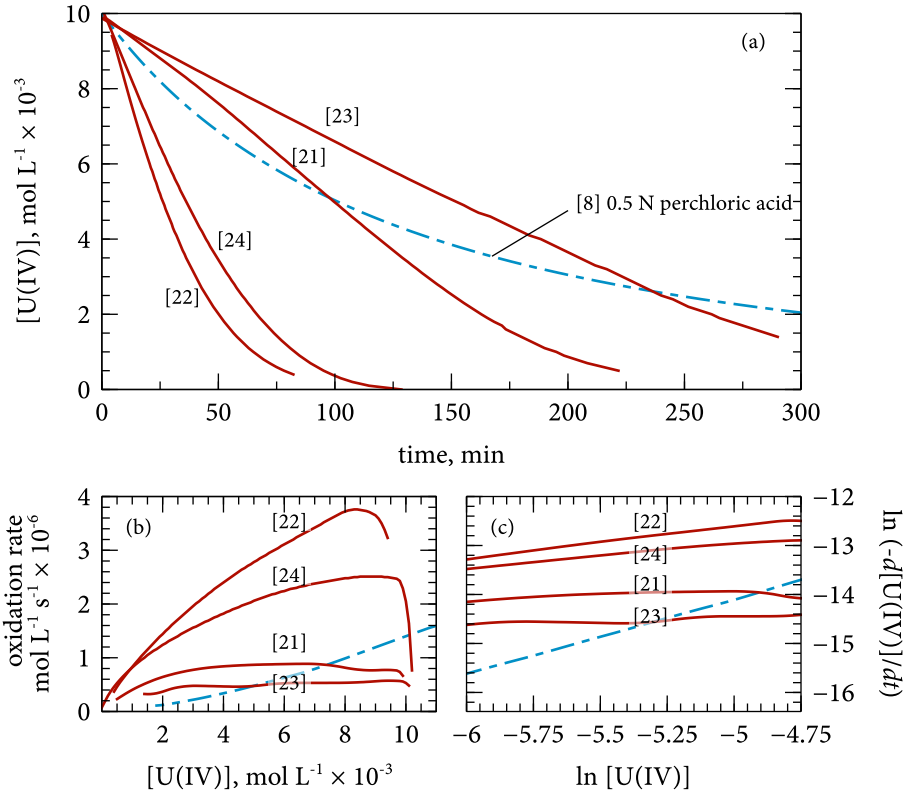

Figure 7.13: Results from four identical oxidation tests in 0.5 N sulfuric acid, 30 °C, oxygen gas, showing non-repeatability. (a): concentration vs. time; (b): rate vs. concentration; (c): ln-ln plot of rate vs. concentration. Dashed line: 0.5 N perchloric acid, for comparison.

Similar tests were conducted at 0.2 N acid, where sodium sulfate was added in various sulfate:uranium ratios, as shown in Fig. 7.15. The addition of sulfate in a 0.1:1 and 1:1 molar ratio with uranium again caused a slowdown in the kinetics, although the reaction order appeared to remain 1.5-order in uranium(IV). At a 10:1 ratio, however, the reaction sped up, and appeared to change to a different underlying mechanism (nominally 0.9-order in uranium(IV) according to the slope of the ln-rate vs. ln-concentration plot).

It would seem, then, that small amounts of sulfate, up to a 1:1 ratio with uranium, cause the kinetics of the oxidation reaction to slow down. This is likely due

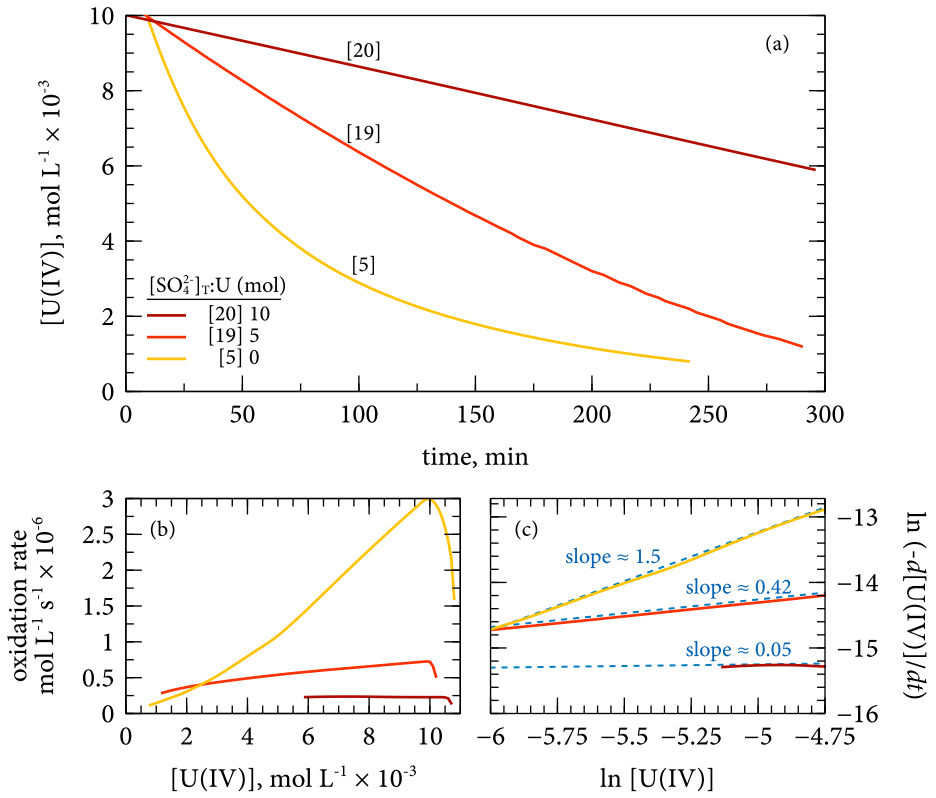

Figure 7.14: The effect of adding sodium sulfate on the oxidation kinetics in 0.3 N perchloric acid. (a): concentration vs. time; (b): rate vs. concentration; (c): ln-ln plot of rate vs. concentration.

the formation of the inactive $U(SO_4)^{2+}$ and $U(SO_4)_{2\ aq}$ species, which effectively reduces the concentration of active UOH^{3+} in solution available to be oxidized. However, as the sulfate:uranium ratio increases to 5:1 or above, the fundamental reaction mechanism appears to change, with a trend towards a constant (i.e., 0-order) reaction rate.

No obvious explanation for the strange kinetic behaviour in the presence of sulfate is forthcoming. Normally, a constant reaction rate could indicate a mass transfer limitation, as might occur if oxygen cannot dissolve and diffuse quickly enough to match the underlying fundamental kinetics. This cannot be the case here, however, because no oxygen mass-transfer limitation was observed in the perchloric

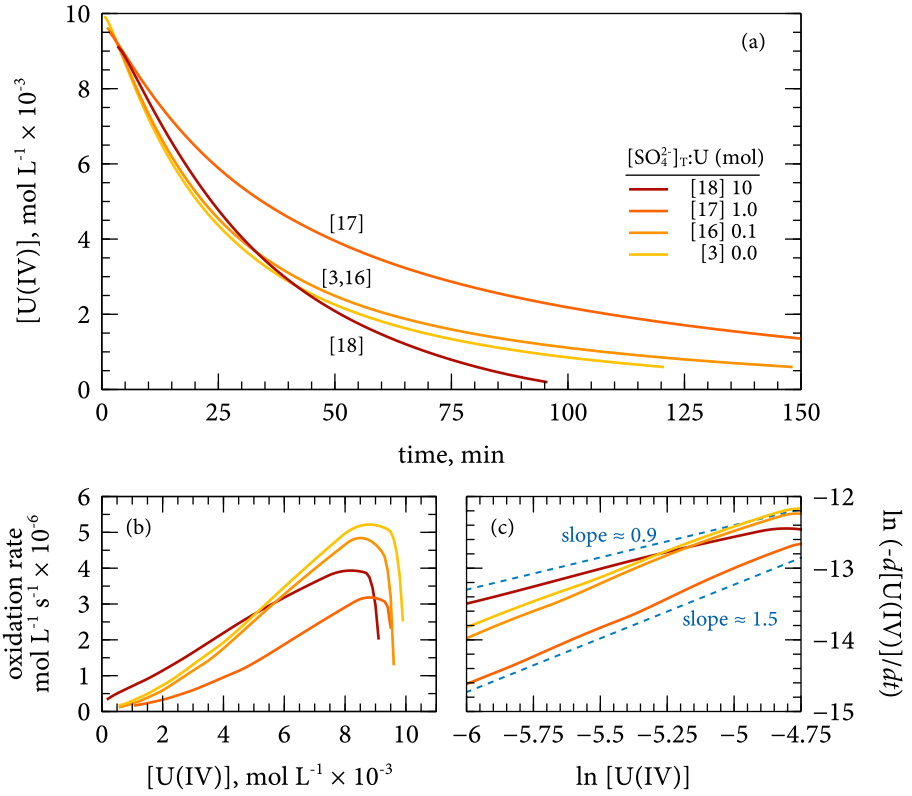

Figure 7.15: The effect of adding sodium sulfate on the oxidation kinetics in 0.2 N perchloric acid. (a): concentration vs. time; (b): rate vs. concentration; (c): ln-ln plot of rate vs. concentration.

acid tests, which were operated under the same conditions. It would seem, then, that the presence of a large amounts of sulfate causes a change in the fundamental underlying reaction mechanism to one independent of uranium(IV) concentration. The unusual non-fractional reaction orders observed in varying amounts of sulfate may indicate the occurrence of two parallel reaction mechanisms, one a 1.5-order reaction involving UOH^{3+} and the other a constant-rate reaction involving $U(SO_4)^{2+}$ or $U(SO_4)_{2\,aq}$.

Further attempts to elucidate the underlying kinetics in sulfuric acid were unsuccessful. The non-repeatability in high-sulfate tests highlighted in Fig. 7.13 made it impossible to objectively compare tests at different acid concentrations and tem-

peratures, so the dependency of the kinetics on acid and temperature could not be established. The non-repeatability in the sulfate system may have indicated advantageous catalysis with an unidentified trace impurity, although the source of such an impurity is unknown given that the same reagents and conditions were used for all of the tests. It could also have been due to an unidentified physical phenomenon, such as differences in the surface conditioning of the titanium impeller, or the formation of a nano-scale intermediary precipitate. However, the good repeatability observed in the perchloric acid system makes these explanations unlikely.

7.8 Conclusions

In the present work, an overall equation to approximate the rate of uranium(IV) oxidation in perchloric acid has been proposed. In the range $[H^+] = 0.2–0.75$ N, it was found that the kinetics follow a 1.5-order relationship with respect to uranium(IV), with the apparent rate constant inversely proportional to the square of $[H^+]$, proportional to oxygen partial pressure, and unaffected by uranium(VI). When $[H^+] \leq 0.1$ N, the underlying mechanism appears to shift towards a first-order relationship in uranium(IV). The results follow the same trends described in work published by other authors [38, 71], but the use of continuous data logging and the application of numerical differentiation in the present work permitted a more detailed study of the kinetics. The fractional exponents in the proposed overall rate law point to a non-elementary, multi-step reaction mechanism possibly involving simultaneous parallel reactions. Further study and analysis is needed, however, before meaningful conclusions on the mechanism can be drawn.

The presence of small amounts of sulfate cause the oxidation rate to decrease, likely due to the preferential formation of uranium(IV) sulfate complexes at the expense of the active species UOH^{3+}. The presence of large amounts of sulfate appears to cause a shift in the underlying reaction mechanism. Substantial variability in the observed kinetics, however, made it impossible to suggest a rate law in the sulfate system.

It may be possible to design conditions under which uranium(IV) is resistant to oxidation by molecular oxygen: namely high-acid and low-temperature. The unpredictable nature of the oxidation kinetics in sulfuric acid, however, as well as the

extremely potent catalytic effect of some cations [38], suggests that it would be unwise to leave a uranium(IV) exposed to air for any length of time in an operating industrial process.

Chapter 8

Demonstration plant

The processes of electrolytic reduction and precipitation of uranous sulfate seems well-suited for consideration as a new hydrometallurgical processing technology. Several authors have demonstrated that the electrolytic reduction of uranyl sulfate solutions proceeds readily, and is a viable method to produce a uranium(IV) solution [6, 28, 55] (not to mention its routine use in the production of uranium(IV) stock solutions for the present work). In Chapter 3, it was shown that uranous sulfate has a low solubility at high temperature and high acid, and that it will precipitate selectively in the presence of Al, Cu, Fe, and Ni. It was also shown that the precipitate takes the form of uranous sulfate tetrahydrate under those conditions. In Chapter 6, it was shown that uranous sulfate tetrahydrate can be converted to $U(SO_4)_2$, UO_2SO_4, or U_3O_8 by thermal decomposition in air, depending on the operating temperature.

Although each of the above steps have been proven individually, a test of the complete process was needed to show its viability as a whole. To achieve this, the process was operated in sequence as a bench-scale demonstration of the technology (or, to take journalistic latitude, a 1.5 microtonne per hour 'demonstration plant', U_3O_8 basis). Starting with a synthetic leach solution containing impurities, the process was taken through electrolytic reduction, acid addition, crystallization of uranous sulfate, filtration, and drying. Thermal decomposition was simulated with TGA analysis on the dried product. The process flow diagram is shown in Fig. 8.1.

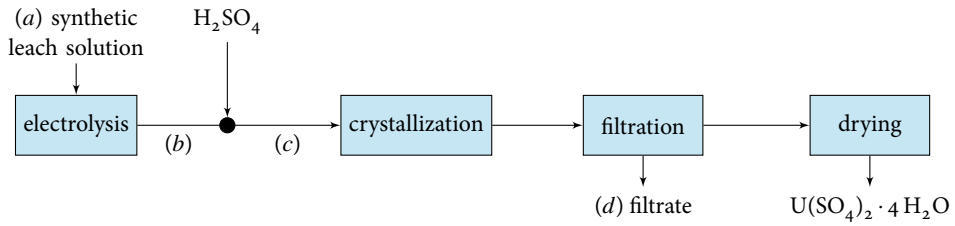

Figure 8.1: Process flow diagram of the demonstration plant

8.1 Experimental setup

8.1.1 Solution preparation

The synthetic leach solution was designed to partly mimic a highly concentrated leach solution that might derive from Saskatchewan's high-grade uranium deposits. Four prominent impurities, Al, Cu, Ni, and Fe, were included, with their concentrations based on an estimate of their prevalence in a high-grade leach solution deriving from a known orebody, as provided by Cameco Corporation. Other less-prevalent impurities, such as As, were not included. The solution was created by dissolving 29.47 g UO_3, 53.12 g $Al_2(SO_5)_3 \cdot 18\,H_2O$, 1.44 g $CuSO_4 \cdot 5\,H_2O$, 12.80 g $FeSO_4 \cdot 7\,H_2O$, 3.40 g $NiSO_4 \cdot 6\,H_2O$, and 45.44 g concentrated sulfuric acid in deionized water and then diluting to 250 mL in a volumetric flask. The resulting solution was filtered to remove the small amount of particulate matter that remained after dissolution of the salts.

The anolyte for electrolysis was prepared by diluting 28.45 g of concentrated sulfuric acid to 200 mL with deionized water in a volumetric flask, matching the free acid of the synthetic leach solution.

A solution for washing the precipitate was prepared by diluting 49.98 g of concentrated sulfuric acid to 250 mL with deionized water in a volumetric flask, matching the expected free acid concentration of the crystallization mother liquor. The wash solution was heated to 90 °C before use.

8.1.2 Equipment and procedure

Electrolytic reduction of the synthetic leach solution was conducted *in situ* in a 100 mL Corning Pyrex No. 1395 bottle using a stainless steel mesh cathode connected to a DC power supply. For the anodic half-cell, a self-contained anolyte chamber with a DSA anode was inserted into the bottle, with a Nafion N117 membrane to allow flow of H^+ between catholyte and anolyte. The superficial single-side cathode and anode surface areas were 1.65 cm^2. The power supply was set to a fixed current of 0.5 A, giving a current density of 3030 $A\,m^{-2}$. The catholyte was stirred with a PTFE-coated magnetic stir bar, and the electrolyzer was immersed in a chilled water bath set to 12 °C in order to keep the temperature low enough to avoid premature precipitation of uranous sulfate.

Precipitation was conducted in the same bottle as electrolysis. After removing the electrolysis apparatus, 10.5 g of concentrated sulfuric acid and 1.0 g of powdered $U(SO_4)_2 \cdot 4\,H_2O$ (63-S, as seed) were added to the bottle, a lid with sampling ports was applied, and the bottle was purged with argon. The sealed bottle was then heated to 90 °C in a water bath placed on top of a magnetic stir plate, and stirred aggressively for 4 hours. Samples of the supernatant were withdrawn for analysis at 0, 1, 2, and 4 hours. The sampling syringes were quenched in ice water to immediately halt the precipitation process, and then samples were filtered through a syringe filter.

After four hours, the hot slurry was filtered over suction on an Osmonics 0.22 µm filter. The supernatant was collected for analysis, then the precipitate was washed twice with the previously-prepared sulfuric acid wash solution at 90 °C, and then twice with isopropanol, until the filtrate ran clear. The solids were allowed to suction-dry for several minutes, and then were transferred to a 60 °C oven in a petri dish for drying overnight.

The dried filter cake was gently broken up into powder with a mortar and pestle, and then transferred to a polypropylene tub for storage. The final sample was analyzed chemically for uranium and sulfate, thermogravimetrically for water, and structurally by XRD.

8.2 Results and analysis

The results from each phase of the demonstration are described below. Chemical assays of the solutions and solids are given in Table 8.1 and Table 8.2, respectively.

8.2.1 Electrolysis

The electrolytic reduction of uranium(VI) to uranium(IV) was effective and straightforward, if not particularly efficient. Figure 8.2 shows the progress of reduction, as well as the cell voltage, over the duration of the test. The progress of reduction was determined by redox titration for uranium(IV) with potassium dichromate. An increase in voltage was observed after approximately 90 min (†), occurring around the same time as a marked increase in hydrogen evolution. The completion of reduction was accompanied by a characteristic increase in cell voltage (*).

The theoretical minimum electrolysis time was 275 min at 100 % current efficiency and a current of 0.5 A, taking into account the reduction of both uranium(VI) and copper(II). In reality, complete reduction was achieved after 443 minutes (as indicated by the midpoint of the voltage increase *), giving an overall current efficiency of 62 %. Judging from the substantial gas generation on the cathode, it would seem that hydrogen evolution was almost entirely responsible for the low efficiency.

The aqueous copper assays suggested that nearly all of the copper was removed by electrolysis. This was not surprising, given that the standard reduction potential for copper (0.340 V) is higher than uranium (0.267 V), and thus should reduce

Table 8.1: Demonstration plant aqueous assays, mol L^{-1}

	U_T	$H_2SO_{4\,free}$	$SO_4{}^{2-}{}_T$	Al	Cu	Fe	Ni
(*a*) Syn. leach sol.	0.405	1.36	3.03	0.638	0.023	0.184	0.052
(*c*) Start of cryst.	0.365	2.17	3.58	0.616	<3.15E-03	0.148	0.046
(*d*) Filtrate	0.101	2.16	3.12	0.632	0.002	0.138	0.047

Table 8.2: Demonstration plant solids assay

Solids assay, mass %						Waters of hydration	XRD Identity
U	SO_4	Al	Cu	Fe	Ni		
47.1%	37.6%	<0.37%	<0.003%	<0.01%	<0.01%	4.23	$U(SO_4)_2 \cdot 4\,H_2O$

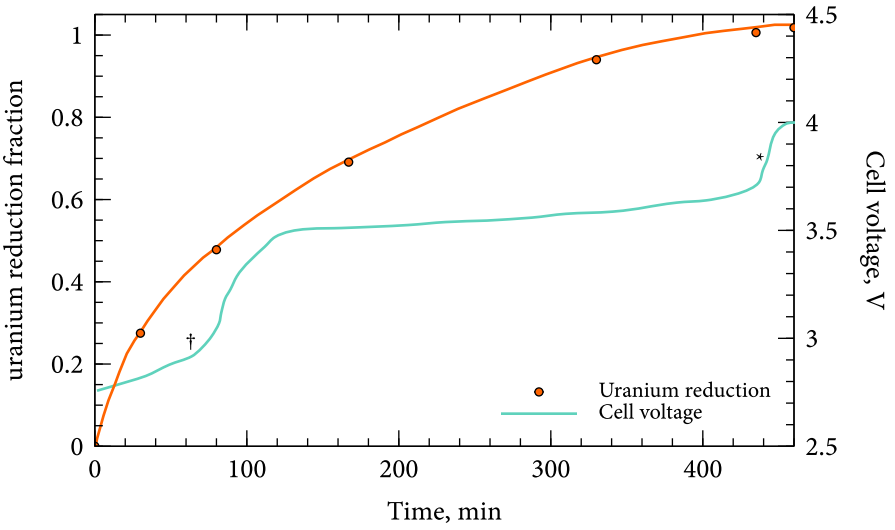

Figure 8.2: Electrolytic reduction of the synthetic leach solution, showing reduction progress (orange) and cell voltage (turquoise). The two notable voltage increase events corresponded with the onset of significant hydrogen evolution (†) and the completion of reduction (*).

first. At the end of the test, the cathode was found to be plated with copper, with a weight gain of 0.1085 g, representing approximately 75 % of the copper in the synthetic leach solution. Aluminum, iron, and nickel were not plated, reflecting their lower reduction potentials, which are all below that of hydrogen evolution. Iron was added to the synthetic leach solution as Fe(II), and so did not consume any current, but in a reality the conversion of Fe(III) to Fe(II) would also be a source of current inefficiency. There was no sign of uranous sulfate precipitate on the cathode or in the cell.

As the hydrogen evolution rate increased, large hydrogen bubbles formed and attached to the cathode surface, masking a portion of the cathode that would have otherwise been in contact with solution, and thus lowering the effective bulk current density. Experience with other electrolysis systems suggests that this could have been solved by improving convective flow in the cell, thereby sweeping the emergent hydrogen bubbles away before they could agglomerate into large bubbles.

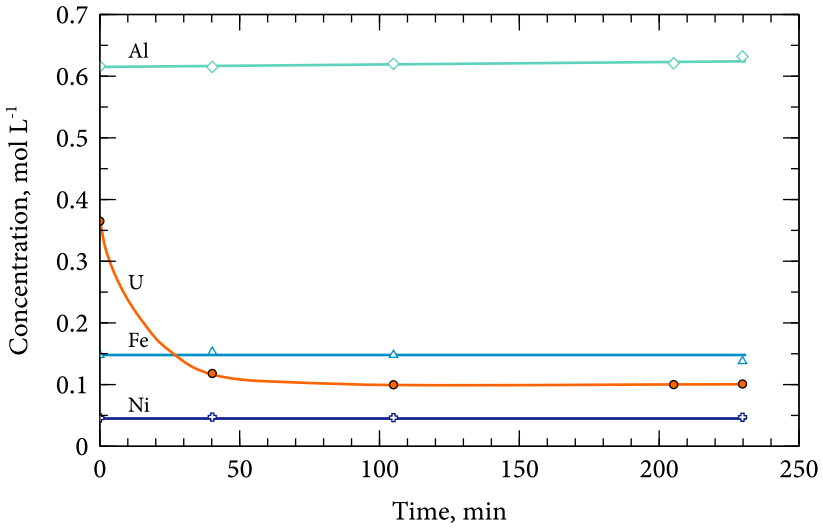

Figure 8.3: Concentrations of U, Al, Fe, and Ni over the course of uranous sulfate precipitation. Cu assays were all below detection limit.

8.2.2 Crystallization

The electrolysed solution was fed directly to the crystallization phase, where it was diluted somewhat by the addition of concentrated sulfuric acid. The resulting uranium concentration of 0.365 mol L^{-1} was about 10 % lower than in the synthetic leach solution. About half of this dilution can be accounted for by sulfuric acid addition, and a small amount by the generation of H_2O by the cathodic reaction, while the rest was likely due to the movement of water across the membrane during electrolysis (Nafion is permeable to water).

The concentrations of uranium, aluminium, iron, and nickel over the course of the 4-hour test are shown in Fig. 8.3. The uranium concentration dropped from 0.365 mol L^{-1} to 0.101 mol L^{-1} in about an hour, representing a recovery of 72.3 %. No change was observed for the remainder of the 4 h test, suggesting that equilibrium had been reached. None of the other metals changed in concentration over the duration of the test. Copper is not shown because it was found to be below the detection limit ($<3.25 \times 10^{-3}$ mol L^{-1}) for all samples.

The final equilibrium uranium concentration of 0.101 mol L^{-1} was substantially higher than predicted by the solubility curves given in Chapter 3 at 90 °C and a

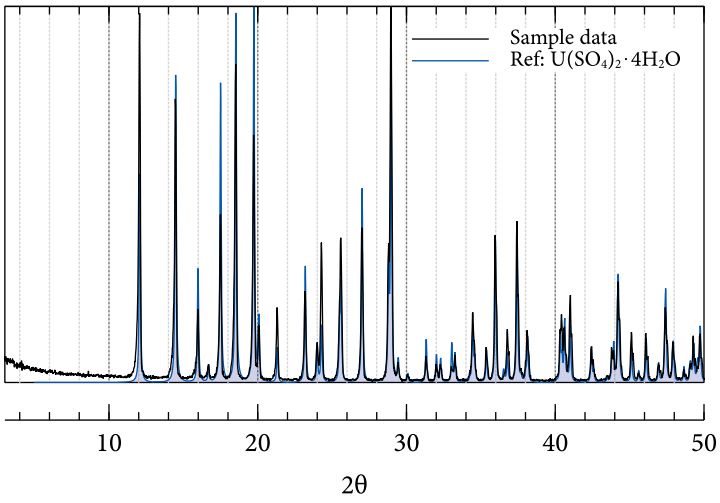

Figure 8.4: XRD pattern for demonstration plant solids, showing a match with $U(SO_4)_2 \cdot 4\,H_2O$.

free sulfuric acid of 2.2 mol L^{-1}. However, it was also shown in Chapter 3 that the presence of impurities increases the solubility of uranous sulfate. Given the high level of impurities in the synthetic leach solution, the results were not surprising.

8.2.3 Solids analysis

12.084 g of fine dry solid precipitate was recovered after filtration, washing, and drying. XRD analysis confirmed that the final product was pure $U(SO_4)_2 \cdot 4\,H_2O$, as shown in Fig. 8.4. Solid assay results are shown in Table 8.2, and confirmed that the material was free from impurities (subject to the detection limit of AA analysis).

Thermogravimetric analysis gave TGA and DSC signals characteristic of uranous sulfate tetrahydrate (see Chapter 6), as shown in Fig. 8.5. The amount of crystalline water, at 4.23 H_2O per uranium, was slightly higher than the theoretical value of 4, which mirrored earlier observations of increased water in solids crystallized from impure solutions. The main water loss peak (W1) in the derivative thermogravimetry (DTG) curve had an area of $\Delta m' = 62.2$, corresponding to a loss of 3.5 H_2O, matching the expected hemihydrate intermediary.

High temperature decomposition also behaved in a manner characteristic of

uranous sulfate tetrahydrate. There were three peaks in the DTG signal collectively corresponding to the oxidation of $U(SO_4)_2$ to UO_2SO_4 (S1, S2a, S2b), with the first starting around 450 °C. Conversion to U_3O_8 began around 600 °C (S3), with the reaction rate increasing rapidly at higher temperatures.

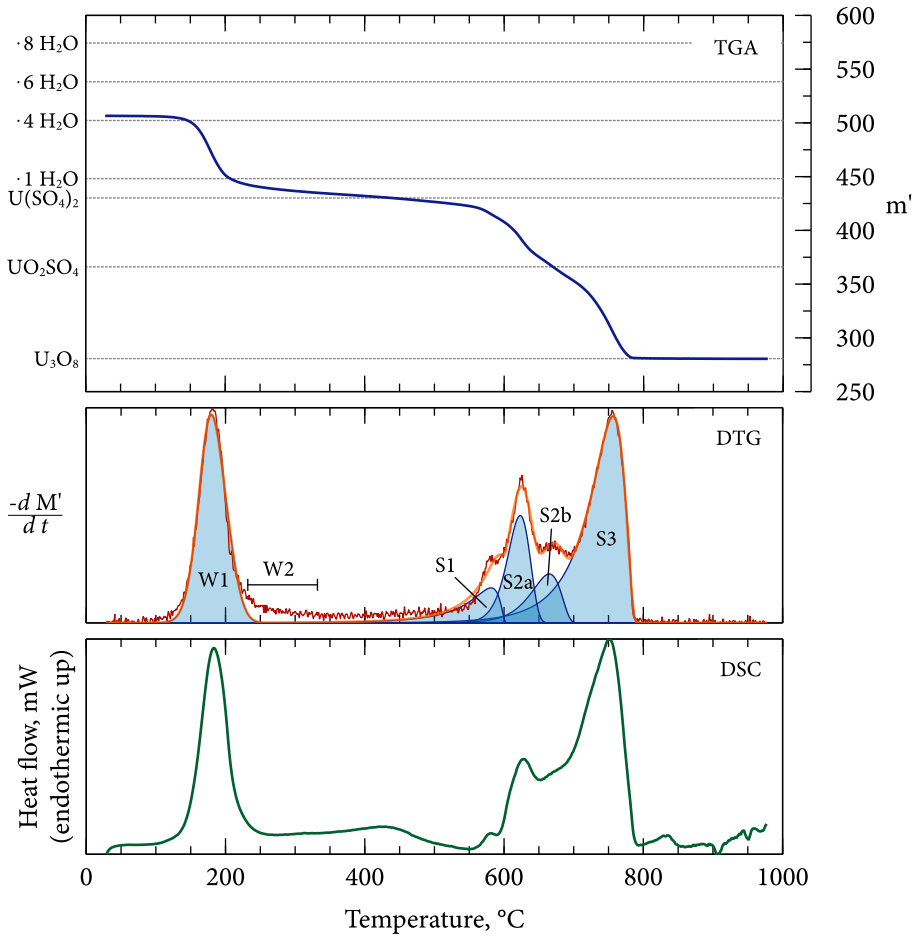

Figure 8.5: Thermal analysis of the demonstration plant solids, matching the signature for $U(SO_4)_2 \cdot 4\,H_2O$.

8.3 Implications for plant design

The basic electrolyzer design used in the demonstration, with oxygen evolution on an anode separated from the catholyte by a proton exchange membrane, functioned quite well, albeit at an uninspiring overall current efficiency. A continuous flow-through variation of this design is recommended. The anolyte composition should be chosen to minimize water transport into the catholyte across the membrane. Hydrogen evolution appeared to be the main competing reaction. An important focus of a future cell design, then, should be on the efficient dispersion and removal of hydrogen bubbles. Optimization of hydrogen evolution could also be a focus of cell design – enough to disrupt the diffusion boundary layer and enhance the mass diffusion rate of uranium(VI), but not so much as to compromise solution-electrode contact. In the demonstration, copper plated onto the cathode, quickly covering the stainless steel mesh surface. Given that any metal with a higher reduction potential than uranium(VI) would quickly plate onto the cathode during continuous operation, the pursuit of an ideal cathode material to maximize current efficiency would seem somewhat futile. Therefore it would be prudent to design a cell that could either facilitate the quick swapping of fouled electrodes for cleaning, or allow for a periodic cleaning cycle, either through the use of an oxidizing cleaning solution or by running the cell in reverse polarity.

The crystallization of uranous sulfate proceeded quickly and effectively in the demonstration, reaching equilibrium in about an hour in a batch reactor and producing pure $U(SO_4)_2 \cdot 4\,H_2O$. A series of three continuous stirred tank reactors (CSTRs) at 90 °C, with acid and seed addition, is recommended for a potential plant design. Unfortunately, the uranium recovery, at 72.3 %, was too low to justify the use of this technology alone. Methods to concentrate the solution, such as membrane water removal or an evaporator, would help with this, but could be costly to operate. Even then, the remaining soluble uranium would need to be recovered either through a secondary recovery circuit, or via a recycle stream. All of these efforts would carry implications related to the buildup of impurities.

The thermal processing of $U(SO_4)_2 \cdot 4\,H_2O$ should be straightforward, with its design dictated largely by the desired final product. Drying in air at 60–100 °C would be sufficient to produce a dry, flowable $U(SO_4)_2 \cdot 4\,H_2O$ product theoreti-

cally containing 47.4 % uranium, which could be packaged as a final product from a mill. To increase the weight percent uranium, the product could be fully dehydrated by heating at 200–400 °C, giving $U(SO_4)_2$ at 55.3 % uranium. If the product were calcined at 700 °C or above to produce U_3O_8, the released SO_2 and SO_3 gases could theoretically be recovered in an acid plant as H_2SO_4, which could be used to offset the acid needed for other parts of the process.

Chapter 9

Flow sheet development

In Chapter 8, it was demonstrated that the electrolytic reduction and precipitation of uranous sulfate is a viable process for selectively extracting uranium from a high-grade leach solution containing impurities at a bench scale. Here, a plant flow sheet is proposed, incorporating electrolysis, crystallization, evaporative concentration, washing and filtration, drying, and calcining. A schematic of the flow sheet is given in Fig. 9.1, and a brief description of each stream is given in Table 9.1.

Note that the flow sheet is presented here as an overview, not a complete mass and energy balance, in order to respect the confidentiality of the project sponsor. A more complete treatment, including a mass balance and rudimentary economic analysis, was published in a confidential report [12].

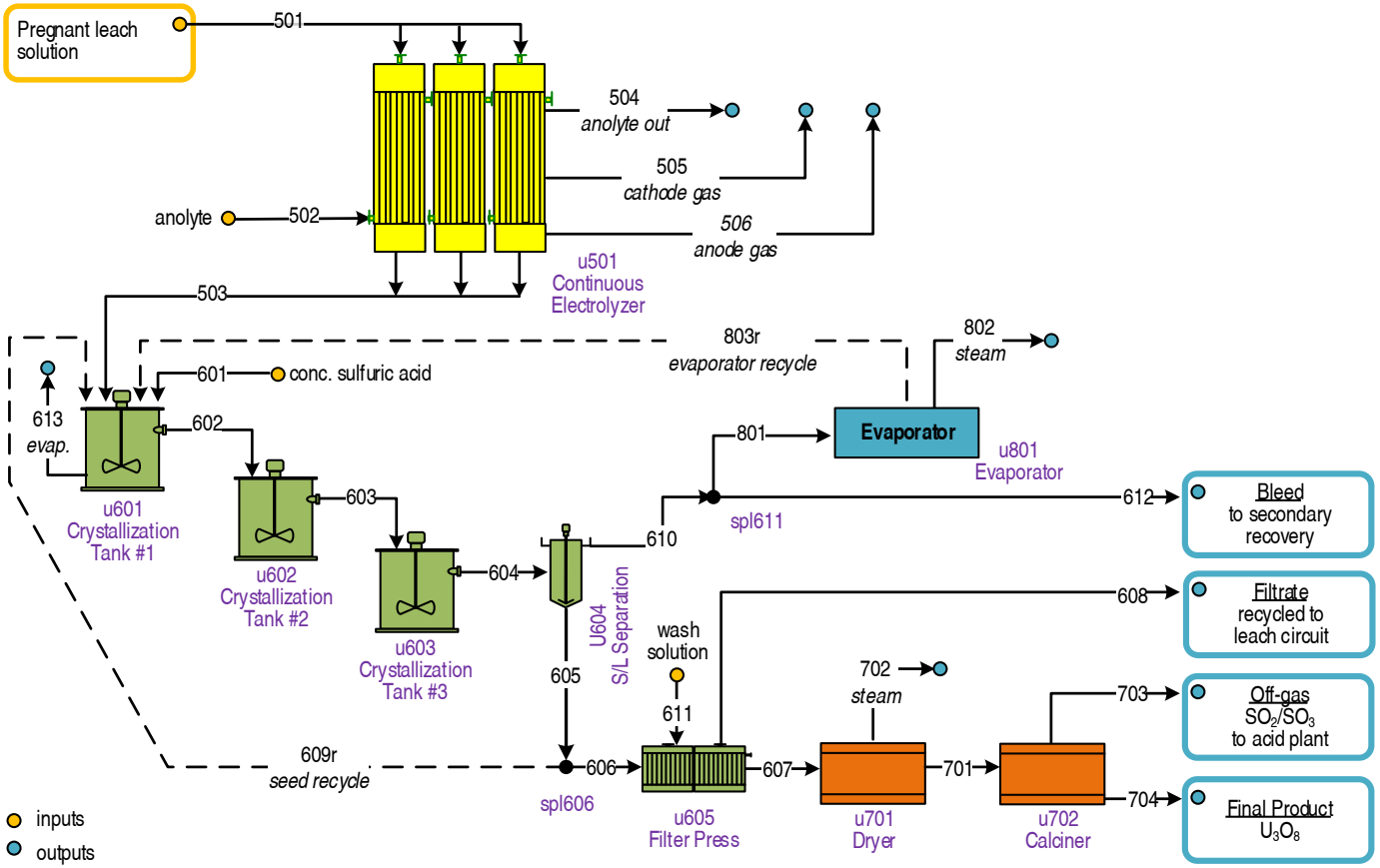

Figure 9.1: Proposed flow sheet for the electrolytic reduction and precipitation of uranous sulfate.

Table 9.1: List and description of flow sheet streams

Stream	Circuit	Description
501	Electrolysis	Electrolyzer feed - high-grade pregnant leach solution
502	Electrolysis	Fresh anolyte to electrolyzer
503	Electrolysis	Reduced catholyte
504	Electrolysis	Anolyte discharge from electrolyzer
505	Electrolysis	Cathode gas (hydrogen)
506	Electrolysis	Anode gas (oxygen)
601	Crystallization	Sulfuric acid to crystalliation circuit
602	Crystallization	Crystallization tank #1 discharge
603	Crystallization	Crystallization tank #2 discharge
604	Crystallization	Crystallization tank #3 discharge
605	Crystallization	S/L sep. underflow
606	Crystallization	S/L sep. underflow to filter press
607	Crystallization	Filter cake to dryer
608	Crystallization	Filtrate recycled to leach circuit
609r	Crystallization	S/L sep. underflow seed recycle
610	Crystallization	S/L sep. overflow
611	Crystallization	Wash solution to filter press
612	Crystallization	S/L sep. overflow bleed to secondary recovery and impurity removal
613	Crystallization	Evaporation from crystallization tanks
701	Drying and calcining	Dried uranous sulfate tetrahydrate
702	Drying and calcining	Water vapour from dryer
703	Drying and calcining	Off-gas from calciner to acid plant
704	Drying and calcining	Final product - U_3O_8
801	Residual U recovery	S/L sep. overflow to evaporator
802	Residual U recovery	Water vapour from evaporator
803r	Residual U recovery	Evaporator recycle to crystallization tank

9.1 Description of unit operations

9.1.1 Continuous electrolysis

A high-grade acidic uranium(VI)-sulfate solution (s501) is continuously fed into a membrane-divided electrolyzer (u501). The uranium is electrolytically reduced to uranium(IV), yielding a reduced uranium(IV) stream (s503), hydrogen gas from the cathode (s505), and oxygen gas from the anode (s506). The temperature is held at approximately 20 °C in order to maintain maximum solubility of uranium(IV), thus preventing precipitation within the electrolyzer. The anolyte is a sulfuric acid solution, and here is shown as a slow-flowing non-recycled stream (s502), although it could potentially be reused and renewed via a slow bleed. The reduced uranium solution is fed onward to the crystallization circuit.

It is worth noting that the cost of electricity is unlikely to be as significant for this technology as it is for other electrometallurgical systems, such as copper electrowinning. The very high molecular weight of uranium (3.75 times greater than copper) means that each kilogram of uranium requires significantly less electricity to process than other metals. In addition, uranium sells for a much higher price than any electrolytically-produced base metal (e.g., Cu, Ni, Zn), even at the depressed prices prevalent in 2011–2014, making the cost of electricity easier to justify.

9.1.2 Crystallization

The reduced uranium solution (s503) is fed into a series of CSTR crystallization tanks (u601, u602, and u603). The tanks are covered, and preferably sealed, to minimize reoxidation of uranium(IV) by air. The precipitation tanks are operated at 90 °C, and extra sulfate is introduced in the form of sulfuric acid (s601), in order to minimize the solubility of uranous sulfate. Any impurities are expected to stay in solution. Also introduced in the first tank is the concentrated uranium(IV)-bearing solution recycled from the evaporator (s803r). Crystal growth is encouraged by rapid agitation and the introduction of seed crystals from the S/L sep. underflow (s609r). The output slurry from the last precipitation tank (s604) contains precipitated uranous sulfate, as well as some residual aqueous uranium(IV).

The slurry from the crystallization tanks is fed to a solid-liquid separation (S/L

sep.) step (u604), with the clear overflow (s610) feeding to the evaporator, and the underflow (s605) split between seed recycle (s609r) and the filter press (s606). A bleed of the S/L separation overflow (s612) is necessary to prevent the uncontrolled buildup of impurities in the recycle loop. The filter press (u605) uses a hot sulfuric acid solution as wash solution (s611), with the aim of displacing the entrained impurity-containing spent solution while minimizing the redissolution of uranous sulfate. The filtrate (s608) is a dilute solution containing the impurities and some redissolved uranium, and can be recycled to the leaching circuit as a source of acid and to recover the uranium. The filter cake (s607), consisting of solid $U(SO_4)_2 \cdot 4\,H_2O$ and entrained sulfuric acid, is fed to the dryer.

9.1.3 Drying and calcining

The washed filter cake from the crystallization circuit (s607) is fed to a dryer (u701), where water is evaporated and released as steam (s702). The dried product (s701) has the composition of $U(SO_4)_2 \cdot 4\,H_2O$, and can be sold or stored indefinitely in this form. If acid recovery is desired, the solids can be calcined at approximately 800 °C (u702), removing the sulfate as SO_2 and SO_3 gas. The off-gas (s703) can be sent to an acid plant for conversion to H_2SO_4. The final product in this case is U_3O_8 (s704). This is the final product of this flow sheet.

9.1.4 Residual uranium recovery and impurity removal

The solution leaving the crystallization circuit still contains a substantial amount of soluble uranium(IV), which represents a major inefficiency of this design. The recovery can be improved by introducing a circuit to remove water from the spent solution, thus increasing its uranium(IV) concentration and encouraging further precipitation. In this flow sheet, this is modelled as an evaporator (u801). Water is removed in the form of steam (s802), and the concentrated solution is recycled to the crystallization tank (s803r). The division of flow between the feed to the evaporator (s801) and the bleed (s612) would depend on the tolerance of the system to the buildup of impurities. It might also be possible to use membrane filtration as an alternative to evaporation.

Ion exchange or solvent extraction could also be used for residual uranium re-

covery. Both techniques are well-established and are widely used, making them a reliable choice. However, their performance on uranium(IV) would need to be evaluated, and it might be necessary to reoxidize the uranium to achieve adequate separation from impurities. The use of solvent extraction or ion exchange would also re-introduce the very technologies targeted for elimination by the present work, albeit at a substantially reduced flow rate.

Impurities are not considered directly in this flow sheet. In the present configuration, the ratio of evaporator recycle to bleed would determine the recirculating load of impurities, which could rise to very high levels. It would almost certainly be necessary to include some accommodation for impurity removal, either through pre-treatment of the electrolyzer feed, or by a removal step after the bleed stage. A bulk neutralization and precipitation process may be the most economical here, although the uranium precipitated thus would need to be recovered. If only a few impurities are found to interfere with the process, ion exchange columns could be used to selectively remove these impurities.

Chapter 10

Summary and conclusions

10.1 Review of objectives

In Chapter 1, it was stated that the overarching objective of this dissertation was to advance the knowledge and practice of the selective precipitation of uranous sulfate as a new uranium hydrometallurgical processing technology. Six questions were posed, covering various aspects of uranous sulfate precipitation deemed critical to the further development of the technology. These questions are revisited below.

1. What are the best operating conditions for the precipitation of uranous sulfate?

The solubility of uranous sulfate tetrahydrate is inversely proportional to temperature and sulfuric acid concentration. The kinetics of precipitation are fastest at high temperature, and nucleation and crystal growth can be enhanced by the inclusion of 'seed' crystals. Aggressive agitation promotes fast, uniform precipitation of fine-grained crystals, and prevents the tubing and reactor walls from being encrusted with precipitate. It is therefore recommended that a future process operate at >90 °C and >2.0 mol L^{-1} sulfuric acid, with fast agitation, a substantial seed recycle, and a residence time of several hours. This will give fine crystalline $U(SO_4)_2 \cdot 4\,H_2O$ precipitate as a product.

2. How do impurities affect the precipitation process?

The precipitates recovered from impure solutions containing Al, Cu, Fe, or Ni are very pure, containing little or no trace of the impurities. Uranium recovery suffers in the presence of impurities, however, as these impurities all appear to increase the solubility of uranous sulfate, even in solutions with otherwise-identical sulfate and free acid concentrations. It seems, then, that uranous sulfate precipitation is highly selective towards uranium in the presence of impurities, but that recovery can suffer.

3. What are the different uranous sulfate polymorphs, and how do they differ from one another?

Uranous sulfate can form many different hydrated salts of the form $U(SO_4)_2 \cdot xH_2O$, with x ranging between 0 and 9. They differ not only in the number of water molecules, but also in the structural arrangement and cross-linking of the sulfates. The tetrahydrate always forms at temperatures >30 °C, while the octahydrate and hexahydrate form at lower temperatures. Lower hydrates and the anhydrate can be produced by controlled thermal decomposition, which drives off water, although it is still unknown whether these compounds are stable under ambient conditions.

A crystallographically-unique compound, called *parisaite* in this work, was found to form as an intermediary during the crystallization of uranous sulfate tetrahydrate. Although its exact form was not identified, it was found to contain approximately four sulfates per uranium, perhaps suggesting that sulfuric acid is incorporated into its structure. *Parisaite* can be eliminated by controlling various parameters, including sulfuric acid concentration and test duration.

4. How does uranous sulfate respond to drying and calcining?

Uranous sulfate x-hydrate decomposes in air or nitrogen in three general steps: water loss to $U(SO_4)_2$; oxidation to UO_2SO_4; and decomposition to U_3O_8. Initial rapid water loss occurs between 80–150 °C, depending on the polymorph, followed by the slow loss of the remaining water. The resulting anhydrous uranous sulfate behaves differently depending on the level of hydration of the original solid, appearing to reflect fundamental differences in their molecular structures. This may be related to the relative difficulty involved in the reconfiguration of bonds during the recrys-

tallization of amorphous anhydrous uranous suflate into crystalline anhydrous uranous sulfate. In a reducing atmosphere of H_2 or NH_3, uranous sulfate can be directly reduced to UO_2. With proper control of temperature and atmosphere, it is therefore possible to convert any uranous sulfate polymorph into $U(SO_4)_2$, UO_2SO_4, U_3O_8, or UO_2 using a calcining process.

5. Is aqueous uranium(IV) stable against oxidation by oxygen gas?

Uranium(IV) will oxidize readily in the presence of oxygen gas. In perchloric acid, the rate of oxidation is 1.5-order in uranium(IV), first-order in oxygen, and inverse-second-order in acid, and follows an Arrhenius relationship with respect to temperature. The presence of sulfate slows oxidation, likely due to the formation of stable sulfate complexes. The presence of sulfate in high amounts, such as when operating in sulfuric acid, gives unreproducible results, making it difficult to predict or model its behaviour.

6. Can uranous sulfate precipitation be developed into a viable extractive metallurgical technology?

There is ample evidence to suggest that uranous sulfate precipitation can be used to selectively extract uranium from an impure leach solution. A possible process might involve electrolytic reduction, precipitation, filtration, drying, and calcining, giving a final product of either $U(SO_4)_2$ or U_3O_8. The main obstacle to the successful implementation of this process is the relatively high solubility of uranous sulfate, which seems to be enhanced by the presence of impurities. An improvement in recovery might be possible through the introduction of recycle streams or a secondary recovery circuit, but this would require further study.

10.2 Contributions to the art

Many of the results presented in this dissertation represent new contributions to the body of scientific knowledge. These contributions span several areas of inorganic chemistry and engineering.

Contributions to the field of inorganic chemistry were mainly through the determination of the crystal structures of $\{[U(SO_4)_2(H_2O)_5] \cdot H_2O\}_n$ (uranous sulfate

hexahydrate) and $[U(SO_4)_2(H_2O)_6] \cdot 2\,H_2O$ (uranous sulfate octahydrate). These have revealed striking differences in the molecular connectivity of the different hydrates, which furthers the understanding of how so-called 'waters of hydration' can impact the molecular structure of uranous sulfate. One tangible benefit of the study is that the powder XRD, Raman, and infrared spectra of the uranous sulfate hydrates are now known, making it much easier to identify their presence in unknown precipitates.

New contributions to the fundamentals of hydrometallurgy were centred on the genesis of uranous sulfate *x*-hydrate from acidic uranium(IV) solutions. The effects of the impurities Al, Cu, Ni, and Fe on the precipitation process were demonstrated, showing that uranous sulfate can be selectively crystallized from impure solutions. A useful phase map was developed from experimental data showing how acid concentration, temperature, and crystallization time dictate which polymorphic form of uranous sulfate is stable, giving a deeper understanding of the polymorphism of uranous sulfate than was known previously. The studies on the oxidation on uranium(IV) with molecular oxygen contributed to the understanding of that system in several ways, namely by identifying the apparent reaction order under various circumstances. Perhaps more importantly, a method of continuous data acquisition and differential analysis was applied which could be applied to other systems to advance the understanding of non-first-order kinetics.

Fundamental contributions were also made to other areas of extractive metallurgy. The study of the thermal decomposition of the uranous sulfate hydrates has granted a solid understanding of how uranous sulfate tetra-, hexa-, and octahydrate respond to calcining, including the temperatures and decomposition pathways involved. This level of detail was previously available only for the tetrahydrate. The studies also revealed significant differences in the decomposition pathways of the three hydrates, the first time such a phenomenon has been identified for uranous sulfate, which could be important when selecting the operating conditions of a calcining process.

Finally, this dissertation has advanced the understanding of uranous sulfate from an engineering perspective. It was demonstrated that the kinetics of the crystallization process can be enhanced significantly using simple engineering controls, such as agitation, seeding, and temperature, whereas previously it was unclear whether

the process could be made to proceed quickly enough to be useful. It was also shown that uranous sulfate can be precipitated selectively from impure solutions, rather than just from pure solutions. A complete potential metallurgical process, including electrolysis, precipitation, filtration, drying, and calcining, was tested beginning to end, and then formulated into a complete conceptual flow sheet. Together, these efforts represent the first time that uranous sulfate precipitation has been demonstrated as a viable processing option under realistic conditions.

10.3 Further work

The pursuit of a PhD degree usually raises more questions than it answers, and this project was no exception. Some of the further work suggested below could be done using equipment presently available in the UBC materials engineering hydrometallurgy laboratory, but most would require the procurement of additional equipment or partnership with another lab.

The solubility of uranous sulfate is fairly well understood between 30–90 °C, which represents reasonable limits for a simple open-air precipitation tank. If a pressurized vessel were used, however, higher temperatures would be possible, and the associated costs might be justified by the enhanced uranium recovery. A future fundamental study could focus on the solubility of uranous sulfate at temperatures >100 °C in an autoclave. Other fundamental work could focus on solutions containing impurities, eventually working towards using real process solutions rather than the synthetic solutions studied thus far. Of particular importance is the effect impurities have on uranous sulfate solubility, which is still poorly understood, and extending such study to anions such as Cl^-, which could cause substantial interference to the process due to their ability to complex with uranium. Attempting to calculate the *real* ionic strength (in contrast to the *formal* ionic strength) might be helpful in furthering this understanding. It would also be worthwhile to explore the relationship between uranium(IV) and HSO_4^- by adjusting $[H^+]$ with a non-complexing acid such as perchloric acid, without changing the total sulfate. This could grant further insight into the intermediate compound *parisaite*, which, with approximately four sulfates per uranium, might have HSO_4^- or H_2SO_4 incorporated into its structure, and thus should be affected by free acid. If *parisaite* indeed forms

as an intermediate compound, the amount of sulfate in the aqueous phase should first drop drastically as *parisaite* is formed, and then recover somewhat as it converts to $U(SO_4)_2 \cdot xH_2O$. An interesting set of experiments would follow both sulfate and uranium concentrations in solution, paired with solids analysis, to validate (or refute) this hypothesis.

The fundamental crystallographic characterization work described in Chapter 4 could be extended to the other compounds identified over the course of work, such as the intermediary hydrates from thermal decomposition. The structure of the so-called *parisaite* in particular could be very revealing, given that it appears to form as a precursor during the crystallization process. If it proves infeasible to produce single crystals of these compounds of a sufficient size and purity for single-crystal x-ray diffraction, it might be worthwhile to investigate electron crystallography using a transmission electron microscope (TEM) as an alternative. Also, recent advancements in cryo-electron microscopy (cryo-EM) could be applied to the study of uncrystallized inorganic compounds, although as of the writing of this dissertation (early 2015) this technique is in its infancy, with near-atomic-level resolution only just becoming possible.

The thermal decomposition of uranous sulfate *x*-hydrate described in Chapter 6 could be investigated more rigorously by controlling the purge gas atmosphere during TGA analysis, either by saturating it with water vapour (for the water loss reactions), or with SO_2 and SO_3 (for the decomposition reactions). This would remove an unknown from the system (the activity of the gases in thermodynamic equilibrium with the solids), making validation of the thermodynamics less speculative, and might also stabilize the intermediate compounds over a wider temperature range. The use of additional on-line analytical techniques to complement the TGA and DSC data would also be useful. Continuous XRD analysis of a powder sample on a temperature-controlled stage could be used to identify the crystallographical form of the various intermediate compounds, and could also be used to study the apparent slow recrystallization of amorphous uranous sulfate. Real-time analysis of the off-gases, using a gas chromatograph or similar, could by used to study the reaction stoichiometry, and might also prove useful for estimating the reaction rates of two simultaneous reactions, a task performed in this work using DTG peak deconvolution. All of these experiments would require equipment currently not available

in the Department.

The oxidation of uranium(IV) by molecular oxygen in the presence of large amounts of sulfate requires much deeper study in order to explain the irreproducibility of some of the data presented in Chapter 7. Any future work should be conducted with the upmost care, such as by using the purest reagents, controlling light exposure, using an all-glass system (including the impeller), and scrupulously cleaning the entire system between tests to ensure uniform surface conditions. A study specifically designed to find the onset of irreproducible behaviour would be helpful – differential reaction order analysis, showing the transition from 1.5-order to a lower order as sulfate is introduced, might be informative. Further development on the theoretical side, namely a refinement of the reaction mechanism in the non-perchloric acid system that accounts for the data presented in this dissertation and elsewhere, could also shed light on how sulfate might interfere with the process.

From an engineering perspective, a great deal of information could be obtained by operating the flow sheet proposed in Chapter 9 on a mini-pilot scale, including electrolysis, precipitation, filtration, drying, and calcining. The electrolysis step must be sped up and optimized, with particular attention to the effect of impurities. The long-term performance of the electrolyzer is currently unknown, particularly with respect to the fouling of the proton-exchange membrane and cathode, and it will almost certainly be necessary to develop techniques to clean the cell using chemical or eletrochemical means, possibly on a regular, automated schedule. The precipitation of uranous sulfate following electrolysis must be studied from an engineering perspective as well, such as by optimizing the pulp density (through the establishment of a recirculating load) to encourage crystallization. It might also be possible to improve recovery by boiling the solution during the precipitation step, rather than operating at 90 °C. Solid-liquid separation and filtration using industrial-style equipment would give a more reasonable idea of losses due to redissolution and the entrainment of mother liquor, rather than the idealized results given by a laboratory filtration setup. Of particularly importance would be the development of a suitable wash liquid – not water – for the filtration process to minimize redissolution. Drying and calcining could be run as a separate campaign, focusing on the recovery of acid from the off-gases and the preparation of the final product in a suitable form for transport.

10.4 Concluding remarks

The selective precipitation of uranous sulfate shows great promise as a new primary purification technique for uranium-containing solutions. This is exciting—new extractive metallurgy technologies surface rarely, and the chance to overturn the status quo should be embraced. Many obstacles remain, however, and it will require a significant investment of resources to develop the concepts presented in this dissertation into a competitive technology. There is no question that the world's demand for energy will increase over the coming decades, and with it the world's demand for uranium. The further development of uranous sulfate precipitation technology would therefore be a wise investment.

References

[1] A. D. Aczel. *Uranium Wars: The Scientific Rivalry that Created the Nuclear Age*. Palgrave Macmillan, 2009. → pages 7

[2] A. Altomare, M. C. Burla, M. Camalli, G. L. Cascarano, C. Giacovazzo, A. Guagliardi, A. G. Moliterni, G. Polidori, and R. Spagna. SIR97: a new tool for crystal structure determination and refinement. *Journal of Applied Crystallography*, 32(1):115–119, 1999. → pages 57

[3] ASTM International. Standard test method for uranium by iron (II) reduction in phosphoric acid followed by chromium (VI) titration in the presence of vanadium. ASTM Standard, 2006. → pages iv, 17

[4] ASTM International. ASTM C788-03, standard specification for nuclear-grade uranyl nitrate solution or crystals. ASTM Standard, 2009. → pages 50

[5] Y. Awakura, K. Sato, H. Majima, and S. Hirono. The measurement of the diffusion coefficient of u (vi) in aqueous uranyl sulfate solutions. *Metallurgical Transactions B*, 18(1):19–23, 1987. → pages 13

[6] Y. Awakura, H. Hiai, H. Majima, and S. Hirono. Fundamental studies on the continuous electrolytic reduction of uranyl sulfate. *Metallurgical and Materials Transactions B*, 20:337–343, 1989. → pages 13, 21, 155

[7] U. Betke and M. S. Wickleder. Oleum and sulfuric acid as reaction media: The actinide examples $UO_2(S_2O_7)$-lt (low temperature), $UO_2(S_2O_7)$-ht (high temperature), $UO_2(HSO_4)_2$, $An(SO_4)_2$ (An= Th, U), $Th_4(HSO_4)_2(SO_4)_7$ and $Th(HSO_4)_2(SO_4)$. *European Journal of Inorganic Chemistry*, 2012(2): 306–317, 2012. → pages 21, 45, 53, 64, 66, 114

[8] R. Bothwell. *Eldorado: Canada's National Uranium Company*. University of Toronto Press, 1984. → pages 7

[9] A. Brodtkorb. NUMDIFFTOOLS v0.6.0 software package, October 24, 2013. URL https://code.google.com/p/numdifftools/. → pages 132

[10] Bruker AXS Inc. SAINT v8.32B software package. Madison, Wisconsin, USA, 1997-2013. → pages 55

[11] Bruker AXS Inc. SADABS software package. Madison, Wisconsin, USA, 2012. → pages 55

[12] A. D. Burns. Electrolytic reduction and precipitation of uranous sulfate: Flow sheet development, mass balance and operating cost analysis. Private report, The University of British Columbia, September 2013. → pages 165

[13] A. D. Burns and D. Dreisinger. The apparent overall oxidation kinetics of uranium(IV) by oxygen gas in aqueous perchloric acid solutions. In E. Asselin, D. Dixon, F. Doyle, D. Dreisinger, M. Jeffery, and M. Moates, editors, *Proceedings of the 7th International Symposium On Hydrometallurgy 2014*, volume 2, pages 789–800. The Metallurgy and Materials Society of CIM, Canadian Institute of Mining, Metallurgy and Petroleum, June 2014. → pages iv, 124

[14] A. D. Burns, B. O. Patrick, A. E. Lam, and D. Dreisinger. The effect of coordinated water on the connectivity of uranium(IV) sulfate x-hydrate: $[U(SO_4)_2(H_2O)_5] \cdot H_2O$ and $[U(SO_4)_2(H_2O)_6] \cdot 2\,H_2O]$, and a comparison with other known structures. *Acta Crystallographica*, C70(7), 2014. → pages iii, 21, 45, 52, 66

[15] S. Casadio and L. Lorenzini. Cyclic voltammetric behavior of uranyl ion in sulfuric acid solutions. application to some nuclear materials characterization. *Analytical Letters*, 6(9):809–820, 1973. → pages 12, 13

[16] E. Cordfunke. The system uranyl sulphate-water—I: Preparation and characterization of the phases in the system. *Journal of Inorganic and Nuclear Chemistry*, 31(5):1327 – 1335, 1969. → pages 80, 81

[17] E. Cordfunke. The system uranyl sulphate-water—II: Phase relationships and thermochemical properties of the phases in the system UO_3-SO_3-H_2O. *Journal of Inorganic and Nuclear Chemistry*, 34(5):1551 – 1561, 1972. → pages 80, 81, 82

[18] CrystalMaker Software Ltd, Oxford, England (www.crystalmaker.com). Crystalmaker 2.7.7, 2014. → pages 57

[19] W. Davies and W. Gray. A rapid and specific titrimetric method for the precise determination of uranium using iron (II) sulphate as reductant. *Talanta*, 11(8):1203–1211, 1964. → pages 17

[20] O. V. Dolomanov, L. J. Bourhis, R. J. Gildea, J. A. Howard, and H. Puschmann. OLEX2: a complete structure solution, refinement and analysis program. *Journal of Applied Crystallography*, 42(2):339–341, 2009. → pages 57

[21] A. E. Duque, M. G. Benach, and F. H. Arroyo. Obtencion de UF_4 pour reduccion electrolica. Technical Report 0081-3397, Spanish Atomic Energy Commission, 1974. → pages 14, 16

[22] A. J. Elliot, S. Padamshi, and J. Pika. Free-radical redox reactions of uranium ions in sulphuric acid solutions. *Canadian journal of chemistry*, 64(2): 314–320, 1986. → pages 128

[23] S. Fallab. Reactions with molecular oxygen. *Angewandte Chemie International Edition in English*, 6(6):496–507, 1967. → pages 128

[24] L. J. Farrugia. WinGX suite for small-molecule single-crystal crystallography. *Journal of Applied Crystallography*, 32(4):837–838, 1999. → pages 57

[25] S. Fell. Electrochemical generation of stable uranium(IV) fluoride-sulphate solutions. *Analyst*, 114(3):325–331, 1989. → pages 22

[26] F. Forward and J. Halpern. Developments in the carbonate processing of uranium ores. *Journal of Metals*, 6(12):1408–1414, December 1954. → pages 1

[27] F. Forward and J. Halpern. Acid pressure leaching of uranium ores. *Journal of Metals*, 7(3):463–466, March 1955. → pages 1

[28] W. Freyberger. Electrolytic reduction of uranyl and ferric sulfate solutions. Technical Report AECD-4101 (MITG-A95), Massachusetts Institute of Tech, Watertown, Massachusetts, May 1950. → pages 21, 155

[29] J. M. Gil, F. M. Villa, and F. J. M. Gil. Thermal decomposition of sulphate complexes of uranium(IV) hydrates. *Journal of Thermal Analysis and Calorimetry*, 17:115–121, 1979. → pages 80

[30] F. Giolitti and G. Bucci. Sui fenomeni di equilibrio fra gli idrati del solfato uranoso. *Gazzetta Chimica Italiana*, 35(2):153, 1905. → pages 21, 80

[31] J. H. Gittus. Metallurgy of the rarer metals. In H. M. Finniston, editor, *Uranium*, volume 8. Butterworths London, 1963. → pages 7

[32] E. Gmelin and S. M. Sarge. Calibration of differential scanning calorimeters. *Pure and applied chemistry*, 67(11):1789–1800, 1995. → pages 84

[33] G. Gordon and H. Taube. Oxygen tracer experiments on the oxidation of aqueous uranium(IV) with oxygen-containing oxidizing agents. *Inorganic Chemistry*, 1(1):69–75, 2014/08/04 1962. → pages 127, 128

[34] I. Grenthe, H. Wanner, and I. Forest. Chemical thermodynamics of uranium. Technical report, OECD Nuclear Energy Agency, Issy-les-Moulineaux, France, 1992. → pages 8

[35] R. Guillaumont and F. J. Mompean. Update on the chemical thermodynamics of uranium, neptunium, plutonium, americium and technetium. Technical report, OECD Nuclear Energy Agency, Issy-les-Moulineaux, France, 2003. → pages 8, 9, 10, 11, 70, 71, 121

[36] Y. Gurinov and Y. Frolov. Intensification of the electrochemical process of reduction of six-valent to four-valent uranium. *Zhurnal Prikladnoi Khimii*, 41(7):1473–1479, 1968. → pages 12, 13

[37] F. Habashi. A short history of uranium. In *Proceedings of the 3rd International Conference on Uranium*, volume 1, pages 3–15. The Metallurgical Society of the CIM, CIM, 2010. → pages 7

[38] J. Halpern and J. G. Smith. Kinetics of the oxidation of uranium(IV) by molecular oxygen in aqueous perchloric acid solution. *Canadian Journal of Chemistry*, 34:1419–1427, 1956. → pages 125, 126, 127, 153, 154

[39] I. Higgins, J. Roberts, C. Hancher, and J. Marinsky. The Excer process. preparing uranium tetrafluoride by ion exchange and electrolysis. *Industrial & Engineering Chemistry*, 50(3):285–292, 1958. → pages 14, 15

[40] International Atomic Energy Agency. Nuclear power and sustainable development. Brochure, 2002. → pages 2

[41] K. Južnič and Š. Fedina. On the kinetics of oxidation of uranium(IV) in sulphuric acid by molecular oxygen. *Journal of Inorganic and Nuclear Chemistry*, 36(11):2609–2610, 11 1974. → pages 126

[42] D. Kern and E. Orlemann. The potential of the uranium (V), uranium (VI) couple and the kinetics of uranium (V) disproportionation in perchlorate

media. *Journal of the American Chemical Society*, 71(6):2102–2106, 1949. → pages 12

[43] L. Khamidullina and S. Lotnik. Formation of excited uranyl in oxidation of tetravalent uranium with oxygen in $HClO_4$ aqueous solutions: IV. enhancement of the chemiluminescent reaction in the presence of Fe_2^+. *High Energy Chemistry*, 45(6):497–500, 2011. → pages 129

[44] L. Khamidullina and S. Lotnik. Involvement of ·OH radicals in the mechanism of excitation of the uranyl ion in the chemiluminescent oxidation of U (IV) by atmospheric oxygen in aqueous solutions of perchloric acid. *Kinetics and Catalysis*, 54(4):400–403, 2013. → pages 129

[45] P. Kierkegaard. The crystal structure of $U(SO_4)_2 \cdot 4\,H_2O$. *Acta Chemica Scandinavica*, 10(4):599–616, 1956. → pages 21, 53, 64, 66

[46] J. M. Leroy and G. Tridot. Sur les hydrates et la décomposition thermique du sulfate uraneux. *Comptes rendus hebdomadaires des séances de l'Académie des sciences*, 261:5505–5808, 1965. → pages 80

[47] J. M. Leroy, J. Tudo, and G. Tridot. Sur les hydrates du sulfate d'uranyle. *Comptes rendus hebdomadaires des séances de l'Académie des sciences*, 260: 5802–5805, 1965. → pages 80, 81, 82

[48] D. Lide. *The CRC Handbook of Chemistry and Physics, 88th Edition*. CRC, Boca Raton, FL, 2008. → pages 223

[49] E. Lofthouse. Electrolytic production of uranium tetrafluoride. United States Patent 2,687,995, September 21 1944. → pages 14, 15

[50] S. Lotnik, L. Khamidullina, and V. Kazakov. Uranyl-catalyzed chemiluminescent reaction of U^{4+} oxidation by dioxygen in aqueous $HClO_4$ solution. *Russian Chemical Bulletin*, 49(9):1512–1517, 2000. → pages 127, 129

[51] S. V. Lotnik, L. A. Khamidullina, and V. P. Kazakov. Strong effect of a solid surface on a liquid-phase radical chain chemiluminescence reaction. oxidation of U(IV) by dioxygen. *Russian Chemical Bulletin*, 48(12): 2339–2341, 1999. → pages 129

[52] D. K. Louie. *Handbook of sulphuric acid manufacturing*. DKL Engineering, Inc., 2005. → pages 74

[53] C. F. Macrae, P. R. Edgington, P. McCabe, E. Pidcock, G. P. Shields, R. Taylor, M. Towler, and J. van de Streek. *Mercury*: visualization and analysis of crystal structures. *Journal of Applied Crystallography*, 39(3):453–457, June 2006. → pages 45, 196, 198, 200

[54] H. Majima, Y. Awakura, and S. Hirono. Electrolytic reduction of U(VI) to U(IV) in acidic chloride and acidic sulfate solutions. *Metallurgical Transactions B*, 17(1):41–50, 1986. → pages 9, 14, 16, 21

[55] H. Majima, Y. Awakura, K. Sato, and S. Hirono. Laboratory reduction rate and current efficiency studies of batch type electrolytic reduction of U(VI) in a sulfate system. *Metallurgical and Materials Transactions B*, 17:69–76, 1986. 10.1007/BF02670820. → pages 155

[56] H. McCoy and H. Bunzel. The speed of oxidation, by air, of uranous solutions, with a note on the volumetric determination of uranium. *Journal of the American Chemical Society*, 31(3):367–373, 1909. → pages 126, 127

[57] Metrohm. Titrimetric determination of sulfate. Application Bulletin. → pages iv, 18, 203

[58] K. Notz and H. Jaffe. Pyrolysis of uranium compounds—I: Uranyl sulphate. *Journal of Inorganic and Nuclear Chemistry*, 25(7):851–857, 1963. → pages 80, 81, 82

[59] K. J. Notz and H. H. Jaffé. Correlation of TGA and DTA temperatures in decomposition reactions. *Journal of the American Ceramic Society*, 43(1): 53–54, 1960. → pages 83

[60] R. A. Nyquist and R. O. Kagel. *Handbook of infrared and raman spectra of inorganic compounds and organic salts: infrared spectra of inorganic compounds*. Academic press, 1971. → pages 63

[61] Outotec Oyj. HSC chemistry. Espoo, Finland, 1974-2014. → pages 70, 74, 75, 76

[62] E. Peters. The leaching of uranium from pitchblende ores by aqueous oxidation techniques. Master's thesis, University of British Columbia, 1951. → pages 1

[63] J. Plášil, K. Fejfarová, M. Novák, M. Dušek, R. Škoda, J. Hloušek, J. Čejka, J. Majzlan, J. Sejkora, V. Machovič, and D. Talla. Běhounekite, $U(SO_4)_2(H_2O)_4$, from Jáchymov (St Joachimsthal), Czech Republic: the first

natural U^{4+} sulphate. *Mineralogical Magazine*, 75(6):2739–2753, 2011. → pages 21, 45, 65, 66, 196

[64] D. Preston. *Before the Fallout: From Marie Curie to Hiroshima*. Walker Publishing Company, Inc., 2005. → pages 7

[65] J. Renaud. Activités nucléaires de la société ugine kuhlmann. *Énergie Nucléaire*, 12(8):313–317, August 1970. → pages 14, 15

[66] T. Sato, F. Ozawa, and S. Ikoma. Thermal decomposition of uranyl sulfate hydrate. *Journal of chemical technology and biotechnology*, 30(1):384–389, 1980. → pages 80, 81, 82

[67] D. D. Schnaars and R. E. Wilson. Uranium(IV) sulfates: Investigating structural periodicity in the tetravalent actinides. *Inorganic Chemistry*, 51 (17):9481–9490, 2012. → pages 21, 40, 45, 53, 64, 66

[68] G. M. Sheldrick. A short history of SHELX. *Acta Crystallographica A*, 64(1): 112–122, 2008. → pages 57

[69] V. Shilov, A. Yusov, V. Peretrukhin, C. Delegard, A. Gogolev, A. Fedosseev, and L. Kazansky. Oxidation of U(IV) by atmospheric oxygen in pH 1.5–7.4 aqueous solutions. *Journal of Alloys and Compounds*, 444-445:333–338, 2007. → pages 125, 128

[70] J. Sobkowski. The oxidation reduction potential of the U (IV)-U (VI) system—III: Photoelectrochemical properties of the U (V) ion. *Journal of Inorganic and Nuclear Chemistry*, 27(11):2351–2359, 1965. → pages 128

[71] J. Sobkowski. Rate of oxidation of tetravalent uranium ions with molecular oxygen. *Roczniki Chemii*, 40:271–80, 1966. → pages 125, 126, 127, 128, 153

[72] A. Stabrovskii. Study of solubility of uranium(IV) and uranium(III) sulfates in sulfuric acid. *Radiokhimiia*, 21(3), 1979. → pages 21

[73] B. N. Sudarikov, O. I. Zakharov-Nartsissov, and A. V. Ochkin. Oxidation of quadrivalent uranium in sulfuric acid solutions with atmospheric oxygen. *Trudy Instituta - Moskovskii Khimiko-Tekhnologicheskii Institut imeni D. I. Mendeleeva*, 43:78–81, 1963. → pages 126

[74] S. Suzuki, S. Hirono, Y. Awakura, and H. Majima. Solubility of uranous sulfate in aqueous sulfuric acid solution. *Metallurgical Transactions B*, 21(5): 839–844, 1990. → pages 21, 31, 33, 80

[75] S. Thein and P. Bereolos. Thermal stabilization of $^{233}UO_2$, $^{233}UO_3$ and $^{233}U_3O_8$. Technical Report ORNL/TM-2000/82, Oak Ridge National Laboratory, 2000. → pages 81

[76] G. Tridot. Applications des methodes des d'analyses thermiques a l'evolution des sulfates de vanadyle, d'uranyle, d'uranium(IV), de titanyle et de leurs derives dans diverses atmospheres controlees. *Pure and Applied Chemistry*, 13(4):543–568, 1966. → pages 81, 118

[77] I. Warren and F. Forward. Hydrometallurgical production of uranium dioxide for reactor fuel elements. *The Canadian Mining and Metallurgical Bulletin*, 54(594):743–749, October 1961. → pages 1

[78] B. Wassink. *Analysis of Acidic Metal Sulfate Solutions for Sulfuric Acid Using pH Electrode and Standard Addition*. University of British Columbia, Department of Materials Engineering, February 1998. → pages iv, 18

[79] M. Wojdyr. Fityk: a general-purpose peak fitting program. *Journal of Applied Crystallography*, 43(5):1126–1128, 2010. → pages 85, 106

[80] A. Yilmaz, L. Hindiyarti, A. D. Jensen, P. Glarborg, and P. Marshall. Thermal dissociation of SO_3 at 1000-1400 K. *The Journal of Physical Chemistry A*, 110 (21):6654–6659, 2006. → pages 74

Appendix A

Production of uranium(IV) solutions by electrolytic reduction

Summary

Laboratory-grade uranium(IV) salts are not commercially available for purchase, so if a uranium(IV) solution is needed for research purposes, it must be produced by reducing uranium(VI). One method is to pass a uranium(VI) solution through a Jones reductor (zinc metal column), but this is cumbersome and could introduce impurities into the solution. Electrolytic reduction is a proven alternative that does not require the uranium solution to come into contact with any reagents, and is also easier to monitor and control.

Below is a brief review of the theory behind the electrolytic reduction of uranium(VI), an experimental procedure that can be used in the laboratory, and example results from a typical electrolysis experiment conducted as a part of the work presented in this dissertation.

Background information

The electrolytic reduction of uranium(VI) can be described by the following half-cell reactions:

Cathodic half-cell:	$UO_2^{2+} + 4H^+ + 2e^- \longrightarrow U^{4+} + 2\,H_2O$	$E^\circ = 0.27\,V$	(A.1)
Anodic half-cell:	$H_2O \longrightarrow \frac{1}{2}O_2 + 2H^+ + 2e^-$	$E^\circ = -1.23\,V$	(A.2)
Overall:	$UO_2^{2+} + 2H^+ \longrightarrow U^{4+} + \frac{1}{2}O_2$	$\Delta E = -0.96\,V$	(A.3)

Since ΔE is negative, the reaction does not proceed spontaneously, and so requires a voltage to be applied using an external power supply.

If the uranium(VI) cannot diffuse to the cathode surface fast enough to consume all of the supplied current (assuming a constant-current cell is being used), hydrogen evolution will occur to make up the difference as a competing reaction, lowering the current efficiency. Hydrogen evolves according to the following half-cell reactions:

Cathodic half-cell:	$2H^+ + 2e^- \longrightarrow H_2$	$E^\circ = 0\,V$	(A.4)
Anodic half-cell:	$H_2O \longrightarrow \frac{1}{2}O_2 + 2H^+ + 2e^-$	$E^\circ = -1.23\,V$	
Overall:	$H_2O \longrightarrow \frac{1}{2}O_2 + H_2$	$\Delta E = -1.23\,V$	(A.5)

The progress of the electrolysis reaction can be described by Faraday's law of electrolysis for a constant-current cell:

$$n = \frac{It}{zF} \tag{A.6}$$

where n is the number of moles of uranium reduced, I is the current (A, or $C\,s^{-1}$), t is the elapsed time (s), z is the number of electrons transferred per mole of uranium reduced (2 in this case), and F is Faraday's constant (96 485 $C\,mol^{-1}$ of e^-). Converting Eq. (A.6) into concentration units and substituting in the values for uranium(VI) reduction gives the following equation for calculating the *minimum* possible time to complete reduction, t_{min}, assuming 100 % current efficiency:

$$t_{min} = (192\,970\,C\,mol^{-1})\,\frac{[U(VI)]_i V}{I} \tag{A.7}$$

where V is the catholyte volume and $[U(VI)]_i$ is the initial concentration of uranium(VI) in the catholyte.

The current efficiency can be approximated by Eq. (A.8):

$$\eta = \frac{t_{\min}}{t} \tag{A.8}$$

where t is the actual electrolysis time.

Experimental procedure

Reagents

- Granulated uranium trioxide (UO_3)
- Concentrated sulfuric or perchloric acid
- Deionized water
- Nitrogen gas (for purging)

Equipment

- Electrolyzer
  - Cathode (e.g., stainless steel mesh)
  - Anode for oxygen evolution (e.g., DeNora DSA)
  - Nafion N117 proton exchange membrane
  - Heat-removal system (e.g., water jacket)
- Power supply capable of 10 A current at 5 V
- Logging multimeter
- Circulating chiller, or other cooling method
- Magnetic stir plate or circulating pump, to mix catholyte

Method

Catholyte preparation

Dissolve an appropriate amount UO_3 in sulfuric or perchloric acid to achieve the desired catholyte composition, accounting for acid consumption shown in Eq. (A.9). Adjust the acidity to the desired concentration, and dilute to a known volume in a volumetric flask.

$$UO_3 + 2H^+ \longrightarrow {UO_2}^{2+} + H_2O \tag{A.9}$$

Anolyte preparation

Dilute concentrated sulfuric or perchloric acid to the desired concentration in a volumetric flask.

Electrolysis

1. Turn on the heat-removal system to the electrolyzer (i.e., connect the circulating chiller, or immerse in water bath).
2. Add catholyte and anolyte (as prepared above) to the appropriate chambers of the electrolyzer.
3. Bubble nitrogen through the catholyte at a slow rate to flush any evolved hydrogen from the headspace of the electrolyzer. This is to prevent the potentially-dangerous buildup of hydrogen gas.
4. Start catholyte circulation. If using magnetic stirrer, add stir-bar to the catholyte chamber and turn on stir plate. If using a circulating pump, turn on pump.
5. Connect the logging multimeter to the electrodes and set to DC Volts mode.
6. Set the power supply to constant current mode and adjust the current until the cell voltage is 3.5–4.0 V. The current that can be achieved will depend on the electrolyzer setup, such as electrode surface area, electrode materials, etc.
7. Allow electrolysis to proceed while monitoring the cell voltage on the multimeter. Take samples periodically and assay for uranium(IV), if desired.
8. When the elapsed time approaches the minimum possible electrolysis time given by Eq. (A.7), begin monitoring the voltage more closely. The cell voltage will rise by ~0.5 V in a distinct S-shaped curve when all of the uranium(IV) has been converted to uranium(VI). Once the cell voltage stabilizes at the higher value, the test is complete. An electrolysis time approximately 40 % longer than t_{min} is typical.
9. Turn off the power supply. Transfer the catholyte to an air-free container for storage. The anolyte can be saved for re-use, if desired.

10. Clean the electrolytic cell thoroughly, and store the membrane wet in tap water.

Example setup and results

Electrolytic reduction of uranium(VI) was performed many times during the experimental work described in this dissertation, in both sulfuric acid and perchloric acid. Electrolysis was generally performed using the electrolyzer shown in Fig. A.1. The cathode chamber was a simple glass jacketed reactor, with 20 °C water circulating through the jacket to maintain uranous sulfate at its maximum solubility. The cathode was a band of stainless steel mesh running around the inner wall of the vessel. The anode chamber was a self-contained submersible compartment wrapped in a Nafion N117 membrane. The anode compartment had a capacity of 100 mL of anolyte and had a built-in DeNora DSA as the anode. The catholyte was circulated using a magnetic stirrer.

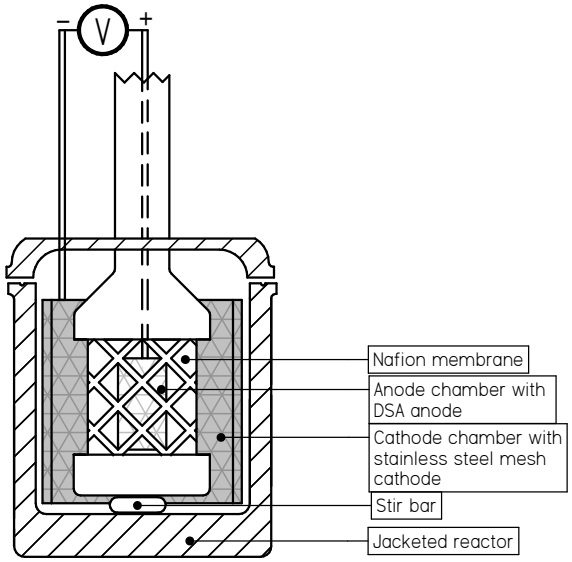

Figure A.1: Electrolyzer with submersible anode chamber.

As an example, the uranium(IV) solution prepared for the production of sample

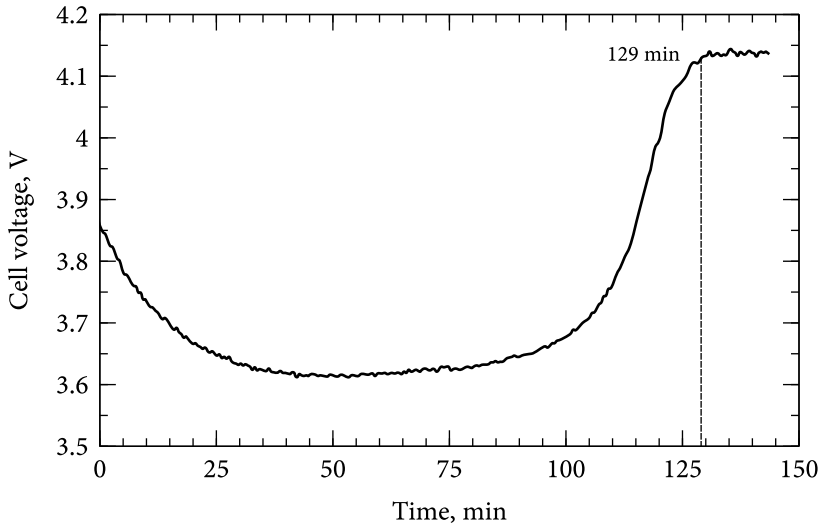

Figure A.2: Cell potential vs. time for a typical electrolysis experiment. Increase in potential at * indicates the completion of reduction. Constant current = 7.5 A.

63-S described in Chapter 3 represents a typical example of how electrolytic reduction was applied for the work described in this dissertation. The catholyte was made by dissolving 60.1 g of pure UO_3 in 52.1 g concentrated sulfuric acid and diluting to 500 mL, which yielded a 100 g L^{-1} uranium solution with 100 g L^{-1} total sulfate and 61 g L^{-1} free H_2SO_4. The anolyte composition was 100 g L^{-1} sulfuric acid.

The power supply was set to operate in a constant current regime, with a fixed operating current of 7.5 A. The voltage between the anode and cathode (i.e., the cell potential) was measured continuously during electrolysis.

Within a few minutes of commencing electrolysis, the catholyte turned from yellow in colour to purple-green colour, and continued to darken as the reduction progressed. Oxygen gas evolved at the anode for the duration of the test. Hydrogen began evolving at the cathode part way through the test. The approach of the end of the test was indicated by a prominant S-shaped rise in cell voltage, as shown in Fig. A.2. Complete reduction was indicated by the stabilization of the voltage at 129 min. Titration of the catholyte for uranium(IV) and total uranium confirmed complete reduction had taken place.

Using Eq. (A.7) to calculate the minimum electrolysis time at 100 % current efficiency, assuming a catholyte volume of 500 mL, gives a value of 90 min. Equation (A.8) yields an approximate current efficiency of 70 %.

Appendix B

Raman, FTIR, and XRD patterns for the uranous sulfate *x*-hydrates

Supporting information for Chapter 4, including uranous sulfate tetrahydrate $U(SO_4)_2 \cdot 4\,H_2O$, uranous sulfate hexahydrate, $[U(SO_4)_2(H_2O)_5] \cdot H_2O$ (complex **1**), uranous sulfate octahydrate, $[U(SO_4)_2(H_2O)_6] \cdot 2\,H_2O$ (complex **2**), and *parisaite*. Refer to Chapter 4 for details on instrumentation used.

B.1 Uranous sulfate tetrahydrate

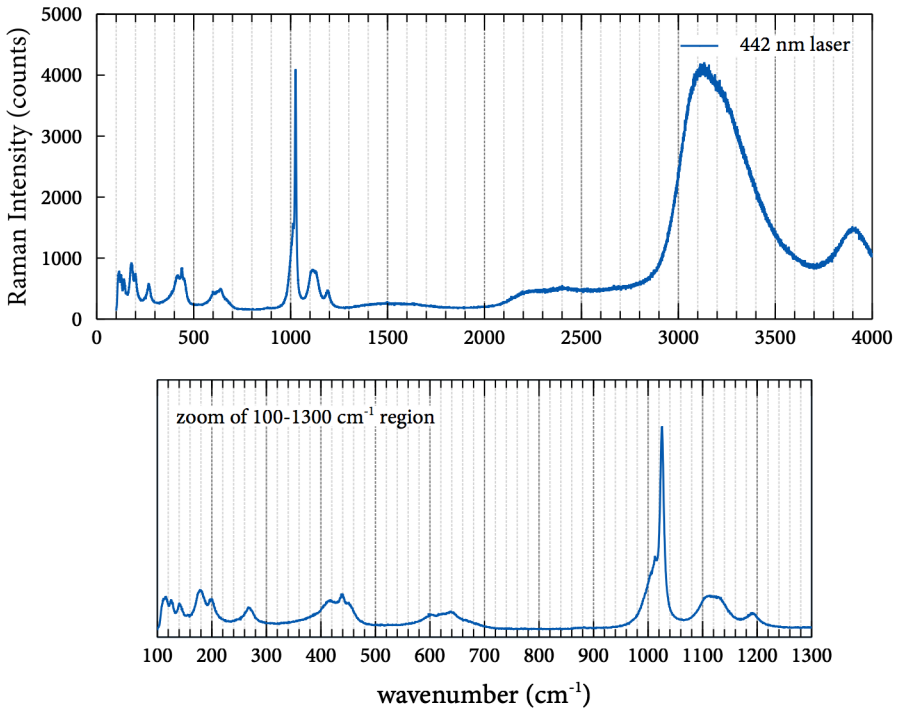

Figure B.1: Raman spectrum for uranous sulfate tetrahydrate, 442 nm laser. Sample: 63-S.

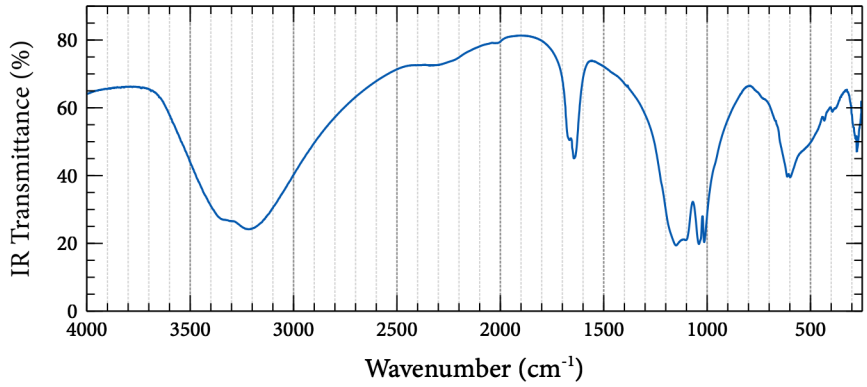

Figure B.2: FTIR spectrum of uranous sulfate tetrahydrate. Sample: 22-A.

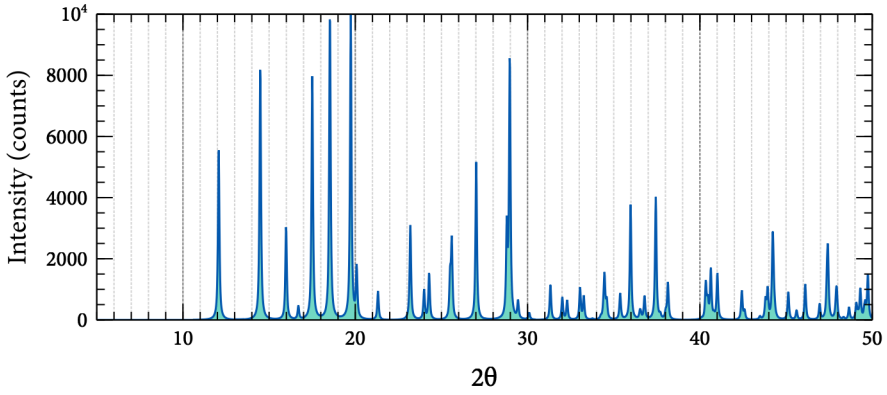

Figure B.3: Powder XRD spectrum of uranous sulfate tetrahydrate. Simulated from the crystal structure published by Plášil et al. [63] using Mercury 3.1 [53].

B.2 Uranous sulfate hexahydrate

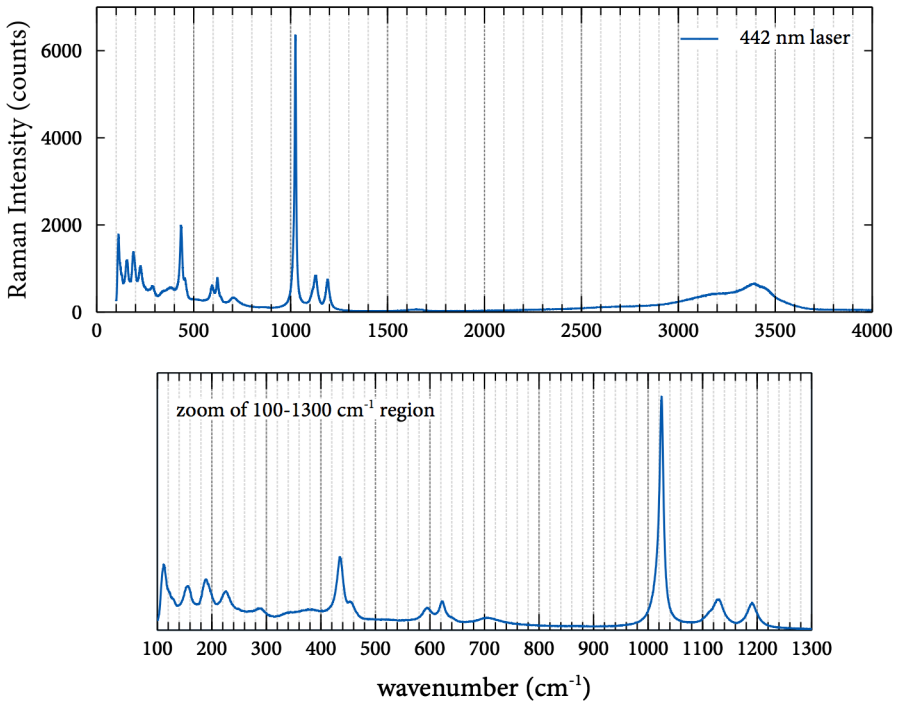

Figure B.4: Raman spectrum for uranous sulfate hexahydrate, complex **1**, 442 nm laser. Sample: 04-A.

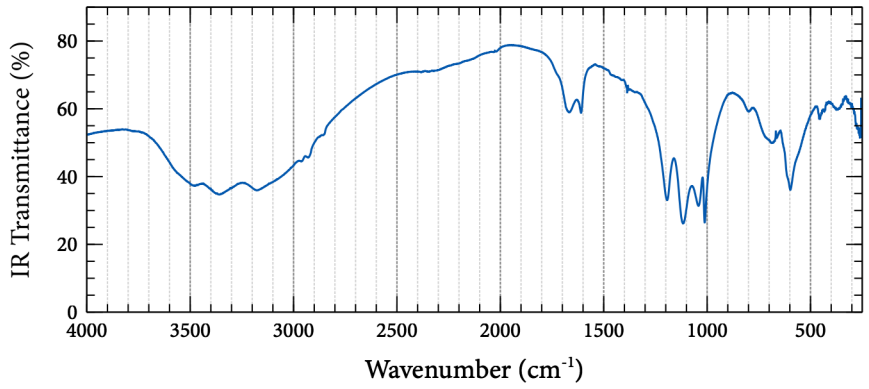

Figure B.5: FTIR spectrum of uranous sulfate hexahydrate, complex **1**. Sample: 04-A.

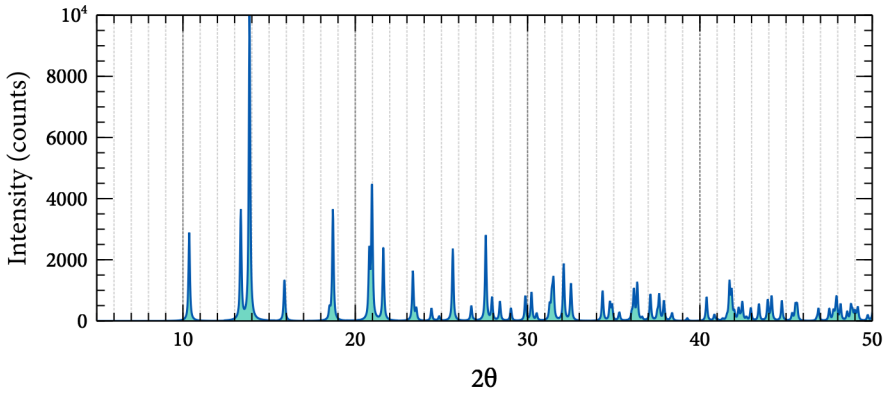

Figure B.6: Powder XRD spectrum of uranous sulfate hexahydrate, complex **1**, simulated from the crystal structure presented in Chapter 4 using Mercury 3.1 [53] (Cu source).

B.3 Uranous sulfate octahydrate

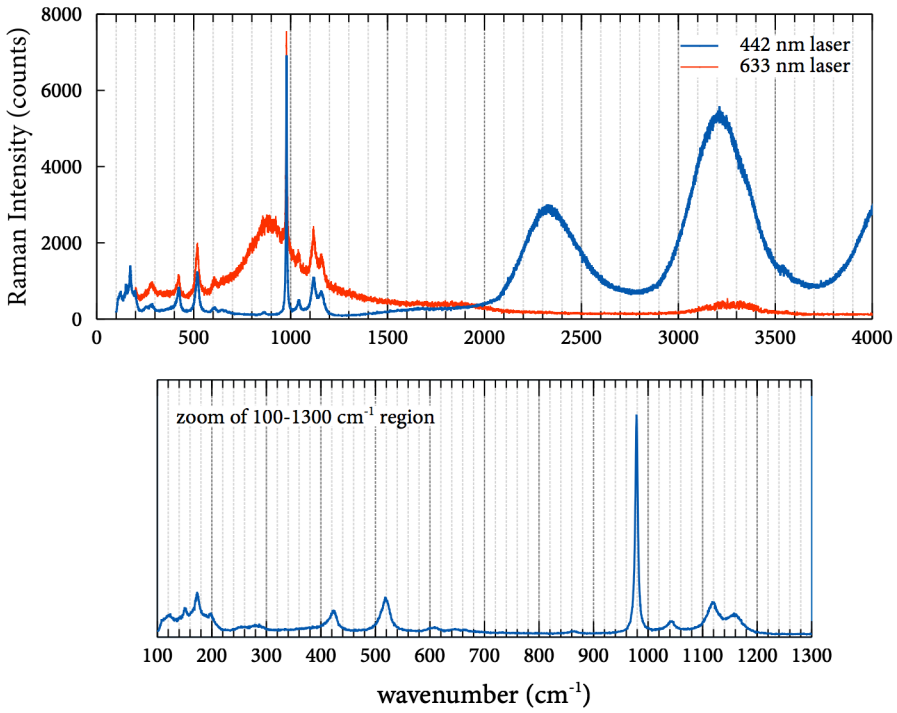

Figure B.7: Raman spectrum for uranous sulfate octahydrate, complex **2**, 442 and 633 nm lasers, showing fluorescence. Sample: 57-S.

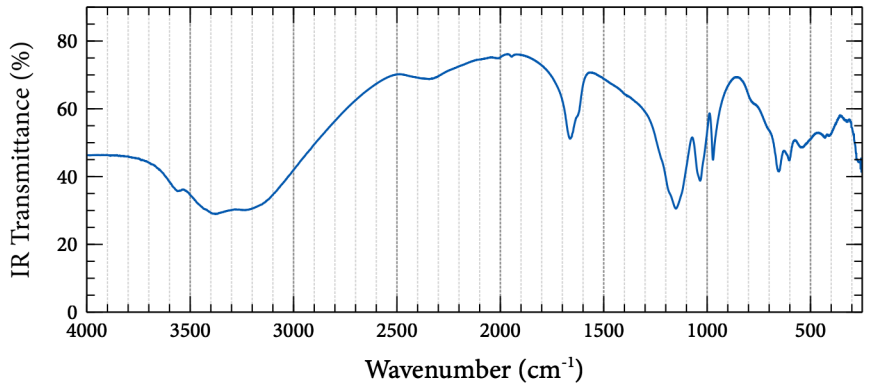

Figure B.8: FTIR spectrum of uranous sulfate octahydrate, complex **2**. Sample: 57-S.

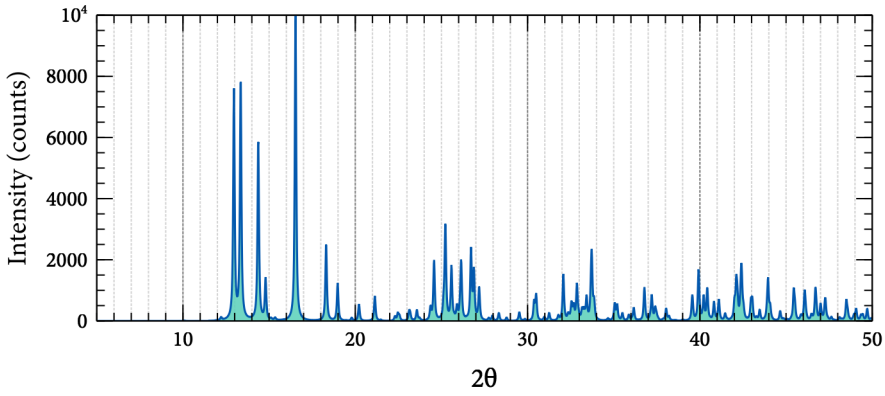

Figure B.9: Powder XRD spectrum of uranous sulfate octahydrate, complex **2**, simulated from the crystal structure presented in Chapter 4 using Mercury 3.1 [53] (Cu source).

B.4 *Parisaite*

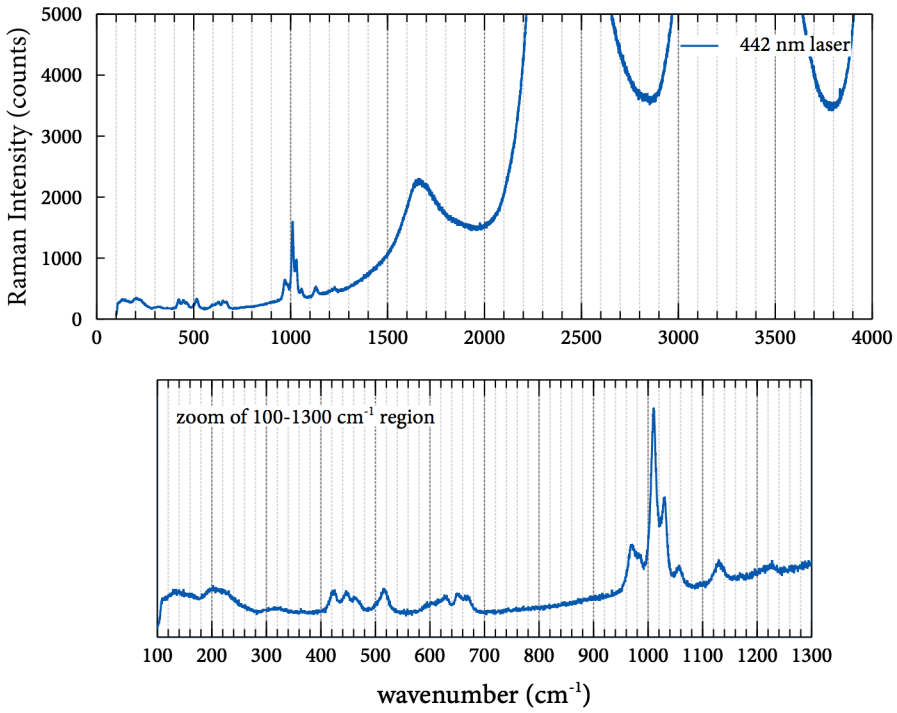

Figure B.10: Raman spectrum for uranous sulfate octahydrate, complex **2**, 442 nm laser, showing fluorescence. Sample: 29-B.

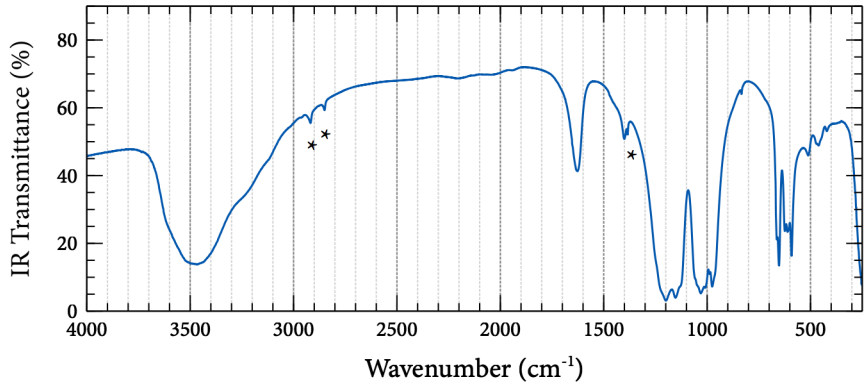

Figure B.11: FTIR spectrum of *parisaite*. * marks signals originating from the matrix, not the sample. Sample: 29-B.

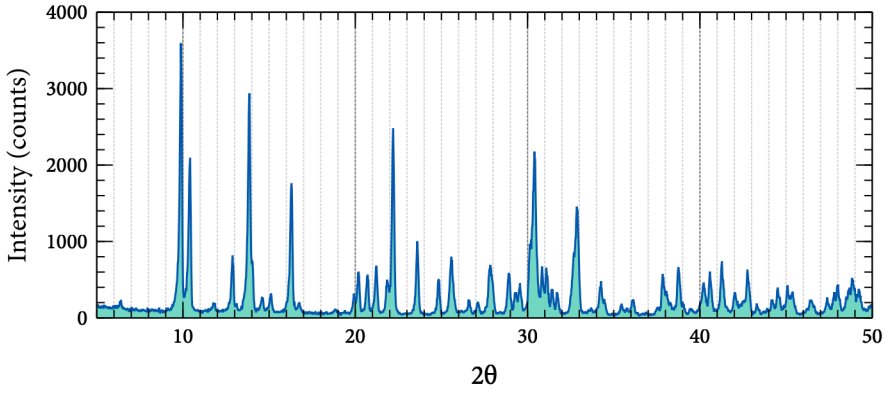

Figure B.12: Powder XRD spectrum of uranous sulfate octahydrate, complex **2**, using Cu source. Sample: 29-B..

Appendix C

Total sulfate determination

Summary

Total sulfate was determined by titration with lead perchlorate, which causes the precipitation of lead sulfate. Uranium interferes with the electrode response, so it is first removed by hydrogen peroxide precipitation at ~pH 5. The titration is conducted in 85 % isopropanol to reduce the solubility of lead sulfate to negligible levels. A Pb^{++} ion-selective electrode is used to detect the endpoint, which manifests as a sharp increase in potential indicating the presence of Pb^{++} when all of the sulfate has precipitated.

This method is based on a method published by Metrohm titled *Titrimetric determination of sulfate* [57].

Reagents

- Deionized water
- Hydrogen peroxide (1 %)
- Ammonium hydroxide (10 %)
- Isopropanol
- Methyl red (0.02 wt. % in 60 vol. % ethanol)
- Lead perchlorate solution (0.010 mol L^{-1} in 85 % isopropanol)

Equipment

- 50 mL volumetric flask
- Pb^{++} ion-selective electrode
- Double-junction reference electrode with KNO_3 outer filling solution
- Automatic titrator capable of potentiometric titration
- 0.45 µm syringe filter
- 5 mL plastic syringe and narrow tubing
- 150 mL beaker
- 1-inch PTFE stir bar

Method

The initial sample for analysis should be an aqueous acidic solution containing no less than $4\,g\,L^{-1}$ sulfate and any amount of uranium. If the sample for analysis is a solid, it can be first digested first in nitric acid, and all transfers and dilutions should be measured by mass to obtain the best accuracy.

Step I: Uranium removal

1. To the 50 mL volumetric flask add an aliquot of sample containing approximately 100 mg of sulfate.
2. Add enough 1 % hydrogen peroxide to oxidize any uranium(IV) to uranium(VI) and to precipitate all uranium as $UO_3 \cdot H_2O_2$, leaving approximately 0.05 % excess peroxide.
3. Partially neutralize the solution with the 10 % ammonia solution using a dropper, swirling frequently to mix. When the solution shows a hint of cloudiness from uranium precipitation, add 3–5 drops of methyl red indicator and continue neutralizing with ammonia until the colour changes from orange/red to canary yellow. Caution: ammonia is toxic. Use proper ventilation.
4. Dilute to 50 mL with deionized water. Mix well, and then allow the solids to settle, at least 10 min. The uranium-containing precipitate should be yellow, and the sulfate-containing supernatant should be clear.
5. Using the syringe and narrow tube, withdraw the supernatant and filter it though the syringe filter into a labeled sample bottle. Discard the first 5 mL

of filtrate.

Step II: Sulfate determination

1. Pipette a 3 mL aliquot of the filtered uranium-free sample into a 150 mL beaker with a 1-inch stir-bar. Add 70 mL of isopropanol and 9 mL of deionized water.
2. Polish the Pb^{++} ion-selective electrode, if necessary.
3. Immerse the electrodes and allow several minutes to reach equilibrium. The starting potential should be between -200 and 0 mV.
4. Titrate with lead perchlorate in 0.1 mL doses. A white lead sulfate precipitate will form with each dose, until all of the sulfate is consumed. The endpoint is indicated by a rapid increase in potential associated with the appearance of unprecipitated Pb^{++} ions, which should appear as a peak in the differential data.

Appendix D

Analysis of acidic metal sulfate solutions for sulfuric acid using a pH electrode and standard addition

Berend Wassink
The University of British Columbia
Department of Materials Engineering

February 1998

Analysis of aqueous metal-containing solutions for acid is complicated by the propensity of many metal ions to hydrolyze and produce acid. Standard titration methods are generally obviated since hydrolysis in many cases may be extensive at pH values well below 7. The higher the hydrolyzable metal ion concentration is relative to the acid concentration, the more serious the problem. Measurement of pH in strongly acidic, high metal concentration solutions is complicated by the high ionic strength of the solution and possible non-linear response of the pH electrode. In addition, in a high sulfate medium, sulfuric acid may not be fully dissociated. Calibration of the electrode response with solutions containing precisely known concentrations of the various metal salts may be workable, however it is often the case that the composition of samples is neither fully known, nor constant. One possible

approach to the problem is to use the method of standard addition. (See for example D.C. Harris *Quantitative Chemical Analysis* W. H. Freeman and Co, 3rd edn. 1991, p. 377-8.)

The pH electrode is used like any other ion selective electrode. The response is recorded in mV rather than in pH units. The electrode is calibrated with standards containing known acid concentrations (e.g., H_2SO_4) in a high ionic strength solution. Only the "slope" (e.g., mV/g/L H_2SO_4) of the electrode is required. The sample of interest is then diluted into the same high ionic strength medium. The electrode response of a known volume of sample is recorded. Next a small volume of known acid is added. The addition should not significantly change the ionic strength. The electrode response is recorded again. If desired further additions of standard acid may be made.

The concentration of acid may be calculated based on the Nernst equation as follows:

$$E_0 = E^* + m \log C_0 \tag{D.1}$$

$$E_1 = E^* + m \log \left(\frac{C_0 V_0 + C_s V_s}{V_0 + V_s} \right) \tag{D.2}$$

E_0	mV reading of the sample
E^*	constant
E_1	mV reading of sample plus spike of standard acid
m	electrode slope (from calibration) in mV/concentration units
C_0	unknown acid concentration in *diluted* sample
V_0	sample volume (mL)
C_s	standard acid concentration (units must be the same as those used for calibration)
V_s	spike volume (mL)

Subtracting Eqs. (D.1) and (D.2):

$$E_1 - E_0 = m \log \left(\frac{C_0 V_0 + C_s V_s}{(V_0 + V_s) C_0} \right) \tag{D.3}$$

Rearranging this gives:

$$C_0 = \frac{C_s V_s}{\left[(V_0 + V_s)\, 10^{(E_1 - E_0)/m}\right] - V_0} \tag{D.4}$$

If more than one spike is added, V_s refers to the total volume of standard acid added. The initial value for E_0 is used for calculating the original acid concentration C_0 after each spike. The results may be averaged. These equations assume a constant activity coefficient for the proton under analysis conditions. If the ionic strength is relatively high and constant, this condition is adequately fulfilled.

A high quality electrode is essential. As will be seen later, ± 1 mV can easily lead to errors on the order 10%. A pH meter with a resolution of 0.1 mV is desirable. Electrodes must be handled with care to avoid scratching or static charging. The glass bulb may be blotted dry, but never rubbed. The requisite procedures for use and maintenance of the electrode, as appropriate, should be consulted. The electrode must be clean and free of excess moisture to avoid contamination or dilution of the sample. Solutions need to be gently stirred to facilitate equilibration. The electrode response is temperature sensitive. The sample and standards should be at about the same temperature. Magnetic stirrers can generate enough heat to warm the sample significantly. Insulation (e.g., a piece of wood) and a thermostatted water bath are advisable. Enough time is required to acquire a stable reading. This may take 3–5 minutes. Spike acid amounts should be in the range of 50-200% of that in the original sample.

Sample dilution may be necessary to lower the sample ionic strength relative to the matrix background (i.e., a salt at high concentration). This may be required to ensure that the calibration slope is applicable to the samples. However, excessive dilution can lead to errors due to a rise in the pH and metal ion hydrolysis. Thus a dilution should be employed such that the proton concentration remains in excess of 0.01 M. Systems capable of buffering (e.g., $H_2SO_4 - SO_4^{2-}$ and $HCl - Cl^-$ and any weak acids) require special caution.

Procedure for H_2SO_4–metal sulfate solutions

The method has been tested with 0.5–0.93 N H_2SO_4 (25–45 g/L) with varying metal ion concentrations. Reagents and standards include the following:

- $MgSO_4 \cdot 7\,H_2O$ (certified ACS grade or better)
- 0.01, 0.075 and 0.2 N H_2SO_4 standards in 2 M $MgSO_4 \cdot 7\,H_2O$ (493 g/L)
- 0.650 N H_2SO_4 in 2 M $MgSO_4 \cdot 7\,H_2O$ (493 g/L)

Prepare the standards. Store in plastic bottles and have a one inch stir bar in each. Dilute your samples so that they contain 0.015–0.065 N H_2SO_4 (0.74–3.2 g/L) and 2M $MgSO_4 \cdot 7\,H_2O$. Use a water bath at constant temperature (25°C or less) to thermostat the standards. The temperature of samples and standards should be within 0.5°C of each other. Measure the mV response of a high quality pH electrode to each standard starting at the most dilute one. Allow a consistent time (3–4 minutes) for the reading to stabilize. Constant drift may be indicative of temperature drift or meter or electrode malfunction. A meter with a resolution of 0.1 mV is preferable. A meter with only 1 mV resolution will give less precise results. The electrode must be clean and dry before immersing it in the solution. Gently blot dry the bulb. Do not rub it. It can be easily damaged. Plot the mV readings versus $\log_{10}$ of the acid concentrations. The slope of the graph is the electrode slope.

Pipette 50.00 mL of a sample into a clean dry 100 mL beaker containing a stir bar. Ensure that the sample is at the same temperature as the standards. Measure the mV reading of the clean and dry pH probe immersed in the solution. Allow a few minutes for equilibration. Add a known volume of the standard acid (0.650 N H_2SO_4 in 2 M $MgSO_4 \cdot 7\,H_2O$. The amount added should be in the range of 50-100% of that in your diluted sample. Record the mV reading. Calculate the acid concentration in your sample from Eq. (D.4) and the sample dilution factor. If desired a second spike may be added and the results averaged. The results described below do not suggest a significant advantage to this. The mV readings for the diluted sample and after additions of spikes must fall within the calibration range.

Results and discussion

The presence of high $MgSO_4 \cdot 7\,H_2O$ in samples, standards and spikes provides a high and relatively constant background sulfate concentration. This facilitates the high ionic strength required and mitigates the interfering effects of relatively low, but variable sulfate levels. $MgSO_4 \cdot 7\,H_2O$ is a convenient choice since Na^+ and K^+ salts of sulfate are not soluble enough. The +2 charge on Mg^{2+} also provides a higher ionic strength. The samples are diluted so that they are within the calibration range. This also lowers the sample sulfate concentration to a value that is small relative to the background sulfate. The acid concentration in the spikes must be high enough to allow addition of a fairly small, but practical volume. However, it cannot be too high since this would result in a substantial volume of mixing error. It is important that the volume of sample plus spikes be accurately known. The accuracy of the method is limited by a number of factors. The two most significant are the intrinsic imprecision associated with pH probes and the fact that standard addition is essentially an extrapolation. An uncertainty of only ± 0.2 mV in a single reading results in an uncertainty of $\sim\pm 1\%$ in concentration associated with that reading. At least two readings are required to ascertain the electrode slope. A further two are needed to establish the concentration. Errors in the readings associated with a sample analysis may be amplified by the extrapolation, i.e., relating back to the initial sample prior to standard addition. Thus precision on the order of 1–5% may be reasonably expected.

Results for three solutions are presented below. These are classified as low acid–high metal, medium acid–medium metal and high acid–low metal samples. *Note that the analyst must verify the validity of the method for particular solution compositions not within the scope of this work.* Solution compositions are shown in Table D.1. Sulfate due to sulfuric acid ranged from 30–62% of total sulfate.

Results for the analysis of the above three samples are presented in Table D.2. Associated calibration data are shown in Table D.3 and Fig. D.1. The equipment used was a Fisher Accumet pH probe (glass body, ceramic junction and refillable, a Corning pH meter with 0.1 mV resolution and a Radiometer ABU80 autoburrete for the spikes. A thermocouple was used to measure temperatures of the samples and to control them within $\pm 0.3^\circ$C.

Table D.1: Solution compositions for testing H_2SO_4 analysis by pH electrode (g/L).

Species[a]	Low Acid- High Metals	Medium Acid- Medium Metals	High Acid- Low Metals
Al^{+3} (g/L)	2.66	2.0	1.33
Co^{+2}	0.80	0.60	0.40
Fe^{+3}	3.99	3.0	2.0
Mg^{+2}	2.00	1.5	1.0
Mn^{+2}	4.66	3.5	2.33
Ni^{+2}	7.98	6.0	4.0
H_2SO_4	24.52 (0.500 N)	36.78 (0.750N)	45.43 (0.9264 N)
Total SO_4^{2-} from metals	54.9	41.3	27.5
Total SO_4^{2-}	78.9	77.3	72.0

[a] all metals added as sulfate salts.

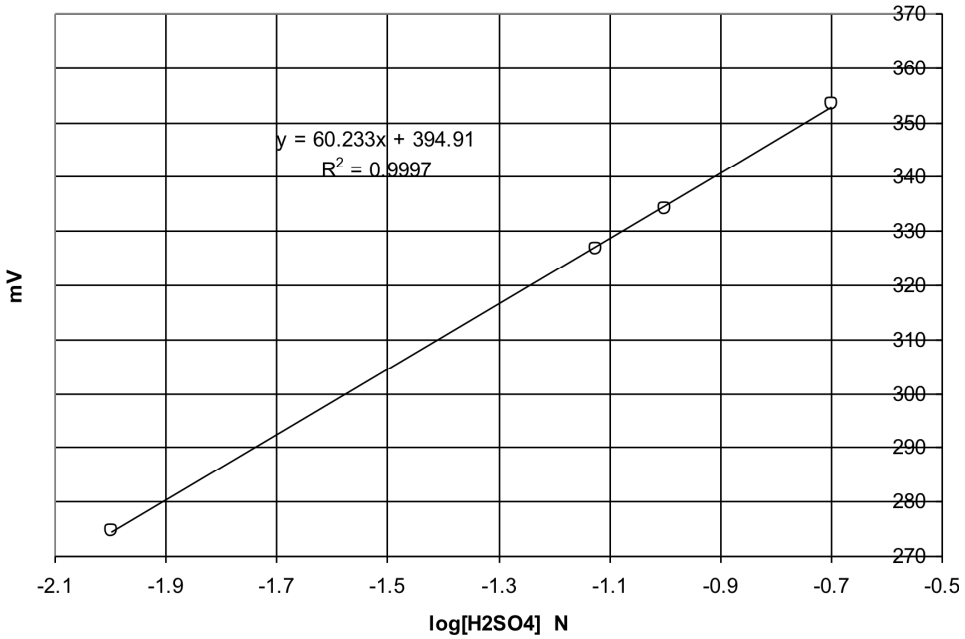

Figure D.1: Calibration plot for H_2SO_4 standards in 2 M $MgSO_4$; 0.1 mV resolution

Table D.2: Analytical results for analysis of H_2SO_4–metal sulfate solutions using a meter with 0.1 mV resolution.

Sample	E_0 mV	Spike Vol. mL[a]	E_1 mV	Analyzed $[H_2SO_4]$ N	Actual $[H_2SO_4]$ N	Accuracy %
Low acid- high metals	299.5 299.5	3.014 5.994	322.1 333.1	0.517 0.512	0.500 24.5 g/L (0.025 N	103.4 102.3
(Average)				(0.514) (25.2 g/L)	in diluted sample)	(102.9)
Medium acid- medium metals	311.0 311.0	3.029 6.491	328.3 338.9	0.747 0.739	0.750 36.8 g/L (0.0375 N	99.6 98.6
(Average)				(0.743) (36.4 g/L)	in diluted sample)	(99.1)
High acid- low metals	316.2 316.2	2.984 7.013	330.7 341.6	0.919 0.907	0.9264 45.4 g/L (0.04632 N	99.2 97.9
(Average)				(0.913) (44.8 g/L)	in diluted sample)	(98.5)

[a] second spike volume refers to the total added; two spikes added per sample
Other conditions:
Electrode slope = 60.233 mV
Sample volume = 50.00 mL
Dilution: 5.00 mL to 100.0 mL in 2 M $MgSO_4$ as $MgSO_4 \cdot 7H_2O$
Spike composition: 0.650 N H_2SO_4 (31.875 g/L) + 2 M $MgSO_4$.
Equilibration time: 3 minutes

Table D.3: Calibration data for analytical results in Table D.2.

$[H_2SO_4]$ N	$[H_2SO_4]$ g/L	$\log_{10}[H_2SO_4]$ N	mV reading
0.0100	0.4904	-2.000	274.7
0.0750	3.678	-1.1249	326.8
0.100	4.904	-1.000	334.1
0.200	9.808	-0.6990	353.5

Note: standards contain 2 M $MgSO_4$ as $MgSO_4 \cdot 7H_2O$
Equilibration time: 3 minutes
Slope = 60.233 mV

The data suggest that fairly good analyses can be obtained with the types of solutions used. Accuracies of 98–103% were found. There might be a trend toward slight overestimation of low acid concentrations in the presence of relatively high metal sulfate concentrations, and underestimation for high acid–low metal solutions. This would need to be verified. Close inspection of the calibration data suggests a slight curvature. A second order equation fit the data very well. However, calculation of the slopes at points in the middle of the mV range for sample plus spike resulted in poorer accuracy. Linear fitting of the data and use of a constant slope value seems to yield the best results. Possible curvature of the calibration plot may mitigate against extending the useful range to higher acid concentrations. Higher $MgSO_4$ concentrations might be worth investigating to give a higher background sulfate level and ionic strength. Lower concentrations may not be practical due to metal ion hydrolysis. *Treating the data for the standards as an ordinary calibration curve yielded quite poor analytical results*. The matrix effects appear to be significant and this is best overcome by standard addition. It would seem plausible that the higher the proportion of acid compared to metal sulfates, the more accurate the analysis should be. The lowest acidity solution contained 2.3 times as much sulfate from metal sulfate salts as that due to the H_2SO_4. This still proved amenable to analysis by this method. Cases where the acid content relative to the metals is lower would need to be checked first to see if the method is applicable. The higher the proportion of metal sulfates, the more serious the problem of metal hydrolysis.

Data for the analysis of the same solutions using a meter with 1 mV resolution is presented in Table D.4. Calibration data are presented in Table D.5 and Fig. D.2. The results show that poorer precision may be anticipated than when a meter with 0.1 mV resolution is used. It is up to the analyst to determine if this is acceptable. A ± 1 mV uncertainty in the mV reading can produce 7–9% uncertainty in the result for the analyses in Table D.4. The extent of the uncertainty depends in the magnitude of the difference between the initial and spike mV readings.

Table D.4: Analytical results for analysis of H_2SO_4–metal sulfate solutions using a meter with 1 mV resolution.

Sample	E_0 mV	Spike Vol. mL[a]	E_1 mV	Analyzed $[H_2SO_4]$ N	Actual $[H_2SO_4]$ N	Accuracy %
Low acid- high metals	288 288	2.777 6.785	309 323	0.535 0.534	0.500 24.5 g/L (0.025 N in diluted sample)	107.1 106.7
(Average)				(0.534) (26.2 g/L)		(106.9)
Medium acid- medium metals	298 298	3.014 7.012	315 327	0.764 0.747	0.750 36.8 g/L (0.0375 N in diluted sample)	101.9 99.6
(Average)				(0.756) (37.0 g/L)		(100.7)
High acid- low metals	303 303	3.003 7.028	318 328	0.891 0.935	0.9264 45.4 g/L (0.04632 N in diluted sample)	96.1 100.9
(Average)				(0.913) (44.8 g/L)		(98.5)
Low acid- high metals *(Sample diluted 3 mL to 100 mL)*	273 273	1.400 2.914	294 305	0.471 0.489	0.500 24.5 g/L (0.015 N in diluted sample)	94.3 97.9
(Average)				(0.480) (23.6L)		(96.1)

[a] second spike volume refers to the total added; two spikes added per sample
Other conditions:
Electrode slope = 60.464 mV
Sample volume = 50.00 mL
Dilution: 5.00 mL to 100.0 mL (unless otherwise noted) in 2 M $MgSO_4$ as $MgSO_4 \cdot 7H_2O$
Spike composition: 0.650 N H_2SO_4 (31.875 g/L) + 2 M $MgSO_4$.
Equilibration time: 4 minutes

Table D.5: Calibration data for analytical results in Table D.4.

$[H_2SO_4]$ N	$[H_2SO_4]$ g/L	$\log_{10}[H_2SO_4]$ N	mV reading
0.0100	0.4904	-2.000	263
0.0750	3.678	-1.1249	315
0.100	4.904	-1.000	323
0.200	9.808	-0.6990	342

Note: standards contain 2 M $MgSO_4$ as $MgSO_4 \cdot 7H_2O$
Equilibration time: 4 minutes
Slope = 60.464 mV

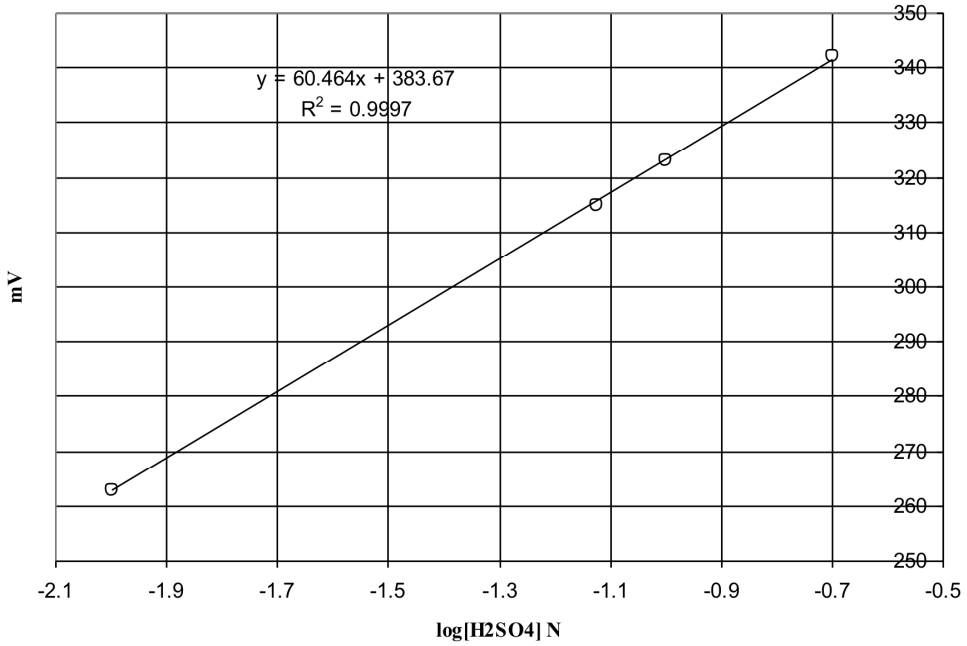

Figure D.2: Calibration plot for H_2SO_4 standards in 2 M $MgSO_4$; 1 mV resolution

Appendix E

Oxidation kinetics worksheet

The operational worksheet and checklist included on the following pages was used for each experiment described in Chapter 7.

Oxidation Study Checklist
v.1.1 May 26, 2014, A.B.

OX-_____

Date	_____	T	_____	°C
Matrix	_____	[U_T]	_____	mM
Gas	_____	[Acid]	_____ M	_____ N

Date/time of test solution creation _____
Date/time added to reactor with N_2 _____

Notes:

T-Log Start Time	_____	Initial Samples	Final Samples
Reaction Start Time	_____	AQU-	AQU-
Reaction End Time	_____	FA-	FA-
STK [U(IV)]	_____	ICP-	ICP-
Bubbler I =	_____	SUL-	
Full scan cycle time	_____		

Periodic Sampling

Sample ID	Sampling Time	Elapsed Time, s	Sample Vol., mL	Frozen?	[U(IV)], M	
					UV-Vis	Titration

Calibration Curve and UV-Vis

Std. #	Abs.

Wavelength: 650.9 nm

Background cell: _____

Oxidation Study Checklist
v.1.1 May 26, 2014, A.B.

OX-_____

Part 1 – Day-Before Preparations

	Get the worksheet	Discuss with Alex which test(s) will be done tomorrow.
	Assemble the reactor	If not already done, assemble the reactor
	Check reagents	Check that there is enough of the U(IV), U(VI), acid, and $MgSO_4$ solutions. If not, prepare them.
	Partially prepare standards	Set out and label volumetric flasks for the standards, as described on the worksheet. Introduce the acid and U(VI) solutions as described, and insert the stopper. Set aside for tomorrow. Do not add U(IV).
	Partially prepare test solution	Similar to preparing the standards, but for the test solution. Add the acid and U(VI) solution to the 500 mL flask and insert stopper. Set aside for tomorrow.
	Prepare sample bottles	As needed, prepare the AQU, FA, ICP and SUL sample bottles. Fill out the computer worksheets and label the bottles. Set aside for tomorrow.
	Install cell holders	Install the 100mm cell holders into the UV-Vis.
	Set out bubbler	Set out the bubbler with the closest ionic strength to tomorrow's test solution.
	Refill water bath	Fill the heating water bath to the line with deionized water.
	Check gas cylinders	Check that there is enough oxygen, air, and nitrogen in the gas cylinders. Make sure they are turned off at the tank at the end of the day.

Part 2 – Morning Checks and Startup

	Check reactor tubing	Check that the reactor inlet and outlet tubes are secure. Check that the UV-Vis circulating lines are all connected. Check that the water bath return line is pointed into the water bath.
	Check reactor body	Check that all instruments are in place through the ports in the lid. The reactor should be level and high. Check that the impeller is free-spinning.
	Check chiller tubing	Check that the chiller return line points into the bath. Check that the chiller circulating lines are connected to the lines leading into the AA room, and that there are no kinks in the line.
	Turn on chiller	Turn on the chiller. Set the temperature to 12°C for >=20°C tests, and to 5°C for colder tests. Verify that the return line is flowing.
	Turn on water bath	Turn on the heating water bath. Set 2°C higher than the test temperature.
	Install bubbler	Top up the bubbler to 200 mL if necessary. Place the bubbler in the water bath. Connect the reactor gas lance to the bubbler outlet. Connect the nitrogen line to the bubbler inlet. Record the ionic strength of the bubbler on the worksheet.
	Turn on UV-Vis	Turn on the UV-Vis (green switch) and computer. Once it has warmed up, start the software "UV Winlab".

OX-_____

Part 3 – Solution, Standard, and Reactor Preparation

	Finish making test solution	Mix up the test solution in a 500 mL volumetric flask according to the recipe on the worksheet.
	Turn on nitrogen	Turn on the nitrogen to 100 cc/min.
	Pour test solution into reactor	Using the funnel, pour the test solution into the reactor. Check that nitrogen is bubbling.
	Turn on gentle stirring	Turn on the stirrer to a low setting. It should be enough to agitate the solution for good heating/cooling, but not enough to cause churning.
	Turn on T-controller	Switch on Omega temperature controller. Ensure the USB cable labeled "solenoid controller" is plugged into the computer. Open the program "CN7-A", and check that "COM Status" is green. Check that it is reading the proper temperature.
	Configure T-controller	In the "CN7-A" software, click "Read Configuration from File". Load the config file that matches the temperature of the test. The files are located in /Documents/Omega Configurations/. Click on "Send Configuration to Instrument". Listen for the clicking sound of the solenoid.
	Finish making standards	Add the U(IV) stock solution to the pre-prepared standard flasks. Be very careful to avoid oxidation, using a nitrogen blanket when possible.
	Pre-heat standards	Put the tightly-capped standard flasks into the water bath.
	Fill background cell	Fill a 20mm quartz cell with the specified background solution, and place in the reference cell holder of the UV-Vis.
	Connect flow cell	Connect the 20mm flow-through cell, with the white fitting on the side with the arrow.
	Increase N_2 flow	Increase nitrogen flow to 300 cc/min.
	Stirrer 700 rpm	Set the stirrer to 700 rpm.

Part 4 – Calibration

	Open method	In the UV Winlab software, open the method /AlexB/"U(IV) Oxidation Calibration"
	Fill in sample info	Fill in the standard names (Std2, Std3, etc.), and "reactor" for the final sample. Also fill in the concentrations of the standards listed on the worksheet.
	Connect sipper and disconnect return line	Disconnect the pump from the reactor and attach the sipper straw. Disconnect the return line from the reactor and point it into a beaker.
	Conduct calibration	Press "Start" and follow the on-screen instructions. Take care to keep the standards in the water bath as long as possible. Flush the cell with air between standards.
	Reconnect tubes	Reconnect the sampling and return lines to the reactor. Turn on pump at full speed.
	Measure initial reactor absorbance	Wait 60 seconds before taking the reading for initial absorbance. Leave the circulation pump running.
	Check calibration curve	Check the calibration curve under Beer's Law → Calibration and make sure it is linear.
	Save file and exit	File → Save Results As → "OX-## Calibration". Exit the calibration window.

OX-_____

Part 5 – Startup

	Load and configure the UV-Vis Method	Open the method /AlexB/"Timedrive U(IV) Oxidation". Change the Sample ID to "OX-##". Change the sampling interval and total time to whatever is appropriate for this test.
	Start T log	Start the temperature log in the CN7-A software. Log in 5-second intervals, 10 hour log time. Record the exact time when the log was started on the worksheet.
	Set oxygen flow	Turn on the oxygen tank and adjust the outlet pressure to 50 psi. Adjust the flow rate to 110 mm, or what is described on the worksheet.
	Stop oxygen flow	Stop the oxygen flow with the valve after the regulator.
	Disconnect nitrogen	Disconnect the nitrogen line from the bubbler.
	Connect oxygen	Connect the oxygen line to the bubbler. Since the valve is off, there should be no gas flow.
	Take sample	***FLUSH THE SAMPLING PORT.*** Take a ~30 mL sample into the pre-labeled bottle "OX-## Initial".
	Start UV-Vis Log	Press "Start" in UV Winlab.
	Conduct baseline correction	Conduct the baseline correction as instructed on the screen.
	Start test - Start oxygen flow - Start UV-Vis log - Record start time	Start the oxygen flow, start the UV-Vis log, and record the exact start time as close to simultaneously as possible.
	Check oxygen flow	Check the oxygen flow and adjust to 110 mm, or what is prescribed on the worksheet, if necessary.

Part 6 – During Test

	Take periodic samples, if required	Either titrate immediately for U(IV) or freeze in liquid nitrogen for future analysis. Record samples on the worksheet.
	Turn off nitrogen	Turn off the nitrogen tank, both at the tank and the valve.
	Prepare samples	Prepare Free Acid, ICP, Sulfate analysis samples on the "OX-## Initial" sample. Record the sample names (AQU-###, etc.) on the worksheet.
	Clean up	Wash glassware, wash and dry pipettes, tidy lab bench.
	Monitor the test	Periodically check on the test. Ensure that the UV-Vis log will not run out of time. Watch for blockages in the UV-Vis return line. Monitor the temperature to ensure it stays ±0.1°C.

Part 7 – Shutdown

	Record time	Record the exact time of the shutdown
	Turn off oxygen	Turn off the oxygen tank
	Take sample	***FLUSH THE SAMPLING PORT.*** Take a final sample into the pre-labeled sample bottle.
	Save UV-Vis file	Stop the test. File → Save Results → Save as a New Task → "OX-##".
	Save temperature file	Stop the Omega temperature control log. Export the data to Dropbox → Other Lab Files → "OX-## Temperature Log.csv".
	Turn off instruments	Shut off the agitator, water bath, UV-Vis pump, chiller, temperature controller, and computer.

OX-_____

Part 8 – Post-production

	Final analysis	Prepare Free Acid and ICP analysis samples on the final reactor sample.
	Turn off N_2 and O_2	Ensure the oxygen and nitrogen tanks are closed.
	Put away bubbler	Attach the lid to the bubbler solution and put away in the cupboard.
	Clean reactor	Empty and dispose of the spent solution. If the next test will be substantially different than this one, or if the reactor will not be used soon, rinse it thoroughly with D.I. water. Suck out as much water as possible with the pump and dry with a paper towel as much as possible.
	Clean reference cell	Empty the reference cell and flush with D.I. water several times. Allow to try upside down on a Kimwipe with a beaker over top to protect it from dust.
	Clean flow cell	Run D.I. water through the flow-through cell. If it is not being used tomorrow, flush with 5M nitric acid, and then again with D.I. water. Disconnect and store in its case.
	Clean U(IV) transfer beaker	Empty remaining liquid to waste, clean, hang upside down to dry.
	Copy data to Dropbox	Copy the test and calibration data to Dropbox via a USB key.
	Return sheets to Alex	Ensure all fields are filled out, then staple and return the worksheet and checklist to Alex.

Appendix F

Radioactive uranium safe handling procedures

Samples were prepared from natural uranium in a radioisotope-certified laboratory by researchers trained in the hazards of radiation. Although the specific activity of natural uranium is relatively low, the reader should be aware that additional safety precautions are necessary when handling any radioactive substance.

Background information

There are three main types types of ionizing radiation: alpha particles, which are helium nuclei; beta particles, which are high-speed electrons; and gamma-type, which are high-energy x-rays and gamma-rays. Natural uranium contains a mixture of three isotopes, all of which are radioactive: ^{238}U (99.27%), ^{235}U (0.72%), and ^{234}U (trace amounts). All have relatively long half-lives exceeding ten thousand years.

All three natural isotopes of uranium are alpha-emitters. Alpha radiation travels only a short distance in air (approximately 5 cm), and can be stopped by a piece of paper or human skin. Alpha emitters can be harmful to human health if they come into close proximity with exposed living tissue, such as in the lungs or gut. They are generally not considered harmful for external exposure.

The decay products of uranium are themselves radioactive, and some are alpha and gamma-emitters. These products build up in natural uranium over time until

pseudo-steady state equilibrium is reached. These products can be more harmful to human health than the uranium itself. The decay product radon, which is a gas (and therefore easy to inhale), can be particularly harmful.

A table of the natural uranium isotopes, their natural abundances, half-lives, and radiation types are given in F.1.

Table F.1: Isotopic abundance, half-life, and emission types for natural uranium. Reference: CRC Handbook, Lide [48].

Isotope	Natural abundance, atom %	Half-life, years	Radiation type
^{234}U	0.0054	2.455×10^5	α
^{235}U	0.7204	7.04×10^8	α
^{238}U	99.2742	4.47×10^9	α

Licensing and training

The laboratory was licensed to work with radioisotopes under the consolidated UBC radiation licence by the UBC radiation safety officer. The licence was issued pursuant to section 24 of the *Nuclear Safety and Control Act*.

All researchers who worked directly with uranium in the laboratory, including summer students, took the UBC Radionuclide Safety and Methodology course, including the receiving of Class 7 dangerous goods.

All shipments of uranium-containing materials, including laboratory samples and waste, were packaged and inspected by a person certified in the shipment of Class 7 dangerous goods, with training provided by the British Columbia Institute of Technology (BCIT).

Source of uranium

All uranium used for test work was obtained from Cameco Corporation, in the form of UO_3 and UO_2. The UO_3 and UO_2 had been through a metallurgical refining process to make it suitable as nuclear fuel, a process which removed most of the natural decay products such as radium and radon. This process did not affect the natural ratio of uranium isotopes. This refined natural uranium was therefore safer

(i.e., less radioactive) than unrefined natural uranium. It could also be considered a nearly pure alpha emitter. A total quantity of 10 kg of contained uranium was sent from Cameco to UBC for test work.

Sample storage

Solid and liquid samples were stored in sealed glass and plastic bottles in a cupboard under the laboratory bench in Frank Forward 406. The wooden door to the cupboard was kept closed when not in use. Small working quantities of uranium-containing solids and solutions were stored on the lab bench for short periods of time during experiments. One bottle of UO_3 containing at most 1 kg of contained uranium was also stored under the lab bench.

As an added precaution, the remainder of the UO_3 and UO_2 was stored in a lead-lined box specifically built to house radioactive samples.

Routine checks and precautions

The laboratory work benchs were covered with either a chemically-resistant epoxy coating or a stick-on PTFE teflon sheet to ease cleaning and prevent the contamination of the underlying surfaces. The laboratory work area and all equipment was cleaned regularly with soap and water. A Geiger–Müller counter was used to check that the work environment within the acceptable limit for radiation. Wipe tests to check for radioactive contamination were conducted periodically on all work areas. These were analyzed at the UBC radiation safety office in the UBC hospital.

Waste management

Uranium-containing aqueous and solid wastes were segregated and stored in a 20 L plastic pail. When full, the contents were neutralized to pH 6–8 with sodium hydroxide. The neutralized aqueous supernatant was sent to UBC waste management for final disposal, while the uranium-containing precipitates was collected for shipment back to Cameco Corporation's Rabbit Lake mine site for disposal by TDG-certified courier. The shipments complied with all relevant packaging and external radiation regulations.